

<https://doi.org/10.15388/vu.thesis.562>

<https://orcid.org/0000-0002-5476-2946>

VILNIUS UNIVERSITY

CENTER FOR PHYSICAL SCIENCES AND TECHNOLOGY

Gintarė Gečė

Search, Synthesis, and Investigation of New Framework Electrode Materials for Aqueous Na-ion Batteries

DOCTORAL DISSERTATION

Natural Sciences

Chemistry (N 003)

VILNIUS 2023

The dissertation was prepared between 2019 and 2023 at the State Research Institute Center for Physical Science and Technology.

Academic supervisor – Dr. Linas Vilčiauskas (State Research Institute Center for Physical Science and Technology, Natural Sciences, Chemistry, N 003)

Academic consultant – Dr. Jurgis Pilipavičius (State Research Institute Center for Physical Science and Technology, Natural Sciences, Chemistry, N 003)

This doctoral dissertation will be defended in a public/closed meeting of the Dissertation Defense Panel:

Chairman – Prof. Habil. Dr. Eimutis Juzeliūnas (State Research Institute Center for Physical Science and Technology, Natural Sciences, Chemistry, N 003).

Members:

Prof. Dr. Henrikas Cesiulis (Vilnius University, Natural Sciences, Chemistry, N 003),

Dr. Arūnas Jagminas (State Research Institute Center for Physical Science and Technology, Natural Sciences, Chemistry, N 003),

Dr. Gints Kučinskis (University of Latvia, Natural Sciences, Physics, N 002),

Prof. Dr. Simas Šakirzanovas (Vilnius University, Natural Sciences, Chemistry, N 003).

The dissertation shall be defended at a public meeting of the Dissertation Defense Panel at 14:00 on December 15th, 2023 in Room A101 of the Center for Physical Science and Technology.

Address: Saulėtekio av. 3, LT-10257, Vilnius, Lithuania.

Tel. +370 5 264 8884; e-mail: office@ftmc.lt

The text of this dissertation can be accessed at the Center for Physical Science and Technology and Vilnius University libraries as well as on the website of Vilnius University:

www.vu.lt/lt/naujienos/ivykiu-kalendorius

<https://doi.org/10.15388/vu.thesis.562>

<https://orcid.org/0000-0002-5476-2946>

VILNIAUS UNIVERSITETAS
FIZINIŲ IR TECHNOLOGIJOS MOKSLŲ CENTRAS

Gintarė Gečė

Naujų karkasinių elektrodų medžiagų tinkamų Na-jonų vandeninėms baterijoms paieška, sintezė ir tyrimai

DAKTARO DISERTACIJA

Gamtos mokslai
Chemija (N 003)

VILNIUS 2023

Disertacija rengta 2019–2023 metais Valstybiniame mokslinių tyrimų institute Fizinių ir technologijos mokslų centre.

Mokslinis vadovas – dr. Linas Vilčiauskas (Valstybinis mokslinių tyrimų institutas Fizinių ir technologijos mokslų centras, gamtos mokslai, chemija, N 003)

Mokslinis konsultantas – dr. Jurgis Pilipavičius (Valstybinis mokslinių tyrimų institutas Fizinių ir technologijos mokslų centras, gamtos mokslai, chemija, N 003)

Gynimo taryba:

Pirmininkas – prof. habil. dr. Eimutis Juzeliūnas (Valstybinis mokslinių tyrimų institutas Fizinių ir technologijos mokslų centras, gamtos mokslai, chemija, N 003).

Nariai:

prof. dr. Henrikas Cesiulis (Vilniaus universitetas, gamtos mokslai, chemija, N 003),

dr. Arūnas Jagminas (Valstybinis mokslinių tyrimų institutas Fizinių ir technologijos mokslų centras, gamtos mokslai, chemija, N 003),

dr. Gints Kučinskis (Latvijos universitetas, gamtos mokslai, fizika, N 002),

prof. dr. Simas Šakirzanovas (Vilniaus universitetas, gamtos mokslai, chemija, N 003).

Disertacija ginama viešame Gynimo tarybos posėdyje 2023 m. gruodžio mėn. 15 d. 14 val. Valstybinio mokslinių tyrimų instituto Fizinių ir technologijos mokslų centro A101 auditorijoje.

Adresas: Saulėtekio al. 3, LT-10257, Vilnius, Lietuva.

Tel. +370 5 264 8884; el. paštas: office@ftmc.lt.

Disertaciją galima peržiūrėti Fizinių ir technologijos mokslų centro ir Vilniaus Universiteto bibliotekose ir VU interneto svetainėje adresu:

<https://www.vu.lt/naujienos/ivykiu-kalendorius>

TABLE OF CONTENTS

LIST OF ABBREVIATIONS	8
INTRODUCTION.....	10
1. LITERATURE REVIEW.....	13
1.1. World energy demand.....	13
1.2. Electrochemical batteries	14
1.3. Rechargeable batteries	16
1.4. Post Li-ion batteries: Na-ion batteries.....	19
1.5. Negative electrode materials	21
1.5.1. Carbonaceous phases	21
1.5.2. Titanium-based materials	22
1.6. Positive electrode materials	23
1.6.1. Layered transition metal oxides	23
1.6.2. Polyanionic compounds	23
1.6.3. Prussian blue analogues	25
1.7. Electrolyte solutions.....	26
2. EXPERIMENTAL METHODOLOGY	28
2.1. Structural characterization	28
2.2. Electrode preparation	29
2.3. Electrochemical characterization	30
3. RESULTS AND DISCUSSION	33
3.1. Titanium-based materials for Na-ion battery negative electrodes	33
3.1.1. Motivation.....	33
3.1.2. Synthesis	34
3.1.3. Structural characterization	35
3.1.4. Electrochemical performance.....	43
3.1.5. Summary	55
3.2. Manganese-based materials for Na-ion battery positive electrodes.....	57
3.2.1. Motivation.....	57

3.2.2. Synthesis	59
3.2.3. Structural characterization	60
3.2.3.1. $\text{Na}_4\text{Mn}_3(\text{PO}_4)_2\text{P}_2\text{O}_7$	60
3.2.3.2. $\text{Na}_3\text{MnPO}_4\text{CO}_3$	62
3.2.4. Electrochemical performance.....	65
3.2.4.1. $\text{Na}_4\text{Mn}_3(\text{PO}_4)_2\text{P}_2\text{O}_7$	65
3.2.4.2. $\text{Na}_3\text{MnPO}_4\text{CO}_3$	69
3.2.5. Summary	72
3.3. Iron-based materials for Na-ion battery electrodes	73
3.3.1. Motivation.....	73
3.3.2. Synthesis	76
3.3.3. Structural characterization	79
3.3.3.1. $\text{Na}_3\text{Fe}_2(\text{PO}_4)_3$	79
3.3.3.2. $\text{Na}_4\text{Fe}_3(\text{PO}_4)_2\text{P}_2\text{O}_7$	80
3.3.3.3. $\text{Na}_{2-x}\text{Fe}[\text{Fe}(\text{CN})_6]\cdot y\text{H}_2\text{O}$	83
3.3.4. Electrochemical performance.....	87
3.3.4.1. $\text{Na}_3\text{Fe}_2(\text{PO}_4)_3$	87
3.3.4.2. $\text{Na}_4\text{Fe}_3(\text{PO}_4)_2\text{P}_2\text{O}_7$	88
3.3.4.3. $\text{Na}_{2-x}\text{Fe}[\text{Fe}(\text{CN})_6]\cdot y\text{H}_2\text{O}$	94
3.3.5. Summary	101
3.4. Vanadium-based materials for Na-ion battery positive electrodes ..	103
3.4.1. Motivation.....	103
3.4.2. Synthesis	104
3.4.3. Structural characterization	105
3.4.4. Electrochemical performance.....	107
3.4.5. Summary	112
3.5. Mixed-transitional metal-based materials for Na-ion battery positive electrodes.....	113
3.5.1. Motivation.....	113
3.5.2. Synthesis	114

3.5.3. Structural characterization	115
3.5.4. Electrochemical performance.....	117
3.5.5. Summary	125
4. CONCLUSIONS.....	126
SANTRAUKA	128
ACKNOWLEDGEMENTS	142
CURRICULUM VITAE	146
LIST OF REFERENCES	148

LIST OF ABBREVIATIONS

a.u.	Arbitrary Unit
BET	Brunner-Emmet-Teller
CE	Counter Electrode
CE%	Coulombic Efficiency
CV	Cyclic Voltammetry
DEC	Diethylene Carbonate
DG	Bis(2-methoxyethyl) Ether (diglyme)
EC	Ethylene Carbonate
EG	Ethylene Glycol
EtOH	Ethanol
GCD	Galvanostatic Charging and Discharging
HER	Hydrogen Evolution Reaction
HC	Hard Carbon
ICP-AES	Inductively-Coupled Plasma Atomic Emission Spectroscopy
IEA	International Energy Agency
LIB	Lithium-ion Battery
MeOH	Methanol
Na-S	Sodium Sulfur Battery
NASICON	Sodium SuperIonic Conductor
NFP	Sodium Iron Phosphate ($\text{Na}_3\text{Fe}_2(\text{PO}_4)_3$)
NFPO	Sodium Iron Pyrophosphate ($\text{Na}_{3.12}\text{Fe}_{2.44}(\text{P}_2\text{O}_7)_2$)
N_7FPO	Sodium Iron (III) Pyrophosphate ($\text{Na}_7\text{Fe}_3(\text{P}_2\text{O}_7)_4$)
NFPP	Sodium Iron Phosphate Pyrophosphate ($\text{Na}_4\text{Fe}_3(\text{PO}_4)_2(\text{P}_2\text{O}_7)$)
Ni-Cd	Nickel Cadmium Battery
Ni-MH	Nickel Metal Hydride Battery

NMP	1-Methyl-2-Pyrrolidinone
NMPC	Sodium Manganese Phosphate Carbonate ($\text{Na}_3\text{MnPO}_4\text{CO}_3$)
NMPP	Sodium Manganese Phosphate Pyrophosphate ($\text{Na}_4\text{Mn}_3(\text{PO}_4)_2(\text{P}_2\text{O}_7)$)
NTP	Sodium Titanium Phosphate ($\text{NaTi}_2(\text{PO}_4)_3$)
NVFP/ N_3VFP	Sodium Vanadium Iron Phosphate ($\text{Na}_3\text{VFe}(\text{PO}_4)_3$)
N_4VFP	Sodium Vanadium Iron Phosphate ($\text{Na}_4\text{VFe}(\text{PO}_4)_3$)
NVPP	Sodium Vanadium Phosphate Pyrophosphate ($\text{Na}_7\text{V}_4(\text{PO}_4)(\text{P}_2\text{O}_7)_4$)
OER	Oxygen Evolution Reaction
1-PrOH	1-Propanol
2-PrOH	2-Propanol
PC	Propylene Carbonate
PBA	Prussian Blue Analog
Pb-acid	Lead Acid Battery
PVDF	Polyvinylidene Fluoride
RE	Reference Electrode
SEI	Solid Electrolyte Interphase
SEM	Scanning Electron Microscopy
SHE	Standard Hydrogen Electrode
SIB	Sodium-ion Battery
SS	Stainless-steel
TEM	Transmission Electron Microscopy
TGA	Thermogravimetry Analysis
THP	Titanium Hydrogen Phosphate Hydrate ($\alpha\text{-Ti}(\text{HPO}_4)_2 \cdot \text{H}_2\text{O}$)
WE	Working Electrode
XRD	X-Ray Diffraction

INTRODUCTION

Electrochemical batteries are sought as one of the most attractive technologies for storing electrical energy. They have superior round-trip energy efficiency, low environmental footprint, easy scalability, and wide available power and energy range. Li-ion batteries (LIB) have become the battery technology of choice due to their exceptional energy and power densities.¹ However, the highly volatile cost and supply of lithium and some necessary transition metals (e.g., cobalt, nickel) as well as safety issues related to the use of highly flammable organic electrolytes requires the search and development of alternatives. Na-ion batteries (SIB), especially those employing aqueous electrolytes, are attracting increasing attention as potential candidates, especially suitable for large-scale applications.^{2, 3} The aqueous aspect makes them significantly safer, non-flammable, low cost and environmentally friendlier with respect to comparable Li-ion technologies. In addition, they are based on accessible and widely spread sodium resources as well as offer the elimination of cobalt and other rare metals.⁴

Various materials have been investigated and reported as suitable positive and negative electrodes for aqueous Na-ion batteries including layered transition metal oxides, NASICON-structured polyanionic, mixed-polyanionic compounds, or Prussian Blue Analogs (PBA). However, there are still several remaining issues such as poor cycle stability, low energy density or low voltage which should be acknowledged, investigated, and understood.⁵

The **main goal** of this work was to find and develop new framework electrode materials which would be suitable for the next generation aqueous Na-ion batteries in terms of their synthesizability, charge capacity, energy density, and stability. The **specific objectives** of this work were as follows:

▣ Development and optimization of hydro(solvo)thermal synthesis procedure for $\text{NaTi}_2(\text{PO}_4)_3$. Investigation of synthesis conditions and their influence on phase purity and particle morphology. Characterization of electrochemical properties and degradation of $\text{NaTi}_2(\text{PO}_4)_3$ electrodes in various aqueous electrolytes using cycling voltammetry, galvanostatic charge/discharge cycling, and elemental analysis.

▣ Preparation and structural characterization of $\text{Na}_4\text{Mn}_3(\text{PO}_4)_2(\text{P}_2\text{O}_7)$ and $\text{Na}_3\text{MnPO}_4\text{CO}_3$. Investigation of the electrochemical performance of these materials in various aqueous and organic electrolytes using cycling voltammetry and galvanostatic charge/discharge cycling.

▣ Preparation and structural characterization of $\text{Na}_3\text{Fe}_2(\text{PO}_4)_3$, $\text{Na}_4\text{Fe}_3(\text{PO}_4)_2(\text{P}_2\text{O}_7)$ and $\text{Na}_{2-x}\text{Fe}[\text{Fe}(\text{CN})_6] \cdot y\text{H}_2\text{O}$. Investigation of the electrochemical performance and properties of these materials in various

aqueous electrolytes and organic electrolytes using cycling voltammetry and galvanostatic charge/discharge cycling.

▣ Solid-state synthesis and structural characterization of $\text{Na}_7\text{V}_4(\text{PO}_4)(\text{P}_2\text{O}_7)_4$. Investigation of its electrochemical performance as an electrode material in various aqueous and organic electrolytes using cycling voltammetry and galvanostatic charge/discharge cycling.

▣ Solid-state synthesis and structural characterization of $\text{Na}_3\text{VFe}(\text{PO}_4)_3$. Investigation of its electrochemical as an electrode material in various aqueous electrolytes using cycling voltammetry and galvanostatic charge/discharge cycling.

The **novelty** of this work stems from the limited scope of prior studies on these materials as electrode material to be used in aqueous media. Most of the studies are primarily focused on the use of organic Na^+ ion conducting electrolytes when investigating these materials.

The **statements** for the defense of this this dissertation are as follows:

▣ $\text{NaTi}_2(\text{PO}_4)_3$ could be prepared via hydro(solvo)thermal method using different synthesis media such as methanol, ethanol, 1-propanol, 2-propanol, ethylene glycol and their mixtures with water. Water activity in the synthesis medium is the key parameter governing the phase purity, size, and shape of nanoparticles. Irreversible capacity fade of $\text{NaTi}_2(\text{PO}_4)_3$ electrodes in aqueous electrolytes is related to an electrochemically induced chemical dissolution of active material and the formation of Ti-rich blocking layers.

▣ $\text{Na}_4\text{Mn}_3(\text{PO}_4)_2\text{P}_2\text{O}_7$ and $\text{Na}_3\text{MnPO}_4\text{CO}_3$ could be successfully synthesized via solid-state and hydrothermal methods, respectively. However, these Mn-based materials show limited electrochemical activity in both aqueous and organic electrolytes.

▣ $\text{Na}_3\text{Fe}_2(\text{PO}_4)_3$ could be successfully synthesized via solid-state method. However, it has limited electrochemical activity in aqueous electrolytes. $\text{Na}_4\text{Fe}_3(\text{PO}_4)_2(\text{P}_2\text{O}_7)$ could be successfully synthesized via solid-state as well sol-gel methods and exhibits moderate capacity even if it suffers from electrochemical degradation during cycling. Different phases of $\text{Na}_{2-x}\text{Fe}[\text{Fe}(\text{CN})_6] \cdot y\text{H}_2\text{O}$ could be successfully synthesized via hydrothermal and co-precipitation methods depending on synthesis temperature, synthesis media and drying conditions. The monoclinic phase of this material shows superior electrochemical performance for one-electron process especially when cycled in acidic aqueous electrolytes.

▣ $\text{Na}_7\text{V}_4(\text{PO}_4)(\text{P}_2\text{O}_7)_4$ could be successfully synthesized via solid-state method. However, it has limited electrochemical activity in aqueous electrolytes and is not a suitable electrode material.

☐ $\text{Na}_3\text{VFe}(\text{PO}_4)_3$ could be successfully synthesized via solid-state method. It exhibits decent capacity and its retention if redox couples of $\text{Fe}^{2+}/\text{Fe}^{3+}$ and $\text{V}^{3+}/\text{V}^{4+}$ are activated separately. The activation of $\text{V}^{4+}/\text{V}^{5+}$ redox couple destabilizes the phosphate framework, leading to vanadium dissolution.

1. LITERATURE REVIEW

1.1. World energy demand

The global energy demand is increasing at a rapid rate. According to the International Energy Agency (IEA), global energy demand increased by 5.3% in 2021 and is expected to continue growing over the next few decades.⁶ However, this trend also means that carbon emissions are growing as well (Fig. 1a). Carbon emissions are a major contributor to greenhouse gas emissions that lead to climate change and global warming. In order to meet the Paris Climate Agreement goals of future energy requirements⁷ as well as climate neutrality by 2050,⁸ fossil fuels must be replaced by cleaner energy sources urgently. IEA predicts that renewables will be the fastest-growing source of energy in the coming decades, with solar and wind energy being the largest contributor to this growth (Fig. 1b).

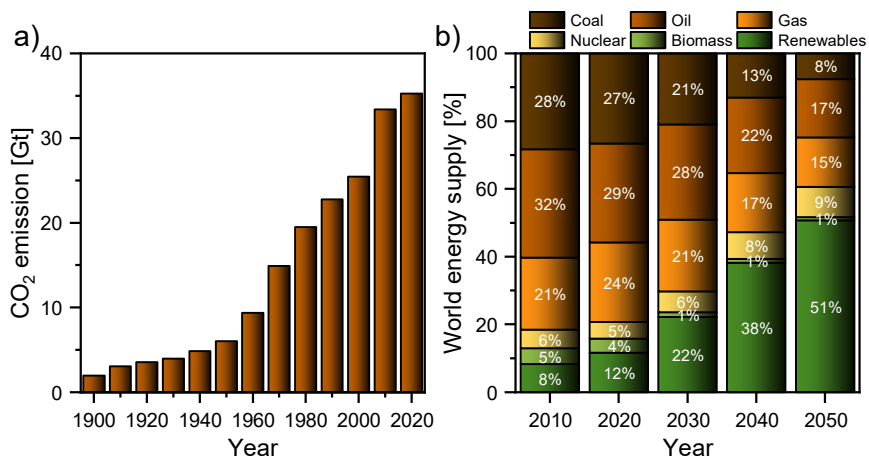


Fig. 1. a) CO₂ emission increase by the year, b) world energy supply mix by the year (IEA predictions).⁶

Although the energy generated by wind turbines, solar panels or hydropower is cleaner and safer than fossil fuels, the supply is intermittent, meaning it is dependent on weather conditions and other factors, and may not always be available when needed. As a result, large-scale energy storage systems are necessary to store excess energy generated during times of high availability, and release it during times of low availability, in order to maintain a reliable and stable electricity grid.⁹ The main energy storage technologies can be classified as mechanical (e.g. flywheel), magnetic (e.g.

superconducting magnetic energy storage), pumped hydro, pneumatic (e.g. compressed air), thermal (e.g. molten salt, water, oil heaters) and electrochemical (e.g. batteries, fuel cells, supercapacitors). The choice of storage technology depends on the specific requirements of the application, and all of them can be competitive depending on the circumstances.^{10, 11} Nowadays, electrochemical batteries are the fastest-growing energy storage technology as they have many desirable features such as modularity which allows to deploy and scale-up them rapidly in almost any location, as well as high round-trip efficiency, wide range of power and energy, long cycle life, minimal maintenance and easy integration into the grid.^{12, 13} The European Commission launched the European Battery Alliance in 2017 to create a competitive and sustainable battery manufacturing value chain in Europe, from raw materials to end-of-life recycling to support the growth of renewable energy storage. The annual market value for this is estimated at €250 billion from 2025 onwards.¹⁴

1.2. Electrochemical batteries

In 1800, A. Volta invented the first electrochemical battery by stacking the discs of copper and zinc separated by cloth soaked in salty water. These ‘voltaic pile’ experiments led to Faraday’s quantitative laws of electrochemistry and the basis for modern batteries.¹⁵

Electrochemical batteries convert the chemical energy stored in the active materials directly into electric energy by electrochemical oxidation-reduction reactions.¹⁶ The basic electrochemical unit is called a ‘cell’ and a combination of one or more cells in series or in parallel comprises a ‘battery’. This gives higher output voltage and/or capacity. Every cell consists of these major components:^{17, 18}

- Ionically and electronically conducting negative electrode;
- Ionically and electronically conducting positive electrode;
- Ionically conducting and electronically insulating electrolyte.

The electric current generated by the electrochemical processes at the electrodes is the main characteristic feature of the electrochemical cell. During discharge, the species are oxidized at the negative electrode giving up the electrons to the external circuit, while they are reduced at the positive electrode taking the electrons from the external circuit. At the same time, the ions of the electrolyte travel between the electrodes to maintain electrical neutrality: the cations move to the negatively polarized positive electrode and anions move to positively polarized negative electrode. During charging, the redox reactions are accordingly reversed (Fig. 2). The total cell voltage

depends on the chemical potential difference of an ion in between the negative and positive electrode materials.¹⁶

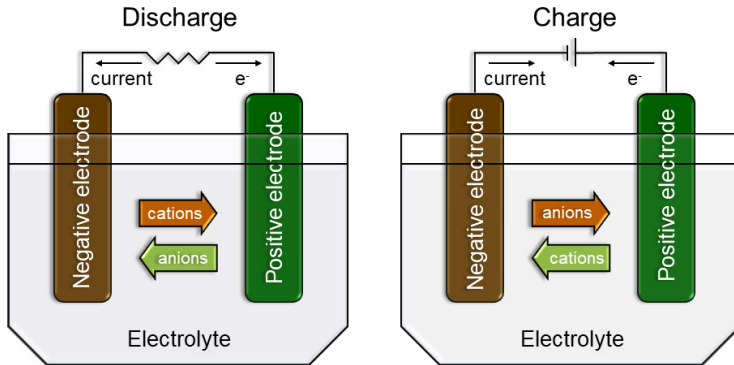


Fig. 2. Schematic view of a battery cell operation.

The existing types of electrochemical energy storage systems are classified according to the nature of the chemical reactions, materials involved, structural features and design. One of the most encompassing classification is based on the reversibility of reactions during cell operation:^{16, 17}

- ❑ Primary cell (non-rechargeable), is characterized by an irreversible electrochemical reaction. The fixed amount of reacting compounds are consumed by discharging and cannot be used again. Examples for primary batteries are alkaline,¹⁹ silver oxide,²⁰ zinc-carbon,²¹ lithium²² and zinc-air.²³
- ❑ Secondary cell (rechargeable), is characterized by reversible electrochemical reactions. After discharge, the reacting compounds are restored to their original form by externally applied electrical energy and this cell could be used once again for multiple cycles. Usually, the cost of secondary cells is higher and the capacity is lower than their primary counterparts. However, they are more sustainable. Examples of the secondary batteries are lead-acid,²⁴ nickel-cadmium,²⁵ nickel-metal hydride,²⁶ sodium-sulfur,²⁷ lithium-ion,²⁸ sodium-ion.²⁹

1.3. Rechargeable batteries

Secondary cells have the advantage of the ability to be recharged together with high-power density, high discharge rate or good low-temperature performance.³⁰ Rechargeable batteries usually are used as energy-storage devices in automotive and aircraft systems, uninterruptible power supplies, consumer electronics, power tools etc. The most common rechargeable batteries are concisely described in this section and compared in Fig. 3.

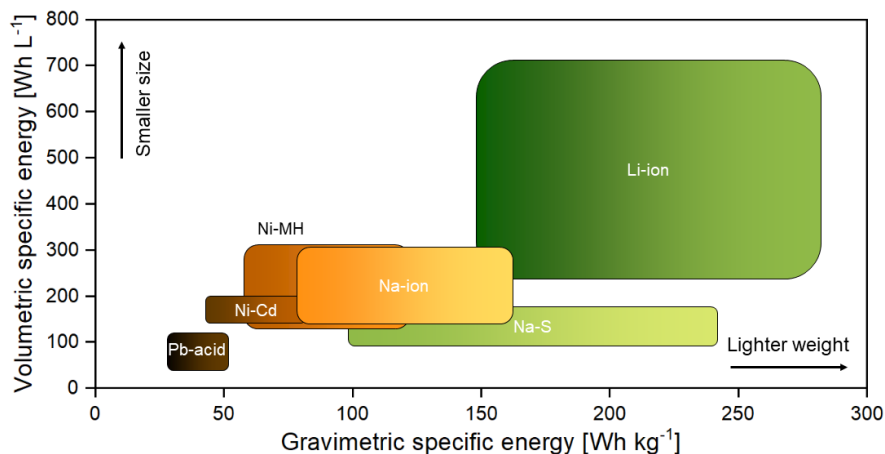
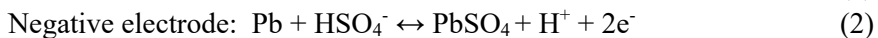


Fig. 3. Comparison of different rechargeable batteries in terms of gravimetric and volumetric power densities.^{17, 31, 32}

Lead-acid (Pb-acid) battery is the oldest system which is still relevant for automotive applications even today due to its low-cost, recyclability, high voltage and good performance. The positive and negative electrode in Pb-acid battery is PbO_2 and Pb , respectively and aqueous sulfuric acid is used as the electrolyte.²⁴ Redox reactions during charging and discharging processes are as follows:

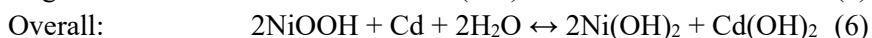
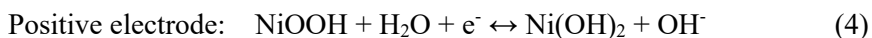


Cell voltage: $\sim 2 \text{ V}$

Due its high weight, lead exhibits a specific charge capacity of only 259 Ahg^{-1} which results in an energy density of only $30 - 50 \text{ Wh kg}^{-1}$ for such battery. Moreover, Pb-acid systems suffer from short lifetimes, toxicity, slow charge

rates and poor performance at low-temperature which limit their usability in small portable devices but they are still applicable as starter batteries in cars.³²

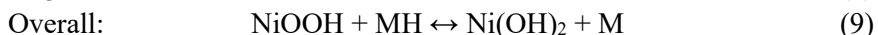
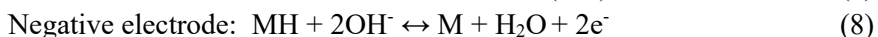
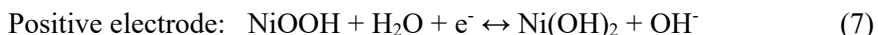
Nickel-cadmium battery (Ni-Cd) is a secondary battery which had been widely used since 1950s in portable electronics, power and medical equipment, emergency back-up power or aerospace due to its good performance at low-temperature, long shelf life, low internal resistance and fast-charge. The positive and negative electrodes of Ni-Cd battery are Ni(OH)₂ and Cd, respectively and KOH_(aq.) is used as an electrolyte.²⁵ The redox reactions during charging and discharging processes are as follows:



Cell voltage: ~1.3 V

As Cd exhibits higher specific charge of 477 mAh g⁻¹, the specific energy of 60 Wh kg⁻¹ of such a battery is reachable. However due to regulations for the usage of Cd, it has been replaced in multiple applications by newer types of rechargeable batteries.³³

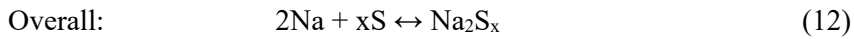
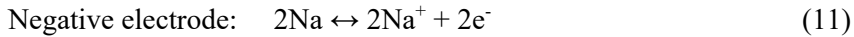
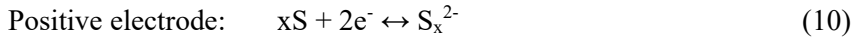
The nickel-metal hydride (Ni-MH) battery uses a hydrogen-absorbing metal alloy made of noble earth elements (e.g. ZrNi, Ti₂Ni, LaNi₅ or TiNi₂) instead of Cd. This makes it an attractive alternative to Ni-Cd due to their lower toxicity and higher energy density (80 Wh kg⁻¹).²⁶ The redox reactions during charging and discharging processes are as follows:



Cell voltage: ~1.3 V

Nowadays, Ni-MH is used in hybrid vehicles, uninterruptible power supplies, consumer application (vacuum cleaners, toothbrushes etc.) due to its higher energy density, superior performance at high temperatures, long cycle life and safety.³⁴

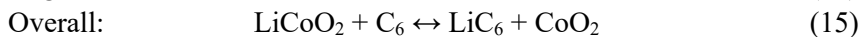
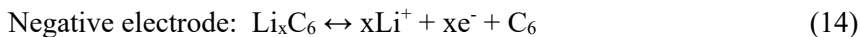
The sodium-sulfur (Na-S) rechargeable battery has been used primarily in large-scale energy storage applications. The positive and negative electrodes of Na-S battery are sulfur and sodium, respectively. Both of them are liquid at the operating temperature (250 – 350 °C). The electrolyte is β''-Al₂O₃ ceramic which is Na-ion conductive.²⁷ The redox reactions during charging and discharging processes are as follows:



Cell voltage: ~ 2.1 V

Sodium has a high specific charge of 1168 mAh g^{-1} which results in a specific energy density of 200 Wh kg^{-1} for such a battery. High energy density, long cycle life, low price and ability to operate at high temperature make Na-S batteries suitable for stationary applications although some safety issues are an important concern.³⁵

Lithium-ion batteries (LIBs) have captured an important share in the energy storage market due to their high specific energy density (currently $\sim 280 \text{ Wh kg}^{-1}$) and excellent shelf life owing to low Li atomic mass (6.94 g mol^{-1}), small ionic radius (0.76 \AA) and low electrochemical reduction potential (-3.04 V vs SHE).³⁶ The development of LIBs started in the 1970s with the investigation of electrochemically active TiS_2 capable of reversible lithium insertion by Whittingham et al.³⁷ This was followed by a study of LiCoO_2 by Goodenough et al. as positive electrode material in the 1980s.³⁸ The LIBs technology was commercially introduced by Sony in 1991 and from then on it is the most common rechargeable battery used in cell phones, power tools, vehicles, stationary storage etc.³⁶ The ‘rocking chair’ concept relies on the intercalation compounds in both electrodes where Li-ions ‘rock’ back and forth, getting inserted into the negative electrode during cell charging and leaving negative electrode to intercalate into positive one as it is discharged. Among a variety of electrode materials, the most typical are layered or tunneled metal oxides such as lithium cobalt oxide or lithium manganese oxide in positive electrodes, and graphitic or hard carbon in negative electrodes. The standard electrolytes are organic-based solutions such as 1 M LiPF_6 in a mixture of ethylene carbonate (EC) and diethyl carbonate (DEC). The redox reactions during charging and discharging processes in $\text{LiCoO}_2/\text{graphite}$ system are as follows:³⁹



Cell voltage: ~ 4.2 V

LIBs offer low self-discharge rate, long cycle life, broad voltage range, high-rate capability, high Coulombic efficiency, and low maintenance. Nevertheless, they have several disadvantages such as high initial cost,

degradation at high temperature and possible thermal runaway when overcharged or crushed. The limited availability and cost of Li, Co, or Ni, as well as safety questions stipulate to find alternative technologies, especially for stationary applications where the cost and sustainability are the main requirements.³⁶

1.4. Post Li-ion batteries: Na-ion batteries

Multiple other types of metal ions such as Na^+ , K^+ , Mg^{2+} , Ca^{2+} , Al^{3+} or Zn^{2+} have been explored as potential alternatives in ‘rocking chair’ metal-ion batteries.⁴⁰ Some of these metals have obvious advantages in terms of abundance and price with respect to lithium (Fig. 4).⁴¹ In the past decade, Na-ion batteries (SIBs) have been intensively reexamined as suitable LIB alternatives. Na is the next smallest and lightest alkali metal after Li and the electrode redox potential of Na is -2.71 V vs SHE, which is only 0.3 V less than Li. In addition to the lower price of sodium compounds possibility to use aluminum foil as current collector for negative electrodes instead of copper as it is necessary for LIBs, SIBs could be considered as one of the most promising potential successors to LIBs.⁴² Al is more abundant and easier to extract than Cu which makes it cheaper (0.5 – 2.0 USD m^{-2} vs 8 – 15 USD m^{-2}), however it undergoes an alloying reaction with Li at low potentials which makes it not suitable for the negative electrodes in LIBs.⁴³

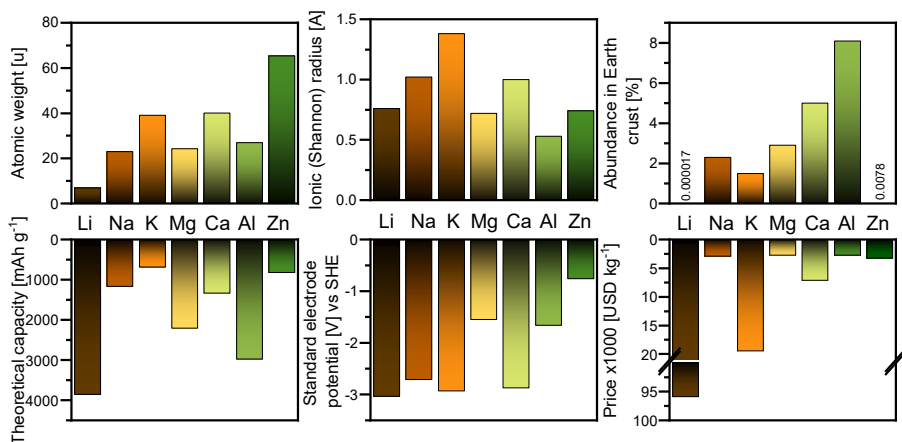


Fig. 4. Comparison of Li, Na, K, Mg, Ca, Al and Zn for metal-ion batteries.^{41, 44, 45}

However, SIBs face several challenges compared to LIBs such as lower energy density, shorter cycle life, and lower rate capability. These disadvantages arise from the larger ionic radius and atomic weight resulting

in lower gravimetric and volumetric energy density. This complicates the application of SIBs for portable devices or electric vehicles. Nevertheless, the primary potential applications for SIBs is stationary energy storage systems where the size and weight of the battery may not be the limiting factor.⁴⁶

The fundamental principle of ‘rocking chair’ SIBs operation does not differ from LIBs - the reversible insertion and deinsertion of Na ions between the positive and negative electrodes (Fig. 5). The basic components of SIB are positive and negative electrodes which are separated by the sodium salt containing electrolyte and mechanical separator. The electrodes are typically composites consisting of an active material which directly participates in electrochemical reactions, a polymeric binder which is responsible for holding the active material particles together and maintaining a strong connection between electrode and a current collector, and conductive carbon filler which increases the electronic conductivity.¹⁷

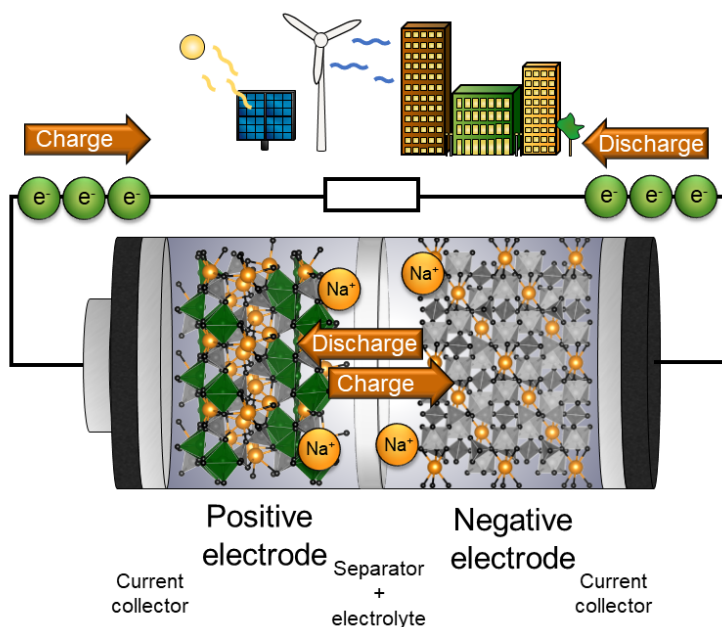


Fig. 5. Scheme of Na-ion battery cell operation.

As SIBs and LIBs share many similarities in their technology, the initial investigations of SIBs have been focused on testing the same electrode materials as used in LIBs. However, it was soon discovered that certain electrode materials, such as graphite, which works effectively with lithium, do not exhibit the same performance characteristics when used with sodium.

Apparently, the larger ionic size of sodium ions, lower energetic stability of binary NaC_x and too low formation potentials, prevent its intercalation and only a limited amount of Na^+ could be stored within the graphite structure. Instead, sodium tends to plate on the surface rather than effectively diffusing into the material.^{47, 48} Consequently, major research effort has been devoted towards exploring and investigating electrode materials that can deliver high performance specifically tailored for SIBs.

1.5. Negative electrode materials

Metallic sodium would be an ideal negative electrode for SIBs as it exhibits high specific capacity and low reduction potential, however it has some issues such as unstable solid electrolyte interphase, dendrite growth and gas evolution all of which lead to capacity fading and safety problems. Moreover, it is not suitable for aqueous electrolytes.⁴⁹ In order to be suitable for SIBs, the negative electrode material should meet the following requirements: as low atomic weight and density as possible, high electronic and ionic conductivity, capability to accommodate high amount of Na, good electrochemical cyclability and stability, its potential should be stable and as close as possible to pure sodium metal, capability of sustaining appreciable currents, chemically stable towards other battery components such as electrolytes, be low cost, easy synthesizable and environmentally friendly.⁵⁰

1.5.1. Carbonaceous phases

Hard carbon (HC) materials are the most common negative electrodes used in non-aqueous SIBs. HC is a non-graphitizable (no matter how high is the carbonization temperature) carbon which could be obtained by thermal or chemical process from environmentally friendly, low price and renewable bio-sources which is a great advantage for commercialization. The typical structure is a mixture of disordered few-layer graphene stacks with nanopores.⁵¹ The interlayer distance is significantly increased compared with graphite which enables access of Na ions to energetically stable sites near defects that results in an almost flat voltage plateau at ~ 0.1 V vs Na^+/Na . However, this value is beyond the aqueous electrochemical window which makes HCs suitable only for organic electrolytes. Additionally, the full understanding of sodium storage mechanism in HC is still incomplete due to unknown exact structure, crystallite size, pore domains and edge termination.⁵² Nevertheless, these electrodes are described by high storage capacity, low working potential and high cycling stability.⁵³

Stevens and Dahn were the first to report the reversible Na intercalation in HC at room temperature.⁵⁴ Their HC electrode obtained from pyrolyzed glucose delivered $\sim 300 \text{ mAh g}^{-1}$.⁵⁴ Appropriate structural and porosity optimization leads to even higher capacities. For example, Komaba et al. successfully synthesized HC via MgO-template method and achieved extremely high value of 478 mAh g^{-1} with good capacity retention and excellent rate performance.⁵⁵

1.5.2. Titanium-based materials

Titanium-based compounds are another type of negative electrodes for SIBs which includes titanium oxides, sulfides, and NASICON-type materials.⁵⁶ The most common natural form of titanium is TiO_2 which is stable, non-toxic, inexpensive and widely abundant. Anatase-type titanium dioxide is one of the oldest known host structures for Li ion insertion.⁵⁷ It has been reported that microsized TiO_2 , which works well in LIBs, is electrochemically inactive in SIBs but the nanosized anatase ($< 30 \text{ nm}$) is active and exhibits capacity of $\sim 150 \text{ mAh g}^{-1}$ (5.5C, organic electrolyte) in the voltage range of $0 - 2.0 \text{ V}$.^{58, 59} Another widely studied negative electrode compound is sodium titanate ($\text{Na}_2\text{Ti}_3\text{O}_7$). It has theoretical capacity of 200 mAh g^{-1} by accommodating two Na ions and a voltage of $0.3 \text{ V vs Na}^+/\text{Na}$ which is the lowest reported value for topotactic ion insertion into oxide electrodes in SIBs and LIBs. On the other hand, it is also too low for aqueous electrolytes. Rudola et. al. has achieved 177 mAh g^{-1} for this material at 0.1C with organic electrolyte and slow capacity fade.⁶⁰

NASICON-type $\text{NaTi}_2(\text{PO}_4)_3$ which has a theoretical capacity of 133 mAh g^{-1} for two Na insertion and $\sim 2.1 \text{ V Na}^+/\text{Na}$ has been reported as an outstanding electrode for aqueous SIBs.⁶¹ Moreover, the third Na could be also inserted at $\sim 0.45 \text{ V Na}^+/\text{Na}$ but it is suitable only for organic SIBs.⁶² NASICON (Sodium SuperIonic Conductor) structured electrode materials exhibit exceptionally high ion conductivity and structural stability. They are named after $\text{Na}_{1+x}\text{Zr}_2\text{P}_{3-x}\text{Si}_x\text{O}_{12}$ ($0 \leq x \leq 3$) by Hong and Goodenough.^{63, 64} A general formula of NASICON-type phosphates could be written as $\text{A}_x\text{Me}'\text{Me}''\text{P}_3\text{O}_{12}$ or $\text{A}_x\text{Me}'\text{Me}''(\text{PO}_4)_3$ where A ($x = 1 - 4$) is typically an alkali (e.g. Li^+ , Na^+ , K^+ etc.) or alkaline earth (e.g. Mg^{2+} , Ca^{2+} , Zn^{2+} etc.) ion, and Me' and Me'' are typically transitional metal ions (e.g. Mn^{2+} , Ti^{3+} , Zr^{4+} , V^{5+} etc.). Additionally, phosphorus could be partially substituted by Si or As. This material has a three-dimensional framework with interconnected channels facilitating ion mobility.⁶⁵

1.6. Positive electrode materials

Suitable SIB positive electrodes should meet the following requirements: as low atomic weight and density as possible, high electronic and ionic conductivity, capability to accommodate high amount of Na, good electrochemical cyclability and stability, relatively high potential, capability of sustaining appreciable currents, chemically stable towards other battery components such as electrolytes, be low cost, easy synthesizable and environmentally friendly.⁵⁰ A variety of compounds have already been investigated as positive electrode for SIBs which could be grouped in three main families: layered transition metal oxides, polyanionic materials and Prussian blue analogues.¹

1.6.1. Layered transition metal oxides

Layered metal oxides are probably the most studied positive electrode materials for SIBs due to a successful implementation of LiMeO_2 (e.g., LiCoO_2 , LiMn_2O_4) in commercial LIBs. Sodium based layered materials are built up of a sheet of edge-sharing $[\text{MeO}_6]$ octahedra and can be categorized into two main groups denoted as O3- or P2-polytypes, where Na ions are accommodated at octahedral or prismatic sites, respectively.⁶⁶ O3-type NaMeO_2 (Me = V, Cr, Mn, Fe, Co, Ni) has three crystallographically different MeO_2 layers (AB, CA, BC) and could be assigned to $R\bar{3}m$ space group. P2-type Na_xMeO_2 consists of two MeO_2 layers (AB, BA) and could be assigned to $P6_3/mmc$ space group.⁵⁶ Both materials show structural phase transitions when Na ions are extracted. P2-type delivers higher capacity and better cycle life in SIBs because Na ion transport is faster than in O3 due to structural differences. For example, O3- $\text{Na}[\text{Fe}_{1/2}\text{Mn}_{1/2}]\text{O}_2$ and P2- $\text{Na}_{2/3}[\text{Fe}_{1/2}\text{Mn}_{1/2}]\text{O}_2$ have capacities of 110 mAh g^{-1} and 190 mAh g^{-1} ($\sim 2.75 \text{ V}$ vs Na^+/Na), respectively.⁶⁷ The main advantages of layered metal oxides as positive electrodes are high theoretical capacity, excellent rate capability and easy preparation. On the other hand, these compounds suffer from air sensitivity, structural degradation and capacity fade.⁶⁸

1.6.2. Polyanionic compounds

Polyanionic type materials contain a series of tetrahedral anionic units $(\text{XO}_4)^{n-}$ or $(\text{X}_m\text{O}_{3m+1})^{n-}$ (X = S, P, Si, As, Mo, or W) which are connected by strong covalently bonded $[\text{MeO}_x]$ polyhedra. Typically, polyanions exhibit lower specific capacity than layered oxides but they have better rate capability,

thermal stability and longer cycling life due to their highly stable 3D framework.⁶⁹

Single polyanionic frameworks, consisting of only one kind of group such as $(\text{SO}_4)^{2-}$, $(\text{PO}_4)^{3-}$, $(\text{P}_2\text{O}_7)^{4-}$ and $(\text{SiO}_4)^{4-}$, show promising electrochemical performance in LIBs and SIBs. Phosphate compounds stand out because they have high structural stability due to strong P-O bonds, low volumetric expansion during Na insertion/deinsertion as well as high safety and low cost.⁷⁰ The most typical representative of phosphate-based materials is olivine-structured NaMePO_4 and NASICON-structured $\text{Na}_x\text{Me}_2(\text{PO}_4)_3$. For example, NaFePO_4 has one of the highest theoretical capacities of 154 mAh g^{-1} among other phosphates and can practically deliver 142 mAh g^{-1} (0.2C, organic electrolyte) for 200 cycles.⁷¹ $\text{Na}_3\text{V}_2(\text{PO}_4)_3$ exhibited a capacity of 93 mAh g^{-1} (0.1C, organic electrolyte) with two plateaus of $\text{V}^{4+}/\text{V}^{3+}$ ($\sim 3.4 \text{ V}$ vs Na^+/Na) and $\text{V}^{2+}/\text{V}^{3+}$ redox reactions (1.6 V vs Na^+/Na).⁷²

Many subclasses of mixed-polyanionic materials can be prepared by combining previously mentioned anions among each other or even adding others such as $(\text{CO}_3)^{2-}$, F^- etc. This mixing could affect the structural properties, strength of inductive effect, or lead to multiple electron redox activity and more robust electrochemical performance.⁷³ The stronger is the electronegativity of the polyanionic group, the higher is the operating potential of a material. The rank of electronegativity of the polyanion groups is $(\text{SiO}_4)^{4-} < (\text{CO}_3)^{2-} < (\text{PO}_4)^{3-} < \text{F}^- < (\text{P}_2\text{O}_7)^{4-} < (\text{SO}_4)^{2-}$ (Fig. 6).⁷⁴ For example, the combination of $(\text{PO}_4)^{3-}$ and $(\text{P}_2\text{O}_7)^{4-}$ shows stronger inductive effect resulting in higher redox potential and energy density but results in slightly lower thermal stability.⁷⁵ Even though the substitution by $(\text{SO}_4)^{2-}$ would lead to even higher potentials, thermal instability above $400 \text{ }^\circ\text{C}$ and solubility in aqueous electrolytes might limit its practical applicability.⁷⁶ Several compounds such as $\text{Na}_4\text{Fe}_3(\text{PO}_4)_2(\text{P}_2\text{O}_7)$,⁷⁷ $\text{Na}_4\text{Mn}_3(\text{PO}_4)_2(\text{P}_2\text{O}_7)$,⁷⁸ $\text{Na}_4\text{Co}_3(\text{PO}_4)_2(\text{P}_2\text{O}_7)$,⁷⁹ $\text{Na}_4\text{Ni}_3(\text{PO}_4)_2(\text{P}_2\text{O}_7)$,⁸⁰ etc. have been reported as promising positive electrode materials for SIBs.

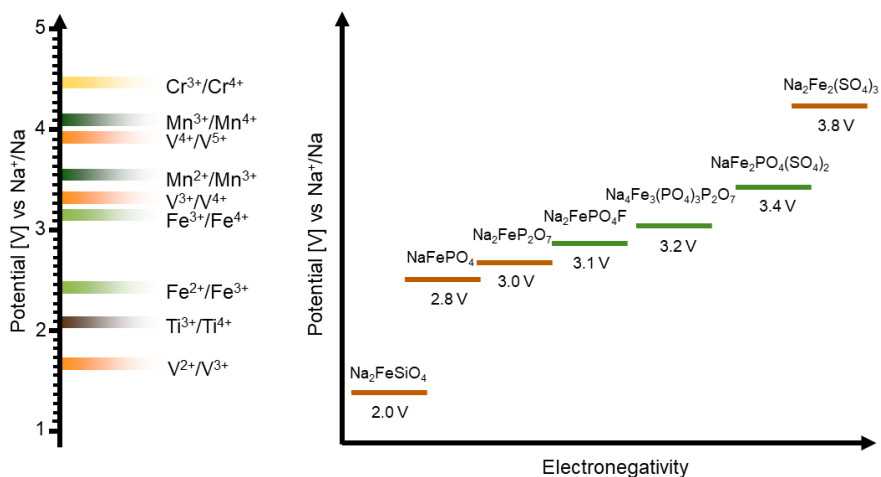


Fig. 6. a) Redox potentials of different transitional metal in $\text{Na}_x\text{Me}'\text{Me}''(\text{PO}_4)_3$ systems, b) diagram of the redox potentials of various Fe-based polyanion positive electrodes.⁷⁴

1.6.3. Prussian blue analogues

Prussian blue analogues (PBA) are a large family of transitional metal hexacyanoferrates. These coordination complexes have a general formula of $\text{A}_x\text{Me}[\text{Fe}(\text{CN})_6]_{1-y}\cdot n\text{H}_2\text{O}$ (A = typically an alkali metal, $\text{Me}=\text{Fe}$, Co , Mn , Ni , Cu etc., $0 \leq x \leq 1$, $0 \leq y \leq 1$). PBA, which was at first known only as a pigment ($\text{Fe}_4[\text{Fe}(\text{CN})_6]_3$), shows a wide range of electrochemical properties such as electrochromism, catalysis, sensorics and energy storage. PBA have been recently investigated as a new alternative for SIBs positive electrodes. This is because of their open framework with large ionic channels and interstitial sites which enable fast and efficient reversible ion insertions.¹⁸ Theoretical capacity for two Na ion insertion/desertion is close to $\sim 170 \text{ mAh g}^{-1}$ in the case of Fe, Mn and Co, and only $\sim 80 \text{ mAh g}^{-1}$ when $\text{Me} = \text{Ni}$, Zn , or Cu .⁸¹ PBA redox potentials are within the stable electrochemical voltage window for aqueous electrolytes. Additionally, the simplicity of synthesis and the abundance of the elements make PBAs attractive for commercial applications. However, they also suffer from reduced capacity and cycling life due to large number of vacancies and interstitial water molecules inside the crystal structure which must be carefully controlled during synthesis and post-treatment.⁸² Various combinations of PBA have been investigated, including $\text{Na}_{0.61}\text{Fe}[\text{Fe}(\text{CN})_6]_{0.94}$ which showed $\sim 170 \text{ mAh g}^{-1}$ ($\sim 3.0 \text{ V}$ vs Na^+/Na , organic electrolyte) with capacity retention of $\sim 99\%$ after 150 cycles.⁸³

$\text{Na}_{1.76}\text{Ni}_{0.12}\text{Mn}_{0.88}[\text{Fe}(\text{CN})_6]_{0.98}$ exhibited $\sim 118 \text{ mAh g}^{-1}$ ($\sim 3.2 \text{ V}$ vs Na^+/Na , organic electrolyte) with capacity retention of $\sim 84\%$ after 800 cycles.⁸⁴ $\text{Na}_{1.32}\text{Fe}[\text{Fe}(\text{CN})_6]_{0.87}\cdot 2\text{H}_2\text{O}$ and $\text{Na}_{1.9}\text{Cu}_{0.95}[\text{Fe}(\text{CN})_6]\cdot 1.9\text{H}_2\text{O}$ were tested in aqueous NaNO_3 electrolyte and delivered $\sim 77 \text{ mAh g}^{-1}$ (2C) and $\sim 93 \text{ mAh g}^{-1}$ (2C), respectively.⁸⁵ Additionally, a full battery was assembled which showed a capacity of 50 mAh g^{-1} (5C, $\sim 0.7 \text{ V}$) with $\sim 86\%$ of capacity retention after 250 cycles.⁸⁵

1.7. Electrolyte solutions

The electrolyte solution plays an important role in rechargeable batteries as it is responsible for transferring the ions (e.g. Na^+) between the negative and positive electrodes. This means that they must have high ionic and exceptionally low electronic conductivity, wide and stable electrochemical window which should ensure high voltage, high specific energy and long cycle life of the battery. Moreover, the electrolyte should be chemically stable against any other cell component (separator, current collector, packaging), thermally stable, non-toxic and non-flammable, and low cost.^{86, 87}

Electrolytes for SIBs could be categorized in several groups: aqueous (sodium salts are dissolved in water),⁸⁸ non-aqueous (sodium salts are dissolved in organic solvents),⁸⁸ ionic liquid,⁸⁹ solid-state (solid polymer or ceramic electrolytes)⁹⁰ and hybrid (mixed aqueous/non-aqueous or liquid/solid components etc.).⁹¹ Organic solvents are mostly used because of their wide electrochemical stability window. Commonly used solvents for organic SIBs are mixtures of ethylene carbonate and propylene carbonate (EC:PC), ethylene carbonate and diethyl carbonate (EC:DEC), ethylene carbonate:dimethyl carbonate (EC:DMC), diglyme (DG) etc. together with NaPF_6 , NaClO_4 , NaTFSI etc. salts. These electrolytes allow the operation of batteries at high voltages above 4 V .⁸⁶ However, the main disadvantages of organic electrolytes are their flammability, toxicity, and high cost.

Aqueous or water-based electrolytes are considered much safer and more environmentally friendly as they are non-flammable, little or non-toxic and low cost.⁹² The use of aqueous electrolytes also results in lower battery production costs because there is no need for a controlled dry/oxygen-free atmosphere during manufacturing process. Additionally, aqueous electrolytes have even higher ionic conductivities than organic ones allowing efficient ion transport and excellent battery rate performance. However, all this comes with certain limitations. The major one is the limited electrochemical stability window of water. The lower limit comes from the reduction potential (due to

hydrogen evolution reaction (HER): $2\text{H}_2\text{O} + 2\text{e}^- \leftrightarrow \text{H}_2 + 2\text{OH}^-$), and the upper limit from the oxidation potential (oxygen evolution reaction (OER): $2\text{H}_2\text{O} \leftrightarrow \text{O}_2 + 4\text{H}^+ + 4\text{e}^-$) of water.⁹³ Thermodynamically, pure water has the electrochemical window of 1.23 V, the absolute position of which varies with pH. For example, at pH 7, water is thermodynamically stable between -0.41 V and 0.82 V vs SHE (Fig. 7a).⁹⁴ The addition of salts, shifts the electrolysis potentials, typically expanding the electrochemical window of water. The most common Na salts in aqueous rechargeable SIBs are Na_2SO_4 , NaNO_3 and NaClO_4 (Fig. 7b). Very high concentration or ‘water-in-salt’ electrolytes tend to significantly reduce water activity which means that fewer water molecules are available for participating in electrochemical reactions also expanding the electrochemical window.⁹⁵

Limited chemical/electrochemical stability of active materials in aqueous electrolytes is also a very common problem followed with dissolution of the material which degrades the battery capacity.^{96, 97} Moreover, side reactions involving dissolved oxygen which might also have malicious effects on the electrode materials. For example, $\text{NaTi}_2(\text{PO}_4)_3$ intercalated with Na^+ ($\text{Na}_3\text{Ti}_2(\text{PO}_4)_3$) reacts with dissolved O_2 and produces OH^- , which increases the pH and could destabilize the active material.^{98, 98} The removal of oxygen by bubbling inert gases, electrode surface treatment, concentrated electrolytes or identification of the right cut-off voltage can reduce these side reactions.⁹⁹ Overall, it is especially important to carefully select and investigate not only the electrode active material but also its compatibility with certain electrolytes.

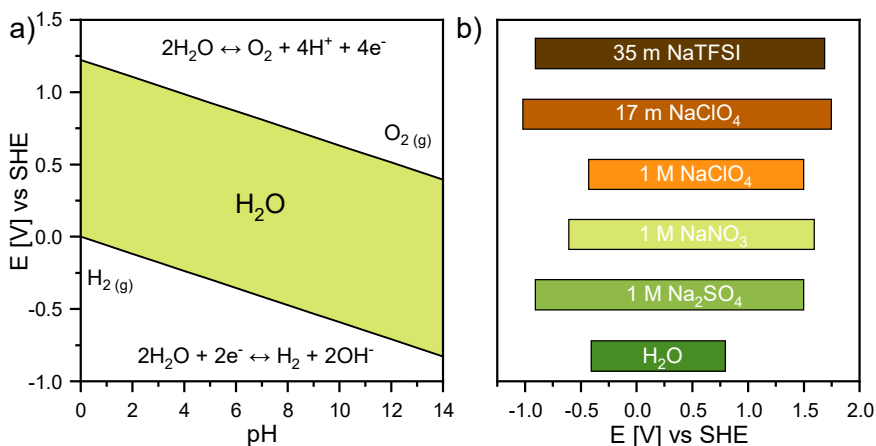


Fig. 7. a) Pourbaix diagram of water and b) electrochemical stability windows of typical aqueous electrolytes with Na salts at various concentrations. Redrawn from D. Pahari et. al.⁹⁹

2. EXPERIMENTAL METHODOLOGY

2.1. Structural characterization

Powder X-ray diffraction (XRD) was used for the determination of materials crystal phase and purity. In this work, a Rigaku SmartLab MiniFlex II and Bruker Phaser D2 and Bruker Advance D8 diffractometers were used with Ni-filtered Cu K α radiation. XRD patterns of powder samples were recorded within the range $10^\circ \leq 2\theta \leq 70^\circ$ using scanning speed and step of 3° min^{-1} and 0.02° , respectively. For Rietveld refinements, XRD patterns were recorded within the range $10^\circ \leq 2\theta \leq 120^\circ$ with the scanning speed and step width of 1° min^{-1} and 0.02° , respectively. Rietveld refinements were performed using GSAS-II software suite.¹⁰⁰ All crystal structures in this work were visualized using Vesta software.¹⁰¹

Scanning electron microscopy (SEM) and **Transmission electron microscopy** (TEM) were used for the determination of materials morphology and particle sizes by Hitachi SU-70, Helios Nanolab 650, FEI and Hitachi TM4000Plus scanning electron microscopes as well as Tecnai G2 F20 X-TWIN, FEI transmission electron microscope. Samples for SEM analysis were prepared by coating 2 mg ml^{-1} dispersion of particles in acetone on silica plate. Samples for TEM analysis were prepared by coating 0.5 mg ml^{-1} dispersion of particles in acetone on copper grid. ImageJ software was used for particle size distribution determination.¹⁰²

Brunauer-Emmett-Teller (BET) adsorption analysis was used to measure the surface area by N $_2$ adsorption isotherms at 77 K using the Anton Paar Brunauer-Emmett-Teller analyzer. Before the gas sorption measurements, all analyzed powder samples were outgassed in vacuum at 90°C for 3 h. Total surface area was estimated by the Brunauer-Emmett-Teller model.

Inductively Coupled Plasma Optical Emission Spectroscopy (ICP-OES) was used for analysis of elemental composition of Prussian blue samples (Na, Fe) and electrolytes after galvanostatic charge/discharge cycling (Ti, Al and P) by PerkinElmer Optima 7000DV inductively coupled plasma optical emission spectrometer. Calibration solutions were prepared by an appropriate dilution of the stock standard solutions (single-element ICP standards 1000 mg L^{-1} , Roth). Prussian blue powders were dissolved in Aqua Regia solution (HCl + HNO $_3$, with molar ratio of 3:1).

Thermal analysis for the determination of carbon or water content of powder samples was carried out on a STA600 PerkinElmer analyzer in the

range of 30 to 700 °C at a heating rate of 20 °C min⁻¹ N₂ in air atmosphere (20 mL min⁻¹).

2.2. Electrode preparation

The working electrode (WE) was prepared by first mixing 70 wt% (usually, 0.70 g) of active material and 20 wt% (0.20 g) of carbon black (CB) (Super-P, TIMCAL) which were previously dried in vacuum at 200 °C for 2 h (Fig. 8). The homogenization was performed in a high-energy ball-mill (Retch PM400) for 1 h at 175 rpm using 3 mm ZrO₂ balls at the ball-to-sample ratio of 10:1. Afterwards, 10 wt% (0.10 g) of polyvinylidene fluoride (PVDF) (HSV1800, Kynar) in N-methyl-2-pyrrolidone (NMP) (~1.5 ml) (Sigma-Aldrich, 99.5%) as a binder and additional NMP as a solvent were added to the mixture. It was homogenized in a planetary ball-mill for 2 h at 350 rpm using 5 mm ZrO₂ balls at the ball-to-sample ratio of 3:1. Then, the slurry was casted as a film (100 or 300 μm) on aluminum foil and dried in vacuum for 3 h at 120 °C. The resulting electrode film was punched into disks (10 – 15 mm in diameter depending on the cell size). For aqueous electrolytes, electrodes were transferred from aluminum foil onto 316L stainless-steel (SS) mesh (#325) using hydraulic press (~6 – 9 t depending on the material) (Fig. 9).

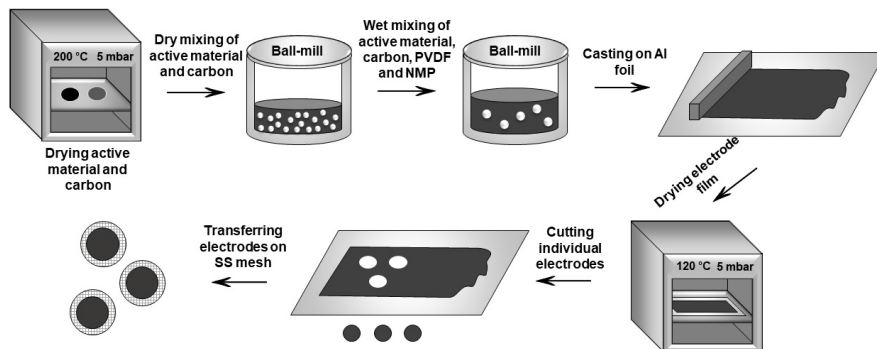


Fig. 8. Electrode preparation process scheme.

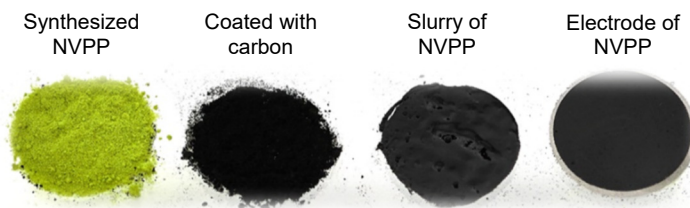


Fig. 9. (left to right) Synthesized and carbon coated $\text{Na}_7\text{V}_4(\text{PO}_4)(\text{P}_2\text{O}_7)_4$ powders; Slurry consisting of NVPP, carbon black and PVDF; Dried electrode transferred onto SS mesh.

2.3. Electrochemical characterization

Cyclic voltammetry (CV) were used to determine the redox processes, the potential at which they occur, and their reversibility. In this work, cyclic voltammetric measurements were performed on a potentiostat-galvanostat (SP-240, Biologic and PGSTAT-302 Metrohm Autolab).

Galvanostatic Charge/Discharge (GCD) cycling was used to evaluate the charge storage properties of materials. The change of voltage over time, capacity and energy density is measured while a controlled current is applied to charge and discharge a material between the chosen potential limits. In a three-electrode cell, the current is applied between the counter electrode and the working electrode while the potential is measured between the working and the reference electrode.

Charge capacity is the total amount of charge consumed or released by electrochemical reactions (Ah or Ah kg^{-1} for specific capacity). The charge or discharge capacity could be calculated from the applied current and total time. Theoretical specific capacity (mAh g^{-1}) of material is calculated as follows:

$$C = \frac{nF}{3600M} \quad (16)$$

where n is the number of electrons in the reaction, F is the Faraday constant ($96485.33 \text{ C mol}^{-1}$) and M is the molecular weight of the material (kg mol^{-1}).

Coulombic efficiency (CE%) is the ratio of the total charge extracted from the battery to the total charge put into the material or a cell over a full cycle (%).

C-rate is the rate at which a battery is charged or discharged relative to its maximum theoretical or practical capacity. A 1C corresponds to complete charge or discharge in 1 h.⁸⁷

In this work, galvanostatic charge-discharge cycling and rate capability experiments were carried out on battery testers (MACCOR, Series 4000 and Neware CT-4008).

Electrochemical properties of the electrodes were characterized in cells of different design depending on a specific experimental goals (Fig. 10): (a) three-electrode bottom-mount beaker-type cell, (b) decoupled three-electrode bottom-mount beaker-type cell where the counter electrode (CE) is separated from working (WE) and reference electrodes (RE) via salt bridge which is filled with 1 M NaNO_3 (aq) and 1% agarose mixture, and (c) three-electrode Swagelok-type cell (T-type cell). Beaker-type cell is the simplest and cost-effective half-cell design for preliminary electrochemical studies, where all three electrodes are immersed in the excess electrolyte solution (~15 mL). Usually, the measurement is performed under ambient air atmosphere with the possibility to apply bubbling of electrolyte with inert gas (e.g., N_2). Decoupled beaker-type cell is similar to beaker-type cell but the WE and CE are separated to avoid the influence of processes, mainly pH changes, which happen on the CE. Swagelok-type or T-type cell is a more realistic setup to a battery cell where the electrodes are separated by a porous separator impregnated with electrolyte, and a compression spring maintains the pressure between these parts. This cell could be used not only for half-cell experiments but also as a full-cell to study positive and negative electrodes simultaneously. Additionally, Swagelok-type cell has very precise and reliable fittings which create leak-free connections. The main body of Swagelok-type cell is made of stainless steel for organic electrolytes or PTFE for aqueous electrolytes while other parts are from stainless steel.

For aqueous electrolyte studies, a graphite rod (60 mm in length and 5 mm in diameter) was used as CE in beaker-type cells, a copper rod (60 mm in length and 5 mm in diameter) in decoupled beaker-type cells, or a self-standing carbon electrode for Swagelok-type cells. $\text{Ag}/\text{AgCl}/3\text{ M KCl}$ was used as RE in all cells. For organic electrolytes, sodium metal discs were used as both CE and RE. Organic Swagelok-type cells were assembled in an Ar-filled glovebox (MBraun, H_2O and $\text{O}_2 < 0.1\text{ ppm}$).

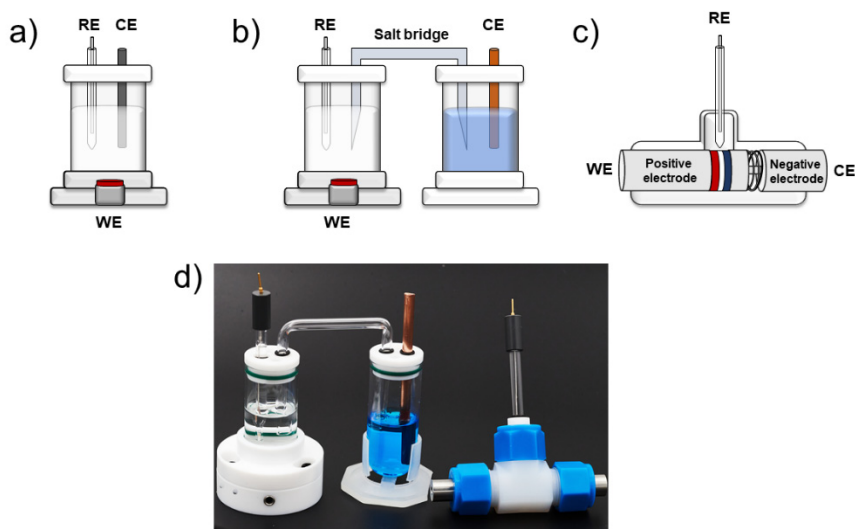


Fig. 10. Electrochemical cells used in this work: a) beaker-type, b) decoupled beaker-type, c) Swagelok-type and d) photograph of decoupled beaker-type and Swagelok-type cells.

Electrochemical performance in aqueous media was investigated using the following salts: 1 M Na_2SO_4 (Lach-ner, 99.3%), 17 m NaClO_4 (Alfa-Aesar, 98%), 8 m NaTFSI (Sodium (I) Bis(trifluoromethanesulfonyl) imide, Solvionic, 99.5%), 28 m $\text{KAc} + 8 \text{ m NaAc}$ ((Potassium Acetate+Sodium Acetate) VWR, 99.5%). For non-aqueous electrolyte cells, 1 M NaPF_6 (FluoroChem, battery grade) in diglyme (DG, Sigma-Aldrich, anhydrous, 99.5%) or ethylene carbonate (EC, UBE, battery grade): diethyl carbonate (DEC, UBE, battery grade) (3:7 by volume) or ethylene carbonate (EC, Acros Organics, 99+): propylene carbonate (PC, Acros Organics, 99.5%) (5:5 by volume) organic solutions were used. All electrolytes were prepared by simply mixing the appropriate amounts of the salts in s solvent at room temperature. Electrochemical measurements in organic electrolyte were performed in order to compare the results with aqueous systems and to verify that the electrochemical activity limitations is mainly related to the electrolyte and not the material itself.

3. RESULTS AND DISCUSSION

3.1. Titanium-based materials for Na-ion battery negative electrodes

3.1.1. Motivation

There is a growing interest in the exploration and development of alternative negative electrode materials due to very low Na intercalation capacity of graphite.^{103, 104} NASICON-structured $\text{NaTi}_2(\text{PO}_4)_3$ (NTP) stands out with its exceptional cycling, rate capability and thermal stability, low volume changes during cycling, low cost and environmental friendliness. NTP has trigonal symmetry with $R\bar{3}c$ (No. 167) space group. It possesses a three-dimensional open framework in which $[\text{TiO}_6]$ octahedra share all corners and $[\text{PO}_4]$ tetrahedra provide large interstitial spaces for Na ion diffusion (Fig. 11).¹⁰⁵ Theoretical capacity of NTP is 133 mAh g^{-1} for two Na ions at the potential of $\sim 2.1 \text{ V vs Na}^+/\text{Na}$ or $-0.8 \text{ V vs Ag/AgCl}$.^{64, 106} Although, this potential is too high for practical non-aqueous batteries, it is suitable for aqueous SIBs because it is very close to the hydrogen evolution potential (negative limitation of aqueous potential window). However, NTP has several drawbacks. For example, its low conductivity and insufficient aqueous stability which limit electrochemical performance due to various parasitic processes leading to pH changes, metal leaching and material dissolution.^{98, 107}

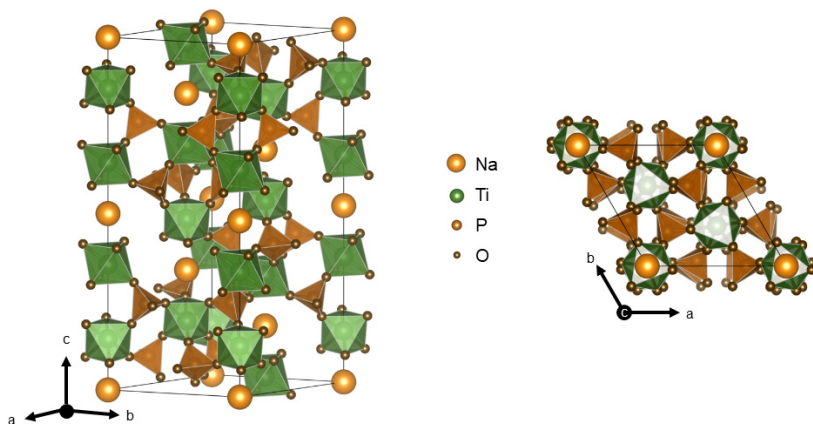


Fig. 11. Crystal structure of $\text{NaTi}_2(\text{PO}_4)_3$.

Ion insertion kinetics, specific capacity, CE% and electrochemical stability highly depend on the structure, morphology, particle size and phase purity of the electrode material.^{16, 17, 108, 109} Several synthesis methods are widely employed for NTP preparation: solid-state,¹¹⁰ sol-gel,¹¹¹ hydrothermal,¹¹² ball-milling,¹⁰⁸ spray-drying,¹¹³ electrospinning,¹¹⁴ *etc.* The solid-state method is simple, low cost, easily scalable. NTP prepared by this route shows decent electrochemical performance including high cycling stability and rate capability.¹¹⁰ However, this method often results in inhomogeneity, may introduce impurities, as well as requires high temperatures, and has poor particle size and morphology control which limits its potential to synthesize nanoscale materials with desired morphology.¹¹⁵ Sol-gel technique is another simple and widely used synthesis method for NTP. The influence of purity, degree of crystallinity, and properties of carbonaceous phase on NTP electrochemical performance were recently investigated.¹¹⁶ However, this method often requires extended processing times and may introduce complexity in the synthesis. Additionally, some sol-gel precursors can be expensive, and scaling up the process for industrial production could present challenges.¹¹⁷ Hydro(solvo)thermal is one of the most suitable soft chemical methods for material synthesis producing high phase purity and crystallinity as well as narrow (nanoscale) size distribution, homogeneity and ability to control particle morphology.¹¹⁸ For instance, particle downsizing and morphology control could improve charge transport of NTP by reducing the ionic and electronic transporting paths, e.g., cubic or spherical particles could pack with lower steric hindrance and better contact.^{109, 119, 120} Several different morphologies of NTP nanoparticles such as cubic,¹²¹ mesoporous microflowers,¹²² plate-like,¹²³ or nanowire clusters,¹²⁴ *etc.* have been reported.

The nucleation rate, temperature, pressure, precursor concentration, agents, synthesis media *etc.* play a significant role in phase and morphology formation in hydro(solvo)thermal synthesis.¹²⁵ A lot of organic solvents used in this synthesis method are expensive, toxic and environmentally harmful.¹²⁶ Water or at least aqueous mixtures would be highly beneficial due to their sustainability.^{127, 128}

3.1.2. Synthesis

NaTi₂(PO₄)₃ nanoparticles were synthesized via a hydro(solvo)thermal method (Fig. 12). In a typical synthesis, CH₃COONa (0.003 mol, Chempur, ≥ 99.0%) was dissolved in H₃PO₄ (10 mL, Reachem, 85 wt%), and then CH₃COOH (10 mL, Lach-ner, 99.8%) together with solvent (40 mL, Honeywell, ≥ 99.8%) were added to the mixture. The solvent consisted of one

of the alcohols: methanol (CH_3OH , Reachem), ethanol ($\text{CH}_3\text{CH}_2\text{OH}$, Honeywell), 1-propanol ($\text{CH}_3\text{CH}_2\text{CH}_2\text{OH}$, Chempur), 2-propanol ($\text{CH}_3\text{CHOHCH}_3$, Reachem), or ethylene glycol ($\text{CH}_2\text{OHCH}_2\text{OH}$, Chempur) and deionized water in different volume ratios (5:0, 4:1, 3:2, and 2:3). Afterwards, a separate mixture of $\text{C}_{16}\text{H}_{36}\text{O}_4\text{Ti}$ (1.4 mL, Acros Organics, $\geq 98\%$) and solvent (10 mL) was prepared and added dropwise into the previous solution under vigorous magnetic stirring. The final solution obtained after continuous stirring for 30 min at room temperature was transferred into a 100 mL Teflon-lined stainless-steel autoclave heated to $180\text{ }^\circ\text{C}$ for 12 h. Additionally, a series of samples was synthesized at different temperatures ($120\text{-}200\text{ }^\circ\text{C}$) when ethanol was used as a solvent.

Eventually, the obtained white precipitate was collected, washed several times by centrifugation with distilled water and ethanol, and subsequently dried at $80\text{ }^\circ\text{C}$ overnight. The resulting particles were coated with a layer of carbon by homogeneously mixing additionally ball-milled (1 h at 900 rpm) NTP powder (70 wt%, (usually, 0.7 g)) and of citric acid (30 wt% (0.3 g), $\text{HOC}(\text{CH}_2\text{CO}_2\text{H})_2$, Lach-ner, G.R.) in distilled water (50 mL). The resulting mixture was dried at $80\text{ }^\circ\text{C}$ for several hours for complete water elimination. The obtained white powder was reground and annealed at $700\text{ }^\circ\text{C}$ for 2 h in N_2 atmosphere.

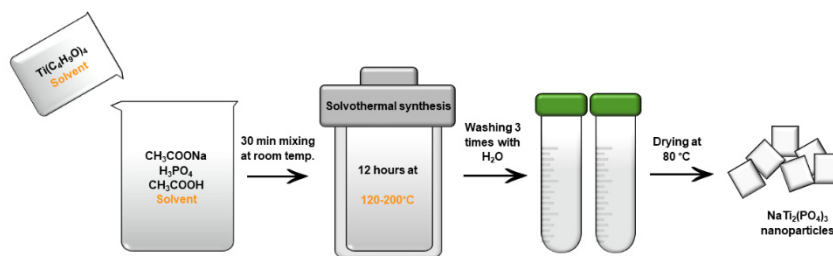


Fig. 12. Hydro(solvo)thermal synthesis scheme of $\text{NaTi}_2(\text{PO}_4)_3$.

3.1.3. Structural characterization

Several different series of $\text{NaTi}_2(\text{PO}_4)_3$ nanoparticle samples were synthesized by a hydro(solvo)thermal method. First, different synthesis temperatures ranging from 120 to $220\text{ }^\circ\text{C}$ were investigated. The obtained powder XRD patterns presented in Fig. 13 show that the studied temperature range does not have strong influence on the NTP phase formation. All

observed sharp peaks indicate a high degree of crystallinity and agree very well those reported in literature^{116, 121, 123} and could be indexed to the $R\bar{3}c$ (No. 167) space group typical for the high-temperature NASICON-type phase.¹²⁹ No additional phases were detected in the XRD.

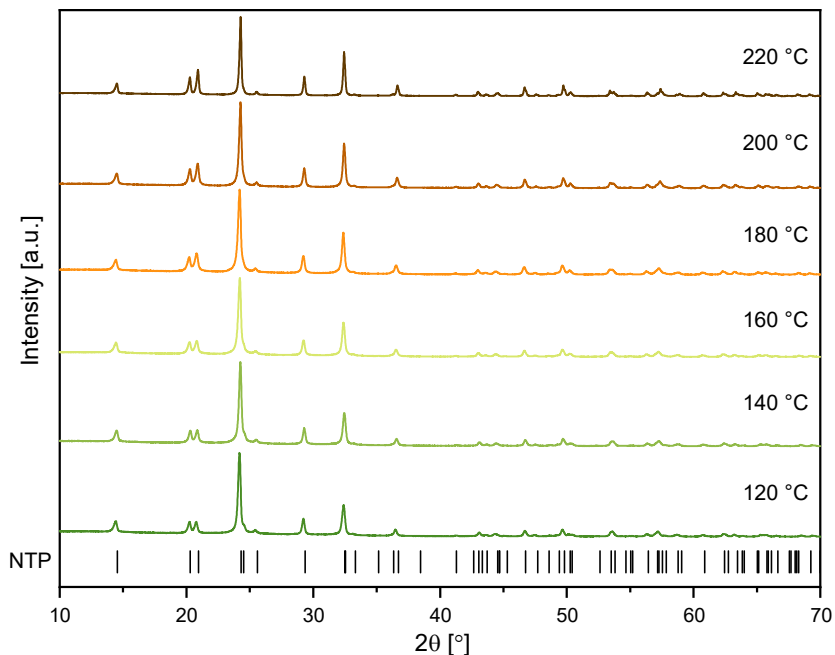


Fig. 13. Powder XRD patterns of NTP samples prepared at different solvothermal synthesis temperatures.¹²⁹

The effect of synthesis temperature for the particle morphology and size were investigated by Scanning Electron Microscopy (SEM). Fig. 14 shows that all synthesized NTP nanoparticles have cubic morphology and an average size of ~60 – 70 nm for 120 – 180 °C. Higher synthesis temperature yields slightly bigger particles ~87 nm and ~142 nm for 200 °C and 220 °C, respectively. For the further investigation, 180 °C was selected due to the suitable average particle size and high degree of crystallinity.

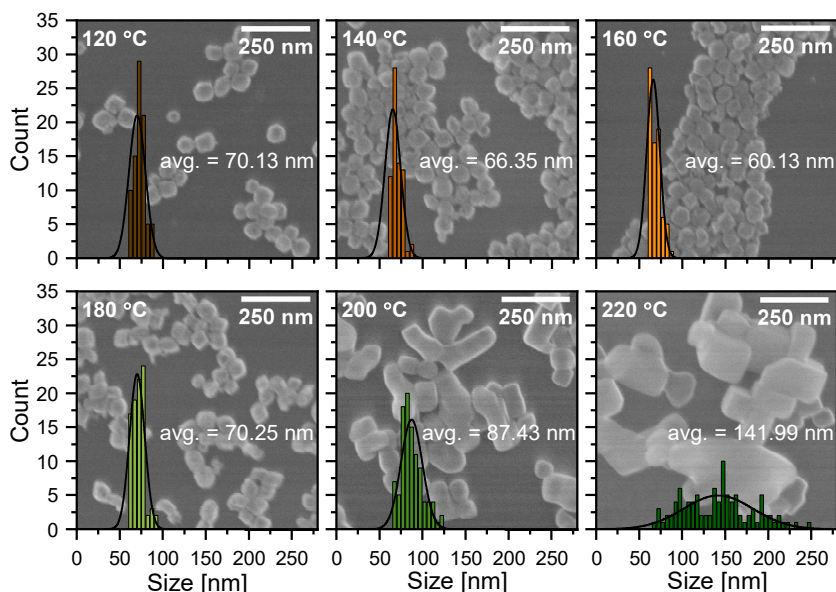


Fig. 14. SEM images and particle size distribution histograms of NTP samples prepared at different solvothermal synthesis temperatures: 120, 140, 160, 180, 200 and 220 °C.

Moreover, the influence of synthesis media on the phase purity and morphology of NTP was also investigated. Five different alcohols such as methanol (MeOH), ethanol (EtOH), 1-propanol (1-PrOH), 2-propanol (2-PrOH), and ethylene glycol (EG) were used either pure (denoted as 5:0 ratio) or mixed with water at different volume ratios: 4:1, 3:2, and 2:3. The obtained powder XRD patterns presented in Fig. 15 show that in the case of pure solvents, NTP phase with a high degree of crystallinity is obtained. However, small additional peaks start to appear at 11.5, 25.7 and 25.9° for 4:1 1-PrOH, 3:2 EtOH, 2-PrOH and EG, and 2:3 MeOH mixtures. Later, the additional peaks grow with increasing water concentration in the reaction media. In all cases, the additional peaks could be attributed to the monoclinic ($P2_1/c$, No. 14) α -Ti(HPO₄)₂·H₂O (THP) phase.¹³⁰ In the presence of water, the appearance of white milky suspension is witnessed during synthesis which is a result of immediate hydrolysis and polycondensation of titanium butoxide to TiO₂ which under solvothermal conditions which further reacts with H₃PO₄ to yield THP.

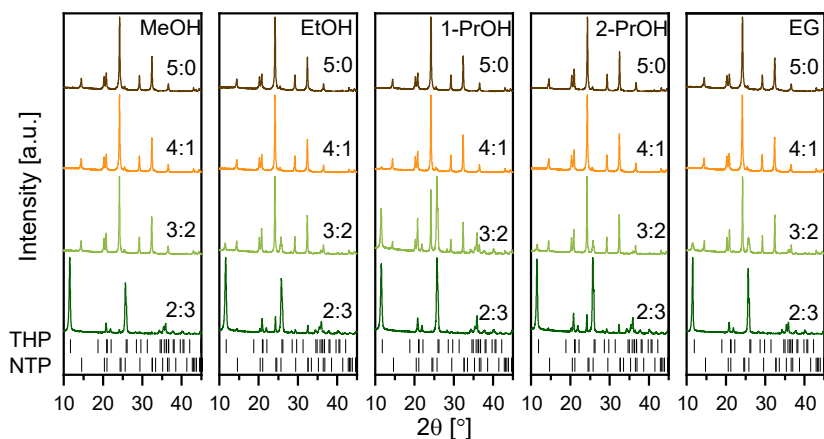


Fig. 15. Powder XRD patterns of NTP samples prepared in different solvothermal synthesis media (5:0, 4:1, 3:2, and 2:3 correspond to volume ratios between water and alcohol).^{129, 130}

The morphology and particle size distribution also depend on the synthesis medium as is shown in Fig. 16 and Fig. 17. In case of pure alcohols, NTP nanoparticles have cubic morphology. One exception is EG, which results in a spheroidal particles with the smallest size of ~ 58 nm. This synthesis media has stronger intermolecular interactions and higher viscosity which limits diffusion and prevents the particle growth.¹³¹ However, the additional water weakens this effect and leads to increasing particle size and sharper shape. Additional water for other alcohols also affects the shape and size of particles. For example, in MeOH, the surface of cubes becomes more defective, and if the ratio is 3:2, the cubic crystals grow on top of each other which is not observed in other samples. In EtOH and 2-PrOH (4:1), particles grow irregular with a lot of surface defects, and resemble agglomerates. However, this is not observed for 1-PrOH and EG (4:1). The addition of water in the synthesis leads to the larger size of the particles but the shape stays cubic and very uniform. THP impurity phase has its specific hexagonal microplate morphology¹³² which could be clearly observed in the samples with higher amount of water (some 2:3, all 3:2) which correlates well with previous XRD results.

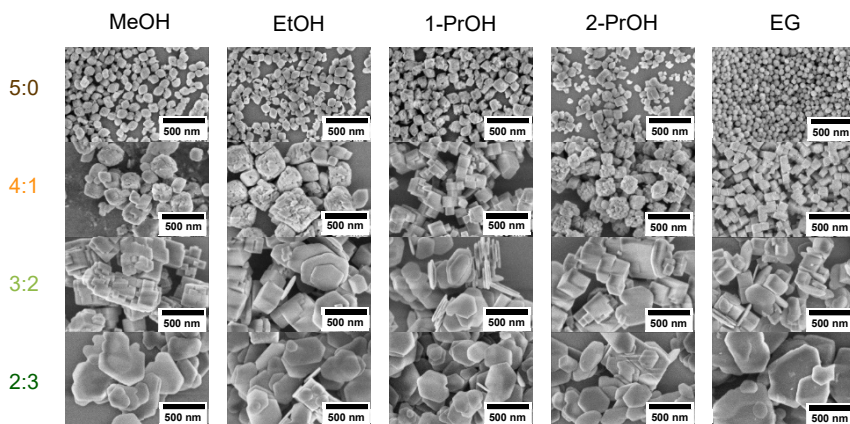


Fig. 16. SEM images of NTP sample nanomorphology prepared in different solvothermal synthesis media.

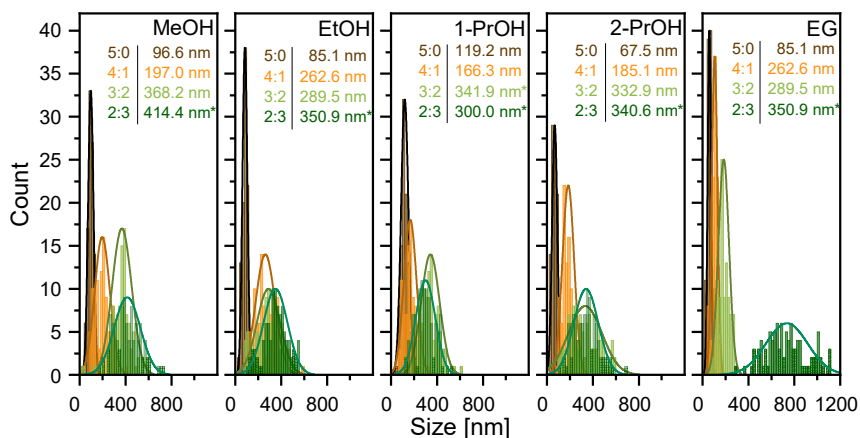


Fig. 17. Particle size distribution histograms of NTP samples prepared in different solvothermal synthesis media as determined by ImageJ software (asterisk (*) denotes that the particles are mostly comprised of impurity phase).

In order to investigate the surface area of NTP nanoparticles, BET analysis was performed. The results in Fig. 18 show a clear correlation between the measured specific surface area and size together with morphology. Smaller nanoparticles synthesized with pure alcohols have higher surface area from 31.9 to 52.6 m² g⁻¹ while those obtained with additional water are characterized by a smaller area of 15.3 – 34.2 m² g⁻¹ which is due to increasing irregularity in particle shape, surface and size.

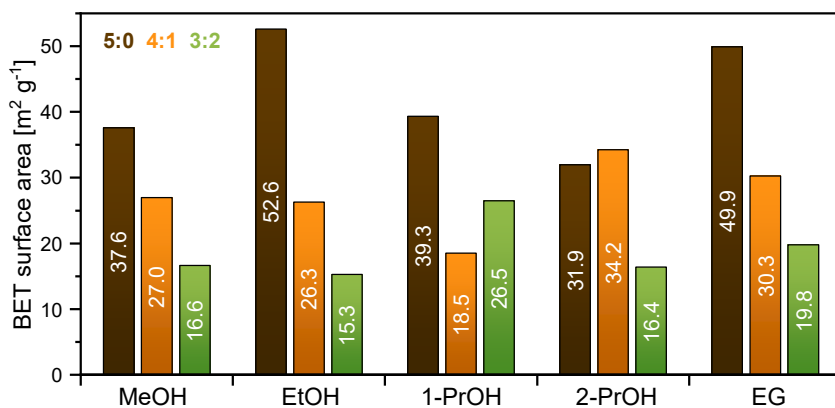


Fig. 18. BET specific surface area analysis results for NTP samples prepared in different solvothermal synthesis media.

The influence of synthesis media on the particle formation was also investigated by TEM. For the more detailed morphology analysis, four different samples were chosen: 5:0 EG with spherical particles, 4:1 EG with uniform cubes, 2:3 – with THP impurity and 4:1 2-PrOH with irregular ones. The results in Fig. 19 show that spherical and irregular particles consist of smaller NTP crystallites, whereas cubic particles are monocrystalline. This could suggest that the spherical and irregular particles have been formed by a coalescent growth while the cubic ones by Ostwald ripening.¹³³ The difference between sample morphology of the same formation mechanism could be related to the distinctive surface tensions of EG and 2-PrOH.^{134, 135}

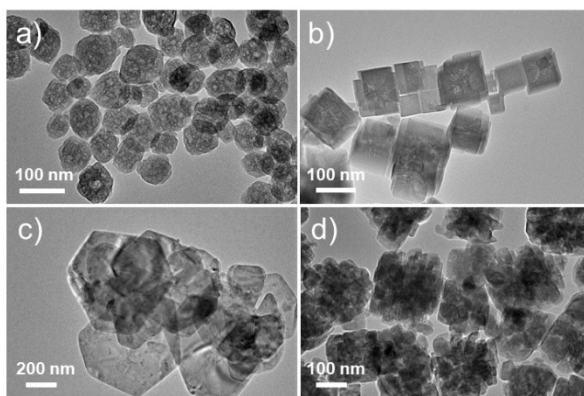


Fig. 19. TEM images of NTP samples prepared in different solvothermal synthesis media: a) pure EG, b) 4:1 EG:water, c) 2:3 EG:water d) 4:1 2-PrOH:water.

All previous results show that the solvent used in hydro(solvo)thermal synthesis plays a crucial role in structural and morphological properties, however there is no obvious correlation in terms of alcohol alkyl chain length, branching or number of hydroxyl groups. The addition of water affects the NTP purity and ability to control morphology, it could mean that different alcohols have distinctive interaction with water and ability to bind it. In order to explain the results and quantify the intermolecular interactions, relative water activity (a_{water}) in these alcohol:water mixtures was chosen as a descriptive parameter. It was estimated by a semi-empirical Aerosol Inorganic–Organic Mixtures Functional Groups Activity Coefficients (AIOMFAC) thermodynamic model designed for the calculation of activity coefficients of different chemical species in inorganic – organic mixtures.¹³⁶⁻¹³⁸ It should be noted that the true system in the hydro(solvo)thermal reactor is significantly more complex due to the presence of salts with varying solubility than the ambient conditions at which relative activities are estimated. Nevertheless, the results in Fig. 20 of water activity with respect to medium composition as a function of volume fraction (ϕ_{water}) and synthesis products serve as good proxy parameters to characterize synthesis results. All alcohols have positive mixing enthalpy with 1-PrOH deviating the most, and EG the least from ideality. This shows that 1-PrOH poorly interacts with water, as a_{water} has the highest value among the studied mixtures. The results indicate that all media where a_{water} exceeds ~ 0.65 yields a significant presence of THP or no NTP phase at all.

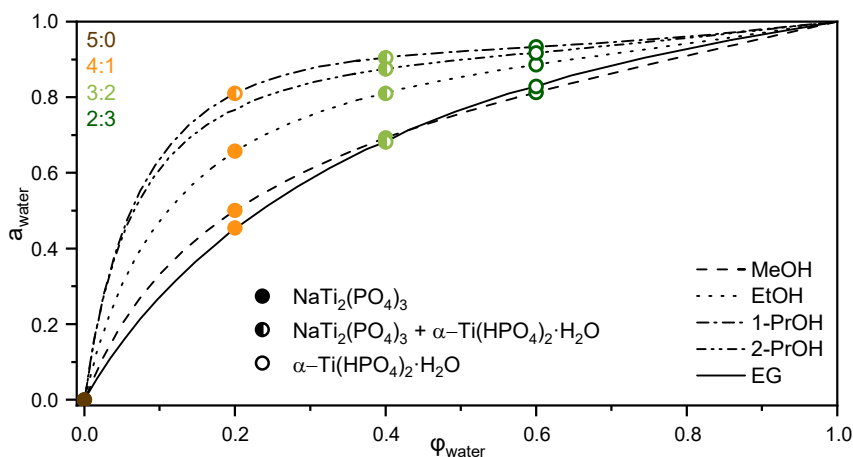


Fig. 20. Relative water activity in different reaction media used in this work as evaluated by the AIOMFAC model together with the syntheses results.¹³⁶⁻¹³⁸

In order to improve the electrochemical properties and the electronic contact between NTP particles, it is common to coat the material with a carbon layer by pyrolysis. The obtained XRD patterns in Fig. 21 show that additional calcination and coating the particles with carbon at 700 °C did not affect the phase purity and crystallinity of the NTP. The morphology and particle size of NTP are also not altered by the additional treatment (Fig. 22). The thermogravimetry results in Fig. 23 show that the amount of carbon is about 4 wt% in all cases irrespective of solvothermal media.

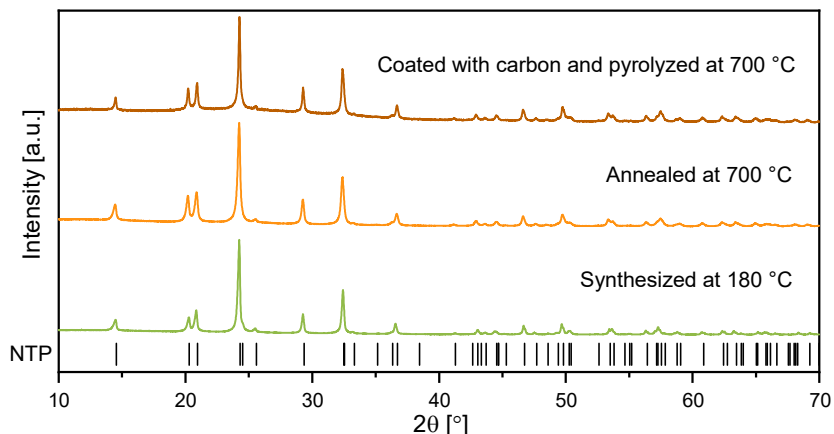


Fig. 21. Powder XRD patterns of NTP samples: (bottom) as synthesized at 180 °C; (middle) annealed at 700 °C; (top) coated with carbon and pyrolyzed at 700 °C.

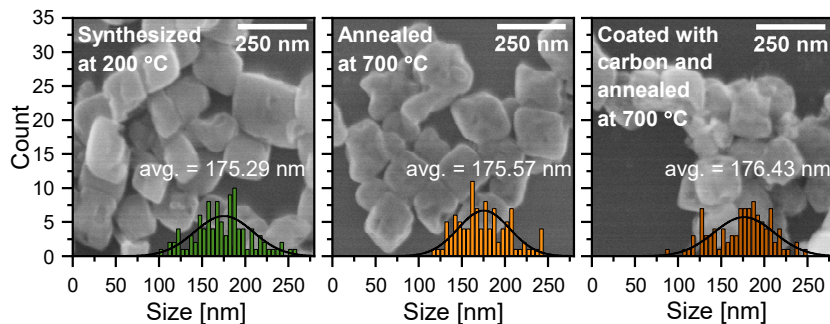


Fig. 22. SEM images and particle size distribution histograms of NTP samples (left to right) as synthesized at 200 °C; annealed at 700 °C; coated with carbon and pyrolyzed at 700 °C.

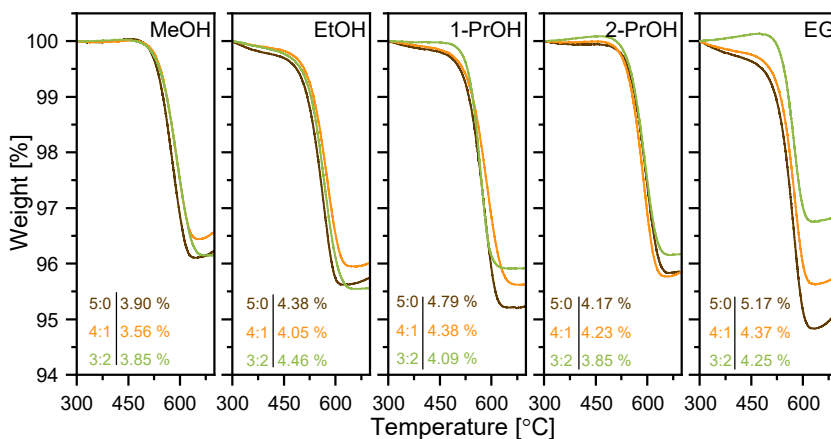


Fig. 23. Thermogravimetric curves of NTP samples prepared in different solvothermal media.

3.1.4. Electrochemical performance

The quality and properties of electrodes affect the final electrochemical performance of a SIB cell. It has been reported that particle size and size distribution have a significant influence on battery behavior.¹³⁹ For this purpose, milling of the active material powders after coating with carbon was investigated. Previous results showed that this coating does not affect the phase and morphology of the NTP particles, but the additional milling improves overall particle size distribution (reduces the size of carbon agglomerates) and enhances the electrochemical performance (Fig. 24a).

The slurry preparation protocol, its composition including binder, solvent, carbon as well as their concentration with solid loading play a crucial role in final electrode quality.¹⁴⁰ In this work, the slurry preparation method was always the same as it is described in the experimental part. However, the electrode thickness was investigated as it directly affects the energy density of the battery. Slurries were casted as 100, 300, 500 and 750 μm films on aluminum foil. It is clear from Fig. 25 that the maximum thickness for this slurry preparation method is 300 μm . Too high mass loading leads to electrode cracking. It should be noted that the real thickness of the electrode on aluminum foil after drying changes to ~ 24 μm and ~ 48 μm from 100 μm and 300 μm , respectively. Even if the electrode obtained from 300 μm thick wet film looks smooth to the naked eye, some microcracks could be observed in the SEM image (Fig. 26). These cracks become less important after transferring the electrode film on the SS mesh due to pressing. The

electrochemical performance of final electrodes obtained from 100 μm and 300 μm wet films do not differ, with 300 μm being just slightly more stable (Fig. 24b). However, thicker electrodes can accommodate more active material, leading to higher capacity and energy storage per area which is important for practical applications.

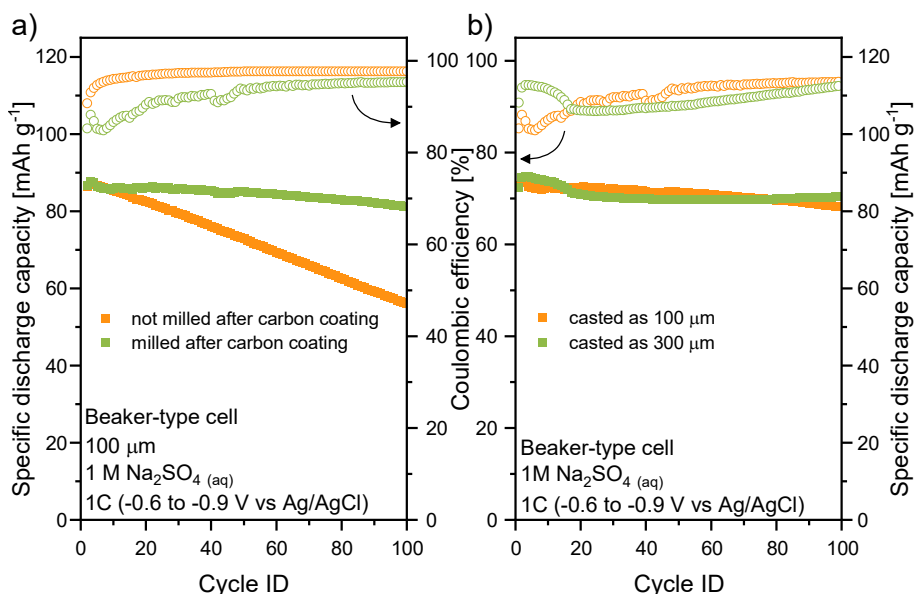


Fig. 24. GCD cycling performance of NTP electrodes prepared at different conditions: a) ball-milled and not ball-milled powders, b) electrodes obtained from 100 μm vs. 300 μm wet film thickness.

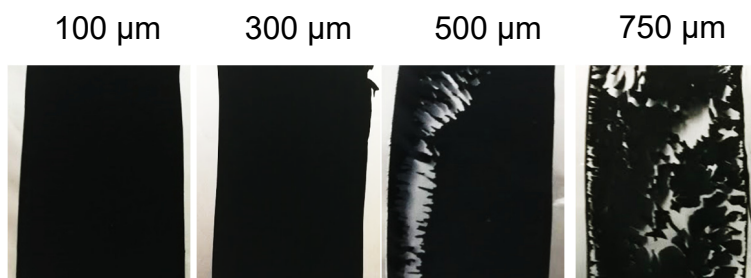


Fig. 25. Photographs of NTP electrodes on aluminum foil obtained at different casting thickness.

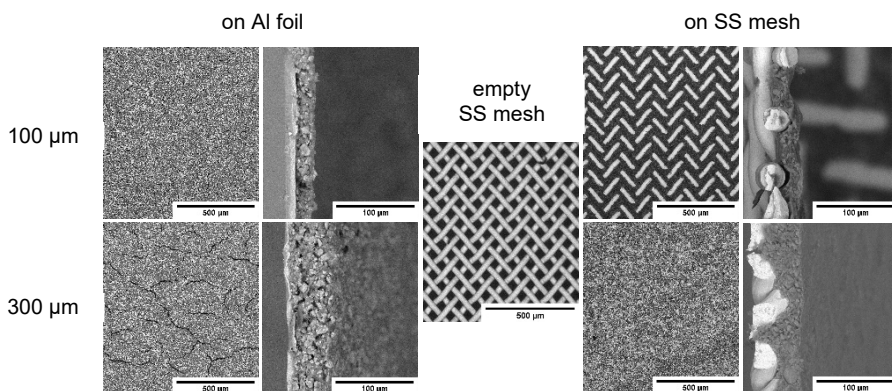
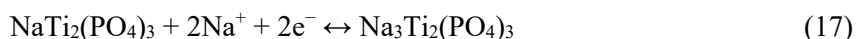


Fig. 26. SEM image of different thickness NTP electrodes on aluminum foil and stainless-steel mesh.

First of all, the electrochemical performance of NTP was evaluated by cyclic voltammetry (CV). Fig. 27 shows CVs of NTP synthesized in different media which were recorded in 1 M Na₂SO₄ (aq) electrolyte at the scanning rate of 5 mV s⁻¹ within the potential window of -1.4 – 0 V vs Ag/AgCl using beaker-type cells. In all cases, a pair of redox peaks could be found at around -1.0 V/-0.6 V which correspond to the reversible conversion of Ti⁴⁺ to Ti³⁺ accompanied by insertion/deinsertion of Na⁺ ions:



Electrodes of NTP synthesized with pure MeOH and EG have sharper current peaks which could be due to a higher specific surface area, less surface defects, better contact with the conductive carbon and more close-packed structure of a composite. In the case of EtOH or 2-PrOH, the current peaks are wider and lower because of more irregular particle shape and broader particle size distribution which affect the electrochemical kinetics. It should be noted that the amount of impurity phase, which is electrochemically inactive, was not subtracted from the electrode mass and the decrease in measured specific current of some samples could be observed.

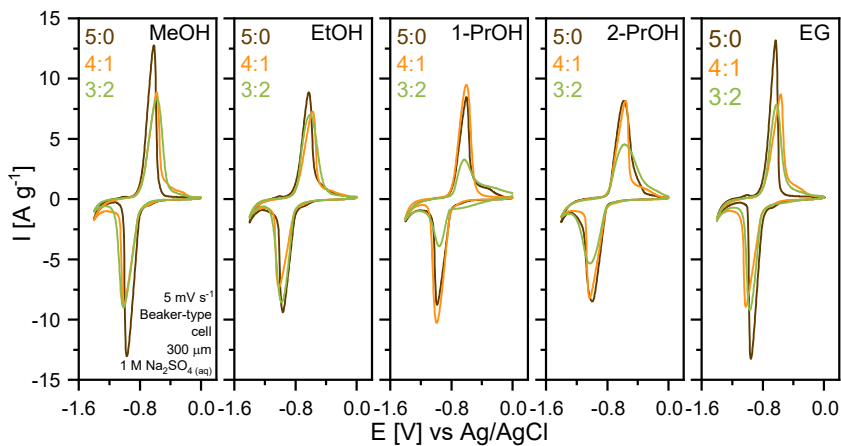


Fig. 27. Cyclic voltammograms of NTP samples prepared in different solvothermal media (2nd CV cycle) recorded at 5 mV s⁻¹ scan rate.

In order to investigate the kinetic processes in NTP electrodes, a series of CVs were recorded at different potential scan rates (v) from 0.1 mV s⁻¹ to 10 mV s⁻¹. This particular electrode was prepared from NTP synthesized in pure EtOH. The results in Fig. 28a show sharp voltametric peaks which retain their shape as potential scan rate increases which could suggest facile and fast Na ion insertion/deinsertion kinetics and exceptionally good charge/discharge rate capability of these electrodes. The peak current values lay perfectly into a linear dependence against $v^{1/2}$ (Fig. 28b) and this indicates that NTP prepared by hydro(solvo)thermal method exhibits an appropriate particle size, morphology and degree of crystallinity resulting in electrochemical performance which is limited only by Na solid-state diffusion.^{141, 142}

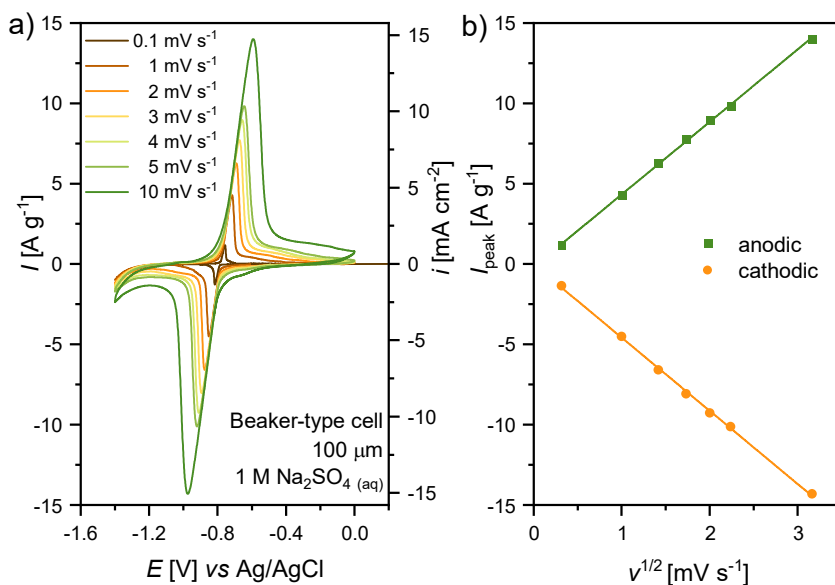


Fig. 28. a) Cyclic voltammograms of an NTP electrode obtained at different potential scan rates (v) in 1 M Na₂SO₄ (aq); b) specific peak current (I_{peak}) dependence on the square root of the potential scan rate ($v^{1/2}$).

Galvanostatic charge/discharge (GCD) cycling was used for evaluating the specific discharge capacity, CE% and capacity retention of NTP synthesized in different media. Fig. 29 and Fig. 30 show the results of GCD cycling for 100 cycles within the potential window from -0.6 V to -0.9 V (Ag/AgCl) in 1 M Na₂SO₄ (aq) electrolyte at 1C ($1C = 0.133 \text{ A g}^{-1}$) rate calculated based on the theoretical capacity of NTP using beaker-type cells. In cases of pure MeOH, 1-PrOH and EG, the initial capacities are higher and capacity degradation is lower due to their smoother surface, better homogeneity, high specific surface area, more active sites, and shorter diffusion path which facilitate the insertion/deinsertion of Na ions. Capacity retention after 100 cycles presented in Fig. 31, for EtOH and 2-PrOH is lower than others due to irregular morphology of particles. As active material dissolution (will be explained later in this section) is the main degradation cause, more particle defects lead to faster capacity decay. The best capacity retention of 95% was obtained in a sample from pure 1-PrOH, this stability could possibly be attributed to the largest particle size among pure alcohols. On the other hand, the growing size of particles by adding water does not lead to better capacity which implies that the particle morphology might be more important once the optimal particle size (in this case $\sim 120 \text{ nm}$) is achieved.

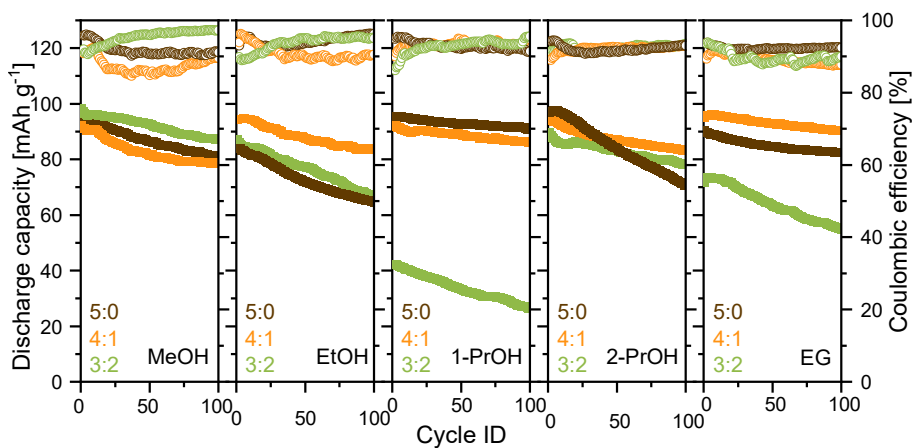


Fig. 29. GCD cycling performance of NTP prepared in different solvothermal media in 1 M Na_2SO_4 (aq) electrolyte at 1C rate using beaker-type cell (-0.6 V to -0.9 V vs Ag/AgCl).

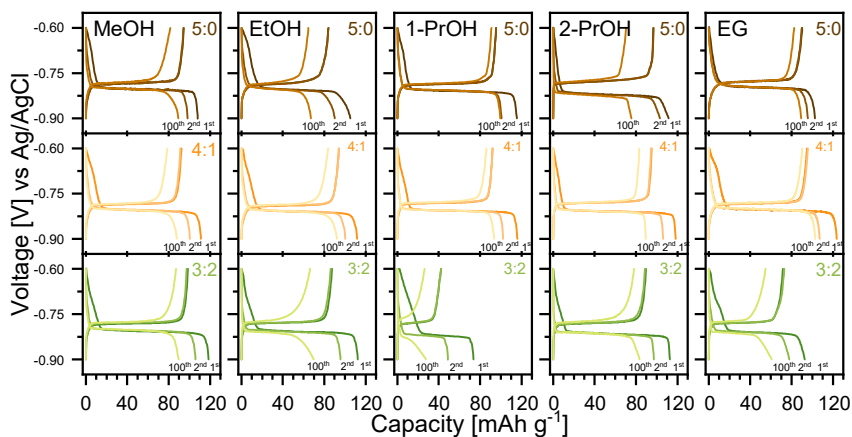


Fig. 30. GCD curves for the first, second, and 100th cycles of NTP prepared in different solvothermal media in 1 M Na_2SO_4 (aq) solution at 1C rate using beaker-type cell (-0.6 V to -0.9 V vs Ag/AgCl).

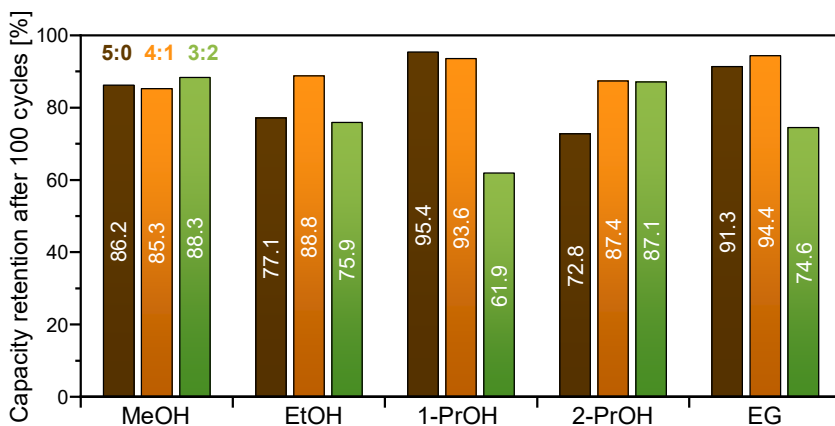


Fig. 31. Capacity retention after 100 cycles of galvanostatic cycling performance of NTP prepared in different solvothermal media in 1 M Na₂SO_{4(aq)} solution at 1C rate.

The effects of aqueous electrolytes on GCD cycling performance at 1C rate using Swagelok-type cells were investigated with EG (4:1) sample. It has been reported that highly concentrated or ‘water-in-salt’ electrolytes could expand the stable voltage window up to ~3.0 V as well as decrease the dissolution of the active material.¹⁴³ In this work two highly concentrated electrolytes such as 17 m NaClO_{4(aq)} and 8 m NaTFSI_(aq) were compared with standard 1 M Na₂SO_{4(aq)}. The results in Fig. 32 confirmed the positive effect of 17 m NaClO_{4(aq)} for enhancing NTP electrochemical performance as the initial capacity (89 mAh g⁻¹), CE% (98.6%) and capacity retention (~96%) is better than in standard 1 M Na₂SO_{4(aq)} electrolyte. The long-term GCD cycling at 1C rate using 17 m NaClO_{4(aq)} electrolyte exhibited excellent results (Fig. 33), the capacity retention of NTP after 900 cycles is 89.9% and CE% is 98.6%.

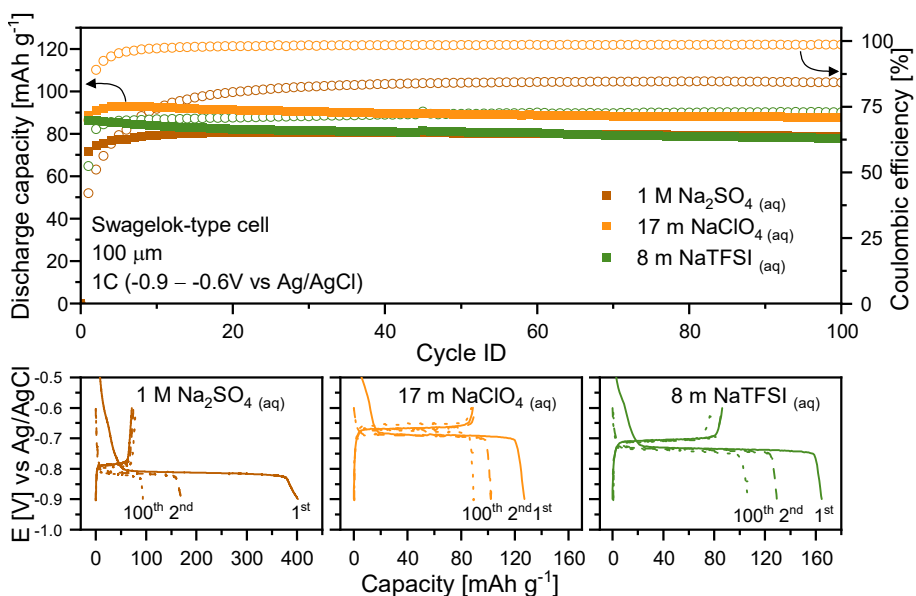


Fig. 32. GCD cycling performance of NTP prepared in EG (4:1) solvothermal media in different electrolytes at 1C rate.

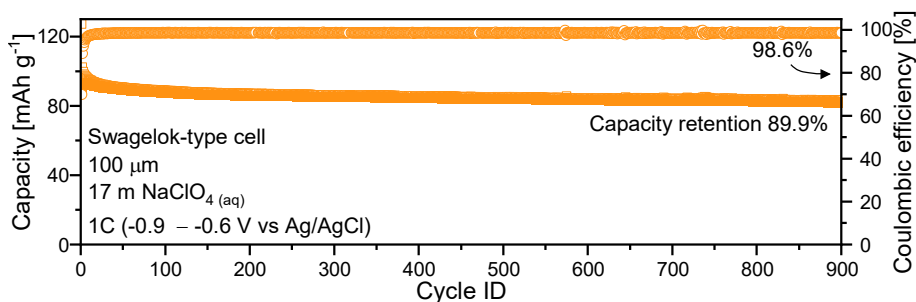


Fig. 33. GCD cycling performance of NTP prepared in EG (4:1) in 17 m NaClO₄(aq) at 1C rate.

GCD cycling at different C-rates (0.1 – 1000C) for NTP synthesized with pure EtOH was also performed. The initial discharge capacity for 1C is ~100 mAh g⁻¹, for 10C is ~90 mAh g⁻¹, for 100C and 1000C is ~75 mAh g⁻¹ (Fig. 34). It should be noted that these 1C results differ from the ones in Fig. 29 for EtOH due to slightly different electrode preparation procedures (no dry mixing) and the different thickness of the electrode. Initial specific discharge capacity, CE% and capacity retention after 100 cycles for other C-rates are summarized in Fig. 35. Capacity degradation is much more pronounced at low rates (2C and below). For example, the capacity of 0.1C rate decreased to

5 mAh g⁻¹ just after 37 cycles, while the capacity retention at 10C rate after 100 cycles was ~90%. It is also clear that CE% increases with C-rate. The capacity values were irreversible, i.e., the initial capacity was not recovered after going back to faster charging,^{144, 145} which suggests that some irreversible process occurred in the electrode during cycling in aqueous media and led to a permanent loss of capacity. Nevertheless, these NTP nanoparticles exhibit outstanding results at very fast charging/discharging.

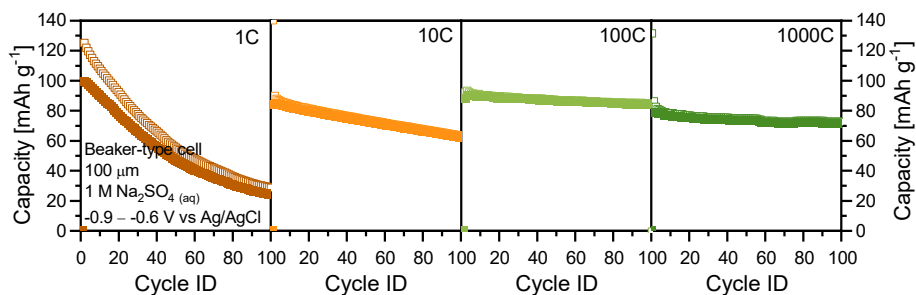


Fig. 34. Specific capacity dependence on C-rate of NTP electrodes during galvanostatic charge/discharge cycling in 1 M Na₂SO₄ (aq).

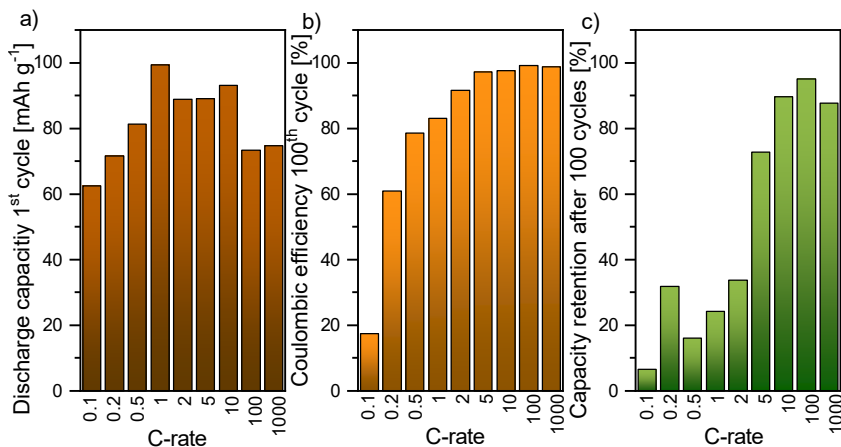


Fig. 35. GCD rate dependence of NTP specific discharge capacity: a) 1st cycle, b) CE% of the 100th cycle and c) electrode capacity retention after 100 cycles. Note: only 37 cycles were recorded at 0.1C rate.

The degradation of NTP during GCD cycling was analyzed using ICP-OES. The electrolyte solution from the cell was collected after 100 cycles at different C-rates together with electrolytes in which electrodes were simply soaked for 24 – 312 h under ambient conditions in order to check for dissolved

amount of Ti and P. The results in Fig. 36 indicate a significant dissolution of NTP during GCD cycling. However, Ti was not detected in the soaked samples while the amount of P (normalized by the active material mass of the electrode) ranged between 0 and $2.4 \cdot 10^{-3}$ mg which is an order of magnitude less than the smallest amount of P found after GCD cycling. Interestingly, the mass ratio of Ti:P should be close to 1:1 ($M(\text{Ti}) = 51.90 \text{ g mol}^{-1}$, $M(\text{P}) = 30.97 \text{ g mol}^{-1}$) in the $\text{NaTi}_2(\text{PO}_4)_3$ but the amount of P detected in the electrolyte is up to 100 times higher than Ti and is decreasing with increasing C-rate. These results are consistent with capacity retention (Fig. 35c), i.e., the more P is dissolved, the less capacity remains after 100 cycles (Fig. 35a). In the case of cycling at 0.1C rate for only 37 cycles, the detected amount of P was equivalent to the total amount of P in the active electrode material and only $\sim 5 \text{ mAh g}^{-1}$ of capacity was remaining which implies a complete dissolution of the active material. Although these results are more qualitative due to high interference from Na present in 1 M Na_2SO_4 electrolyte and analyzed elements in ICP-OES. As there is no obvious correlation between GCD results and the amount of dissolved Ti (Fig. 35b), this suggests that P is leached out to the electrolyte while Ti remains insoluble either as part of a host structure or forming an interphasial layer on the electrode surface during electrochemical degradation of NTP.¹⁰⁷ ICP-OES results suggest that the dissolution of NTP is electrochemically induced process and one of the main contributors to the capacity degradation in aqueous electrolytes. Material degradation is also related to the duration the electrode stays polarized at a certain potential range during cycling as the capacity loss was much more pronounced at lower C-rates ($< 5\text{C}$).

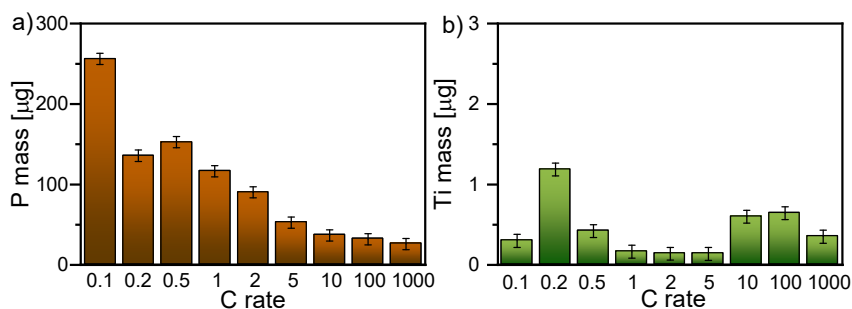
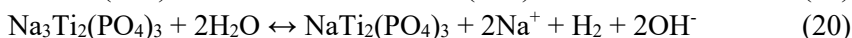
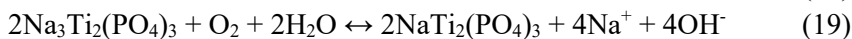


Fig. 36. Variation of the a) P and b) Ti amount detected in electrolyte after 100 GCD cycles with respect to the C-rate. The experiments were performed under ambient conditions; the elemental weights were normalized by the active material weight in a given electrode. Note: only 37 cycles were recorded at 0.1C rate.

The formation of interphasial layer of amorphous $\text{Ti}(\text{HPO}_4)_2/\text{Ti}(\text{H}_2\text{PO}_4)_4$ on the electrode surface during electrochemical degradation of NTP in aqueous media was suggested by Zhan and Shirpour.¹⁰⁷ These layers inhibit the diffusion of Na ions into the active particles and cause capacity fade. Another study showed that NTP chemical dissolution is related to pH. In aqueous solutions of NaOH it slowly begins at $\text{pH} > 11$ and accelerates after $\text{pH} > 13$. The same study also suggested that the formation of secondary phase acts as a sink for dissolved Ti.¹⁴⁶ Reactions which can generate OH^- and increase the pH in this system and probably lead to dissolution are as follows:



Reaction (18) is the hydrogen evolution reaction (HER) which could appear on the surface of the active material, carbon black or SS-mesh current collector. Even if the HER is thermodynamically possible at $E < -0.61 \text{ V}$ vs Ag/AgCl ($\text{pH} \sim 7$), the overpotential for this reaction on the surfaces mentioned previously is usually relatively high.¹⁴⁷ Additionally, the CV measurements (Fig. 27 and Fig. 28) show that HER is almost negligible at $E > -1.3 \text{ V}$ vs Ag/AgCl.

Reaction (19) is the chemical self-discharge reaction between reduced form of NTP and dissolved oxygen, while Reaction (20) is the self-discharge process moderated by water. Both are thermodynamically possible under the typical experimental conditions.

Previous results^{107, 146} showed that increasing pH leads to chemical dissolution of NTP together with formation of some, likely amorphous, layer on the surface which, apparently, is not a sufficient protection from dissolved oxygen even kinetically. There are strategies used to stop the degradation in aqueous SIBs. One is related to the engineering of the electrolyte and different additives to form Solid Electrolyte Interphase (SEI),^{148, 149} another – the engineering of the surface of active material by forming various protective layers by top-down or bottom-up techniques. The atomic layer deposition (ALD) is one of the most popular of the previous one, it has been widely reported that ALD of Al_2O_3 , TiO_2 or SiO_2 *etc.* on active material particles or electrodes themselves leads to the suppression of transition metal dissolution and leaching.¹⁵⁰⁻¹⁵² ALD experiment was also successfully performed in this work on NTP electrodes. The results show a significant decrease of the self-discharge rate and degradation of capacity, especially $> 1\text{C}$ rates.^{153, 154}

Electrochemical performance study of NTP prepared by hydro(solvo)thermal method using EG (4:1) as synthesis media was additionally carried out in an organic electrolyte in order to compare it with aqueous system and to verify that the capacity loss is mainly related to the electrolyte and not the material itself. Fig. 37 shows CVs which were recorded in 1 M NaPF₆ in DG electrolyte at the scanning rate of 0.5 mV s⁻¹ within the potential window of 1 – 3.5 V vs Na⁺/Na using a Swagelok-type cell. A pair of redox peaks of Ti³⁺/Ti⁴⁺ could be found at around 2 V/2.2 V which agrees well with previous aqueous results (Fig. 28) and those reported in the literature.^{122, 155}

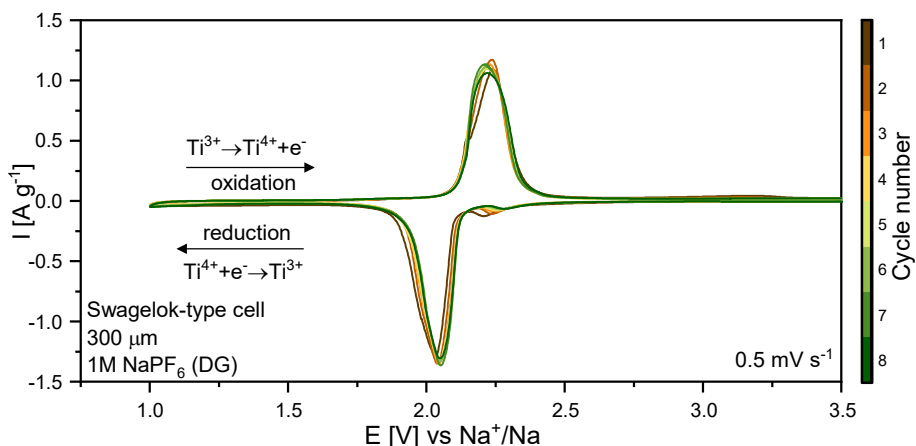


Fig. 37. Cyclic voltammograms of NTP sample prepared in EG (4:1) solvothermal media in organic electrolyte recorded at 0.5 mV s⁻¹ scan rate.

GCD measurements were performed for 300 cycles within the potential window from 1.5 to 2.9 V vs Na⁺/Na at 1C with 1 M NaPF₆ in EC:DEC (3:7 vol%) and 1 M NaPF₆ in DG electrolytes using a Swagelok-type cell (Fig. 38). The results in DG electrolyte indicate a more stable electrochemical performance of NTP than in the mixture of EC:DEC which could be attributed to the difference of SEI chemical composition.¹⁵⁶ Initial discharge capacity, CE% and capacity retention after 100 cycles in DG electrolyte are 103 mAh g⁻¹, 99.9% and 98%, respectively, which is much better than the previous results in aqueous media. The C-rate capability (0.1 – 20C) of NTP with DG electrolyte experiment (Fig. 39) shows that increasing rate leads to lower capacity due to kinetic limitations.¹⁵⁷ NTP electrode delivers 65 mAh g⁻¹ at 20C which fully recovers to the initial capacity values of 1C and 0.1C and suggests excellent reversibility.

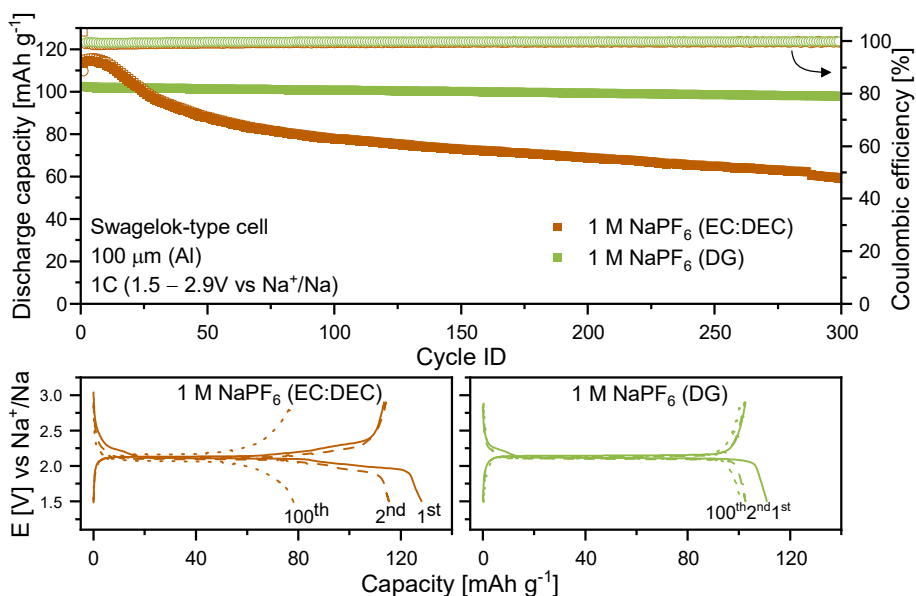


Fig. 38. GCD cycling performance of NTP prepared in EG (4:1) solvothermal media in organic electrolyte at 1C rate.

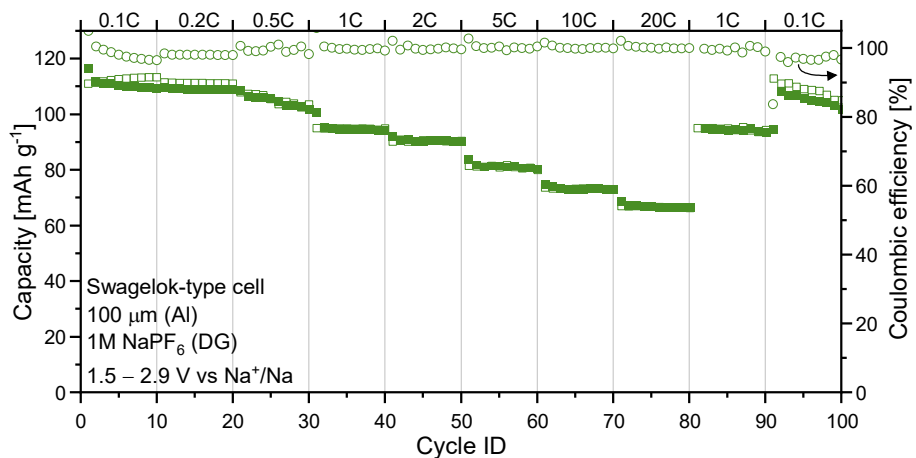


Fig. 39. GCD cycling performance of NTP prepared in EG (4:1) solvothermal media in organic electrolyte at different C-rates.

3.1.5. Summary

NaTi₂(PO₄)₃ nanoparticles were successfully prepared by a hydro(solvo)thermal method. Increasing synthesis temperature

(120 – 220 °C) results in larger particle size (60 – 142 nm), however it does not affect the phase purity of NTP.

☐ Hydro(solvo)thermal synthesis medium (methanol, ethanol, 1-propanol, 2-propanol, and ethylene glycol and their mixtures with water at volume ratios of 4:1, 3:2, 2:3, respectively) significantly affects the nanoparticle shape, size and phase purity. The addition of water leads to the formation of α -Ti(HPO₄)₂·H₂O impurity phase as well as increase in particle size of NTP.

☐ The relative water activity in the mixtures with different alcohols is the key parameter for controlling the hydro(solvo)thermal synthesis product. 1-Propanol shows the highest water activity even at low water contents while ethylene glycol is the closest to the ideal mixing with lowest relative water activity among studied alcohols.

☐ NTP nanoparticles with irregular shape and more surface defects result in lower initial capacities and faster capacity fade.

☐ Irreversible NTP capacity decay is related to a chemical degradation process during electrochemical cycling, which is especially significant at low C-rates (< 1C). There is no direct relation between the capacity fade and the amount of dissolved titanium but a direct one with the amount of dissolved phosphorus which could be explained by the formation of titanium containing insoluble passivating layers.

☐ Self-discharge related to oxygen reduction is the main cause of local pH increase which leads to NTP degradation together with fast capacity decay and low Coulombic efficiency.

3.2. Manganese-based materials for Na-ion battery positive electrodes

3.2.1. Motivation

Among various electrode materials such as oxides, polyanionic materials, Prussian blue analogous, and organic compounds those containing Mn are attracting a lot of attention because of its wide abundance, low cost, non-toxicity and environmental friendliness.¹⁵⁸⁻¹⁶⁰ Mn has multiple oxidation states: Mn^{2+} , Mn^{3+} , Mn^{4+} , Mn^{6+} and Mn^7 . $\text{Mn}^{2+}/\text{Mn}^{3+}$ and $\text{Mn}^{3+}/\text{Mn}^{4+}$ redox reactions are typically electrochemically accessible and show interesting electrochemical properties such as high electrode potential, and high specific capacity.¹⁵⁸ Recently, various Mn-based compounds such as $\text{Na}_2\text{MnPO}_4\text{F}$,¹⁶¹ $\text{Na}_2\text{MnP}_2\text{O}_7$,¹⁶² Na_xMnO_2 ,¹⁶³ $\text{Na}_2\text{MnFe}(\text{CN})_6$ ¹⁶⁴ *etc.* were widely studied. For example, MnO_2 has a theoretical capacity of 308 mAh g^{-1} or 617 mAh g^{-1} for one or two electron transfer, respectively. However, in aqueous electrolytes it reversibly exhibits only ~ 80 mAh g^{-1} .¹⁶⁵

Mn dissolves from active material into the electrolyte during electrochemical cycling process which compromises the application of such electrodes.^{166, 167} Mn dissolution results in structural degradation and capacity fade together with Mn-based materials deposition on the negative side.⁹⁷ There are reported several mechanisms of such dissolution which include the dissolution by electrolyte or Jahn-Teller distortion effect of Mn^{3+} , however all of them require further investigation.^{168, 169} Material doping, structural or surface modifications and electrolyte optimization could be used to address these issues.¹⁷⁰⁻¹⁷²

$\text{Na}_4\text{Mn}_3(\text{PO}_4)_2(\text{P}_2\text{O}_7)$ (NMPP) is one of a particularly promising mixed-polyanionic SIBs materials with a theoretical capacity of 129 mAh g^{-1} and electrode potential of 0.9 V vs Ag/AgCl. NMPP has orthorhombic $Pna2_1$ (No. 33) space group where infinite chains of $[\text{Mn}_3\text{P}_2\text{O}_{13}]_\infty$ parallel to the b-c plane are connected along the a-axis by $[\text{P}_2\text{O}_7]$ groups (Fig. 40). This disphosphate connection produces large channels for Na ion movement. There are four Mn octahedral sites which are connected via edge or corner sharing.¹⁷³ Kim et al. have reported that ionic mobility of Na is not decreased by the structural changes induced by Jahn-Teller distortion but, oppositely, it opens up the Na diffusion channels and enhances the Na insertion/deinsertion kinetics.⁷⁸ Their NMPP sample demonstrated initial capacity of 129 mAh g^{-1} at C/20 rate using organic electrolyte with capacity retention of 82% after 100 cycles.⁷⁸

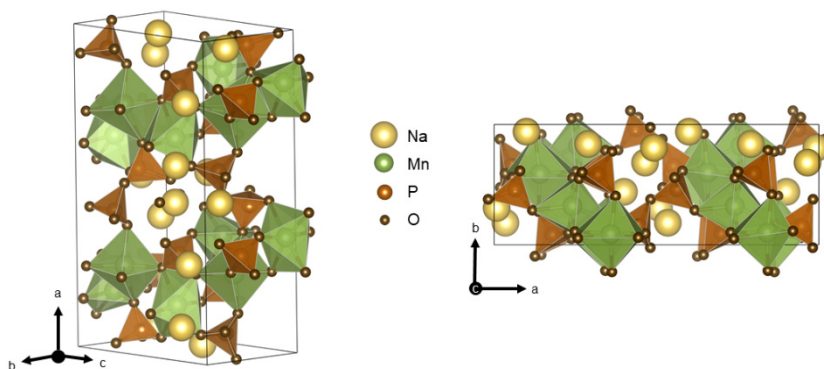


Fig. 40. Crystal structure of $\text{Na}_4\text{Mn}_3(\text{PO}_4)_2(\text{P}_2\text{O}_7)$.

$\text{Na}_3\text{MnPO}_4\text{CO}_3$ (NMPC) is another material similar to NMPP which demonstrates high potential (~ 4 V vs Na^+/Na), high theoretical capacity of 191 mAh g^{-1} for two-electron reaction per formula unit via redox of $\text{Mn}^{2+}/\text{Mn}^{3+}$ and $\text{Mn}^{3+}/\text{Mn}^{4+}$. Sidorenkite NMPC crystallizes in the monoclinic $P2_1/m$ (No. 11) space group (Fig. 41). Each Mn is at the center of an octahedron which shares 4 vertices with tetrahedral $[\text{PO}_4]$ groups and an edge with a $[\text{CO}_3]$ group while Na ions occupy two different sites: coordinated by 7 and 6 oxygen atoms.¹⁷⁴ Xie et al. have reported that their NMPC sample synthesized by a ball-milling method exhibited $\sim 134 \text{ mAh g}^{-1}$ in organic electrolyte at $1/30\text{C}$ and the same capacity value in $17 \text{ m NaClO}_4(\text{aq})$ electrolyte at 0.5C , however only for 30 cycles.¹⁷⁵

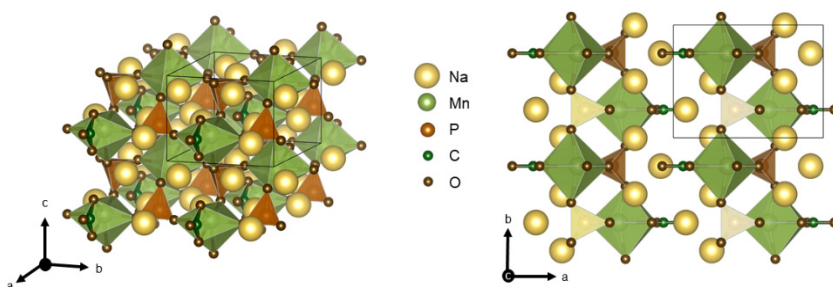


Fig. 41. Crystal structure of $\text{Na}_3\text{MnPO}_4\text{CO}_3$.

3.2.2. Synthesis

$\text{Na}_4\text{Mn}_3(\text{PO}_4)_2\text{P}_2\text{O}_7$ was synthesized via a solid-state method (Fig. 42a). In a typical synthesis, $\text{Na}_4\text{P}_2\text{O}_7$ (0.0081 mol, ChemPur, p.a.), MnC_2O_4 (0.0145 mol, ChemPur, p.a.), and $\text{NH}_4\text{H}_2\text{PO}_4$ (0.0097 mol, Honeywell, 99+%) were mixed using wet (2-propanol) ball-milling at 350 rpm for 2 h. The dried mixture was calcined at 300 °C for 6 h and subsequently at 600 °C for 6 h, in ambient air. Obtained light brown powders were post-processed at 350 rpm for 2 h using a ball-mill. The resulting particles were coated with a layer of carbon by homogeneously mixing additionally ball-milled (1 h at 900 rpm) NMPP powder (70 wt%, (usually, 0.7 g)) and of citric acid (30 wt% (0.3 g), $\text{HOC}(\text{CH}_2\text{CO}_2\text{H})_2$, Lach-ner, G.R.) or glucose (0.3 g, $\text{C}_6\text{H}_{12}\text{O}_6$, Reachem, G.R.) in distilled water (50 mL). The resulting mixture was dried at 80 °C for several hours for complete water elimination. The obtained powder was reground and annealed at 600 °C for 6 h under N_2 atmosphere. The resulting black powders were again ball-milled at 350 rpm for 2 h to achieve a uniform final particle size distribution.

$\text{Na}_3\text{MnPO}_4\text{CO}_3$ was synthesized via a hydrothermal method (Fig. 42b). In a typical synthesis, Na_2CO_3 (0.0943 mol, ChemPur, 99.8%) together with $(\text{NH}_4)_2\text{HPO}_4$ (0.02 mol, ThermoFisher, 98%) were dissolved in distilled water (50 mL) to form a clear solution. At the same time, $\text{Mn}(\text{NO}_3)_2$ (0.01 mol, ChemPur,) was dissolved in 25 mL of water and then quickly transferred to the first solution under vigorous magnetic stirring. The white suspension obtained after continuous stirring for 30 min at room temperature was transferred into a 100 mL Teflon-lined stainless-steel autoclave and heated at 180 °C for 15 h. Several series of NMPC samples were prepared by different synthesis temperature (120, 160 and 180 °C) and amounts of precursors: $(\text{NH}_4)_2\text{HPO}_4$ (0.03, 0.02, 0.015 and 0.001 mol), $\text{Mn}(\text{NO}_3)_2$ (0.02, 0.015, 0.01 and 0.005 mol) in the final hydrothermal solution (75 mL). The obtained light brown precipitate was collected and washed several times by centrifugation with distilled water and acetone, and subsequently dried at 80 °C overnight. The dried sample was again ball-milled at 350 rpm for 1 h to achieve a uniform particle size distribution.

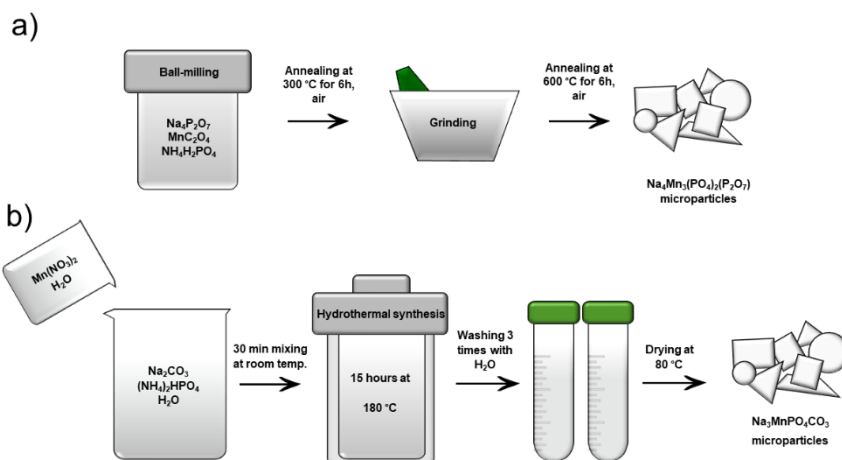


Fig. 42. a) Solid-state synthesis scheme of $\text{Na}_4\text{Mn}_3(\text{PO}_4)_2\text{P}_2\text{O}_7$ and b) hydrothermal synthesis scheme of $\text{Na}_3\text{MnPO}_4\text{CO}_3$.

3.2.3. Structural characterization

3.2.3.1. $\text{Na}_4\text{Mn}_3(\text{PO}_4)_2\text{P}_2\text{O}_7$

$\text{Na}_4\text{Mn}_3(\text{PO}_4)_2\text{P}_2\text{O}_7$ was synthesized by a conventional solid-state method. The powder XRD pattern and its Rietveld refinement results in Fig. 43 show the presence of sharp diffraction peaks which indicate high crystallinity. This crystal structure was determined to be orthorhombic $Pna2_1$ (space group No. 33).⁷⁸ The calculated lattice parameters are as follows: $a = 17.99993(27) \text{ \AA}$, $b = 10.74550(17) \text{ \AA}$, $c = 6.64863(10) \text{ \AA}$ and $V = 1285.97(4) \text{ \AA}^3$. However, $\sim 22.0 \text{ wt\%}$ of NaMnPO_4 impurity was also detected in this sample by XRD. The morphology of NMPP was investigated using SEM. Fig. 44 indicates that particles are irregularly shaped and few micrometers in size with broad size distribution.

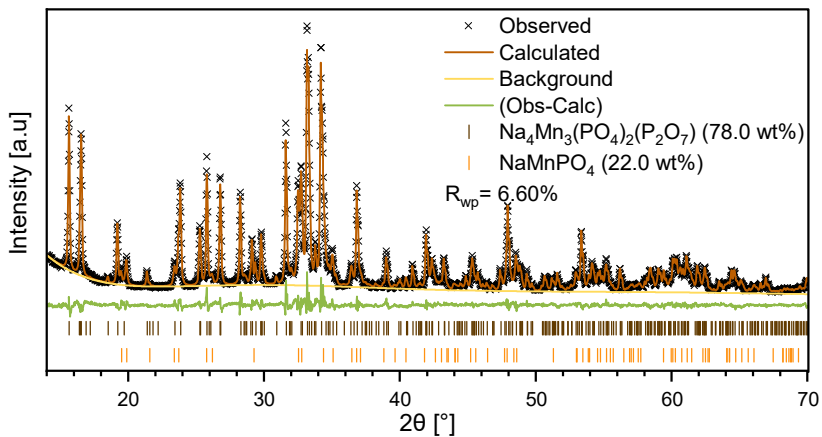


Fig. 43. Powder XRD patterns and Rietveld refinement results of NMPP synthesized by solid-state method.^{78, 176}

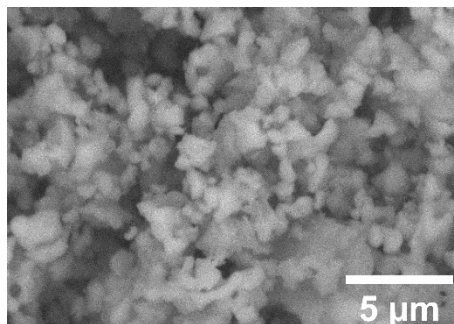


Fig. 44. SEM image of NMPP synthesized by solid-state method.

In order to improve the electronic contact between ceramic particles, the NMPP was additionally coated by a carbon layer using post-synthetic pyrolysis. Citric acid or glucose are usually used as carbon precursors as these carbon-rich compounds are low cost, easily decompose and homogeneously distributed on the material surface.¹⁷⁷⁻¹⁷⁹ In this case, only glucose is suitable for carbon coating which results in ~5 wt% of carbon (Fig. 45 and Fig. 46). XRD pattern shows that with citric acid NMPP mainly decomposes to Mn_2O_3 , possibly due to NMPP solubility in acidic media at higher temperature. Moreover, additional heating at 600 °C with glucose results in a decreasing amount of impurities which could suggest that more heating could lead to a better yield and phase purity.

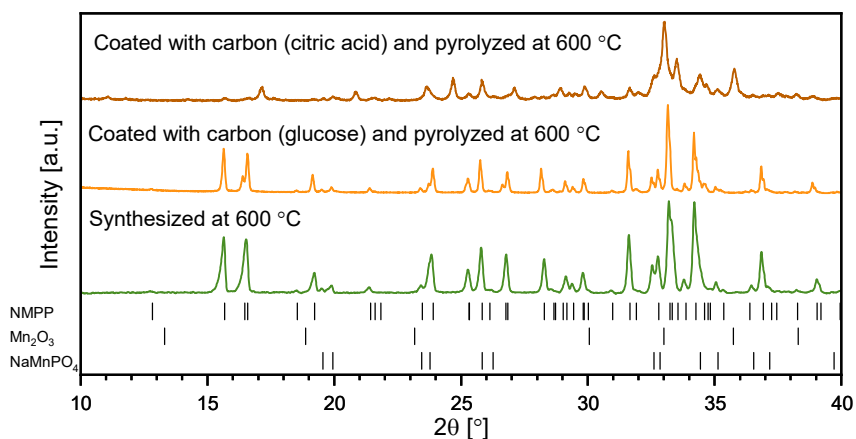


Fig. 45. Powder XRD patterns of NMPP samples: (bottom) as synthesized at 600 °C; (middle) coated with carbon (glucose) and pyrolyzed at 600 °C.; (top) coated with carbon (citric acid) and pyrolyzed at 600 °C.^{78, 176, 180}

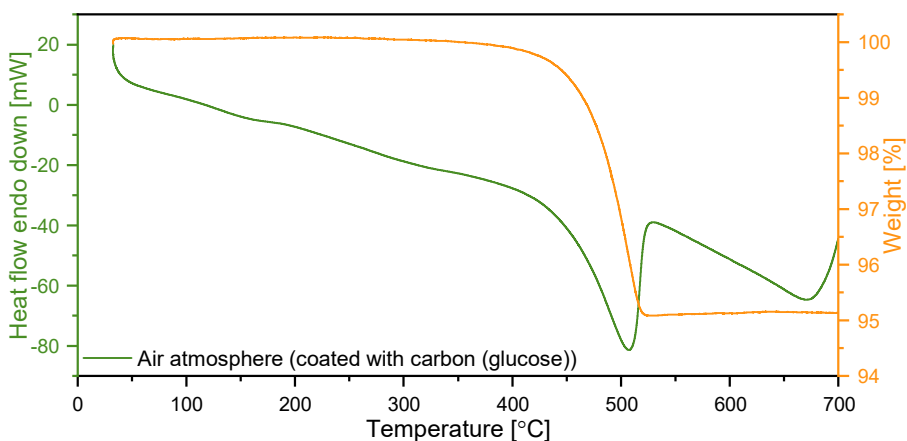


Fig. 46. Thermogravimetric and DSC curves of NMPP.

3.2.3.2. $\text{Na}_3\text{MnPO}_4\text{CO}_3$

$\text{Na}_3\text{MnPO}_4\text{CO}_3$ was synthesized by a hydrothermal method. First, the suitable synthesis temperature was determined. Powder XRD analysis (Fig. 47) revealed that 120 °C temperature is too low to obtain pure NMPC as additional impurity of MnCO_3 is also visible. NMPC prepared at 160 °C and 180 °C exhibits pure phase and sharp peaks which indicate high crystallinity. This crystal structure was determined to be monoclinic $P2_1/m$ (space group No. 11).¹⁸¹

Even if the XRD results show pure materials, during centrifugation with water. Two different phases with light and dark brown colors were clearly visible (Fig. 49b). This could suggest the formation of additional impurity of some amorphous phase. In order to reduce this impurity, different ratios of precursors ($\text{Mn}(\text{NO}_3)_2$ and $(\text{NH}_4)_2\text{HPO}_4$) were used. If the amount of $\text{Mn}(\text{NO}_3)_2$ is 0.02 mol or 0.015 mol, while $(\text{NH}_4)_2\text{HPO}_4$ is 0.01 mol in all cases, the XRD patterns (Fig. 48a) show the formation of NMPC together with the impurity of MnCO_3 . If the amount of $\text{Mn}(\text{NO}_3)_2$ is lower (0.01 or 0.005 mol) XRD shows pure phase NMPC. However, all these cases show two visible phases appearing during centrifugation (Fig. 49a, b, c and d). On the other hand, it is clear that increasing the amount of $(\text{NH}_4)_2\text{HPO}_4$ leads to lower amount of the ‘dark’ phase (Fig. 49e, f, g and h) but too much of it (0.03 mol) brings additional impurity of NaMnPO_4 (Fig. 48b). In this study, the most appropriate ratio was chosen as follows: 0.01 mol of $\text{Mn}(\text{NO}_3)_2$, 0.02 mol of $(\text{NH}_4)_2\text{HPO}_4$ and synthesis temperature of 180 °C based on XRD results and visibly less of amorphous phase. Further investigation of electrochemical performance was conducted with this sample.

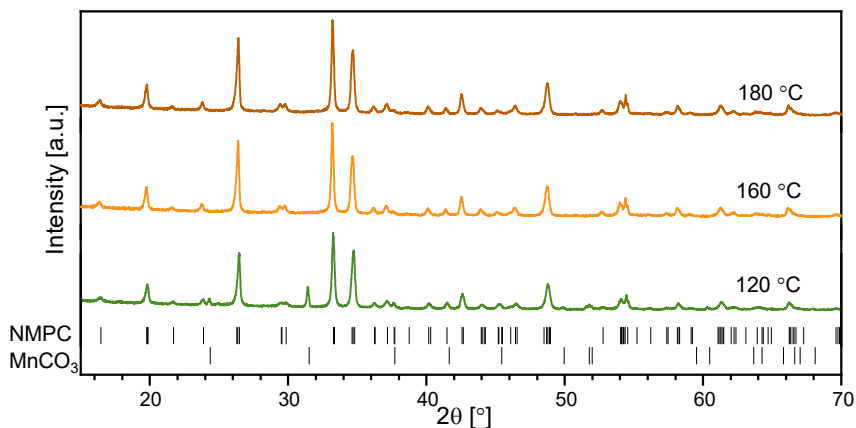


Fig. 47. Powder XRD patterns of NMPC samples prepared at different hydrothermal synthesis temperatures.^{181, 182}

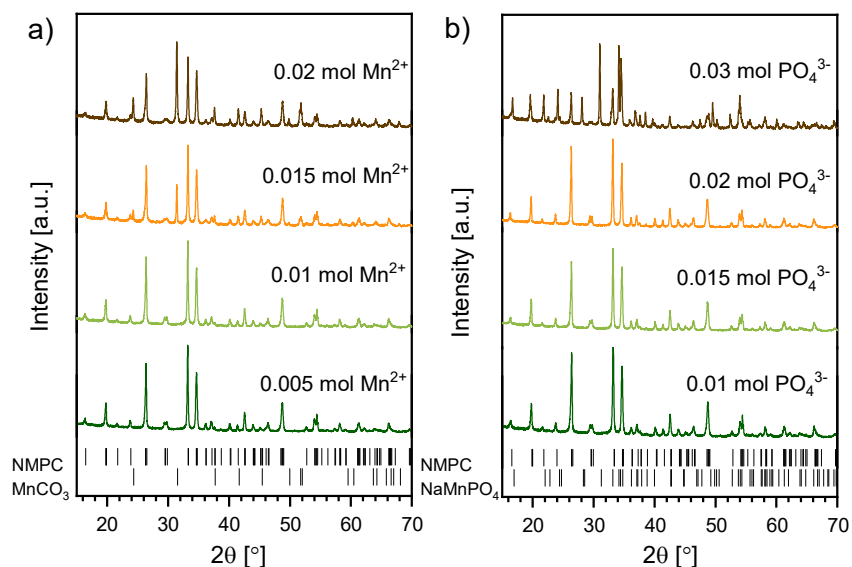


Fig. 48. Powder XRD patterns of NMPC samples prepared with different amounts of a) $\text{Mn}(\text{NO}_3)_2$ and b) $(\text{NH}_4)_2\text{HPO}_4$ precursors.^{176, 181, 182}

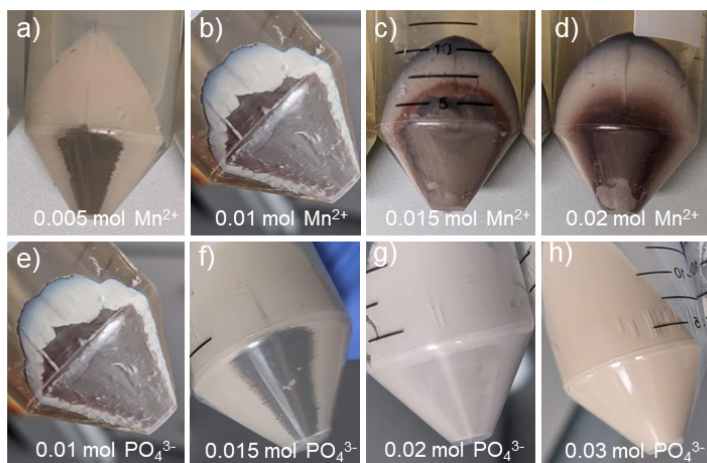


Fig. 49. NMPC samples after centrifugation prepared with different amounts of a-d) $\text{Mn}(\text{NO}_3)_2$ and e-f) $(\text{NH}_4)_2\text{HPO}_4$ precursors.

The morphology of a selected NMPC sample was investigated using SEM. Fig. 50 indicates that particles are of irregular shape and few micrometers in size. In order to analyze the stability of this material, TGA under air or N_2 atmosphere was performed. The results in Fig. 51 show that the decomposition

of probably less stable $[\text{CO}_3]$ group starts at $550\text{ }^\circ\text{C}$. The additional coating with carbon layer was not performed for NMPC in this work because it could only be done at temperatures above $600\text{ }^\circ\text{C}$ which, in this case, is too high.

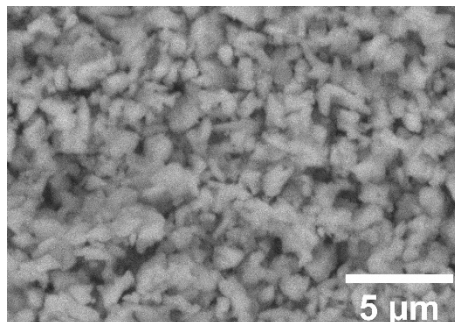


Fig. 50. SEM image of NMPC prepared with 0.01 mol of $\text{Mn}(\text{NO}_3)_2$ and 0.02 mol of $(\text{NH}_4)_2\text{HPO}_4$ at $180\text{ }^\circ\text{C}$ by hydrothermal synthesis.

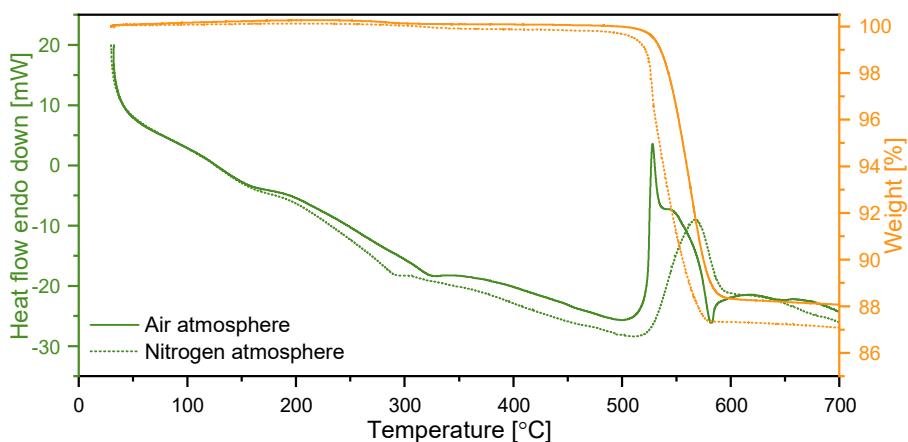


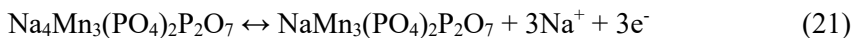
Fig. 51. Thermogravimetric and DSC curves of NMPC prepared with 0.01 mol of $\text{Mn}(\text{NO}_3)_2$ and 0.02 mol of $(\text{NH}_4)_2\text{HPO}_4$ at $180\text{ }^\circ\text{C}$ by hydrothermal synthesis.

3.2.4. Electrochemical performance

3.2.4.1. $\text{Na}_4\text{Mn}_3(\text{PO}_4)_2\text{P}_2\text{O}_7$

For the initial electrochemical characterization, CVs of NMPP samples were performed using $1\text{ M Na}_2\text{SO}_4$ (aq) electrolyte at the scanning rate of 5 mV s^{-1} within the potential window of $0 - 1.4\text{ V}$ vs Ag/AgCl using beaker-

type cells. In this case, a pair of redox peaks should be at around 0.8 V/1.0 V which would correspond to the reversible conversion of Mn^{2+} to Mn^{3+} accompanied by insertion/deinsertion of Na^+ ions:⁷⁸



The first cycle (Fig. 52) shows only a single anodic peak at 1.0 V vs Ag/AgCl which corresponds to one electron redox of $\text{Mn}^{2+}/\text{Mn}^{3+}$. However, it disappears in further cycling, which indicates fast active material electrochemical degradation.¹⁸³

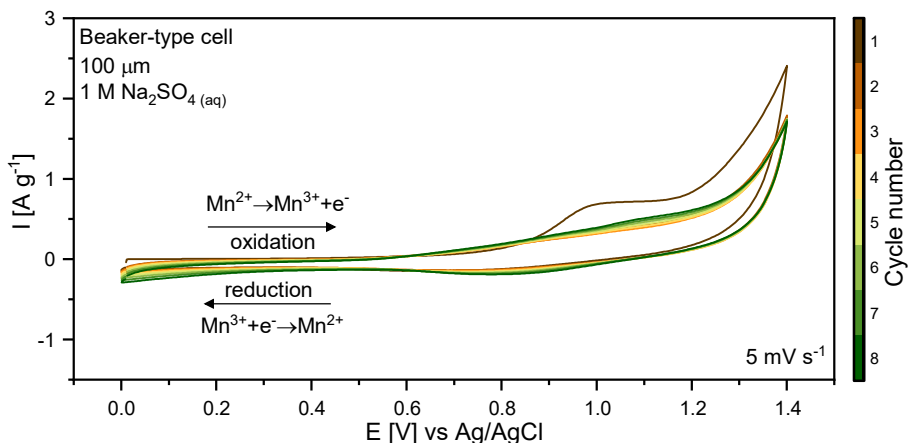


Fig. 52. Cyclic voltammograms of NMPP 1 M $\text{Na}_2\text{SO}_4(\text{aq})$ at 5 mV s^{-1} scan rate.

GCD cycling was used for the determination of specific discharge capacity and CE% of NMPP electrodes. Fig. 53 shows the GCD cycling for 100 cycles within the potential window from 0 V to 1.2 V (Ag/AgCl) at 1C ($1\text{C} = 0.129 \text{ A g}^{-1}$) rate calculated based on the theoretical capacity of NMPP in 1 M $\text{Na}_2\text{SO}_4(\text{aq})$ or 17 m $\text{NaClO}_4(\text{aq})$ using Swagelok-type cells. Specific initial charge and discharge capacities for standard electrolyte are 74 mAh g^{-1} and 15 mAh g^{-1} , respectively, which agree with the CV results for the first cycle. Charge capacity drops rapidly in the second cycle and stays at only $\sim 24 \text{ mAh g}^{-1}$ which is too low for a suitable SIBs positive electrode material. In concentrated electrolytes of 17 m $\text{NaClO}_4(\text{aq})$, the initial specific charge and discharge capacities are much lower: 23 and 8 mAh g^{-1} , respectively, which suggest that a more concentrated electrolyte does not help to decrease the rapid degradation of NMPP.

Previous studies of Mn-based materials showed that there is a significant Mn dissolution (but not all) into the electrolyte due to the stability of $\text{Mn}^{2+}_{(\text{aq})}$ species. However, this cannot explain the full capacity loss.¹⁸³ Probably, there is a formation of insoluble and electrochemically inactive layer in the initial cycles which blocks Na-ions insertion/deinsertion and limits the performance, similar to the previously discussed NTP degradation mechanism. The slightly higher capacity in standard electrolyte (Fig. 53) could come from these newly formed Mn-based layers as NMPP should dissolve faster in it than in concentrated electrolytes which show much lower capacity values.

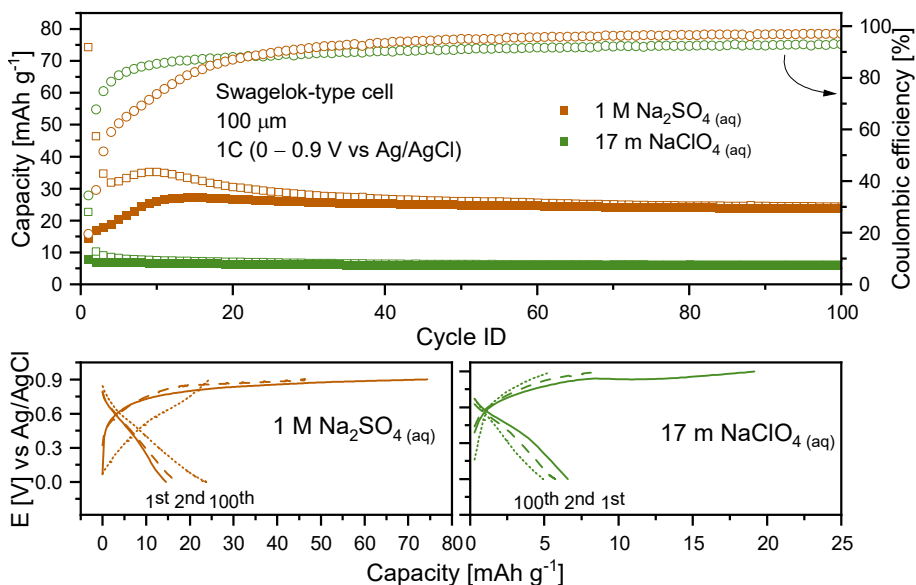


Fig. 53. GCD cycling performance of NMPP in different aqueous electrolytes at 1C rate.

Electrochemical performance investigation of NMPP was also done in organic electrolytes in order to compare it with aqueous systems. Fig. 54 shows CVs which were recorded in 1 M NaPF_6 in DG electrolyte at the scanning rate of 0.5 mV s^{-1} within the potential window of 1.5 – 4.5 V vs Na^+/Na using Swagelok-type cells. Only the first two cycles show anodic and cathodic redox peaks at around 3.6 V/4.0 V for $\text{Mn}^{2+}/\text{Mn}^{3+}$ with very low currents which completely fade out in further cycles and suggest fast NMPP degradation even in organic electrolytes.

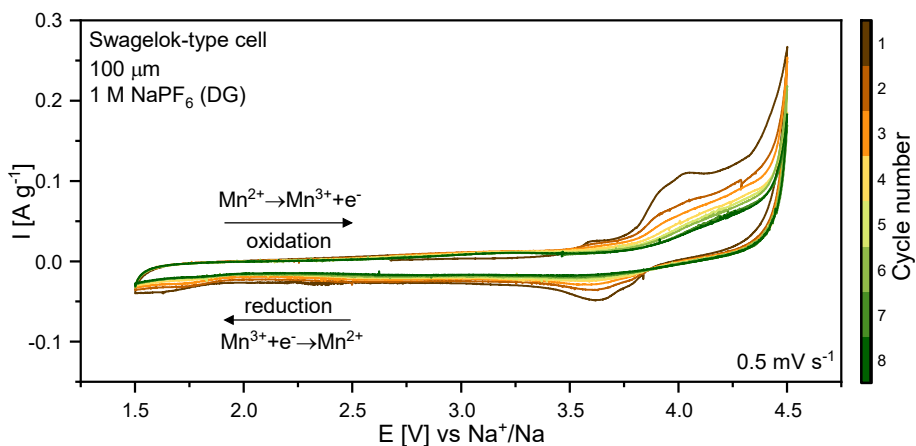


Fig. 54. Cyclic voltammograms of NMPP in organic electrolyte at 0.5 mV s^{-1} scan rate.

GCD measurements were performed for 100 cycles within the potential window from 1.7 to 4.5 V vs Na^+/Na at 1C with 1 M NaPF_6 in EC:DEC (3:7 vol%) and 1 M NaPF_6 in DG electrolytes using Swagelok-type cells (Fig. 55). Both electrolytes show similar electrochemical performance. Initial discharge capacity, CE% and capacity retention after 100 cycles of DG electrolyte are 20 mAh g^{-1} , 98.8% and 51%, respectively, which does not differ much from the previous results in aqueous media. Actually, there are only a few publications which claim NMPP to be a reasonable positive electrode material for SIBs.^{78, 184} However, even if the synthesis method and structural results of this study are similar to them, the electrochemical performance suggests that NMPP is not a suitable material neither for aqueous nor for organic SIBs.

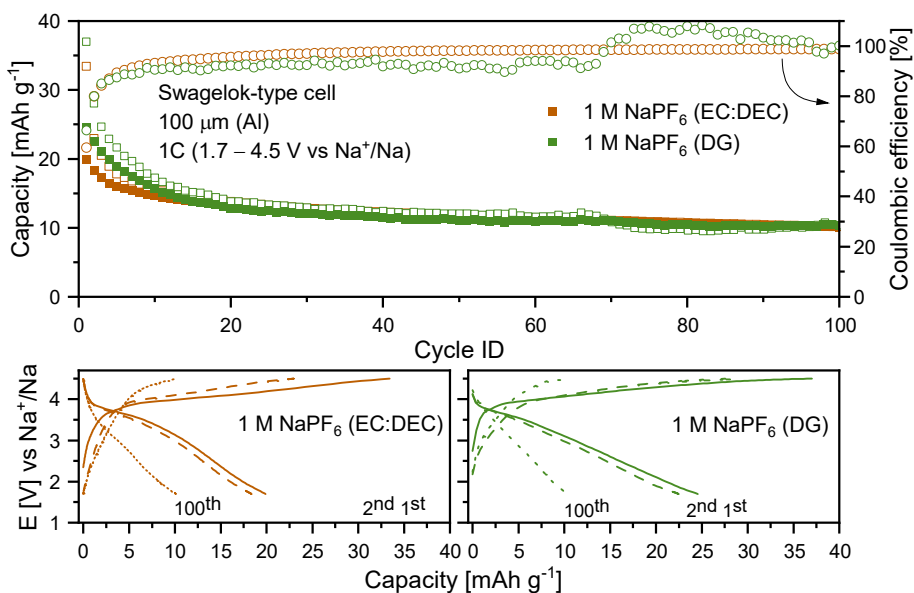
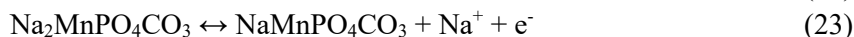
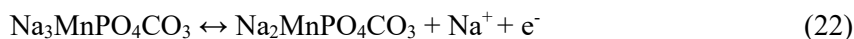


Fig. 55. GCD cycling performance of NMPP in organic electrolytes at 1C rate.

3.2.4.2. $\text{Na}_3\text{MnPO}_4\text{CO}_3$

For the initial electrochemical characterization, CV of a NMPC sample was performed in 1 M Na_2SO_4 (aq) electrolyte at the scanning rate of 5 mV s^{-1} within the potential window of 0 – 1.4 V vs Ag/AgCl using beaker-type cells. In this case, two pairs of redox peaks at around 0.5 V/0.6 V and 1.0 V/1.2 V vs Ag/AgCl are visible which would correspond to the two-step reversible conversion of Mn^{2+} to Mn^{4+} accompanied by insertion/deinsertion of Na^+ ions:¹⁸⁵



The first cycle (Fig. 56) shows only anodic peaks at 0.7 V and 1.1 V vs Ag/AgCl which probably corresponds to two-electron redox of $\text{Mn}^{2+}/\text{Mn}^{4+}$. In the second cycle, no peaks are visible, whereas from the 4th cycle, there is a reversible pair of redox peaks at around 0.85 V / 1.0 V vs Ag/AgCl appearing which remains stable in later cycles. This change of peaks could suggest the dissolution of NMPC in the first cycle and the formation of an additional Mn-based phase which is electrochemically active in later cycles.

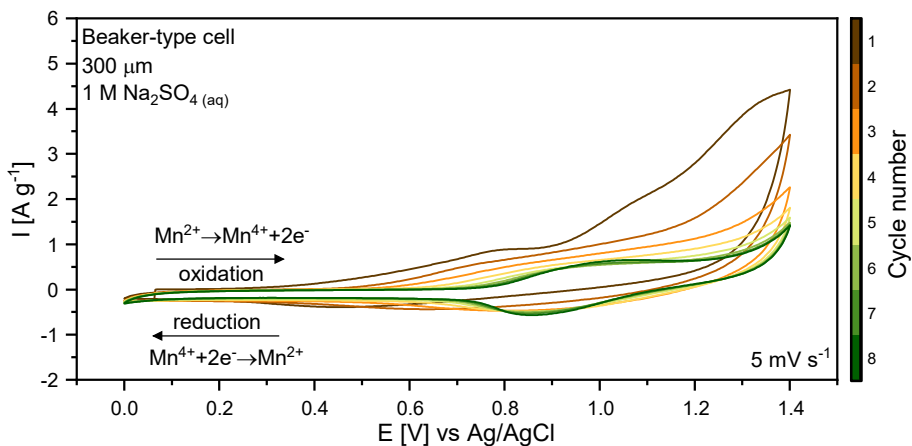


Fig. 56. Cyclic voltammograms of NMPC in 1 M $\text{Na}_2\text{SO}_4(\text{aq})$ at 5 mV s^{-1} scan rate.

GCD cycling was used for the determination of specific discharge capacity and CE% of NMPC electrodes. Fig. 57 shows the results of GCD cycling for 100 cycles within the potential window from 0.6 V to 1.2 V (Ag/AgCl) at 1C ($1\text{C} = 0.191 \text{ A g}^{-1}$ based on the theoretical capacity of NMPC) in 1 M $\text{Na}_2\text{SO}_4(\text{aq})$ electrolyte using beaker-type cells. The initial charge and discharge capacities of NMPP are 233 and 30 mAh g^{-1} , respectively, which decrease rapidly in the following cycles and stay $\sim 10 \text{ mAh g}^{-1}$, likely due to dissolution similarly to the NMPP case. Therefore, NMPC is also not a suitable positive electrode material for aqueous SIBs due to the lack of stability.

Electrochemical performance of NMPC was also investigated in organic electrolytes in order to compare it with aqueous systems. Fig. 58 shows CVs which were recorded in 1 M NaPF_6 in DG at the scanning rate of 0.5 mV s^{-1} within the potential window of 1.5 – 4.5 V vs Na^+/Na using Swagelok-type cells. No peaks were observed during cycling, suggesting either limited electrochemical activity or very fast capacity loss of NMPP even in organic electrolytes.

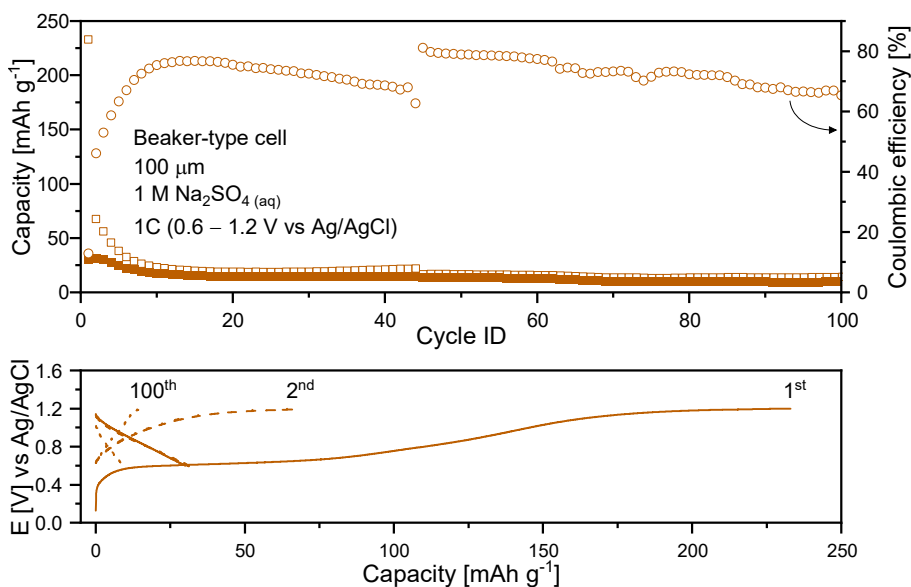


Fig. 57. GCD cycling of NMPC in 1 M $\text{Na}_2\text{SO}_4(\text{aq})$ electrolyte at 1C.

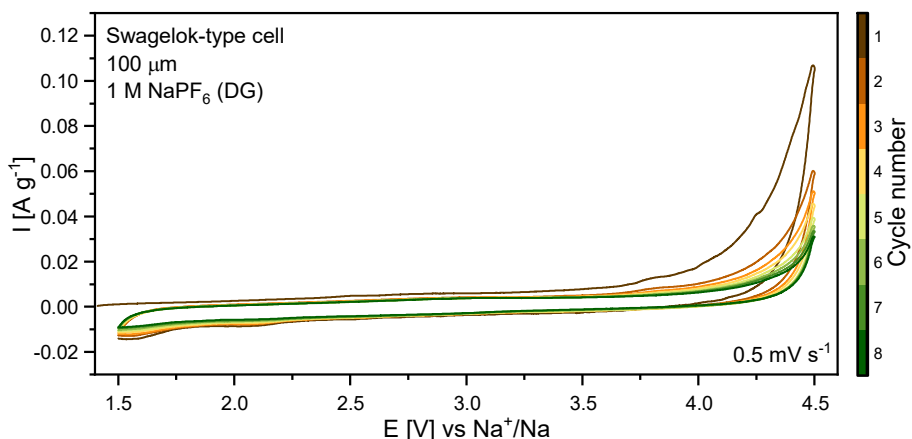


Fig. 58. Cyclic voltammograms of NMPC in organic electrolyte at 0.5 mV s^{-1} scan rate.

GCD measurements were also performed for 100 cycles within the potential window from 1.5 to 4.5 V vs Na^+/Na at 1C in 1 M NaPF_6 in DG electrolyte using Swagelok-type cells (Fig. 59). Initial charge capacity is only 12.6 mAh g^{-1} which decreases in the following cycles down to $\sim 4 \text{ mAh g}^{-1}$. The results in organic and aqueous electrolytes suggests that the NMPC framework is electrochemically inactive due to possible dissolution or

formation of insoluble and inactive phases which limit its electrochemical response.

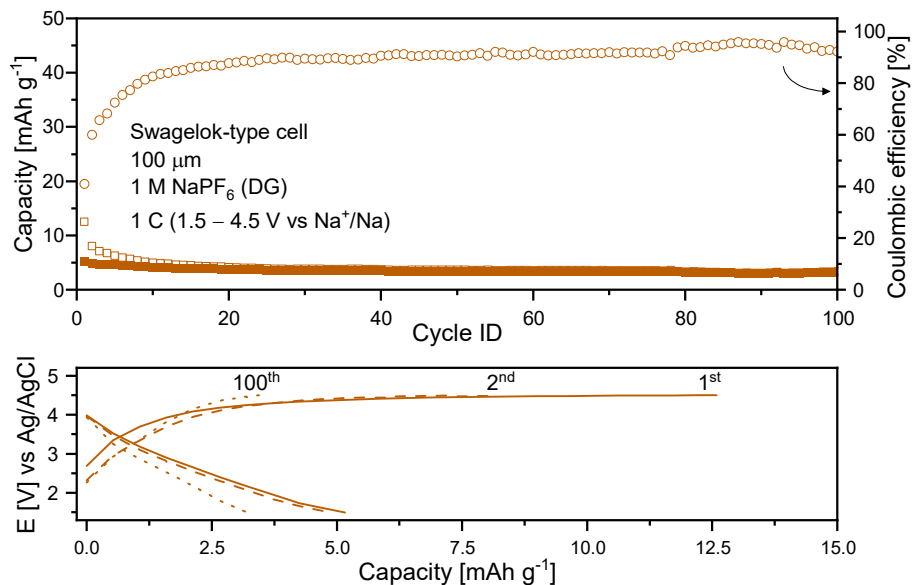


Fig. 59. GCD cycling of NMPC electrode in organic electrolyte at 1C.

3.2.5. Summary

Na₄Mn₃(PO₄)₂P₂O₇ was successfully synthesized via conventional solid-state method. However, XRD results showed some additional impurity phase of NaMnPO₄.

Na₃MnPO₄CO₃ was successfully synthesized via hydrothermal method. Appropriate synthesis conditions such as temperature (180 °C) and precursor ratio (0.01 mol of Mn(NO₃)₂ and 0.02 mol of (NH₄)₂HPO₄) were determined.

NMPP and NMPC have very limited electrochemical activity in both organic and aqueous electrolytes. The results suggest that degradation processes such as material dissolution and/or formation of insoluble and inactive surface phases make these materials electrochemically unstable and inactive. Therefore, the results suggest that NMPP and NMPC are not suitable as positive electrode materials neither for aqueous nor non-aqueous SIBs.

3.3. Iron-based materials for Na-ion battery electrodes

3.3.1. Motivation

Iron is the fourth most common element in the Earth's crust, and it exists in a wide range of oxidation states from -2 to +7. Iron-based compounds, inspired by a great success of LiFePO_4 ,¹⁸⁶ have been widely investigated as Na insertion host materials due to low cost, structural stability and high safety.¹⁸⁷ In spite of easy preparation of olivine LiFePO_4 , olivine NaFePO_4 cannot be synthesized directly and can only be accessed by chemical/electrochemical Na ion insertion into FePO_4 or ion exchange route. This complicates and increases the price of its production.^{188, 189} Although maricite NaFePO_4 could be prepared by solid-state route, it is electrochemically inactive due to the lack of Na ion migration channels.¹⁹⁰

$\text{Na}_3\text{Fe}_2(\text{PO}_4)_3$ (NFP) belongs to the NASICON type structure family. Electrochemically active $\text{Fe}^{2+}/\text{Fe}^{3+}$ redox couple of NFP yields a theoretical capacity of 115 mAh g^{-1} for two electrons at a potential of $-0.4 \text{ V vs Ag/AgCl}$ which means that NFP is more suitable as a negative electrode. NFP has a monoclinic $C2/c$ (No. 15) space group which consists of corner sharing $[\text{PO}_4]$ tetrahedra and octahedra $[\text{FeO}_6]$ forming $[\text{Fe}_2(\text{PO}_4)_3]$ units also known as "lantern units" (Fig. 60). These units arrange in a three-dimensional structure which exhibits large interstitial channels for fast Na ion diffusion. Sodium is located in the two crystallographic sites in this structure. There are several reports that NFP delivers $\sim 60 \text{ mAh g}^{-1}$ at 1C in aqueous and even organic electrolytes.^{191, 192} This suggests that NFP might suffer from unsatisfactory cyclability due to its low electronic conductivity. Carbon coating, doping or morphology engineering has already been tested for improving NFP electrochemical performance.^{193, 194} For example, doping with potassium increased the initial capacity up to 101 mAh g^{-1} (0.1C, organic electrolyte),¹⁹⁵ however, deeper investigation of NFP, especially in aqueous electrolytes is still necessary.

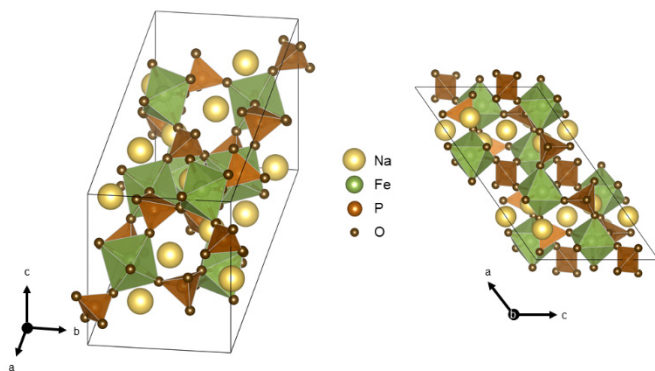


Fig. 60. Crystal structure of NASICON-structured $\text{Na}_3\text{Fe}_2(\text{PO}_4)_3$.

$\text{Na}_4\text{Fe}_3(\text{PO}_4)_2(\text{P}_2\text{O}_7)$ (NFPP) is a mixed-polyanionic SIBs material which has a theoretical capacity of 129 mAh g^{-1} with a working potential of 0.3 V vs Ag/AgCl and low volume change ($< 4\%$) during ion insertion. NFPP is easily obtained using simple solid-state or sol-gel methods. It has an orthorhombic $Pna2_1$ (No. 33) space group where infinite chains of $[\text{Fe}_3\text{P}_2\text{O}_{13}]_\infty$ parallel to the b-c plane are connected along the a-axis by $[\text{P}_2\text{O}_7]$ groups (Fig. 61). This diphosphate connection produces large channels for Na ions. There are four Fe octahedral sites which are connected via edge or corner sharing.¹⁷³ The first electrochemical activity of NFPP was reported by Kim et. al. where specific capacity of 113.5 mAh g^{-1} was achieved.¹⁷³ However, NFPP has several issues such as formation of NaFePO_4 and $\text{Na}_2\text{FeP}_2\text{O}_7$ impurities during synthesis which are not well controlled, and low electronic conductivity which restrict its capacity and power density.¹⁹⁶ To promote electrochemical performance of NFPP, further investigation of the synthesis and material engineering (carbon layer, electrolyte etc.) is required.

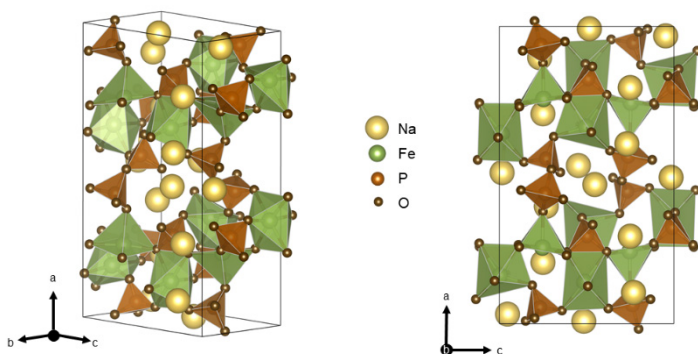


Fig. 61. Crystal structure of $\text{Na}_4\text{Fe}_3(\text{PO}_4)_2(\text{P}_2\text{O}_7)$.

$\text{Na}_{2-x}\text{Fe}[\text{Fe}(\text{CN})_6]\cdot y\text{H}_2\text{O}$ (NFCN) belongs to a different class of materials known as Prussian Blue Analogs (PBA). This material has attracted significant attention due to its simple and low-cost preparation, abundant elemental composition, high theoretical capacity of 170 mAh g^{-1} for two Na ions together with relatively high potential of $\sim 0.3 \text{ V vs Ag/AgCl}$.^{18, 197} The biggest challenge for PBA synthesis is controlling the content of sodium, water and vacancies. Water and vacancies lead to poor electrochemical performance and structural degradation.¹⁹⁸ The number of vacancies depends on the initial synthesis conditions while water can be removed after synthesis. As NFCN is considered to be a positive electrode material, it is crucial to have a maximum amount of sodium which could be achieved by understanding each step of the synthesis.¹⁹⁹

There are three possible NFCN phases depending on the amount of Na and oxidation state of both Fe: Prussian green ($x = 2$, $\text{Fe}^{3+}\text{Fe}^{3+}$), Prussian blue ($x \geq 1$, $\text{Fe}^{2+}\text{Fe}^{3+}$) both of which have cubic $Fm\bar{3}m$ (No. 225) space group, and Prussian white ($x < 1$, $\text{Fe}^{2+}\text{Fe}^{2+}$) which could have either monoclinic $P2_1/n$ (No. 14) (hydrated) or rhombohedral $R\bar{3}$ (No. 148) (anhydrous) space group (Fig. 62).¹⁸ It has been reported that rhombohedral NFCN shows the best electrochemical performance. It can achieve a capacity of $\sim 158 \text{ mAh g}^{-1}$ (organic electrolyte).^{197, 199} However, this material is sensitive to air and humidity which makes it not suitable for aqueous electrolytes.²⁰⁰ On the other hand, monoclinic NFCN which also possesses high content of sodium, does not require dry conditions and could be a suitable positive electrode for aqueous SIBs. Yet, there are only a few publications on NFCN performance in aqueous media and none of them are related to the monoclinic phase. For example, Ropero et. al.²⁰¹ and Lucero et. al.²⁰² achieved initial capacity of $\sim 65 \text{ mAh g}^{-1}$ (0.2C, 1 M $\text{Na}_2\text{SO}_4(\text{aq})$) and $\sim 75 \text{ mAh g}^{-1}$ (1C, 17 m $\text{NaClO}_4(\text{aq})$), respectively, for one Na ion transfer with cubic NFCN electrodes.

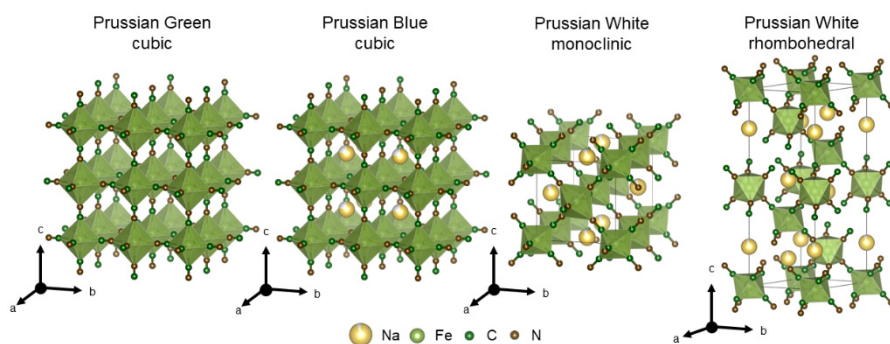


Fig. 62. Crystal structures of $\text{Na}_{2-x}\text{Fe}[\text{Fe}(\text{CN})_6]\cdot y\text{H}_2\text{O}$.

3.3.2. Synthesis

$\text{Na}_3\text{Fe}_2(\text{PO}_4)_3$ was synthesized via solid-state method (Fig. 63). In a typical synthesis, Na_2CO_3 (0.0097 mol, Glentham, 99+%), Fe_2O_3 (0.0064 mol, Eurochemicals, G.R.) and $\text{NH}_4\text{H}_2\text{PO}_4$ (0.0193 mol, Honeywell, 99+%) were mixed using wet (2-propanol) ball-milling at 350 rpm for 2 h. The dried mixture was calcined at 700 °C for 10 h, in the air atmosphere. Obtained powders were post-processed at 350 rpm for 2 h in a ball-mill. The resulting particles were coated with a layer of carbon by homogeneously mixing additionally ball-milled (1 h at 900 rpm) NFP powder (70 wt%, (usually, 0.7 g)) and of citric acid (30 wt% (0.3 g), $\text{HOC}(\text{CH}_2\text{CO}_2\text{H})_2$, Lach-ner, G.R.) in distilled water (50 mL). The resulting mixture was dried at 80 °C for several hours for complete water elimination. The obtained powder was reground and annealed at 700 °C for 2 h in N_2 atmosphere. The resulting black powders were again ball-milled at 350 rpm for 2 h to achieve a uniform final particle size distribution.

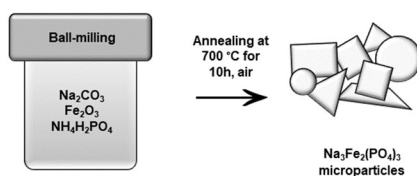


Fig. 63. Solid-state synthesis scheme of $\text{Na}_3\text{Fe}_2(\text{PO}_4)_3$.

$\text{Na}_4\text{Fe}_3(\text{PO}_4)_2\text{P}_2\text{O}_7$ was synthesized via a solid-state and sol-gel methods (Fig. 64). In a typical solid-state synthesis, $\text{Na}_4\text{P}_2\text{O}_7$ (0.0064 mol, ChemPur, p.a.), $\text{FeC}_2\text{O}_4 \cdot 2\text{H}_2\text{O}$ (0.0192 mol, Chempur, p.a.), and $\text{NH}_4\text{H}_2\text{PO}_4$ (0.0128 mol, Honeywell, 99+%) were mixed using wet (2-propanol) ball-milling at 350 rpm for 2 h. The dried mixture was calcined at 300 °C for 6 h and subsequently at 500 °C for 12 h, in N_2 atmosphere. Obtained powders were post-processed at 350 rpm for 2 h using a ball-mill. The resulting particles were coated with a layer of carbon by homogeneously mixing additionally ball-milled (1 hour at 900 rpm) NFPP powder (70 wt%, (usually, 0.7 g)) and of citric acid (30 wt% (0.3 g), $\text{HOC}(\text{CH}_2\text{CO}_2\text{H})_2$, Lach-ner, G.R.) or glucose (30 wt% (0.3 g), $\text{C}_6\text{H}_{12}\text{O}_6$, Reachem, G.R.) in distilled water (50 mL). The resulting mixture was dried at 80 °C for several hours for complete water elimination. The obtained powder was reground and annealed at 500 °C for 12 h in N_2 atmosphere. The resulting black powders were again

ball-milled at 350 rpm for 2 h to achieve a uniform final particle size distribution.

In a typical sol-gel synthesis of NFPP, CH_3COONa (0.008 mol, Honeywell, p.a.), $\text{NH}_4\text{H}_2\text{PO}_4$ (0.0092 mol, Honeywell, 99+%) and glucose ($5.55 \cdot 10^{-4}$ mol, $\text{C}_6\text{H}_{12}\text{O}_6$, Rechem, G.R.) are dissolved in distilled water (40 mL). Afterwards, $\text{FeC}_4\text{H}_2\text{O}_4$ (0.006 mol, Roth, 97%), citric acid (0.006 mol, $\text{HOC}(\text{CH}_2\text{CO}_2\text{H})_2$, Lach-ner, G.R.) and hexadecyltrimethylammonium bromide ($2.74 \cdot 10^{-4}$ mol, $\text{C}_{19}\text{H}_{42}\text{BrN}$ (CTAB), Acros Organics, 99+%) are dissolved separately in distilled water (40 mL) and added dropwise into the previous solution under vigorous magnetic stirring. The complexation process is carried out for several hours on a hot plate (solution temperature is $\sim 80^\circ\text{C}$) under constant stirring. After water evaporation, a viscous gel is obtained and dried at 80°C overnight. The obtained xerogels were thoroughly grounded and pyrolyzed for 12 h at 500°C in flowing N_2 atmosphere. The resulting black powder was again ball-milled at 350 rpm for 2 h to achieve a uniform final particle size distribution. Additionally, several samples were prepared with $\text{Fe}(\text{CH}_3\text{COO})_2$ (0.006 mol, Alfa Aesar, p.a.) instead of $\text{FeC}_4\text{H}_2\text{O}_4$ or with ethylenediamine tetraacetic acid (0.006 mol, $\text{C}_{10}\text{H}_{16}\text{N}_2\text{O}_8$ (EDTA), Rechem, p.a.) instead of citric acid.

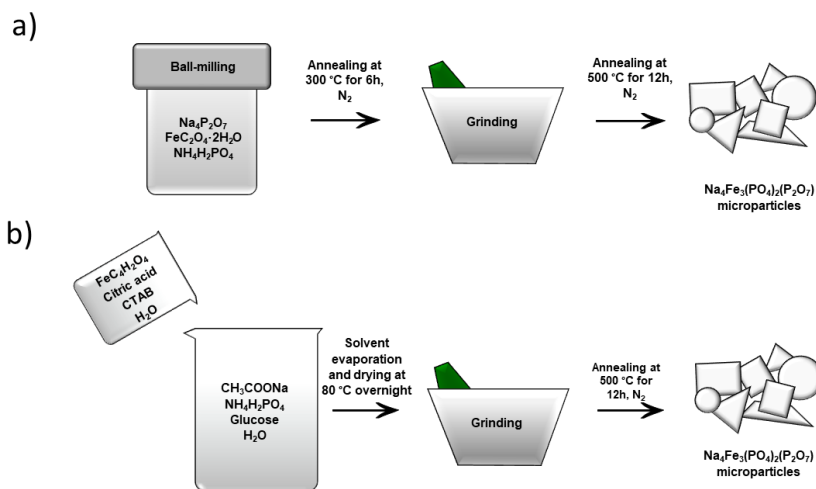


Fig. 64. a) Solid-state and b) sol-gel synthesis schemes of $\text{Na}_4\text{Fe}_3(\text{PO}_4)_2\text{P}_2\text{O}_7$.

$\text{Na}_{2-x}\text{Fe}[\text{Fe}(\text{CN})_6] \cdot y\text{H}_2\text{O}$ (monoclinic Prussian White) was synthesized via hydrothermal and co-precipitation methods (Fig. 65). In a typical hydrothermal synthesis, $\text{Na}_4\text{Fe}(\text{CN})_6 \cdot 10\text{H}_2\text{O}$ (0.0018 mol, Acros Organics)

and L-Ascorbic acid (0.0018 mol, $C_6H_8O_6$, Thermo Scientific, 99+%) are dissolved in distilled water (60 mL). The clear solution is transferred into a 100 mL Teflon-lined stainless-steel autoclave heated to 80 – 140 °C for 20 h. The obtained light blue powder was washed several times by centrifugation with distilled water and ethanol, and subsequently dried at 80 °C overnight. In a typical co-precipitation synthesis, $Na_4Fe(CN)_6 \cdot 10H_2O$ (0.008 mol, Acros Organics) and L-ascorbic acid (0.016 mol, $C_6H_8O_6$, Thermo Scientific, 99+%) are dissolved in distilled water (200 mL). The solution is bubbled with N_2 to remove oxygen for 24 h at 80 °C under constant stirring. The obtained light blue powder was washed several times by centrifugation with distilled water and ethanol, and subsequently dried at 80 °C overnight.

In order to obtain $Na_{2-x}Fe[Fe(CN)_6] \cdot yH_2O$ (rhombohedral Prussian White), the powder obtained by co-precipitation method was additionally dried at 170 °C under vacuum (10^{-2} mbar) for 24 h. All the following procedures (slurry, electrode and cell preparations) of this material were performed in an Ar-filled glovebox.

$Na_{2-x}Fe[Fe(CN)_6] \cdot yH_2O$ (cubic Prussian Blue) was synthesized by the same co-precipitation procedure as monoclinic Prussian White only by additionally adding HCl (20 mL, Thermo Scientific, 37%).

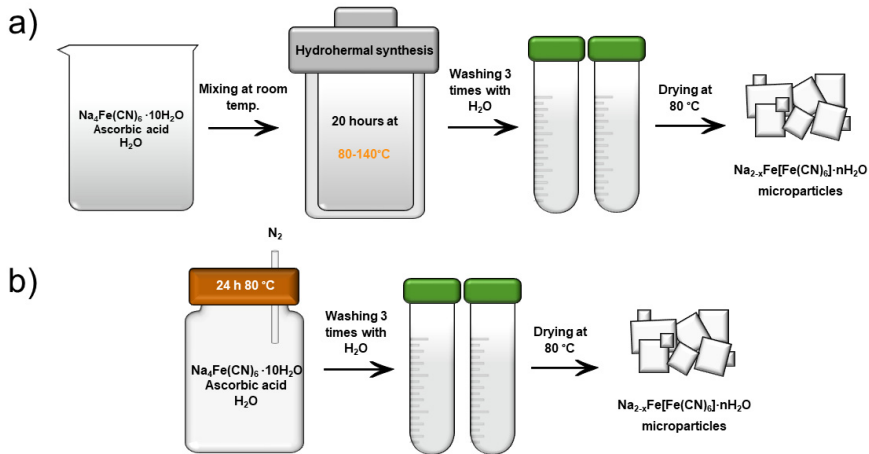


Fig. 65. a) Hydrothermal and b) co-precipitation synthesis schemes of $Na_{2-x}Fe[Fe(CN)_6] \cdot yH_2O$.

3.3.3. Structural characterization

3.3.3.1. $\text{Na}_3\text{Fe}_2(\text{PO}_4)_3$

Fig. 66 shows the XRD pattern of NFP synthesized via solid-state method. Sharp diffraction peaks indicate a high degree of crystallinity and agrees well with monoclinic structure $C2/c$ (No. 15).¹⁹¹ No additional impurities phases were detected. The morphology of NFP was investigated using SEM. Fig. 67 demonstrates that microparticles have irregular shape and broad size distribution.

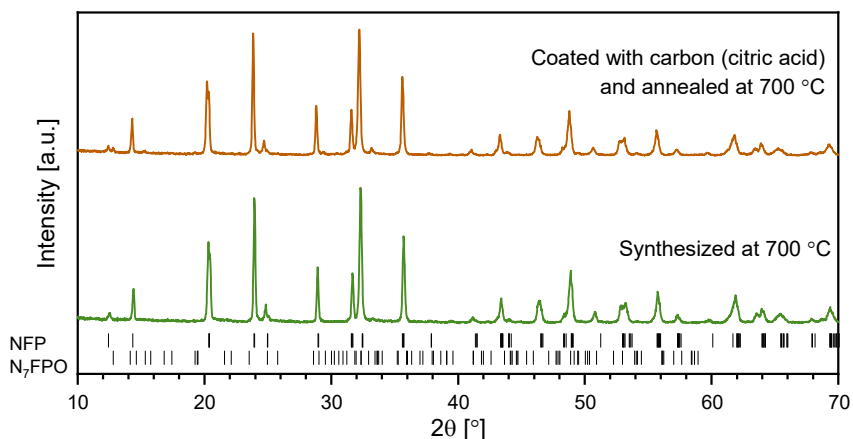


Fig. 66. Powder XRD pattern of NFP.^{191, 203}

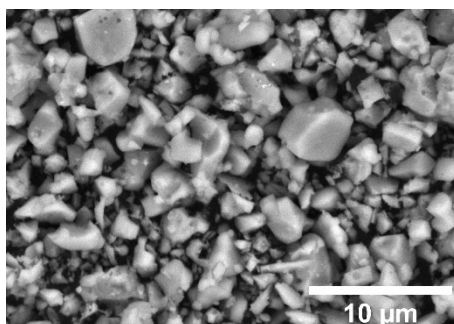


Fig. 67. SEM image of NFP powders.

In order to improve the electronic contact between ceramic particles, the NFP were additionally coated by a carbon layer using post-synthetic pyrolysis of citric acid. The XRD pattern in Fig. 66 shows that such treatment does not

alter the main phase structure. However, traces of an additional phase of $\text{Na}_7\text{Fe}_3(\text{P}_2\text{O}_7)_4$ (N_7FPO) could be observed. The resulting carbon content obtained by this procedure was evaluated by TGA and found to be 5.9 wt% (Fig. 68).

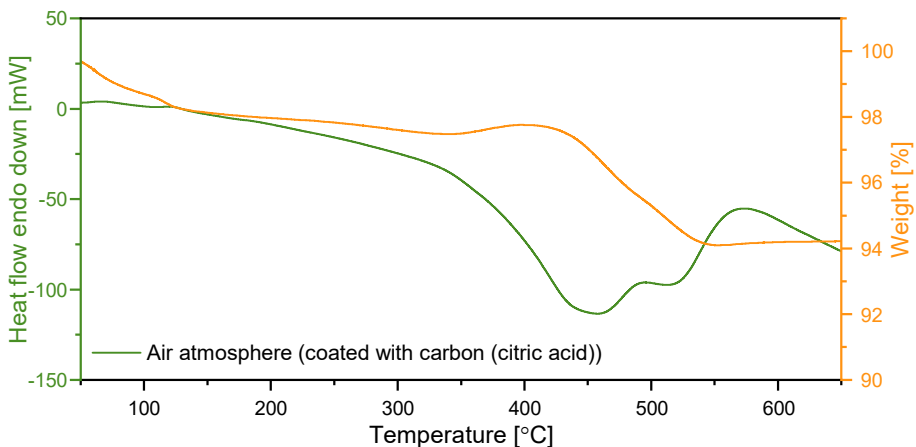


Fig. 68. Thermogravimetric and DSC curves of NFP coated with a carbon layer.

3.3.3.2. $\text{Na}_4\text{Fe}_3(\text{PO}_4)_2\text{P}_2\text{O}_7$

$\text{Na}_4\text{Fe}_3(\text{PO}_4)_2\text{P}_2\text{O}_7$ was synthesized via sol-gel and solid-state methods. For the sol-gel synthesis, different precursors of iron (Fe-acetate, Fe-fumarate) and coordinating agents (EDTA, CTAB, citric acid) were investigated. The XRD patterns (Fig. 69) show that NFPP is not pure when Fe-acetate was used because an additional phase of $\text{Na}_{3.12}\text{Fe}_{2.44}(\text{P}_2\text{O}_7)_2$ (NFPO) could be observed. The same impurity is also detected in the case of Fe-fumarate; however, the amount is much lower. In terms of EDTA and citric acid precursors, NFPP pure phase was obtained only with citric acid. However, the crystallinity differs with EDTA resulting in much higher crystallinity which suggests that it is a better coordinating agent. NFPP of high crystallinity is achieved also by a conventional solid-state method. In all cases, the NFPP phase agrees well with the orthorhombic $Pna2_1$ (No. 33) space group.²⁰⁴ In the case of solid-state sample, Rietveld refinements were performed (Fig. 70). The resulting lattice parameters were determined to be $a = 18.0892(10)$ Å, $b = 10.6565(6)$ Å, $c = 6.5401(3)$ Å and $V = 1260.72(15)$ Å³ which are in good agreement with those reported in the literature.⁷⁷

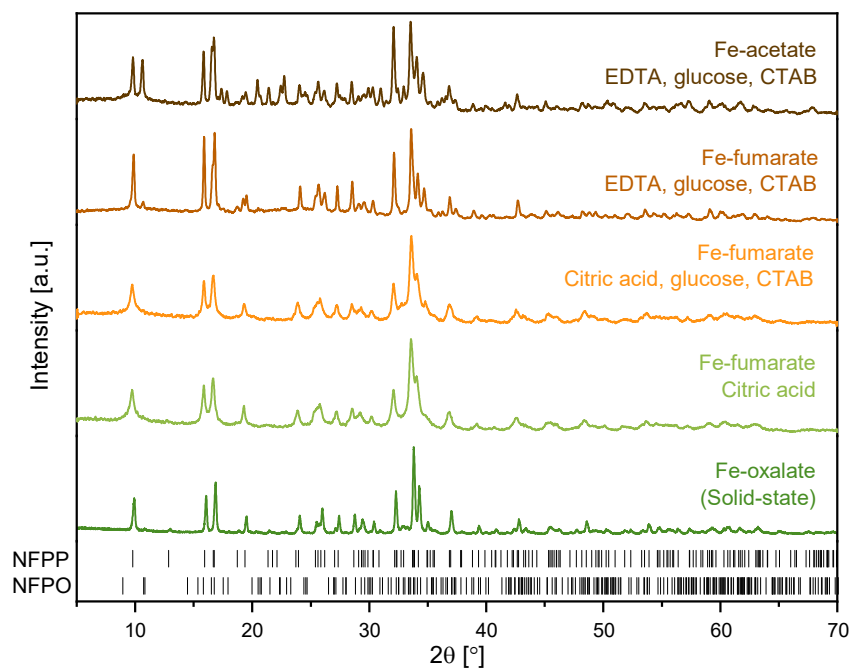


Fig. 69. Powder XRD patterns of NFPP samples synthesized with different precursors and coordinating agents.^{204, 205}

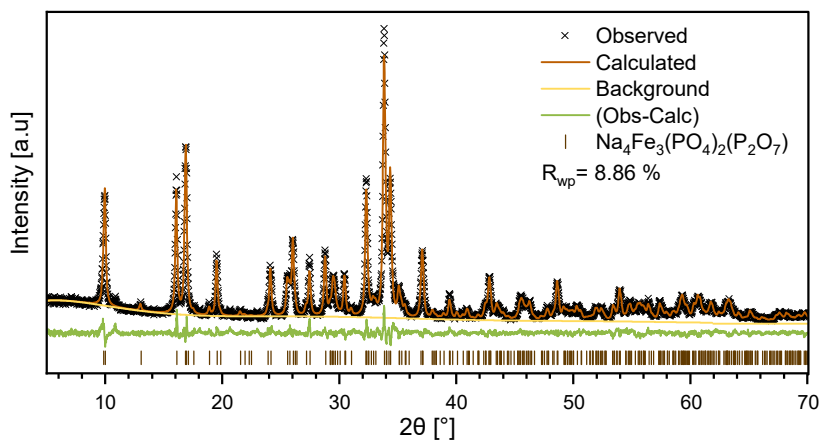


Fig. 70. Powder XRD pattern and Rietveld refinements of NFPP synthesized by a solid-state method.²⁰⁴

The morphology of samples synthesized by sol-gel (Fe-fumarate, EDTA, glucose, CTAB) and solid-state methods before the ball-milling was characterized by SEM. Images presented in Fig. 71 show that sol-gel yields

much larger particles of tens of micrometers while particles from solid-state synthesis are irregularly shaped and a few micrometers in size. In both cases, the size distribution is relatively broad.

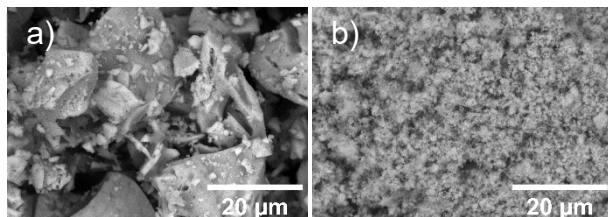


Fig. 71. SEM image of NFPP samples synthesized by a) sol-gel and b) solid-state synthesis methods.

In order to improve the electronic contact between ceramic particles obtained by solid-state synthesis, NFPP were additionally coated by a carbon layer using post-synthetic pyrolysis. Citric acid or glucose were used as carbon precursors. XRD results (Fig. 72) show that glucose is a better suitable precursor because citric acid results in formation of an additional NFPO phase. NFPP particles obtained by sol-gel synthesis do not require additional coating as this method yields the carbon layer by itself. TGA results presented in Fig. 73 demonstrate that sol-gel (Fe-fumarate, EDTA, glucose, CTAB), solid-state (glucose) and solid-state (citric acid) results in ~ 21.3 wt%, ~ 8.5 wt% and ~ 4.0 wt% of carbon, respectively.

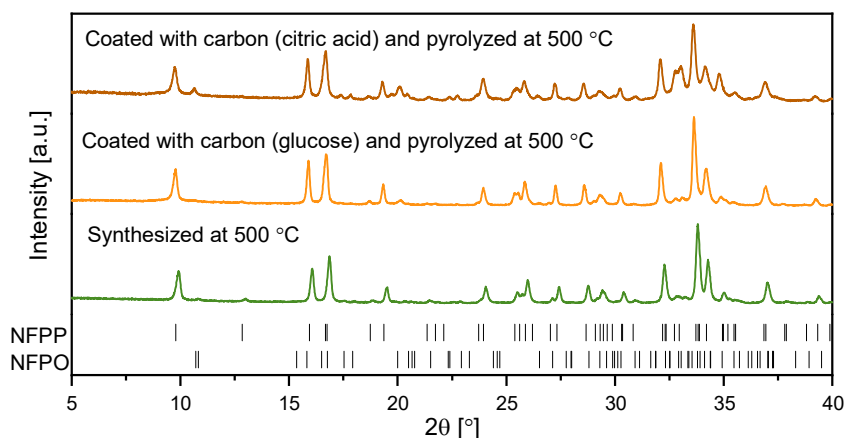


Fig. 72. Powder XRD patterns of NFPP samples: (bottom) as synthesized at 500 °C by solid state method; (middle) coated with carbon (glucose) and pyrolyzed at 500 °C.; (top) coated with carbon (citric acid) and pyrolyzed at 500 °C.^{204, 205}

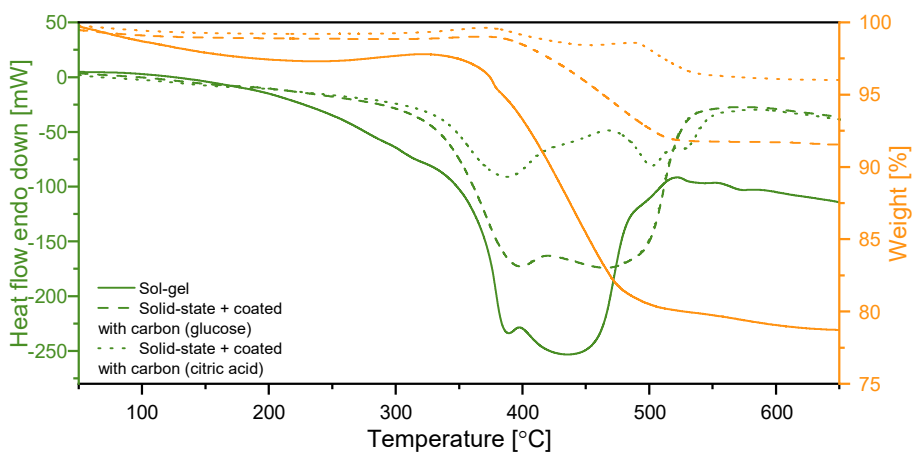


Fig. 73. Thermogravimetric and DSC curves of NFPP s synthesized by sol-gel and solid-state and coated with carbon layer.

3.3.3.3. $\text{Na}_{2-x}\text{Fe}[\text{Fe}(\text{CN})_6] \cdot y\text{H}_2\text{O}$

At first, $\text{Na}_{2-x}\text{Fe}[\text{Fe}(\text{CN})_6] \cdot y\text{H}_2\text{O}$ was synthesized via a hydrothermal method to investigate the different morphology of monoclinic phase and its influence on electrochemical performance. However, the XRD patterns (Fig. 74) of NFCN synthesized at different temperatures (60 – 140 °C) showed that monoclinic phase is obtained only at 80 °C and below, while higher temperature yields cubic phase, which is not the desired target in this work. As the temperature of 80 °C is relatively low for hydrothermal synthesis, it was decided to change the synthesis method to simpler, cheaper, and better yielding co-precipitation method.

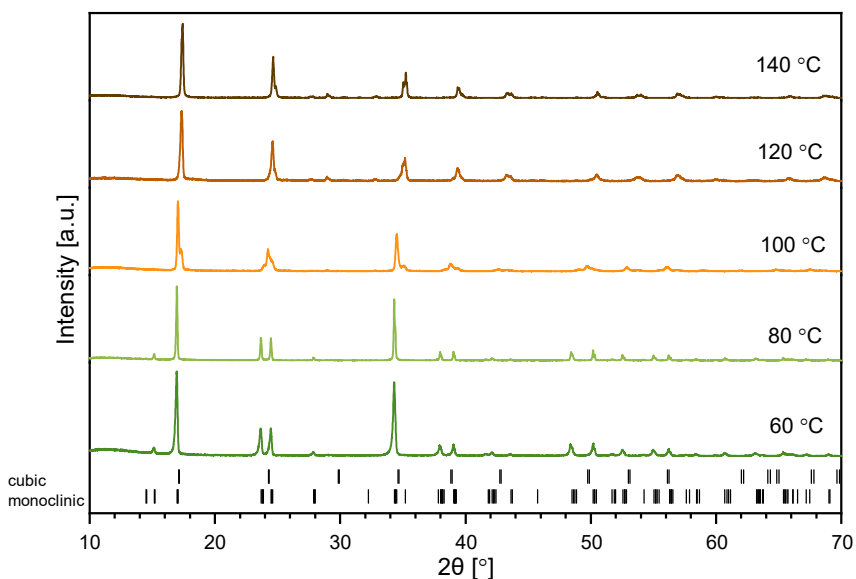


Fig. 74. Powder XRD patterns of NFCN samples prepared by different hydrothermal synthesis temperatures.^{199, 206}

Co-precipitation synthesis under nitrogen atmosphere at 80 °C yielded the monoclinic NFCN phase ($P2_1/n$ (No. 14) space group) without any additional impurities.¹⁹⁹ The presence of sharp diffraction peaks in Fig. 75 indicates a high crystallinity of the material. Additionally, this sample was further dried at deep vacuum for 24 h at 170 °C and pure anhydrous rhombohedral phase with $R\bar{3}$ (No. 148) space group was obtained.²⁰⁰ However, this phase is extremely sensitive to air and was tested only in organic electrolytes. In order to synthesize all possible NFCN phases, HCl was additionally added to the initial NFCN-monoclinic synthesis mixture. The resulting XRD pattern of this sample shows pure cubic $Fm\bar{3}m$ (No. 225) space group.²⁰⁶ The morphology of cubic and monoclinic NFCN samples was investigated using SEM. Fig. 76 indicates that particles have cuboid shape and are few micrometers in size with broad size distribution. Monoclinic ones have slightly larger sizes. Elemental analysis of these two samples was carried out by ICP-OES in order to estimate the Na content. The results revealed that cubic and monoclinic NFCN are $\text{Na}_{0.26}\text{Fe}[\text{Fe}(\text{CN})_6]\cdot n\text{H}_2\text{O}$ and $\text{Na}_{1.86}\text{Fe}[\text{Fe}(\text{CN})_6]\cdot n\text{H}_2\text{O}$, respectively which agrees well with reported results.^{83, 199}

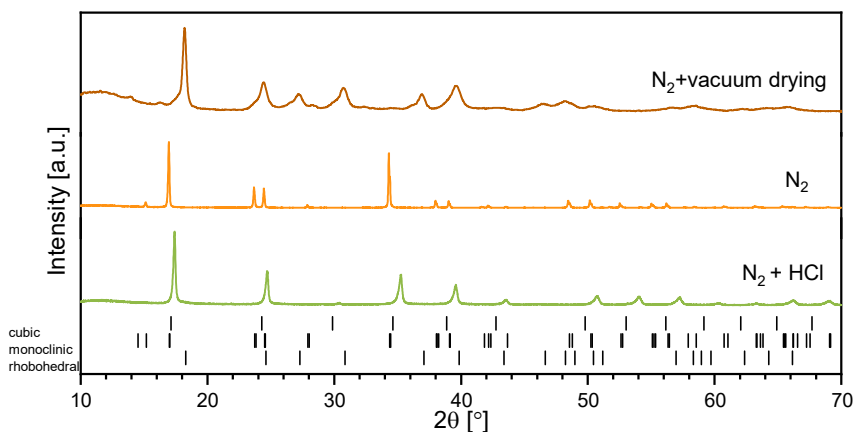


Fig. 75. Powder XRD patterns of NFCN samples prepared by co-precipitation method at different conditions: (bottom) synthesized in N_2 atmosphere with HCl; (middle) synthesized in N_2 atmosphere; (top) synthesized in N_2 atmosphere and dried in vacuum at $170\text{ }^\circ\text{C}$.^{199, 200, 206}

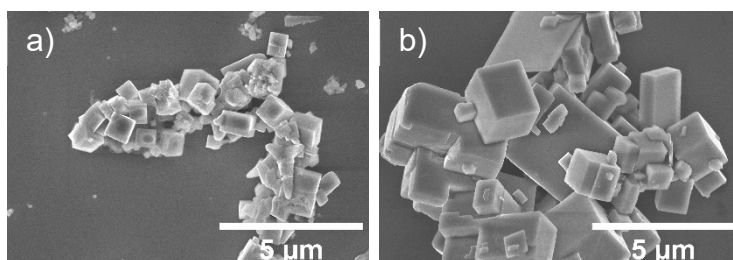


Fig. 76. SEM images of a) cubic phase and b) monoclinic phase NFCN samples.

Different ratios of initial co-precipitation synthesis precursors $\text{Na}_4\text{Fe}(\text{CN})_6 \cdot 10\text{H}_2\text{O}$: ascorbic acid (1:1, 1:2, 1:4 and 1:6) was examined to investigate its influence on the phase and final amount of sodium. The XRD patterns (Fig. 77) show that this ratio does not affect the monoclinic phase and its purity. The ICP-OES analysis demonstrated the following compositions: $\text{Na}_{1.82}\text{FCN}$, $\text{Na}_{1.86}\text{FCN}$, $\text{Na}_{1.86}\text{FCN}$ and $\text{Na}_{1.79}\text{FCN}$ when the ratios were 1:1, 1:2, 1:4 and 1:6, respectively. Additionally, the higher amount of ascorbic acid produced a higher amount of final powder. Therefore, it could be concluded that the best one is 1:4.

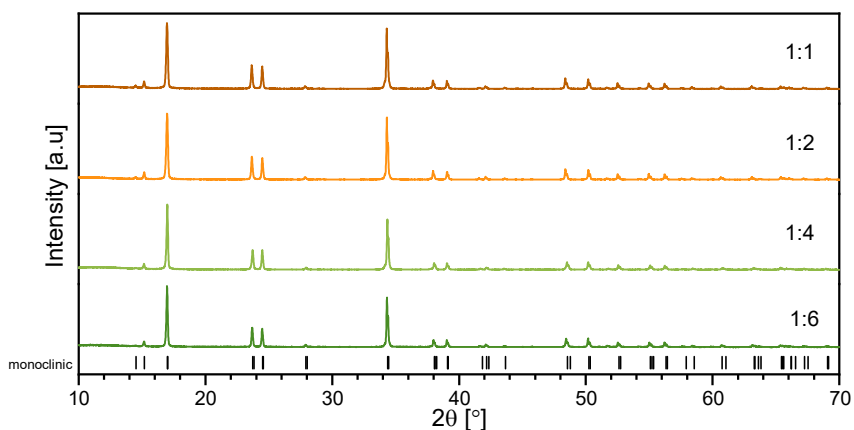


Fig. 77. Powder XRD patterns of NFCN samples prepared with different $\text{Na}_4\text{Fe}(\text{CN})_6 \cdot 10\text{H}_2\text{O}$: ascorbic acid ratios via a co-precipitation method.¹⁹⁹

Thermogravimetric analysis was performed to determine the water amount in the formula and the thermal stability of NFCN. The final formula of monoclinic phase is $\text{Na}_{1.86}\text{Fe}[\text{Fe}(\text{CN})_6] \cdot 2.28\text{H}_2\text{O}$ which was calculated from the results in Fig. 78. The results also suggest that monoclinic phase is more thermally stable than cubic, although it is not stable enough for additional carbon coating by pyrolysis.

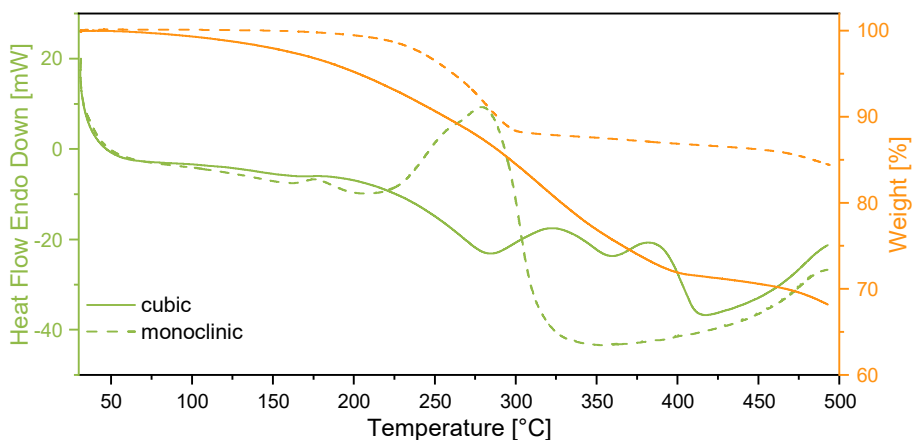


Fig. 78. Thermogravimetric and DSC curves of cubic and monoclinic phase NFCN samples (N_2 atmosphere).

3.3.4. Electrochemical performance

3.3.4.1. $\text{Na}_3\text{Fe}_2(\text{PO}_4)_3$

For the initial electrochemical characterization, CVs of NFP samples were recorded in 1 M Na_2SO_4 (aq) electrolyte at the scanning rate of 5 mV s^{-1} within the potential window of $-0.95 - 1.05 \text{ V}$ vs Ag/AgCl using beaker-type cells. Several redox peaks could be observed at around $-0.5 \text{ V}/-0.35 \text{ V}$, $-0.1 \text{ V}/0.0 \text{ V}$ and $-0.05 \text{ V}/0.2 \text{ V}$ which are stable during cycling (Fig. 79). These peaks correspond to reversible multistep conversion of Fe^{3+} to Fe^{2+} accompanied by insertion/deinsertion of Na^+ ions:²⁰⁷

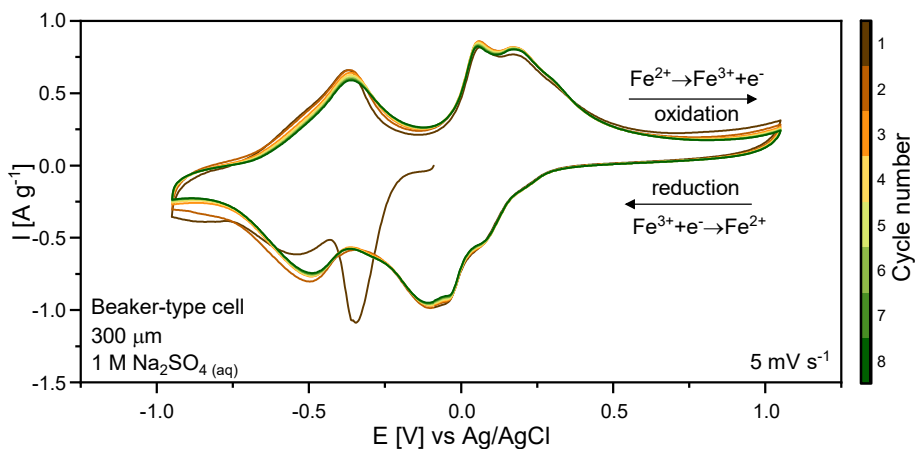
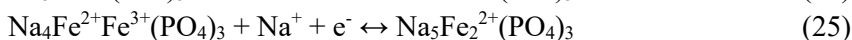
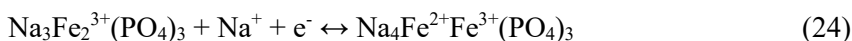


Fig. 79. Cyclic voltammograms of NFP electrode recorded at 5 mV s^{-1} scan rate.

GCD cycling was used to determine specific discharge capacity and CE% of NFP electrodes. Fig. 80 shows the GCD cycling results of NFP for 100 cycles within the potential window from -0.75 V to 0.65 V (Ag/AgCl) at 1C ($1\text{C} = 0.115 \text{ A g}^{-1}$) rate calculated based on the theoretical capacity of NFP in 1 M Na_2SO_4 (aq) using beaker-type cells. The initial specific charge and discharge capacities are 42 mAh g^{-1} and 17 mAh g^{-1} , respectively, which is far from the theoretical value (115 mAh g^{-1}). In the second cycle, the discharge capacity increased but later it went down back to $\sim 15 \text{ mAh g}^{-1}$ which could be attributed to the dissolution of active material into the electrolyte.

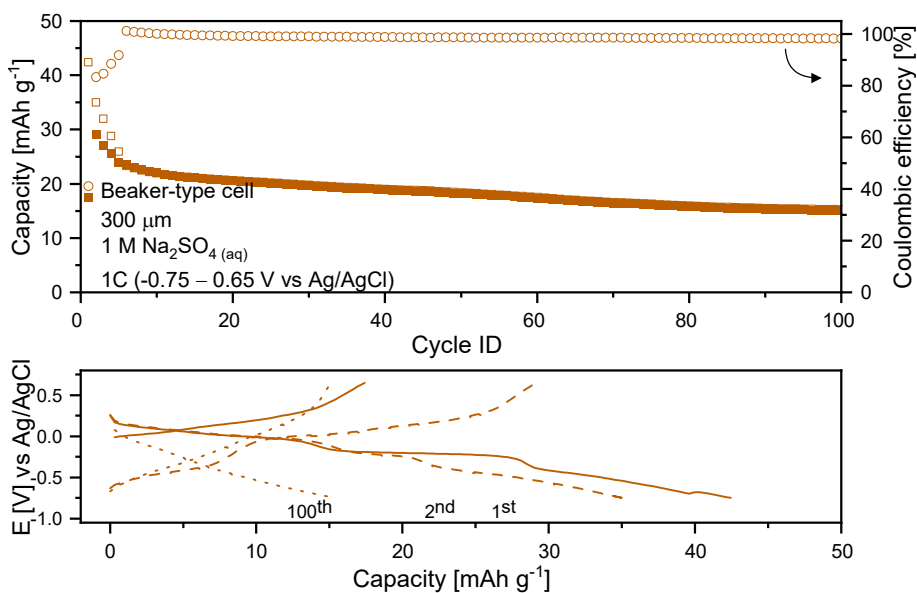
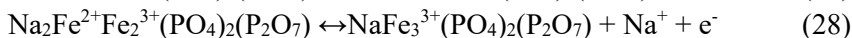
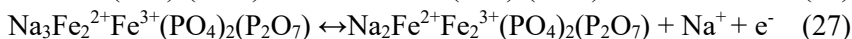
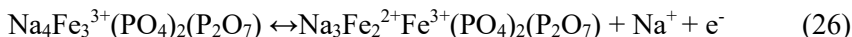


Fig. 80. GCD cycling of NFP electrode in 1 M Na₂SO₄(aq) electrolyte at 1C.

3.3.4.2. Na₄Fe₃(PO₄)₂P₂O₇

For the initial electrochemical characterization, CVs of NFPP synthesized by sol-gel and solid-state methods were performed in 1 M Na₂SO₄(aq) electrolyte at the scanning rate of 5 mV s⁻¹ within the potential window of -0.4 V/0.9 V or -0.7 V/1.0 V vs Ag/AgCl using beaker-type cells. In the case of a sol-gel prepared NFPP electrodes (Fig. 81), there are several reversible redox peaks in the potential range of 0 – 0.4 V which correspond to multistep redox reaction of Fe³⁺/Fe²⁺ accompanied by insertion/deinsertion of Na⁺ ions from three different crystallographic sites:²⁰⁸



The number of oxidation and reduction peaks is unequal, suggesting that insertion/deinsertion of Na ions take place through an asymmetrical mode.²⁰⁹ The most pronounced and stable peaks with the highest current could be observed in Fe-fumarate + citric acid sample which apparently exhibits the lowest crystallinity. Moreover, the first two sol-gel samples show more

pronounced degradation during cycling, possibly due to impurities. In the case of solid-state samples, the peaks are much broader, lower and not that well defined, which could be associated with slower redox kinetics.

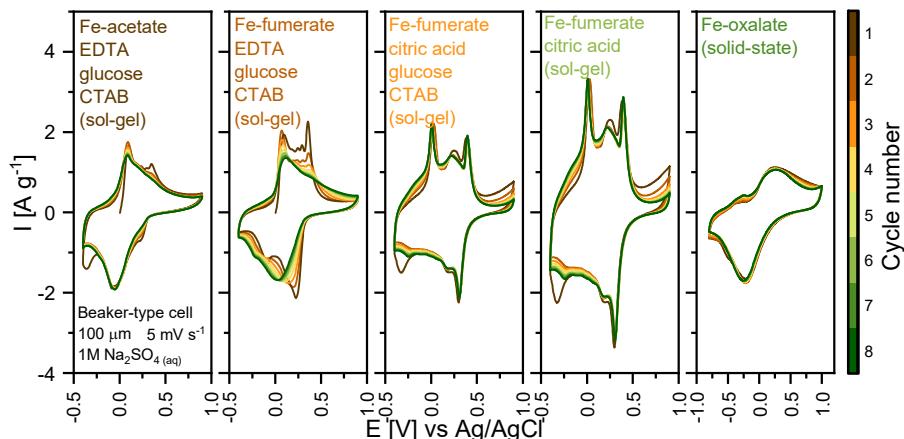


Fig. 81. Cyclic voltammograms of NFPP synthesized by different precursors and methods recorded at 5 mV s^{-1} scan rate.

GCD cycling was used for specific discharge capacity and CE% determination of NFPP prepared by sol-gel method. Fig. 82 shows the GCD cycling results for 100 cycles within the potential window from -0.4 V to 0.8 V (Ag/AgCl) at 1C ($1\text{C} = 0.129 \text{ A g}^{-1}$) rate calculated based on the theoretical capacity of NFPP in $1 \text{ M Na}_2\text{SO}_4(\text{aq})$ electrolyte using beaker-type cells. The best results were achieved with the Fe-fumarate + citric acid + glucose + CTAB sample. The initial discharge capacity and its retention after 100 cycles are 65.9 mAh g^{-1} and 38% , respectively.

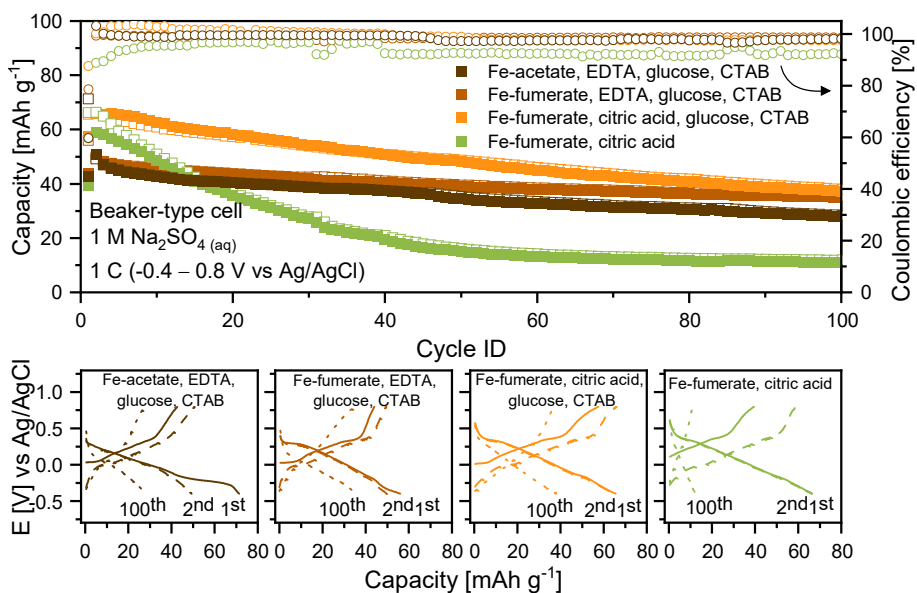


Fig. 82. GCD cycling of NFPP synthesized by sol-gel method in $1 \text{ M Na}_2\text{SO}_4(\text{aq})$ electrolyte at 1C .

The electrodes from the solid-state prepared samples of NFPP were tested using four different aqueous electrolytes: $1 \text{ M Na}_2\text{SO}_4(\text{aq})$, $17 \text{ m NaClO}_4(\text{aq})$, $8 \text{ m NaTFSI}(\text{aq})$, and $28 \text{ m KAc} + 8 \text{ m NaAc}(\text{aq})$ (Fig. 83). The initial specific capacity and its retention after 100 cycles are 60.1 mAh g^{-1} and 43.9% in $1 \text{ M Na}_2\text{SO}_4(\text{aq})$, 53.5 mAh g^{-1} and 59.4% in $17 \text{ m NaClO}_4(\text{aq})$, 54.5 mAh g^{-1} and 11.2% in $8 \text{ m NaTFSI}(\text{aq})$, and 33.4 mAh g^{-1} and 27.2% for $28 \text{ m KAc} + 8 \text{ m NaAc}(\text{aq})$. ‘Water-in-salt’ electrolytes show significantly worse performance than standard ones. Moreover, the potential profiles show sloping which could imply some kinetic limitations possibly due to some resistive interphasial layer formation from the electrode or electrolyte degradation products.

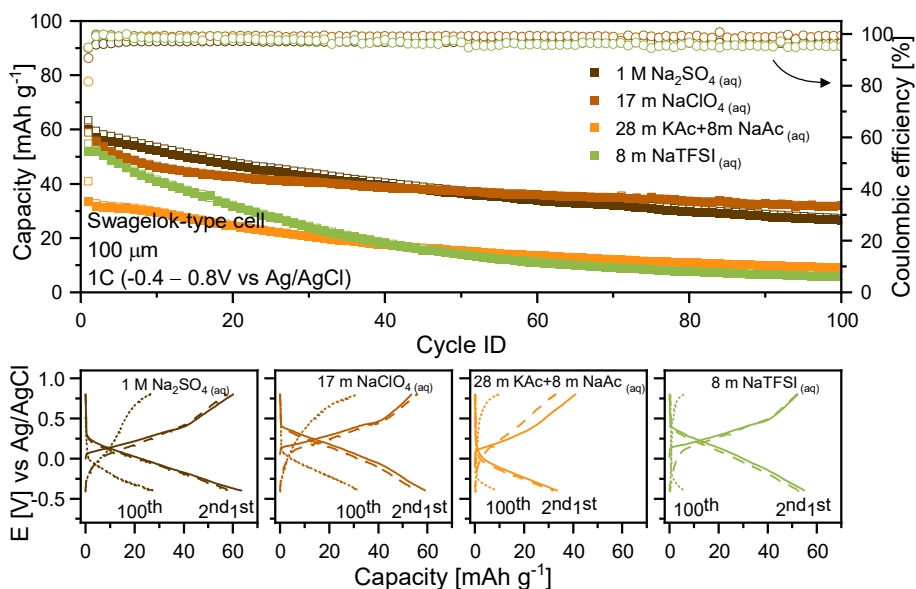


Fig. 83. GCD cycling of NFPP synthesized by solid-state method in different aqueous electrolytes at 1C.

The rate capability of NFPP was evaluated in 17 m NaClO₄ (aq) electrolyte. A set of different specific currents corresponding to 0.1, 0.2, 0.5, 1, 2, 5, 10 and 20C were used (Fig. 84). The specific discharge capacity was only 29.3 mAh g⁻¹ at 0.1C rate and dropped to negligible values at 20C, although it came back to 13.8 mAh g⁻¹ at 0.1C. This poor rate capability suggests some kinetic limitations. The capacities of the first cycles at 0.1C were lower than the ones at 1C (Fig. 83), it indicates some dissolution-based degradation mechanisms because the longer time the electrode spends in the electrolyte results in lower capacities. This requires further studies to understand if this is related to the Fe dissolution or instability of such phosphate-pyrophosphate framework. On one hand, it could be related to the pH of aqueous electrolytes. For example, higher pH values expected in 28 m KAc + 8 m NaAc (aq.) not only result in higher aqueous stability of FeO₄⁻² (according to the Pourbaix diagram), but also significantly stronger instability of phosphates.²¹⁰ The neutral or slightly acidic pH of aqueous Na₂SO₄ and NaClO₄ could result in better NFPP framework stability and better capacity retention.

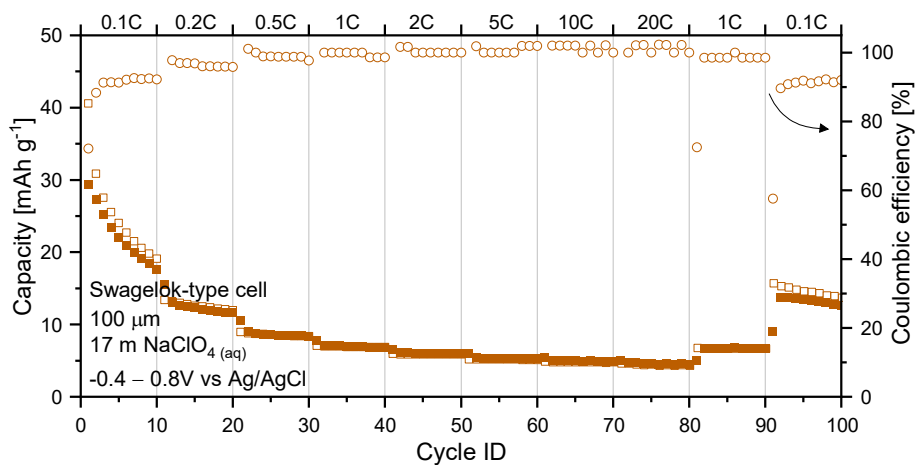


Fig. 84. Rate capability of GCD cycling of NFPP synthesized by solid-state method in 17 m NaClO₄(aq) electrolyte.

Electrochemical investigation of the NFPP was additionally carried out in organic electrolytes to compare it with aqueous systems and to verify that the capacity loss is mainly related to the electrolyte and not the material itself. Fig. 85 shows CVs which were recorded in 1 M NaPF₆ in DG electrolyte at the scanning rate of 0.5 mV s⁻¹ within the potential window of 2 – 4 V vs Na⁺/Na using Swagelok-type cells. Several reversible current peaks attributed to Fe²⁺/Fe³⁺ could be seen in the potential range of 2.5 – 3.3 V vs Na⁺/Na which agrees well with previous aqueous results (Fig. 81) and those reported in the literature.⁷⁷

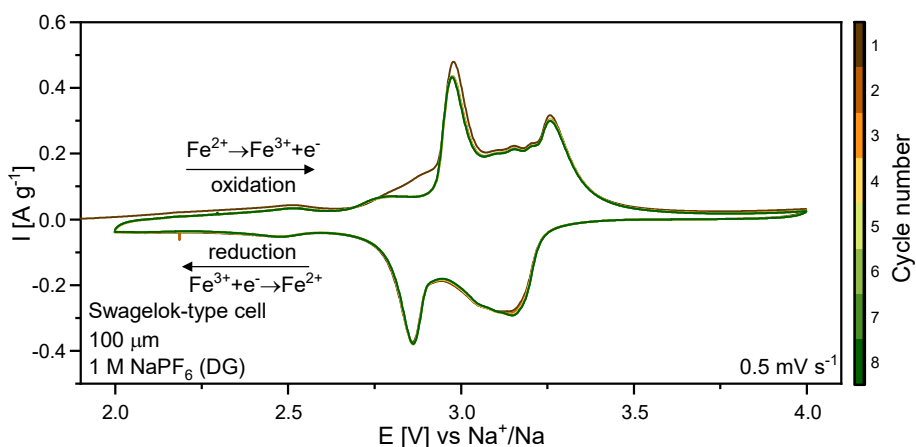


Fig. 85. Cyclic voltammograms of NFPP synthesized by solid-state method recorded in organic electrolyte at 0.5 mV s⁻¹ scan rate.

GCD measurements were performed for 300 cycles within the potential window from 1.8 to 4.0 V vs Na⁺/Na at 1C with 1 M NaPF₆ in EC:DEC (3:7 vol%) and 1 M NaPF₆ in DG electrolytes using Swagelok-type-cells (Fig. 86). DG electrolyte shows more stable electrochemical performance of NFPP than the mixture of EC:DEC which could be attributed to the different chemical composition, narrower distribution, thickness, and stability of the solid electrolyte interphase and the electrolyte interphase on the Na and the positive electrode formed in DG electrolytes.¹⁵⁶ Initial discharge capacity, CE% and capacity retention after 100 cycles of DG electrolyte are 86 mAh g⁻¹, 98.7% and 95%, respectively, which is much better than the previous results in aqueous media. The C-rate capability (0.1 – 20C) of NFPP with DG electrolyte experiment (Fig. 87) shows that increasing rate leads to lower capacity due to kinetic limitations.¹⁵⁷ The specific capacity at 0.1C rate is 93.9 mAh g⁻¹, decreases only to 49.1 mAh g⁻¹ at 20C but is fully recovered to 93.3 mAh g⁻¹ after the rate was switched back to 0.1C. This indicates excellent rate capability of NFPP electrodes in organic electrolytes.

Overall, NFPP seems to be a potential candidate electrode material for aqueous SIBs but likely requires additional understanding of its degradation mechanism and designing of an appropriate prevention strategy. Additionally, it is a suitable positive electrode material for organic SIBs.

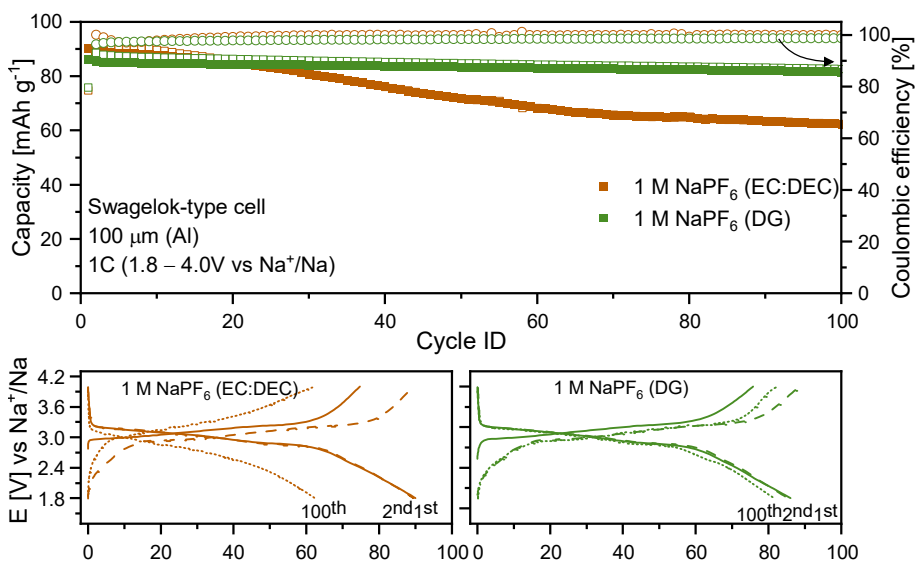


Fig. 86. GCD cycling of NFPP synthesized by solid-state method in organic electrolyte at 1C.

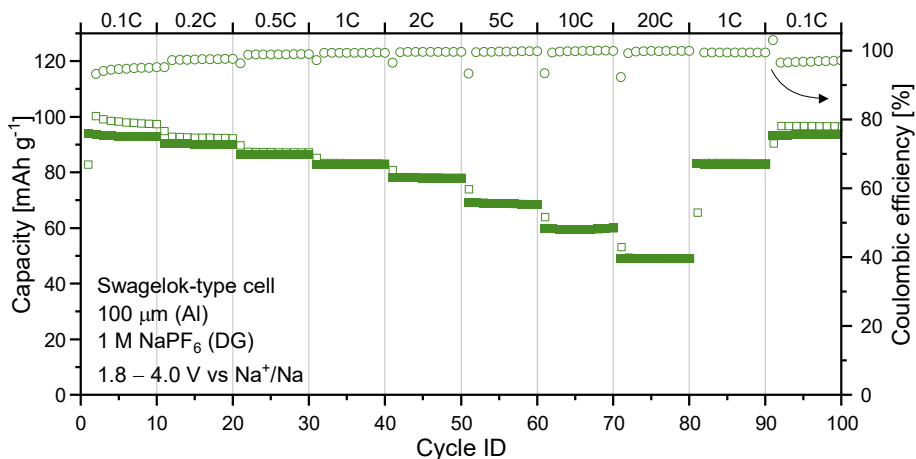
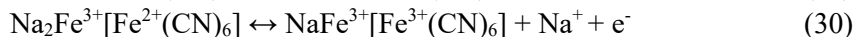
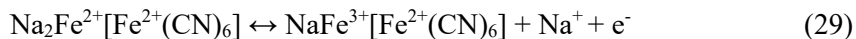


Fig. 87. Rate capability of GCD cycling of NFPP synthesized by solid-state method in an organic electrolyte.

3.3.4.3. $\text{Na}_{2-x}\text{Fe}[\text{Fe}(\text{CN})_6] \cdot y\text{H}_2\text{O}$

For the initial electrochemical characterization, CVs of cubic and monoclinic NFCN samples were performed using 1 M Na_2SO_4 (aq) electrolyte at the scanning rate of 5 mV s^{-1} within the potential window of $-0.6 - 1.4 \text{ V}$ vs Ag/AgCl using beaker-type cells. Several redox peaks could be observed at around $-0.05 \text{ V}/0.25 \text{ V}$ and $1 \text{ V}/1.2 \text{ V}$ vs Ag/AgCl which are stable during cycling (Fig. 88). The two-electron redox reaction processes could be ascribed to the high-spin-state nitrogen-coordinated couple ($\text{Fe}^{3+}/\text{Fe}^{2+}\text{-N}$) and low-spin-state carbon-coordinated couple ($\text{Fe}^{3+}/\text{Fe}^{2+}\text{-C}$). The first peak of cubic phase has slightly higher current than the second peak, while in monoclinic sample it is the opposite – the second peak is higher than the first one. The peaks would correspond to the two-step reversible conversion of Fe^{2+} to Fe^{3+} accompanied by insertion/deinsertion of Na^+ ions.^{197, 211}



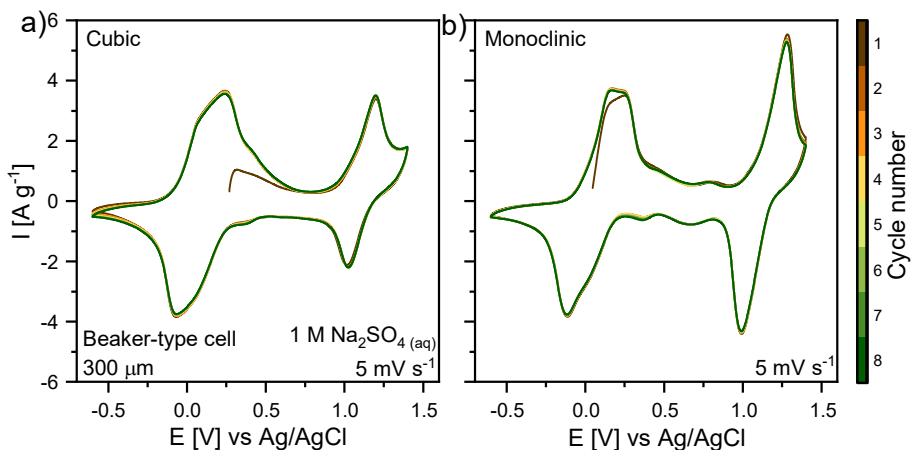


Fig. 88. Cyclic voltammograms of a) cubic and b) monoclinic phase of NFCN recorded at 5 mV s^{-1} scan rate.

GCD cycling was used for the determination of specific discharge capacity and CE% of monoclinic NFCN electrodes at 1C ($1\text{C} = 0.170 \text{ A g}^{-1}$) rate calculated based on the theoretical capacity of NFCN in $1 \text{ M Na}_2\text{SO}_4(\text{aq}) + 0.1 \text{ M citrate buffer (pH} = 4)$ electrolyte using decoupled beaker-type cells. As the second redox peak is very close to the limit of the water stability window, it is especially important to correctly choose the cut-off potential. First, it was set to -0.3 V and 1.0 V vs Ag/AgCl (Fig. 89a) where two plateaus are observed during charging, which corresponds to 104 mAh g^{-1} , and only one at lower voltage during discharging process – 74 mAh g^{-1} . This suggests that some of the “second” iron is reached but not all of it, as the theoretical capacity is only 170 mAh g^{-1} . GCD cycling at this potential resulted in low average CE% of $\sim 80\%$ and relatively high 81% capacity retention after 100 cycles (Fig. 90). Later, the upper potential limit was increased to 1.05 V vs Ag/AgCl which still did not show the discharging plateau of the second redox peak (Fig. 89b). This time, the initial charge and discharge capacities were 163 mAh g^{-1} and 115 mAh g^{-1} (Fig. 90), respectively. The average CE% and discharge capacity retention is even lower this time $\sim 68\%$ and 69% , respectively. If the upper potential cut-off is increased to 1.1 V vs Ag/AgCl, the charging becomes endless at 1.08 V vs Ag/AgCl which suggests that oxygen evolution reaction (OER) already takes place and limits the availability of full NFCN capacity in aqueous electrolytes. OER could be moved to more positive voltage by optimizing the electrolyte (pH, additives) but HER at the other side should also be taken into consideration.²¹²

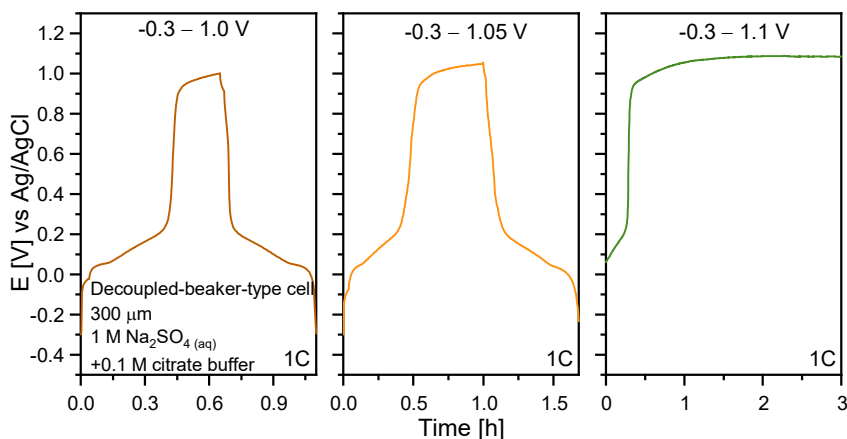


Fig. 89. GCD cycling of monoclinic phase NFCN electrode in aqueous citrate buffered (pH = 4.0) electrolyte at different potential limits (voltage vs time).

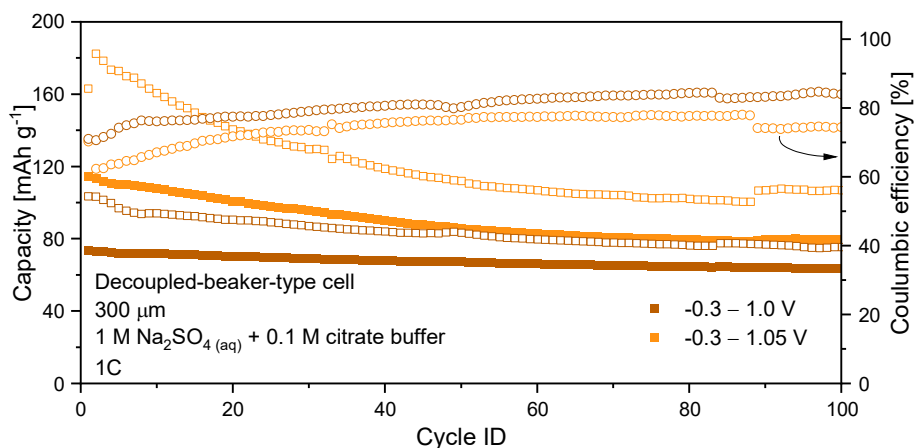


Fig. 90. GCD cycling of monoclinic phase NFCN electrode in aqueous citrate buffer electrolyte (pH = 4) at different potential limits.

As the second redox peak of iron is already in the OER range it limits its electrochemical performance. Further GCD cycling was performed only for the first redox peak within the potential limits of $-0.3 - 0.5$ V vs Ag/AgCl at 1C which was calculated based on the theoretical capacity of 85 mAh g^{-1} . Fig. 91 presents the comparison of cubic and monoclinic phase electrodes. In both cases, the CE% ($\sim 98.8\%$) is much better than before but the capacity retention after 100 cycles was only $\sim 53\%$ and 65% for cubic and monoclinic samples, respectively.

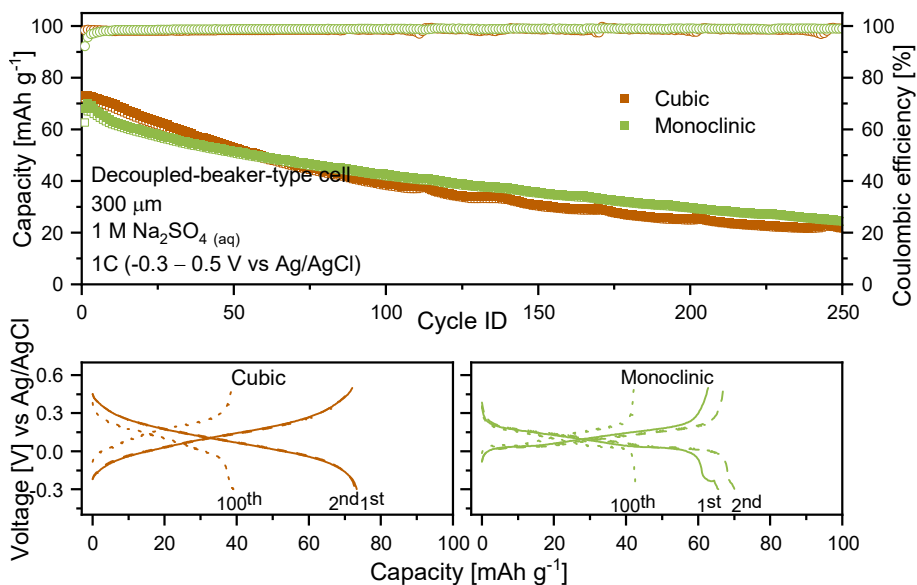


Fig. 91. GCD cycling of a) cubic and b) monoclinic phase of NFCN electrodes.

GCD cycling of monoclinic NFCN electrodes was also performed in 1 M Na_2SO_4 (aq) with different buffers such as 0.1 M citrate (pH = 4.0), 0.1 M phosphate (pH = 7.0) and 0.1 M borate (pH = 10.0) to investigate the influence of pH to material electrochemical performance. 200 cycles were recorded at 1C using decoupled beaker-type cells. The results (Fig. 92) clearly show that NFCN is electrochemically stable in acidic pH but degrades rapidly in alkaline media. This could be explained by the destruction of the Fe-CN bond leading to iron dissolution which is the result of strong interaction between hydroxide and ferric ions to form $\text{Fe}(\text{OH})_3$ at pH higher than 6.4. The solution to this problem, for example, could be the formation of an external protective layer.²¹³ Electrochemical stability of monoclinic NFCN electrodes in the citrate buffer was extended to 1000 cycles at 1C (Fig. 93). The initial charge and discharge capacity together with capacity retention for this sample are 73 mAh g^{-1} , 71 mAh g^{-1} and 88%, respectively, which suggest excellent stability in aqueous electrolytes.

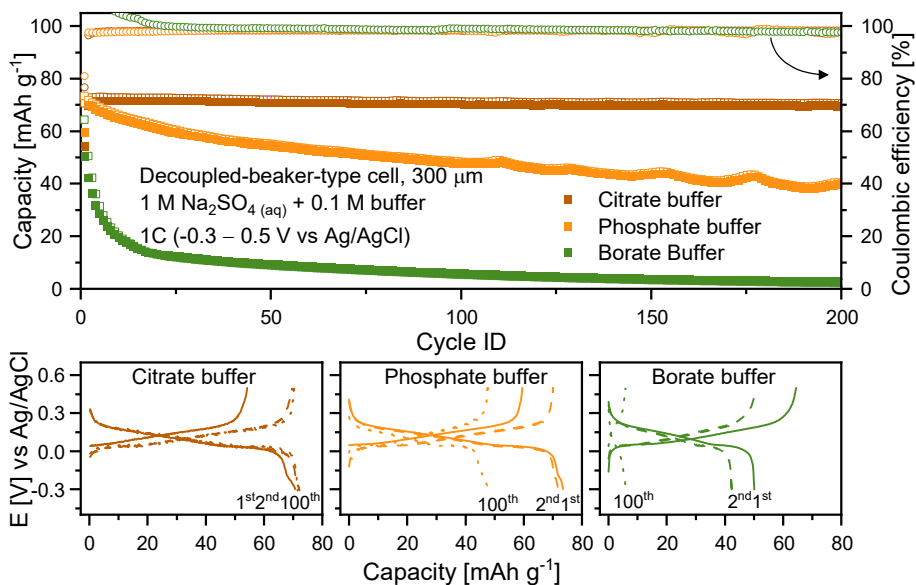


Fig. 92. GCD cycling of monoclinic phase NFCN electrodes in aqueous electrolytes with different pH at 1C.

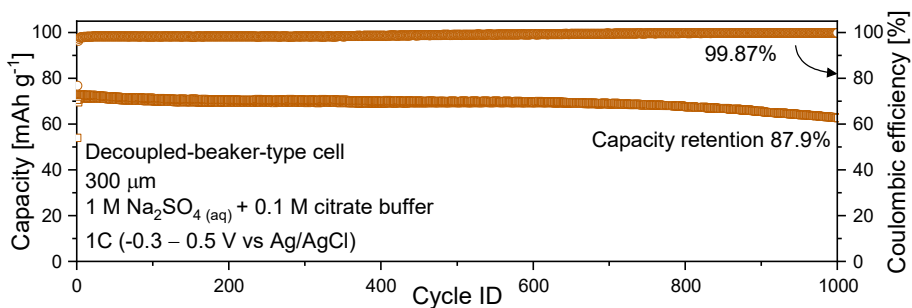


Fig. 93. GCD cycling of monoclinic phase NFCN electrodes in aqueous citrate buffer (pH = 4) electrolyte at 1C.

Additionally, the rate capability of monoclinic NFCN was evaluated in 1 M Na_2SO_4 (aq) with 0.1 M citrate buffer electrolyte at a set of different specific currents corresponding to 0.1, 0.2, 0.5, 1, 2, 5, 10 and 20C (Fig. 94). The specific capacity was 68 mAh g^{-1} at 0.1C rate, which slightly dropped to 58 mAh g^{-1} at 20C rate and came back to 64 mAh g^{-1} when the C rate was 0.1C again. This indicates an excellent rate capability of NFCN in acidic aqueous electrolytes.

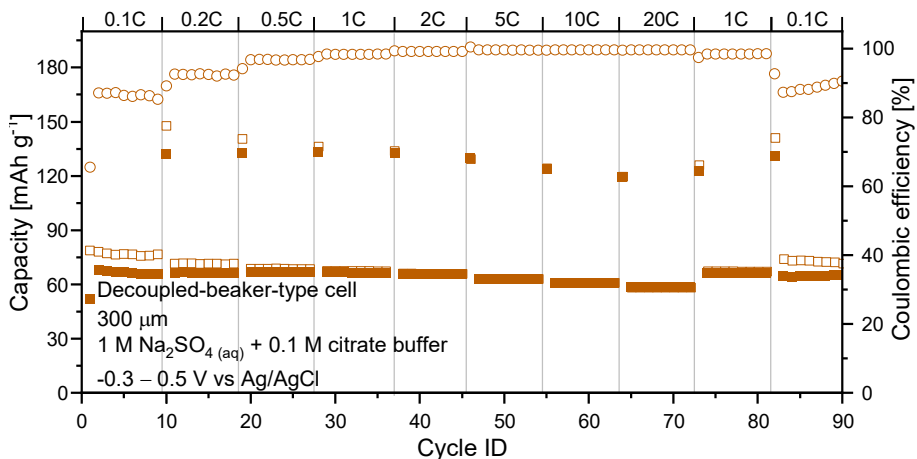


Fig. 94. Rate capability of GCD cycling of monoclinic NFCN electrodes.

Electrochemical investigation of monoclinic and rhombohedral NFCN materials was also carried out in organic electrolyte in order to compare with aqueous systems. Fig. 95 shows a CV which was recorded in 1 M NaPF_6 in EC:PC (1:1 vol%) electrolyte at the scanning rate of 0.1 mV s^{-1} within the potential window of 2 – 4.5 V vs Na^+/Na using a Swagelok-type cell. For the monoclinic sample, three reversible current peaks of $\text{Fe}^{2+}/\text{Fe}^{3+}$ could be found at 2.8 V/3.05 V, 3.25 V/3.3 V and 3.7 V/4.0 V. The first two correspond to the high-spin-state nitrogen-coordinated couple ($\text{Fe}^{3+}/\text{Fe}^{2+}\text{-N}$) and the low-spin-state carbon-coordinated couple ($\text{Fe}^{3+}/\text{Fe}^{2+}\text{-C}$), which grow over cycling. On the other hand, rhombohedral sample has the same two first current peaks at 2.9 V/3.1 V and 3.25 V/3.3 V, and the third peak at 3.7 V/4.0 V exists only in the first two cycles which could come from some remaining residue of monoclinic phase. The position of the peaks differs from aqueous electrolytes due to coordinating water ligand field effects on the $\text{Fe}^{2+}/\text{Fe}^{3+}$ energy levels and crystallographic symmetry. However, the confirmation of such hypothesis requires much deeper investigation using theoretical calculations which was not the objective of this work.

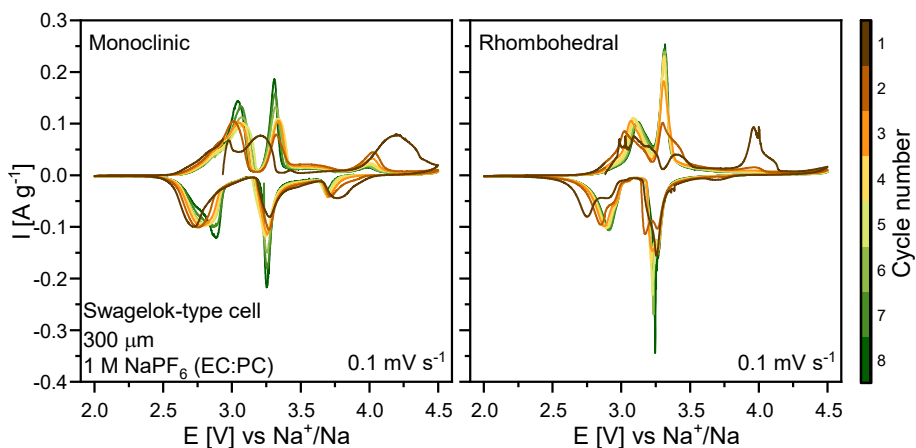


Fig. 95. Cyclic voltammograms of a) monoclinic and b) rhombohedral phase NFCN electrodes recorded at 0.1 mV s^{-1} scan rate in organic electrolyte.

GCD measurements of these two NFCN samples were performed for 300 cycles within the potential window from 2.5 to 4.2 V vs Na^+/Na at 1C with 1 M NaPF_6 in EC:PC (1:1 vol%) and 1 M NaPF_6 in DG electrolytes using Swagelok-type cells (Fig. 96). The initial discharge capacity and its retention after 100 cycles for monoclinic and rhombohedral phases are 111 mAh g^{-1} and 64%, 98 mAh g^{-1} and 77%, respectively. The capacity drops rapidly in the first 10 cycles for both cases suggesting that the third redox peak is not electrochemically stable, which is also visible at voltage plateaus. However, the achieved capacities are still off from those reported in the literature¹⁹⁹ which could be related to necessary electrolyte optimization.

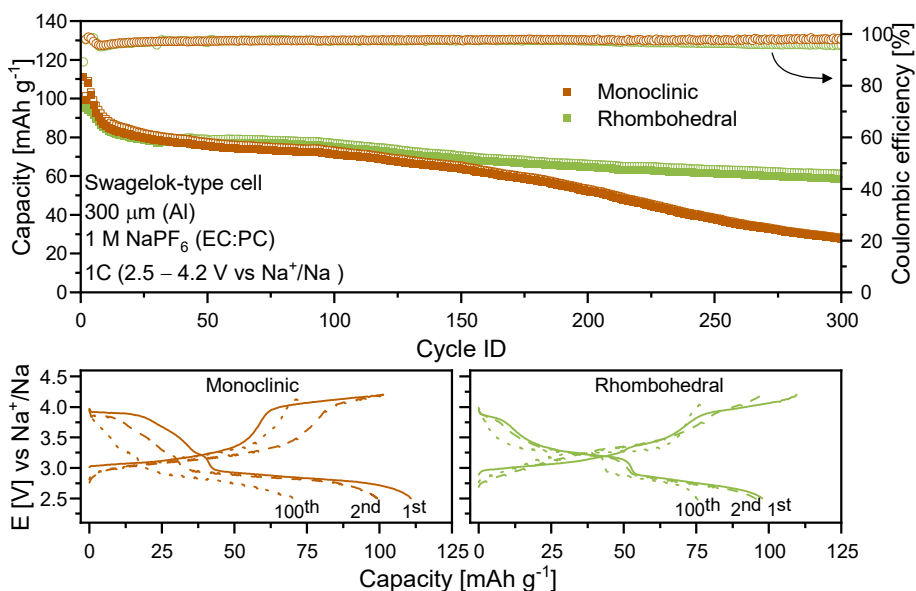


Fig. 96. GCD cycling of monoclinic and rhombohedral phases NFCN electrodes in organic electrolyte at 1C.

3.3.5. Summary

☐ $\text{Na}_3\text{Fe}_2(\text{PO}_4)_3$ was successfully synthesized via solid-state method. The particles have irregular morphology. Electrochemical investigation showed very poor performance (low initial capacity) which suggests that it is not suitable as a negative electrode material for aqueous SIBs.

☐ $\text{Na}_4\text{Fe}_3(\text{PO}_4)_2\text{P}_2\text{O}_7$ was successfully synthesized via solid-state and sol-gel methods. Electrochemical results showed some degradation related to Fe dissolution or instability of mixed phosphate-pyrophosphate framework, which results in kinetic limitations of this material. Mitigation strategies such as electrolyte additives or protective layers are necessary to enable this material for aqueous applications. On the other hand, $\text{Na}_4\text{Fe}_3(\text{PO}_4)_2\text{P}_2\text{O}_7$ shows very good cycling stability and rate capability in organic electrolytes.

☐ $\text{Na}_{2-x}\text{Fe}[\text{Fe}(\text{CN})_6] \cdot y\text{H}_2\text{O}$ was successfully synthesized via a hydrothermal method. Cubic phase is obtained if the synthesis temperature is higher than 100°C , and monoclinic at $\leq 80^\circ\text{C}$. Pure cubic, monoclinic and rhombohedral phases were additionally synthesized via co-precipitation method. This synthesis yielded cubic shape particles with the size of a few micrometers.

☐ Two-electron iron redox process in aqueous electrolytes is limited due to oxygen evolution reaction.

☐ Monoclinic $\text{Na}_{1.86}\text{Fe}[\text{Fe}(\text{CN})_6]\cdot 2.28\text{H}_2\text{O}$ electrode has outstanding electrochemical performance in aqueous 1 M Na_2SO_4 + 0.1 M citrate buffer electrolyte with 88% capacity retention after 1000 cycles at 1C for one electron reaction. In organic electrolytes, the same electrode shows two-electron reaction and achieves the initial capacity of 98 mAh g^{-1} with capacity retention of 77% after 100 cycles. $\text{Na}_{2-x}\text{Fe}[\text{Fe}(\text{CN})_6]\cdot y\text{H}_2\text{O}$ shows a decent electrochemical performance to be a suitable as a positive electrode material for aqueous and non-aqueous SIBs.

3.4. Vanadium-based materials for Na-ion battery positive electrodes

3.4.1. Motivation

Vanadium is known as an electrochemically rich (V^{2+} to V^{5+}) transition metal with relatively low-cost and abundance. A large number of vanadium-based electrodes owing to their high theoretical capacity and energy density have been explored for SIBs.²¹⁴ In addition to different chemical compositions (vanadium oxides (e.g., V_2O_5 ²¹⁵), bronzes (e.g., Na_xVO_2 ²¹⁶), phosphates (e.g., $Na_3V_2(PO_4)_3$ ²¹⁷) and mixed-polyanions (e.g., $NaVPO_4F$ ²¹⁸) etc.), these materials could come in various structures (tunnel, layered, open-framework) which are tunable for good electrochemical performance and storage efficiency.²¹⁹

$Na_7V_4(PO_4)(P_2O_7)_4$ (NVPP) belongs to a family of mixed-polyanion compounds. It is a promising positive electrode candidate for SIBs due to its high operating potential at ~ 1.0 V vs Ag/AgCl and theoretical capacity of 93 mAh g^{-1} .²²⁰ NVPP has a tetragonal structure with $P\bar{4}2_1c$ (No. 114) space group where $[V_4(P_2O_7)_4(PO_4)]_\infty$ is constructed through each $[PO_4]$ tetrahedron sharing corners with four adjacent $[VO_6]$ octahedra and each $[P_2O_7]$ group sharing corners with two adjacent $[VO_6]$ (Fig. 97).²²¹ There are three interstitial sites for Na ions which can easily diffuse along the well-defined channels in this three-dimensional framework enabling the reversible Na intercalation/deintercalation with good electrochemical performance. There are several reports confirming this idea, for example, S. Y. Lim et. al. demonstrated the capacity retention of 78% after 1000 cycles (0.5C, organic electrolyte) with initial capacity of 91 mAh g^{-1} for NVPP.²²¹ Moreover, Deng et. al. showed that nanorods of NVPP have achieved discharge capacity of 92 mAh g^{-1} (0.05C, organic electrolyte) which is almost equal to the theoretical value and could be attributed to high purity and well-defined morphology of their sample.²²² Same group have also tested NVPP in aqueous media and they achieved the initial capacity of 51 mAh g^{-1} (0.86C, 1 M Na_2SO_4 (aq)),²²³ however there is still a lack of detailed investigations of NVPP in aqueous media.

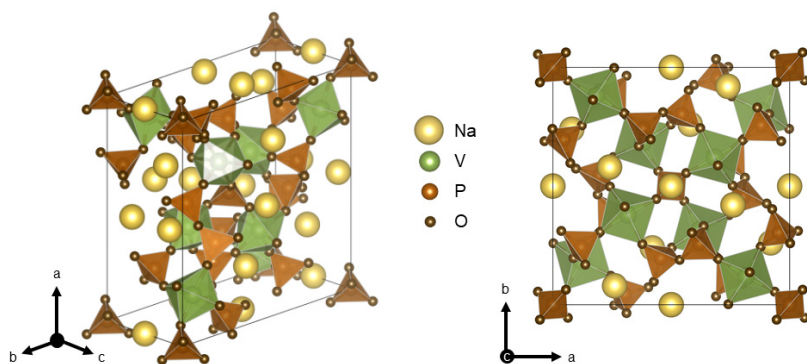


Fig. 97. Crystal structure of $\text{Na}_7\text{V}_4(\text{PO}_4)(\text{P}_2\text{O}_7)_4$.

3.4.2. Synthesis

$\text{Na}_7\text{V}_4(\text{PO}_4)(\text{P}_2\text{O}_7)_4$ was synthesized via a solid-state method (Fig. 98). In a typical synthesis, Na_2CO_3 (0.0091 mol, Glentham, 99+%), NH_4VO_3 (0.0104 mol, Reachem, 99.5%), and $\text{NH}_4\text{H}_2\text{PO}_4$ (0.0234 mol, Honeywell, 99+%) were mixed using wet (2-propanol) ball-milling at 350 rpm for 2 h. The dried mixture was calcined at 600 °C for 5 h and subsequently at 800 °C for 10 h, in N_2/H_2 (95/5%) atmosphere. The obtained light green powder was post-processed at 350 rpm for 2 h using ball-mill. The resulting particles were coated with a layer of carbon by homogeneously mixing additionally ball-milled (1 h at 900 rpm) NVPP powder (70 wt%, (usually, 0.7 g)) and of citric acid (30 wt% (0.3 g), $\text{HO}(\text{CH}_2\text{CO}_2\text{H})_2$, Lach-ner, G.R.) in distilled water (50 mL). The resulting mixture was dried at 80 °C for several hours for complete water elimination. The obtained powder was reground and annealed at 700 °C for 2 h in N_2 atmosphere. The resulting black powder was again ball-milled at 350 rpm for 2 h to achieve a uniform final particle size distribution.

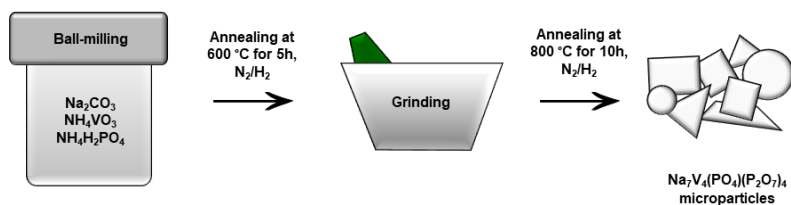


Fig. 98. Solid-state synthesis scheme of $\text{Na}_7\text{V}_4(\text{PO}_4)(\text{P}_2\text{O}_7)_4$.

3.4.3. Structural characterization

$\text{Na}_7\text{V}_4(\text{PO}_4)(\text{P}_2\text{O}_7)_4$ was successfully synthesized via a conventional solid-state method. The XRD pattern and its Rietveld refinement results in Fig. 99 present sharp diffraction peaks which indicate high sample crystallinity and are consistent with the tetragonal space group $P4_21c$ (No. 114).²²⁴ The lattice parameters were determined to be $a = 14.22427(13) \text{ \AA}$, $c = 6.37216(9) \text{ \AA}$ and $V = 1289.28(3) \text{ \AA}^3$, they are in good agreement with the literature data.²²⁰ However, the synthesized NVPP sample is not pure, $\text{Na}_3\text{V}_2(\text{PO}_4)_3$ (~10.2 wt%) and $\text{NaV}(\text{P}_2\text{O}_7)$ (~6.6 wt%) impurities were also detected, which is quite common in conventional solid-state synthesis of this material.^{221, 225} The morphology of NVPP was investigated using SEM. Fig. 100 indicates that particles are irregularly shaped and few micrometers in size with broad size distribution.

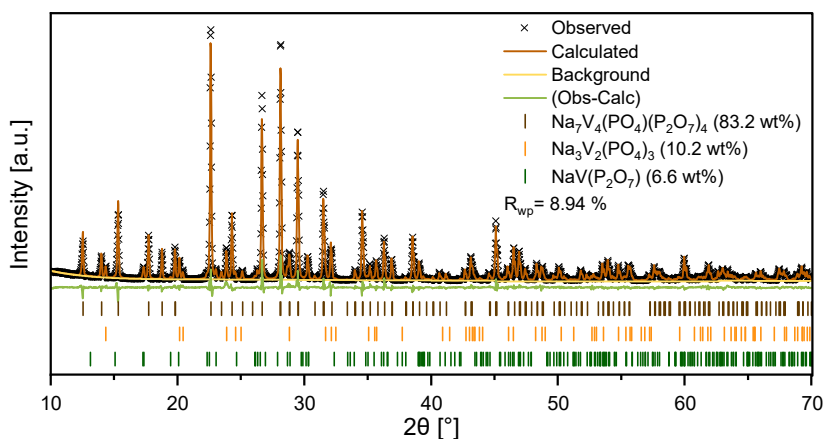


Fig. 99. Powder XRD pattern and Rietveld refinements results for NVPP sample.^{224, 226, 227}

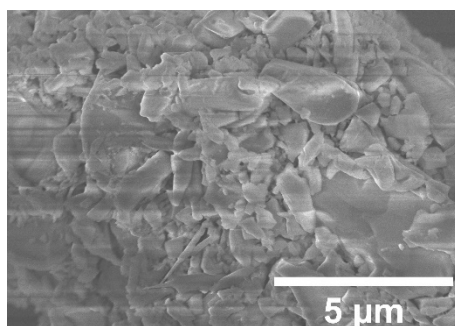


Fig. 100. SEM image of NVPP sample.

In order to improve the electronic contact between ceramic particles, the NVPP was additionally coated by a carbon layer using post-synthetic pyrolysis of citric acid. The XRD pattern in Fig. 101 shows that such treatment does not alter the main phase structure. The resulting carbon content obtained by this procedure was evaluated by TGA and found to be 2.97 wt% (Fig. 102).

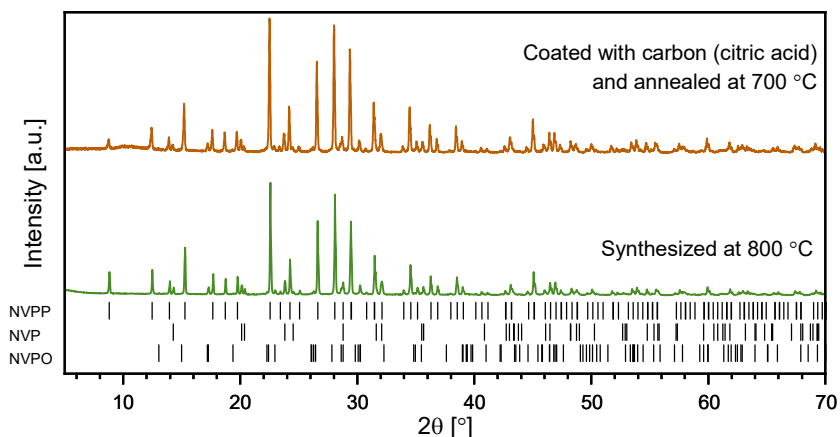


Fig. 101. Powder XRD patterns of NVPP samples: (bottom) as synthesized at 800 °C by solid state method; (top) coated with carbon (citric acid) and pyrolyzed at 700 °C.^{224, 226, 227}

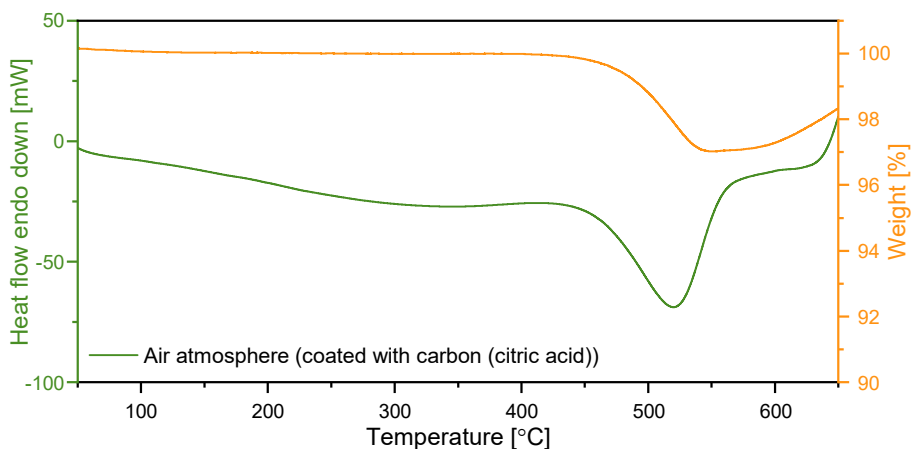
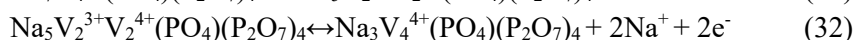
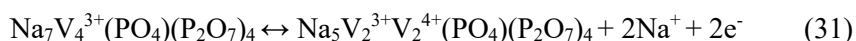


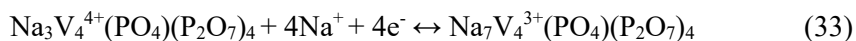
Fig. 102. Thermogravimetric and DSC curves of NVPP.

3.4.4. Electrochemical performance

For the initial electrochemical characterization, CVs of NVPP samples were performed using 1 M Na₂SO₄ (aq) electrolyte at the scanning rate of 5 mV s⁻¹ within the potential window of -0.6 – 1.0 V vs Ag/AgCl using beaker-type cells (Fig. 103). The NVPP displays several well pronounced and reversible current peaks. The first set of small reversible peaks at 0 V/0.1 V are attributed to the V³⁺/V⁴⁺ redox transition originating from Na₃V₂(PO₄)₃ impurity.²²⁸ This peak disappears after 3 full cycles. Only two anodic peaks at ~0.63 V and 0.72 V could be assigned to the V³⁺/V⁴⁺ redox transition in NVPP followed by a two-stage Na ion deinsertion:²²²



On the other hand, the reversible insertion of Na ion during reduction appears as a single cathodic peak at ~0.3 V and suggest a single-stage process:



However, the current values for these peaks fade in just a few cycles which indicates very poor stability of NVPP in aqueous electrolyte.

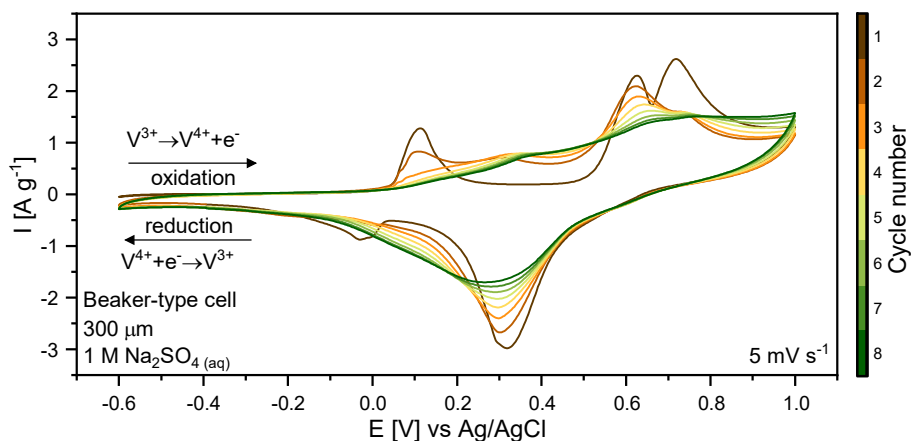


Fig. 103. Cyclic voltammograms of NVPP recorded in 1 M Na₂SO₄ (aq) electrolyte at 5 mV s⁻¹ scan rate.

GCD cycling was used for specific discharge capacity and CE% of NVPP electrode determination. Fig. 104 shows the GCD cycling for 100 cycles within the potential window from 0.2 V to 1.15 V (Ag/AgCl) at 1C (1C = 0.093 A g⁻¹) rate calculated based on the theoretical capacity of NMPP in 1 M Na₂SO₄(aq) or 17 m NaClO₄(aq) using Swagelok-type cells. The initial capacity and its retention after 100 cycles at 1C are 55 mAh g⁻¹ and 2.4%, and 51 mAh g⁻¹ and 19% for 1 M Na₂SO₄(aq) and 17 m NaClO₄(aq) electrolytes, respectively. These poor electrochemical results suggest very rapid degradation of NVPP in aqueous electrolyte which is not significantly improved even by using high concentration ‘water-in-salt’ electrolyte. It could be related to the dissolution and instability of V⁴⁺ in aqueous media.²²⁹ On the other hand, the NVP plateau disappears faster than those of NVPP, suggesting that NVPP mixed-polyanionic framework is slightly more stable in aqueous environment than NVP.

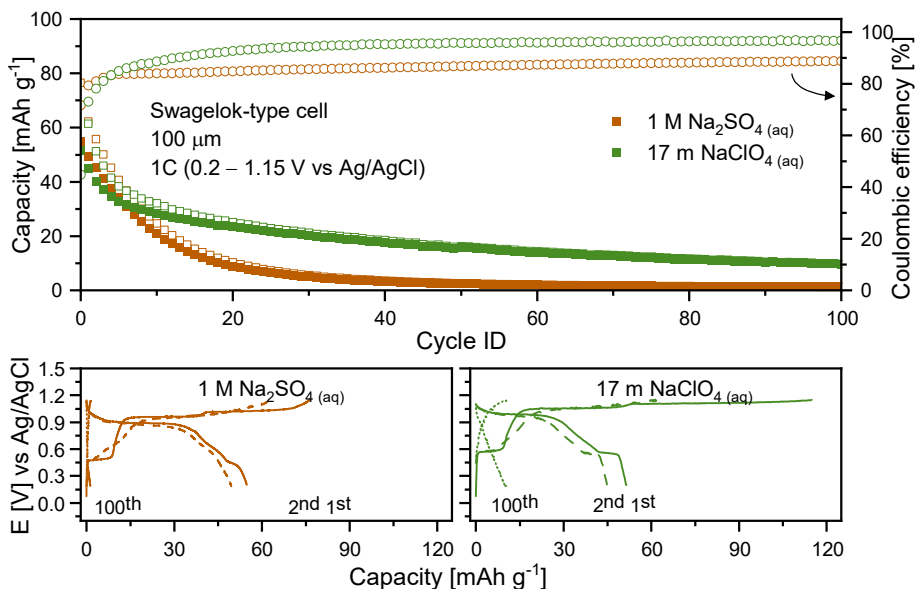


Fig. 104. GCD cycling of NVPP electrodes in different aqueous electrolytes at 1C.

Electrochemical performance investigation of NVPP was additionally carried out in organic electrolytes to compare the results with aqueous systems and to verify that the capacity loss is mainly related to the electrolyte and not the material itself. Fig. 105 shows CVs which were recorded in 1 M NaPF₆ in DG electrolyte at the scanning rate of 0.5 mV s⁻¹ within the potential window

of 2.5 – 4.5 V vs Na⁺/Na using a Swagelok-type cell. All observed peaks agree well with previous aqueous results of NVP and NVPP (Fig. 104) and those reported in the literature.^{225, 228} There is no degradation or decrease of current peaks current which suggests that this sample is very stable in organic electrolyte.

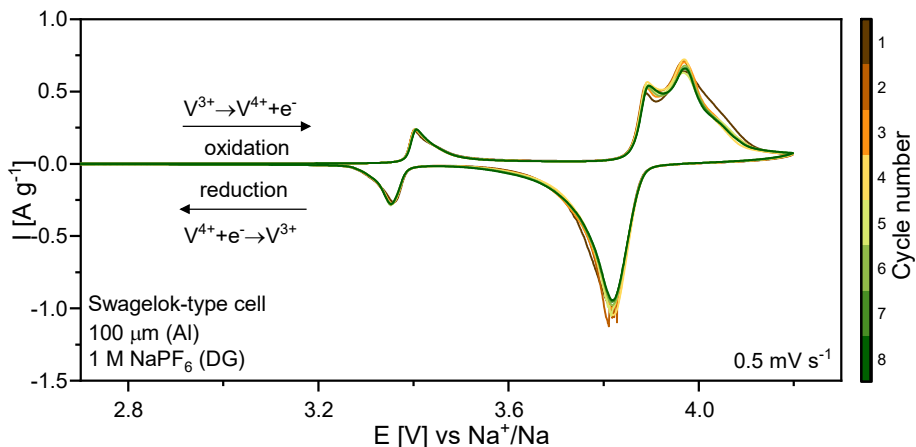


Fig. 105. Cyclic voltammograms of NVPP recorded at 0.5 mV s⁻¹ scan rate in organic electrolyte.

GCD measurements were performed for 300 cycles within the potential window from 2.5 to 4.2 V vs Na⁺/Na at 1C with 1 M NaPF₆ in EC:DEC (3:7 vol%) and 1 M NaPF₆ in DG electrolytes using Swagelok-type cells (Fig. 106). Both electrolytes show similar performance. The initial capacity and its retention after 100 cycles at 1C are 79 mAh g⁻¹ and 83%, and 80 mAh g⁻¹ and 85% for DG and EC:DEC electrolytes, respectively. These results suggest that NVPP is a very stable material with good electrochemical performance in organic electrolytes. The potential profiles exhibit two close plateaus at 3.88 and 3.98 V vs Na⁺/Na during charging and a single plateau at 3.86 V during discharging. Additional small plateaus at 3.41 and 3.36 V vs Na⁺/Na correspond to NVP impurity which agrees well with CV results (Fig. 105).

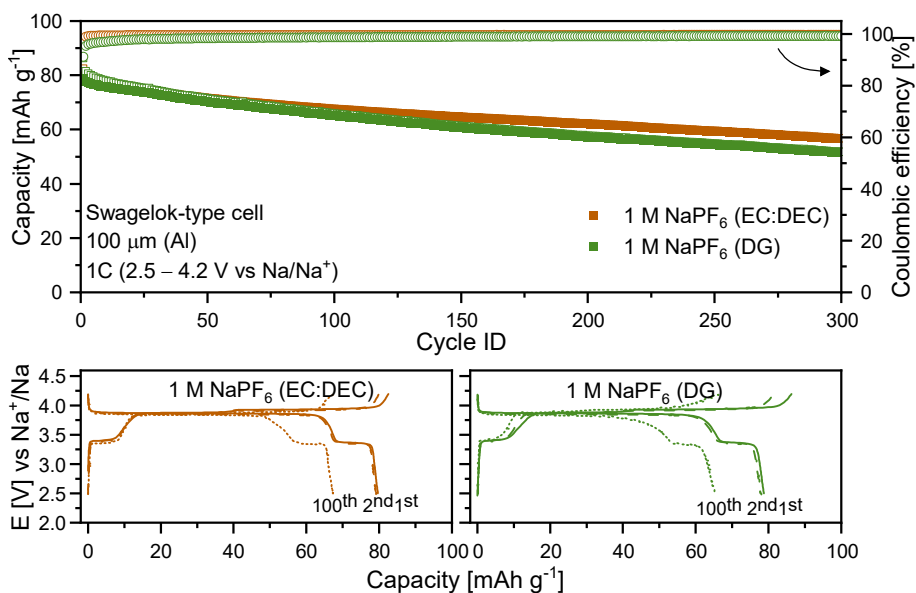


Fig. 106. GCD cycling results of NVPP electrodes in different organic electrolytes at 1C.

The C-rate capability (0.1 – 20C) experiment of NVPP in DG electrolyte (Fig. 107) shows that increasing C-rate leads to lower capacity due to kinetic limitations.¹⁵⁷ The specific capacity at 0.1C rate was 82 mAh g⁻¹, decreased to 60 mAh g⁻¹ at 1C, and was negligible at 20C. However, the capacity was recovered when the rate came back to 0.1C. The plateaus in potential profiles shift to higher potentials at higher currents and become virtually indistinguishable at high rates indicating significant polarization effects (Fig. 108).

Overall, NVPP seems to be not the most optimal electrode material for aqueous SIBs. However, it is a suitable positive electrode for organic SIBs.

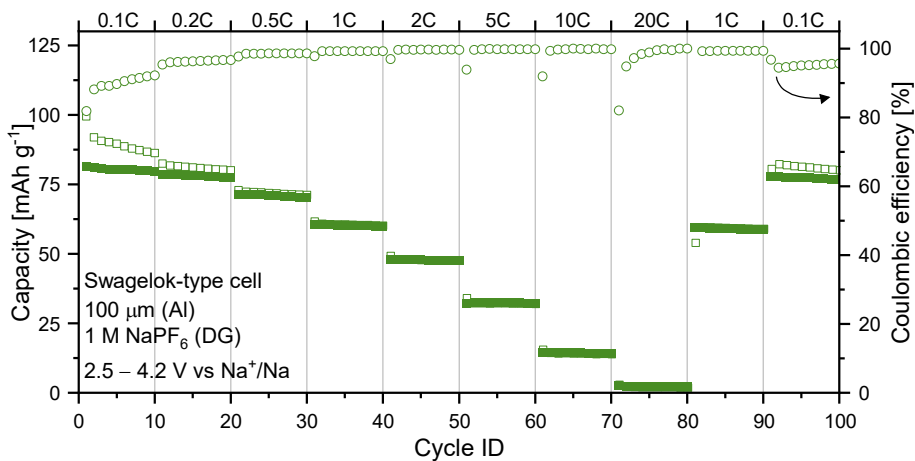


Fig. 107. Rate capability of GCD cycling of NVPP in organic DG electrolyte (capacity vs cycle number).

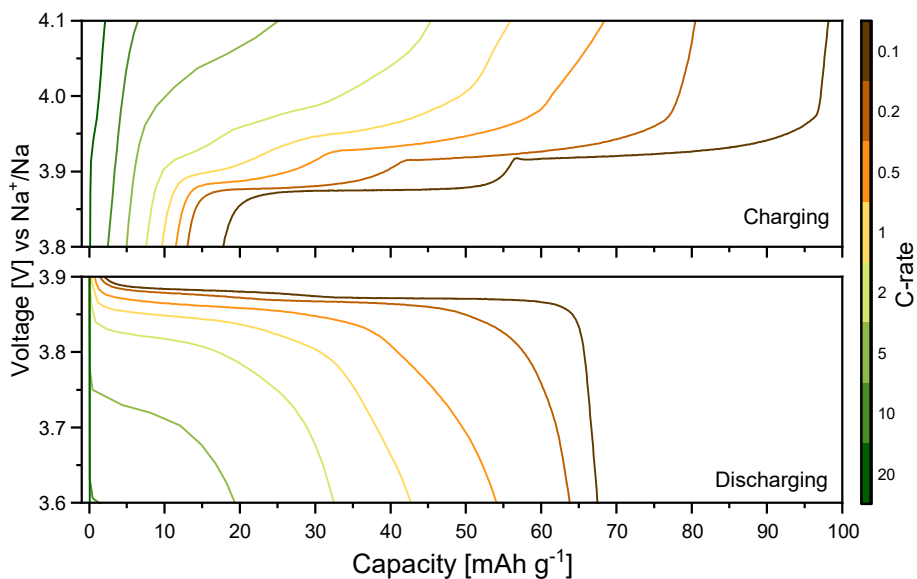


Fig. 108. Rate capability of GCD cycling of NVPP in organic DG electrolyte (capacity vs potential).

3.4.5. Summary

☐ $\text{Na}_7\text{V}_4(\text{PO}_4)(\text{P}_2\text{O}_7)_4$ was successfully synthesized via a conventional solid-state method. However, $\text{Na}_3\text{V}_2(\text{PO}_4)_3$ (~10.2 wt%) and NaVP_2O_7 (~6.6 wt%) impurities were also detected by XRD.

☐ Electrochemical investigation of NVPP electrodes show poor performance in aqueous electrolytes due to fast degradation which is most likely related to the dissolution of V^{4+} in aqueous media. NVPP is not a suitable positive electrode for aqueous SIBs, and additional stabilization strategies are required.

☐ NVPP electrodes exhibit very good electrochemical performance (initial capacity, its retention and rate capability) in organic electrolytes which makes it a suitable positive electrode for organic SIBs.

3.5. Mixed-transitional metal-based materials for Na-ion battery positive electrodes

3.5.1. Motivation

NASICON-structured material can accommodate a wide selection of transitional metals or even several of them. This could be utilized to develop new cost-effective electrode materials. Indeed, several mixed-transitional metal compounds such as $\text{Na}_3\text{MnTi}(\text{PO}_4)_3$ ^{230, 231}, $\text{Na}_3\text{MnZr}(\text{PO}_4)_3$ ²³², $\text{Na}_4\text{MnV}(\text{PO}_4)_3$ ²³³, and $\text{Na}_3\text{VTi}(\text{PO}_4)_3$ ²³⁴ with good electrochemical performance were reported.

$\text{Na}_3\text{VFe}(\text{PO}_4)_3$ (N_3VFP) and $\text{Na}_4\text{VFe}(\text{PO}_4)_3$ (N_4VFP) have the advantages of vanadium, iron, and NASICON structure all together. N_3VFP and N_4VFP have monoclinic symmetry with $C2/c$ (No. 15) space group and a trigonal symmetry with $R\bar{3}c$ (No. 167) space group, respectively. V and Fe share the same position with 50% occupancy each (Fig. 109). These materials are particularly interesting because of three Na ion exchange through the successive activations of $\text{Fe}^{2+}/\text{Fe}^{3+}$, $\text{V}^{3+}/\text{V}^{4+}$, and $\text{V}^{4+}/\text{V}^{5+}$ redox couples which could enable a theoretical capacity of 175 mAh g^{-1} and 166 mAh g^{-1} of N_3VFP and N_4VFP , respectively. Even if these materials have a lot of potential to be used for SIBs, there are only a few reports related to their electrochemical performance so far. Hadouchi et. al. attempted to synthesize N_4VFP but obtained a sodium-deficient composition $\text{Na}_{3.41}\square_{0.59}\text{FeV}(\text{PO}_4)_3$ with mixed valence $\text{Fe}^{2+}/\text{Fe}^{3+}$, however, they still achieved the initial charge capacity of 163.5 mAh g^{-1} and 119 mAh g^{-1} (0.5C, organic electrolyte) for three and two Na ion insertion, respectively, with almost perfect capacity retention (95 – 99%) at higher C-rates.²³⁵ Park et. al. published two reports related to the crystal structure of N_3VFP and N_4VFP and an asymmetric Na-ion insertion/extraction mechanism in N_4VFP . They achieved the initial discharge capacity of 138 mAh g^{-1} (0.05C, organic electrolyte) for 3-electrons which decreased down to 109 mAh g^{-1} after 20 cycles.^{236, 237} Zhou et. al. has investigated electrochemical behavior of N_3VFP , their electrode exhibited 103 mAh g^{-1} (1C, organic electrolyte) with capacity retention of 95% after 1000 cycles.²³⁸ However, there are no reports about the performance of these materials in aqueous electrolytes.

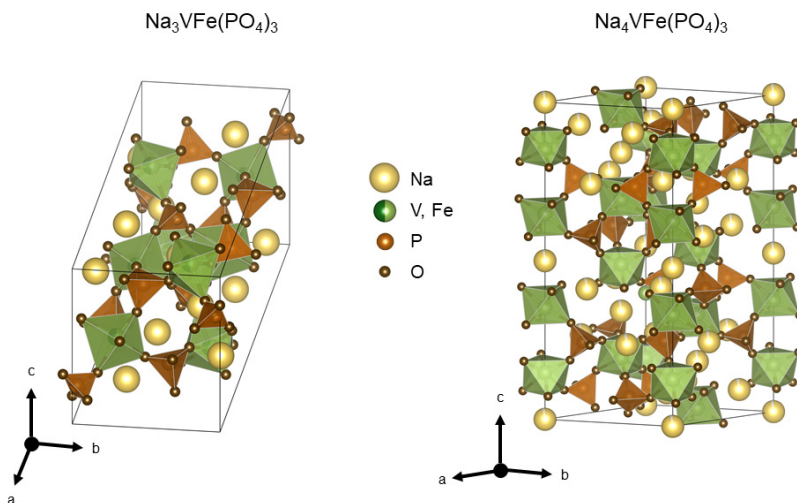


Fig. 109. Crystal structures of $\text{Na}_3\text{VFe}(\text{PO}_4)_3$ and $\text{Na}_4\text{VFe}(\text{PO}_4)_3$.

3.5.2. Synthesis

$\text{Na}_3\text{VFe}(\text{PO}_4)_3$ was synthesized via a solid-state method (Fig. 110). In a typical synthesis, Na_2CO_3 (0.0165 mol, Glentham, 99+%), V_2O_3 (0.0041 mol), $\text{FeC}_2\text{O}_4 \cdot 2\text{H}_2\text{O}$ (0.0082 mol, Chempur, p.a.) and $\text{NH}_4\text{H}_2\text{PO}_4$ (0.0248 mol, Honeywell, 99+%) were mixed using wet (2-propanol) ball-milling at 350 rpm for 2 h. The dried mixture was calcined at 400 °C for 8 h and subsequently at 700 °C for 8 h, in N_2 atmosphere. The obtained powders were post-processed at 350 rpm for 2 h using ball-mill. The resulting particles were coated with a layer of carbon by homogeneously mixing additionally ball-milled (1 h at 900 rpm) NVFP powder (70 wt%, (usually, 0.7 g)) and of citric acid (30 wt% (0.3 g), $\text{HOC}(\text{CH}_2\text{CO}_2\text{H})_2$, Lach-ner, G.R.) in distilled water (50 mL). The resulting mixture was dried at 80 °C for several hours for complete water elimination. The obtained powder was reground and annealed at 700 °C for 2 h in N_2 atmosphere. The resulting black powder was again ball-milled at 350 rpm for 2 h in order to achieve a uniform final particle size distribution.

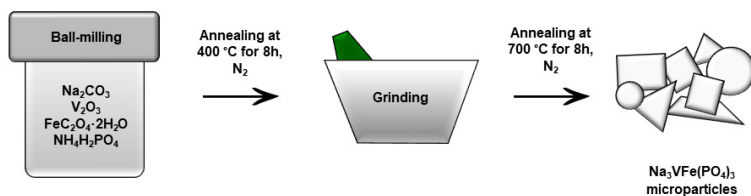


Fig. 110. Solid-state synthesis scheme of $\text{Na}_3\text{VFe}(\text{PO}_4)_3$.

3.5.3. Structural characterization

The aim of this part of the work was to synthesize $\text{Na}_4\text{VFe}(\text{PO}_4)_3$. However, the XRD analysis (Fig. 111) showed that $\text{Na}_3\text{VFe}(\text{PO}_4)_3$ was obtained instead by a solid-state synthesis which agrees with the literature data that pure N_4VFP could only be achieved through electrochemical sodiation of N_3VFP .²³⁶ As there is a lack of research on N_3VFP , especially, in aqueous electrolytes, it was decided to continue with this one, which will be denoted as NVFP from this point. The XRD pattern of NVFP shows sharp diffraction peaks which indicate a high degree of crystallinity and agrees well with monoclinic $C2/c$ (No. 15) space group.²³⁸ A small amount of additional phase of NaFePO_4 was also detected. The morphology of NVFP was investigated using SEM analysis. Fig. 112 indicates that particles are irregular and a few micrometers in size.

In order to improve the electronic contact between ceramic particles, NVFP was additionally coated by a carbon layer using post-synthetic pyrolysis of citric acid. The XRD pattern in Fig. 111 shows that such treatment does not alter the main phase structure. The resulting carbon content obtained by this procedure was evaluated by TGA and found to be ~ 4.6 wt% (Fig. 113).

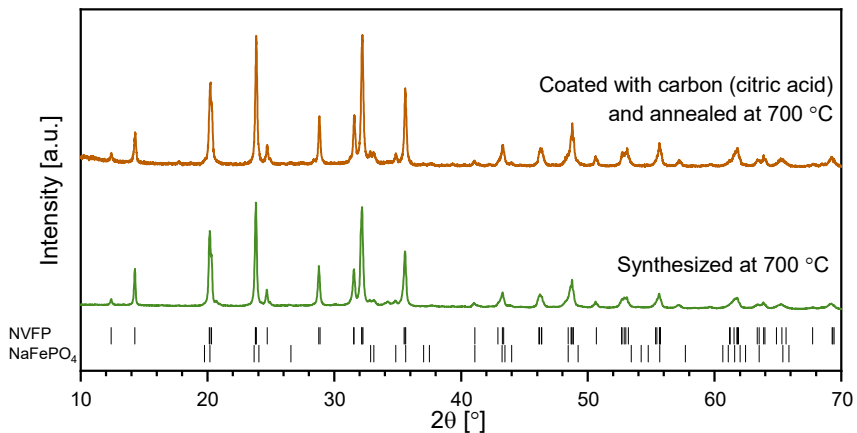


Fig. 111. Powder XRD patterns of NVFP samples: (bottom) as synthesized at 700 °C by solid state method; (top) coated with carbon (citric acid) and pyrolyzed at 700 °C.^{238, 239}

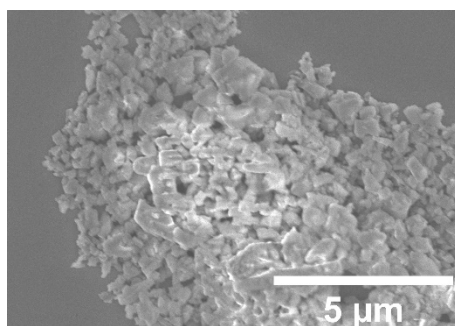


Fig. 112. SEM image of a NVFP sample.

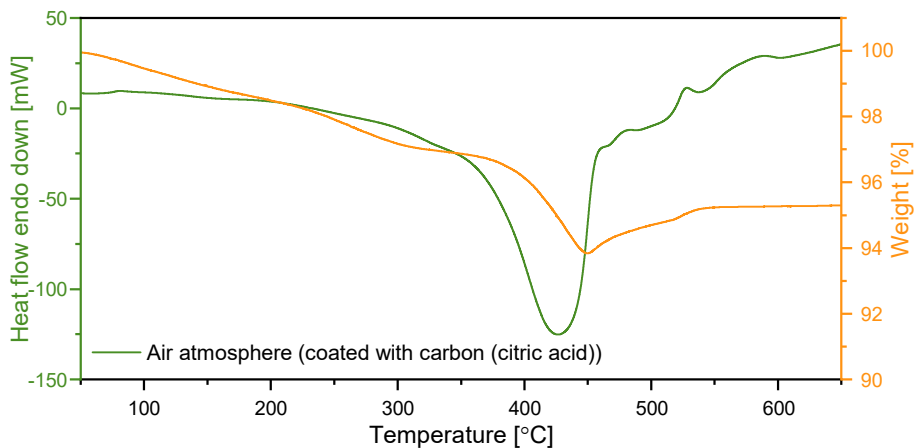


Fig. 113. Thermogravimetric and DSC curves of NVFP.

3.5.4. Electrochemical performance

For the initial electrochemical characterization, CVs of NVFP were recorded using 1 M Na₂SO₄ (aq) electrolyte at the scanning rate of 5 mV s⁻¹ within different potential windows using beaker-type cells. When the potential limits were from -1.0 V to 1.4 V vs Ag/AgCl (Fig. 114), three anodic peaks at around -0.3 V, 0.6 V and 1.16 V which correspond to Fe²⁺/Fe³⁺, V³⁺/V⁴⁺ and V⁴⁺/V⁵⁺ were observed, respectively. However, only one cathodic peak at ~0.43 V which corresponds to V³⁺/V⁴⁺ redox was observed in the first cycle. If the potential window is limited to Fe²⁺/Fe³⁺ and V³⁺/V⁴⁺ redox couples (-1.0 – 0.9 V), iron has a much more pronounced cathodic peak at ~-0.5 V and vanadium is much more stable during further cycling. If the potential window is set from 0 V to 1.4 V, the V⁴⁺/V⁵⁺ redox couple still showed response only in the anodic side for one cycle, and reversible redox peaks of V³⁺/V⁴⁺ degrade with every further cycle. The presence of only one cathodic peak in this potential window could also confirm the hypothesis of asymmetric and irreversible electrochemical reactions of V³⁺/V⁴⁺ and V⁴⁺/V⁵⁺.²³⁷ Moreover, if the potential window is limited only to separate Fe²⁺/Fe³⁺ (-1.0 – 0.2 V) or V³⁺/V⁴⁺ (0 – 0.9 V) windows, the peaks are reversible, well pronounced and very stable in both cases. All these results suggest that V⁴⁺/V⁵⁺ redox couple destabilizes this framework in aqueous media and will be excluded from the following investigation.

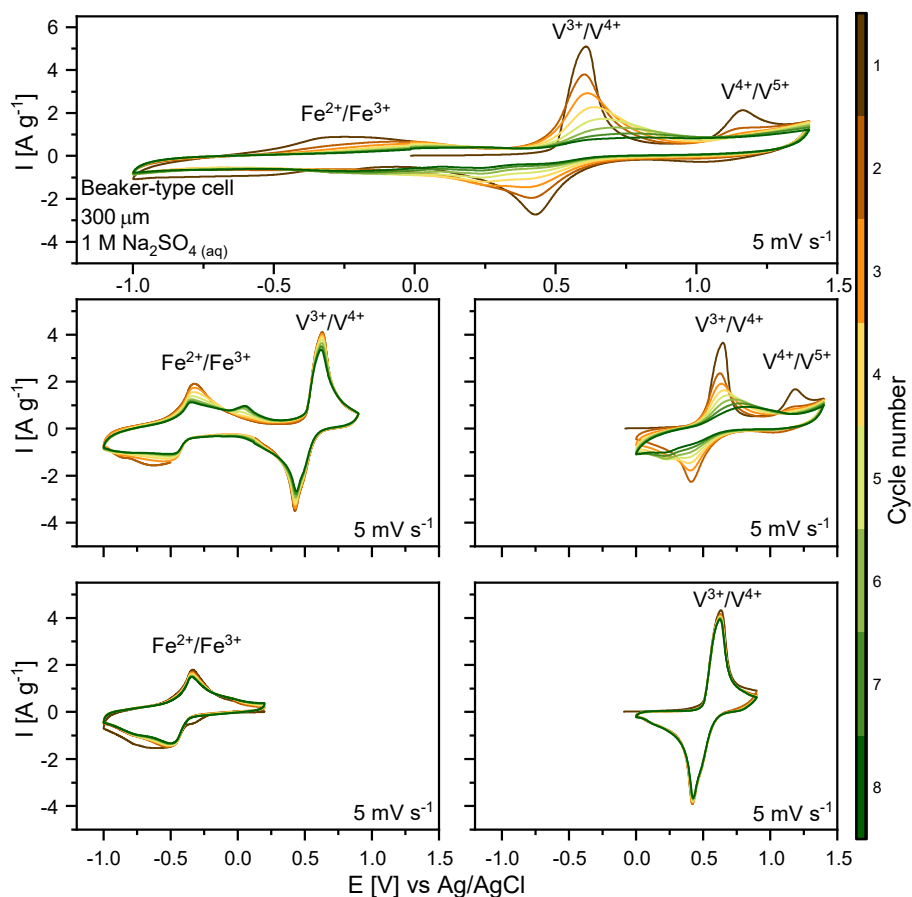


Fig. 114. Cyclic voltammograms of NVFP of different voltage windows recorded at 5 mV s^{-1} scan rate.

GCD cycling was used for estimating the specific discharge capacity and CE% of NVFP. First, GCD cycling for 100 cycles was performed for both $\text{Fe}^{2+}/\text{Fe}^{3+}$ and $\text{V}^{3+}/\text{V}^{4+}$ redox couples within the potential window of $-0.9 - 0.9 \text{ V}$ (Ag/AgCl) at 1C in aqueous electrolytes using Swagelok-type cells. The rate ($1\text{C} = 0.117 \text{ A g}^{-1}$) is calculated based on the theoretical capacity of NVFP for two electrons. Four different aqueous electrolytes: $1 \text{ M Na}_2\text{SO}_4$ (aq), 17 m NaClO_4 (aq), 8 m NaTFSI (aq), and $28 \text{ m KAc} + 8 \text{ m NaAc}$ (aq) were investigated (Fig. 115). The initial specific capacity and its retention after 100 cycles are 87.8 mAh g^{-1} and 7.5% in $1 \text{ M Na}_2\text{SO}_4$ (aq), 72.4 mAh g^{-1} and 38.6% in 17 m NaClO_4 (aq), 88.4 mAh g^{-1} and 16.6% in 8 m NaTFSI (aq), and 66.9 mAh g^{-1} and 14.6% for $28 \text{ m KAc} + 8 \text{ m NaAc}$ (aq). Fast degradation of the capacity was observed in all cases which is probably due to the dissolution of NVFP framework in aqueous media. However,

slightly better performance is achieved with concentrated 17 m NaClO_4 (aq) electrolyte which reduces the dissolution, as was also observed with NFPP and NVFP materials in previous studies. In all cases, two clear potential plateaus could be observed at around -0.43 V and 0.5 V which correspond to $\text{Fe}^{2+}/\text{Fe}^{3+}$ and $\text{V}^{3+}/\text{V}^{4+}$ redox, respectively, and agree well with those reported in literature.²³⁸

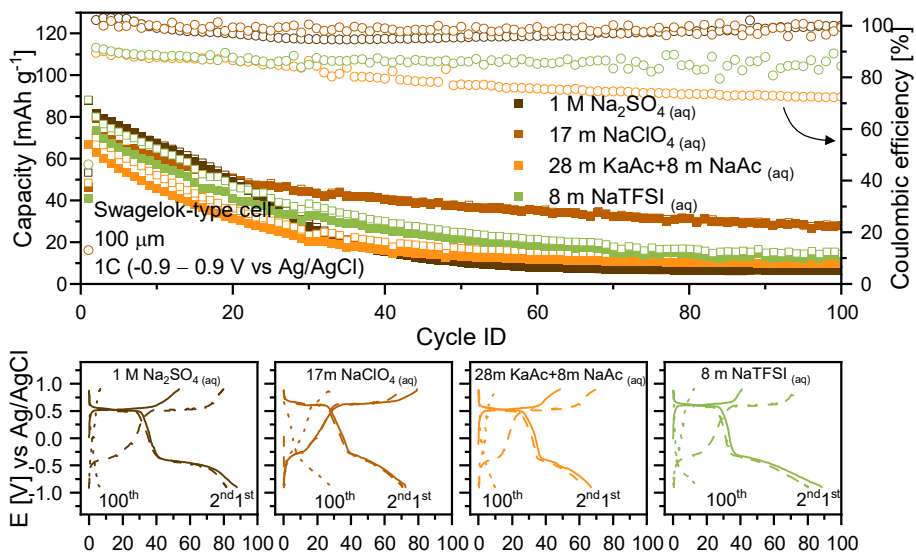


Fig. 115. GCD cycling of NVFP electrode ($\text{Fe}^{2+}/\text{Fe}^{3+} + \text{V}^{3+}/\text{V}^{4+}$) in different aqueous electrolytes at 1C.

GCD cycling of NVFP electrodes was also performed in 1 M Na_2SO_4 (aq) with different buffers such as 0.1 M citrate (pH = 4.0), 0.1 M phosphate (pH = 7.0) and 0.1 M borate (pH = 10.0) to investigate the influence of pH to materials electrochemical performance. 100 cycles were recorded for $\text{Fe}^{2+}/\text{Fe}^{3+}$ and $\text{V}^{3+}/\text{V}^{4+}$ redox couples within the potential window of -1.0 – 0.9 V (Ag/AgCl) at 1C using beaker-type cells. The results presented in Fig. 116 show rapid capacity degradation in acidic buffer, but slightly better retention in alkaline buffer.

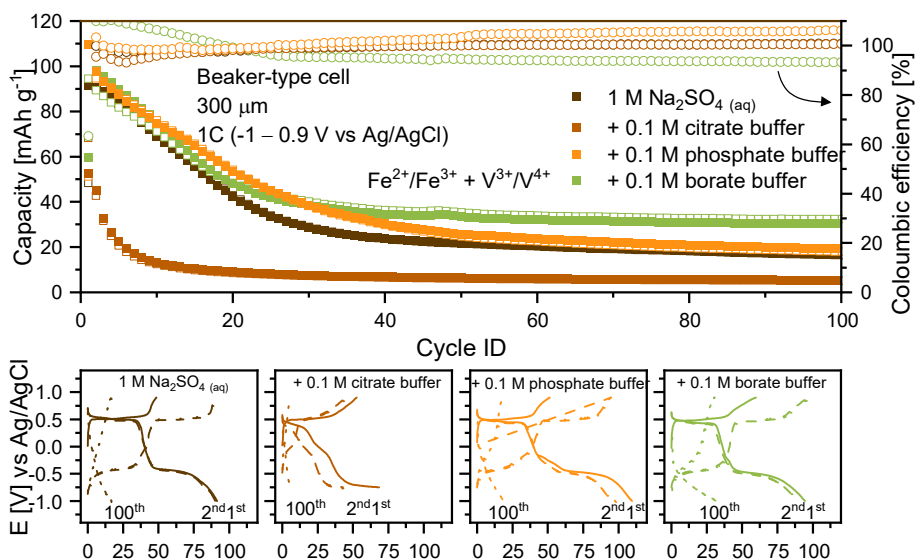


Fig. 116. GCD cycling of NVFP electrodes ($\text{Fe}^{2+}/\text{Fe}^{3+} + \text{V}^{3+}/\text{V}^{4+}$) in aqueous electrolytes with different pH at 1C.

The initial capacities of NVFP electrodes in all tested aqueous electrolytes (except acidic one) could be considered as sufficient for aqueous SIBs, however, they rapidly degrade in just ~ 20 cycles. In order to find out which redox couple ($\text{Fe}^{2+}/\text{Fe}^{3+}$ or $\text{V}^{3+}/\text{V}^{4+}$) is limiting or that both of them are not stable, GCD cycling was performed for each redox couple separately at different pH 1 M Na_2SO_4 (aq) electrolytes. 100 cycles were recorded within the potential window of $-1.0 - 0$ V ($\text{Fe}^{2+}/\text{Fe}^{3+}$) or $0.2 - 0.9$ V ($\text{V}^{3+}/\text{V}^{4+}$) at 1C ($1\text{C} = 0.059 \text{ A g}^{-1}$) using beaker-type cells. The results presented in Fig. 117 show that $\text{Fe}^{2+}/\text{Fe}^{3+}$ redox couple is considerably more stable at all pHs. However, the best result is achieved in an alkaline electrolyte, where the initial discharge capacity and its retention after 100 cycles were 48 mAh g^{-1} (theoretical 58.5 mAh g^{-1}) and 91.8%, respectively. On the other hand, vanadium results (Fig. 118) do not exhibit such stability. All electrolytes show much lower initial capacities ($16 - 39 \text{ mAh g}^{-1}$) and the best capacity retention after 100 cycles reached was only 20.1% with standard 1 M Na_2SO_4 (aq) electrolyte. All these results suggest that the stability limiting process is $\text{V}^{3+}/\text{V}^{4+}$ redox which lowers the total capacity of NVFP due to probably faster V dissolution. The same stability tendencies were also observed before in NFPP and NVPP, which confirms that iron is a more suitable transition metal than vanadium and manganese making it more suitable for aqueous SIBs.

NVFP shows much better potential as a suitable Na-ion battery positive material, but the mitigation of the dissolution should be considered and further developed.

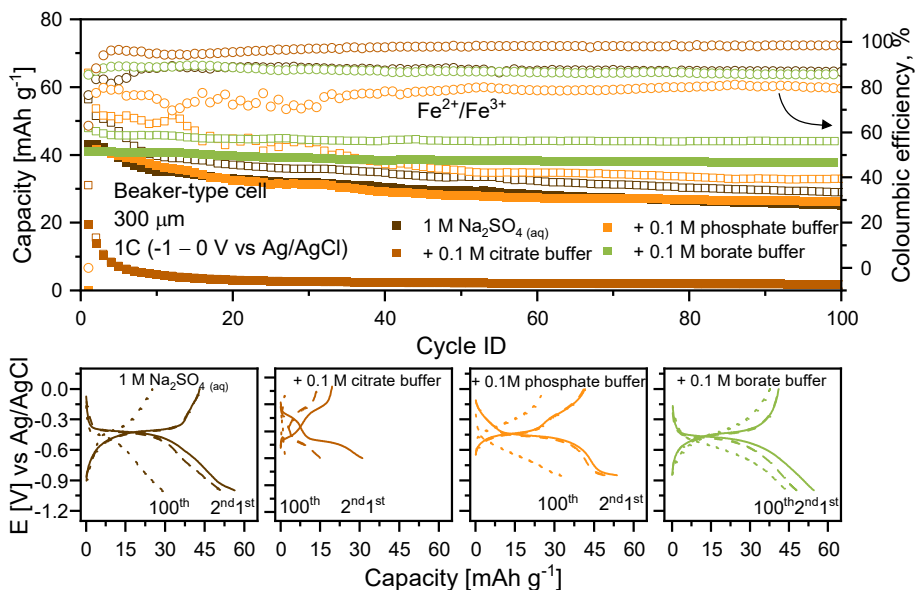


Fig. 117. GCD cycling of NVFP electrodes ($\text{Fe}^{2+}/\text{Fe}^{3+}$) in aqueous electrolytes at different pH at 1C.

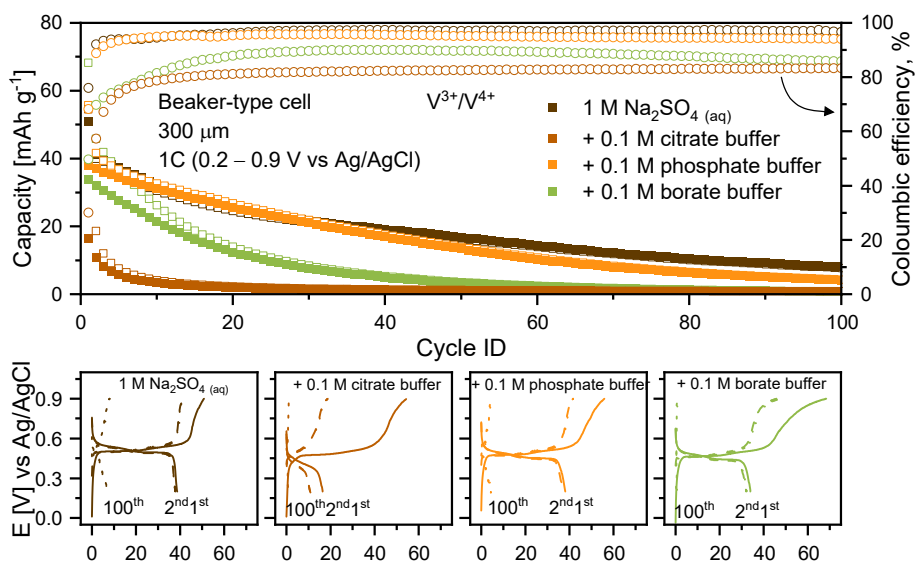


Fig. 118. GCD cycling of NVFP electrode ($\text{V}^{3+}/\text{V}^{4+}$) in aqueous electrolytes at different pH at 1C.

Electrochemical characterization of NVFP was additionally carried out in organic electrolytes in order to compare it with aqueous systems and to verify that the capacity loss is mainly related to the electrolyte and not the material itself. Fig. 119 shows CVs which were recorded in 1 M NaPF₆ in DG electrolyte at the scanning rate of 0.5 mV s⁻¹ within the potential window of 1.8 – 4.5 V vs Na⁺/Na using a Swagelok-type cell. No well pronounced reversible current peaks of Fe²⁺/Fe³⁺ could be found at around 2.4 V/2.6 V vs Na⁺/Na, while V³⁺/V⁴⁺ redox couple has very pronounced but not stable and shifting peaks at 3.4 V/3.5 V vs Na⁺/Na. Identically to aqueous electrolytes, the V⁴⁺/V⁵⁺ redox is observed only on the anodic side of the first cycle which suggests that this couple is not stable neither in aqueous nor in organic electrolytes.

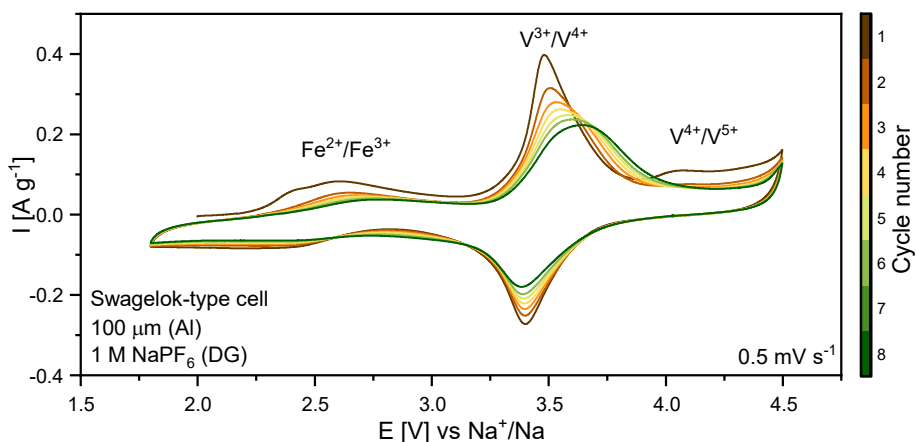


Fig. 119. Cyclic voltammograms of NVFP electrodes in organic electrolyte recorded at 5 mV s⁻¹ scan rate.

GCD measurements of NVFP electrodes for 3 electron process (Fe²⁺/Fe³⁺, V³⁺/V⁴⁺ and V⁴⁺/V⁵⁺) were performed for 300 cycles within the potential window from 2.0 to 4.4 V vs Na⁺/Na at 1C with 1 M NaPF₆ in EC:DEC (3:7 vol%) and 1 M NaPF₆ in DG electrolytes using Swagelok-type cells (Fig. 120). The results in DG electrolyte indicate slightly more stable electrochemical performance than a mixture of EC:DEC. It could be attributed to the different chemical composition, narrower distribution, thickness, and stability of the solid electrolyte interphase on Na and the positive electrode formed in DG electrolyte.¹⁵⁶ The initial discharge capacity, CE% and capacity retention after 100 cycles in DG electrolyte were 98.5 mAh g⁻¹, 98.6% and 58.3%, respectively, which is only slightly better than the results in aqueous

media. In the first cycles, three charging and only two discharging voltage plateaus could be observed which confirms asymmetrical Na ion insertion/deinsertion mechanism.

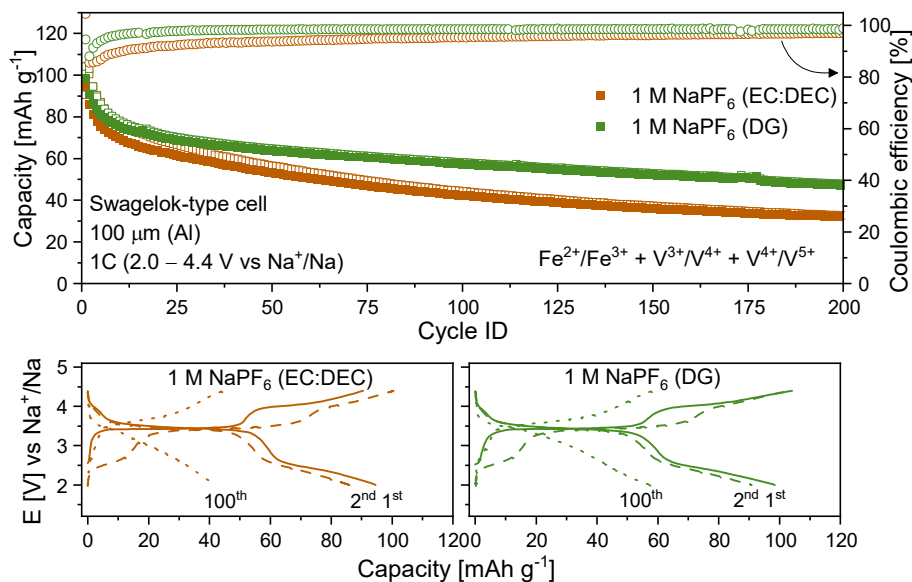


Fig. 120. GCD cycling of NVFP electrode ($\text{Fe}^{2+}/\text{Fe}^{3+} + \text{V}^{3+}/\text{V}^{4+}$) in different organic electrolytes at 1C.

However, low initial capacity and its retention could also suggest that this framework is not stable for full potential range and redox couple of $\text{V}^{4+}/\text{V}^{5+}$ could destabilize the material. In order to determine the stability limitation, GCD cycling was also performed for different combinations of redox couples in 1 M NaPF₆ in DG electrolyte for 250 cycles at 1C rate using Swagelok-type cells. First, the pairs of $\text{Fe}^{2+}/\text{Fe}^{3+}$ and $\text{V}^{3+}/\text{V}^{4+}$ were tested within the potential window of 2.0 – 3.8 V vs Na⁺/Na. The results in Fig. 121 (dark brown) show a more stable performance than previously in the full potential window, the initial discharge capacity, CE% and capacity retention after 100 cycles are 79.5 mAh g⁻¹ (theoretical is 117 mAh g⁻¹), 96.2% and 98.8%, respectively. If the potential is limited to 3.0 – 4.4 V for $\text{V}^{3+}/\text{V}^{4+}$ and $\text{V}^{4+}/\text{V}^{5+}$ (Fig. 121 (brown)), the initial discharge capacity, CE% and capacity retention after 100 cycles are 52.8 mAh g⁻¹ (theoretical is 117 mAh g⁻¹), 95.7% and 77.7%, respectively. Although, the first charging capacity of 95.8 mAh g⁻¹ drops after two cycles down to 54 mAh g⁻¹, this indicates that $\text{V}^{4+}/\text{V}^{5+}$ is active only in the first charging cycle and all of its capacity comes from the redox couple of

V^{3+}/V^{4+} only. This is also confirmed by GCD cycling of only V^{3+}/V^{4+} couple within the potential window of 3.0 – 3.8 V (Fig. 121 (orange)), with the capacity results identical to the previous ones. On the other hand, if the potential is limited to 2.0 – 3.0 V (Fig. 121 (light green)), only the Fe^{2+}/Fe^{3+} couple is active. The initial discharge capacity, CE% and capacity retention after 100 cycles were 33.6 mAh g⁻¹ (theoretical is 58.5 mAh g⁻¹), 99.8% and 92.4%, respectively. All of the obtained results suggest that V^{4+}/V^{5+} redox process destabilizes the NVFP framework in organic electrolytes, but vanadium shows better electrochemical performance than iron even if both of them are very stable separately.

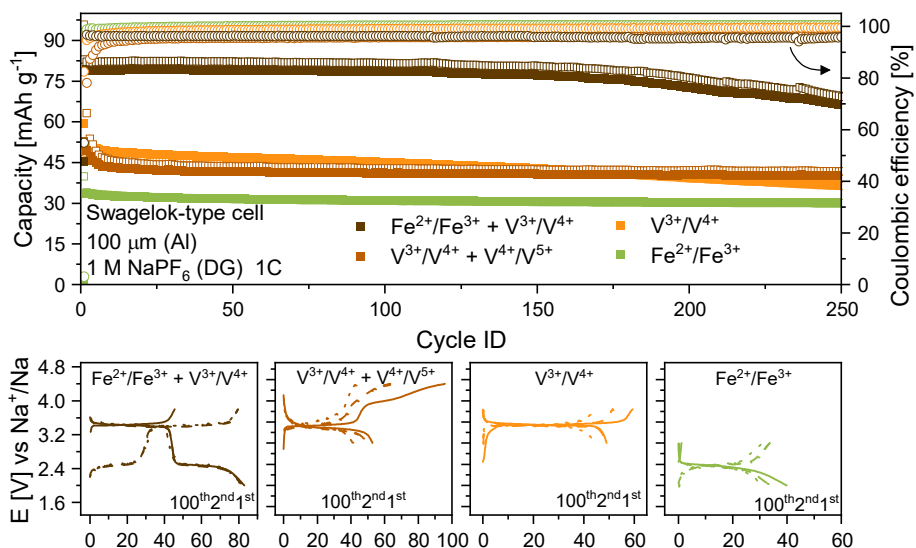


Fig. 121. GCD cycling of NVFP electrodes at different voltage windows in organic electrolyte at 1C.

The C-rate capability (0.1 – 20C) of NVFP with DG electrolyte was investigated for two (Fe^{2+}/Fe^{3+} , V^{3+}/V^{4+}) and for all three redox couples (Fe^{2+}/Fe^{3+} , V^{3+}/V^{4+} and V^{4+}/V^{5+}). In the case of Fe^{2+}/Fe^{3+} and V^{3+}/V^{4+} (Fig. 122a), the initial discharge capacity at 0.1C rate is 89.3 mAh g⁻¹, which decreases to 31.8 mAh g⁻¹ at 20C and is almost fully recovered to 84.6 mAh g⁻¹ after the rate was switched back to 0.1C. This indicates a sufficient rate capability of NVFP in organic electrolytes. The results in Fig. 122b confirm that the second V^{4+}/V^{5+} redox couple clearly destabilizes the NVFP framework and its charge capacity. On the other hand, the initial charge capacity when C-rate is 0.1C reaches 165 mAh g⁻¹ which is close to the

theoretical value. However, this value decreases in every cycle and does not recover back after high C-rate testing.

Overall, NVFP seems to be a potential suitable electrode material for aqueous SIBs. However, some additional understanding of its degradation mechanism and designing of an appropriate prevention strategy is still needed. Additionally, it is an outstanding positive electrode for organic SIBs if V^{4+}/V^{5+} redox is avoided.

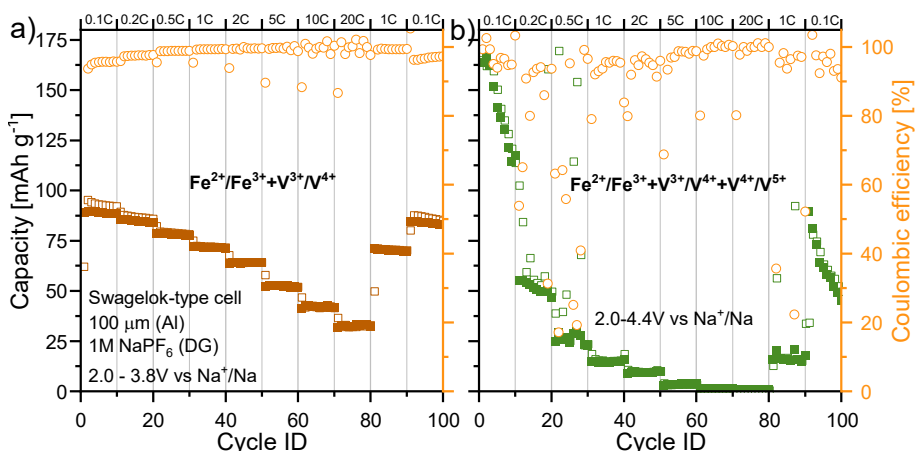


Fig. 122. Rate capability of GCD cycling of NVFP in organic DG electrolyte a) for Fe^{2+}/Fe^{3+} and V^{3+}/V^{4+} and b) for Fe^{2+}/Fe^{3+} , V^{3+}/V^{4+} and V^{4+}/V^{5+} .

3.5.5. Summary

Na₃VFe(PO₄)₃ was successfully synthesized via a conventional solid-state method. The obtained particles are of irregular shape and a few micrometers in size. The materials were additionally coated with a carbon layer by pyrolysis of citric acid.

Na₃VFe(PO₄)₃ exhibits limited electrochemical stability when all three redox couples (Fe^{2+}/Fe^{3+} , V^{3+}/V^{4+} , and V^{4+}/V^{5+}) are simultaneously utilized irrespective of aqueous or organic electrolytes. V^{4+}/V^{5+} redox couple causes phosphate framework destabilization and capacity loss, likely due to V dissolution. Fe^{2+}/Fe^{3+} couple is much more stable than V^{3+}/V^{4+} couple in aqueous electrolytes.

Na₃VFe(PO₄)₃ shows a decent potential as a suitable electrode material for aqueous SIBs. However, additional mechanistic understanding of degradation processes and application of appropriate prevention means are still need for a successful utilization of this material in batteries.

4. CONCLUSIONS

☐ **NaTi₂(PO₄)₃** nanoparticles could be successfully prepared by hydro(solvo)thermal synthesis method. The synthesis temperature affects particle size but not the phase purity. The appropriate choice of synthesis media such as alcohol-water mixtures allows for a careful control and engineering of nanoparticle morphology. Nanoparticles with irregular shapes and ample surface defects result in reduced initial capacities and faster capacity fade.

☐ The irreversible capacity loss of **NaTi₂(PO₄)₃** in aqueous electrolytes during cycling is linked to its electrochemically-induced degradation. This is especially pronounced at low charging/discharging rates. Oxygen reduction induced self-discharge and local pH increase is indicated as the leading cause of **NaTi₂(PO₄)₃** degradation. The capacity loss was correlated to the amount of phosphorus dissolved in the electrolyte but not with that of titanium. This indicates the formation of Ti-rich interphasial layer on the particle surface. Overall **NaTi₂(PO₄)₃** is a suitable negative electrode material for aqueous and non-aqueous Na-ion batteries.

☐ Manganese-based **Na₄Mn₃(PO₄)₂P₂O₇** and **Na₃MnPO₄CO₃** could be successfully prepared by conventional solid-state and hydrothermal methods, respectively. The optimal synthesis conditions and precursor ratios are suggested. However, **Na₄Mn₃(PO₄)₂P₂O₇** and **Na₃MnPO₄CO₃** materials demonstrated limited electrochemical activity in both aqueous and organic electrolytes, with very fast capacity loss. This is likely due to electrochemically-induced materials dissolution and aqueous stability of Mn²⁺ species. The results indicate that these materials are not suitable as Na-ion battery positive electrodes neither in aqueous not organic electrolytes.

☐ **Na₃Fe₂(PO₄)₃** could be successfully prepared by solid-state method with irregular particle morphology. It also showed relatively poor electrochemical performance even with low initial capacity making it an unsuitable electrode material for aqueous Na-ion batteries. In contrast, **Na₄Fe₃(PO₄)₂P₂O₇** could be prepared via solid-state and sol-gel methods and shows promising electrochemical characteristics. However, it still suffers from electrochemical degradation likely associated to iron dissolution and/or instability of the mixed phosphate-pyrophosphate framework. In order to enable its application in aqueous environments, mitigation strategies such as electrolyte additives or protective layers are necessary. Nevertheless, this

material showcased exceptional cycling stability and rate capability in organic electrolytes. $\text{Na}_{2-x}\text{Fe}[\text{Fe}(\text{CN})_6] \cdot y\text{H}_2\text{O}$ Prussian Blue Analogues could be successfully prepared by hydrothermal and co-precipitation methods. They adopt different crystalline phases depending on the synthesis temperature, media and drying conditions. The results demonstrate the superior electrochemical performance of this material for one-electron process in aqueous electrolytes and for two-electron process in organic electrolytes. These materials serve as versatile and suitable positive electrode materials for both aqueous and non-aqueous Na-ion batteries.

▣ $\text{Na}_7\text{V}_4(\text{PO}_4)(\text{P}_2\text{O}_7)_4$ could be successfully prepared using by solid-state method. The electrodes made from $\text{Na}_7\text{V}_4(\text{PO}_4)(\text{P}_2\text{O}_7)_4$ show relatively poor performance in aqueous electrolytes, likely due to degradation caused by the dissolution of V^{4+} into the electrolyte. This points to the need of additional stabilization strategies for preventing such dissolution. However, these electrodes demonstrated very good electrochemical performance, including initial capacity, its retention, and rate capability in organic electrolytes, making them suitable as non-aqueous Na-ion battery positive electrodes.

▣ Mixed transition metal based $\text{Na}_3\text{VFe}(\text{PO}_4)_3$ could be successfully prepared by conventional solid-state method. The electrochemical characterization reveals that $\text{Na}_3\text{VFe}(\text{PO}_4)_3$ is not very stable when all three redox couples ($\text{Fe}^{2+}/\text{Fe}^{3+}$, $\text{V}^{3+}/\text{V}^{4+}$, and $\text{V}^{4+}/\text{V}^{5+}$) are utilized irrespective of aqueous or organic electrolytes. The activation of $\text{V}^{4+}/\text{V}^{5+}$ redox couple destabilizes the phosphate framework, leading to possible vanadium dissolution. In contrast, the $\text{Fe}^{2+}/\text{Fe}^{3+}$ redox couple alone without the activation of $\text{V}^{3+}/\text{V}^{4+}$ exhibits much greater stability in aqueous electrolytes. This makes $\text{Na}_3\text{VFe}(\text{PO}_4)_3$ a potentially suitable candidate electrode material for aqueous Na-ion batteries. Nevertheless, the challenges associated with electrochemical degradation must still be further addressed for practical applications.

SANTRAUKA

1. Įvadas

Intensyviai augantis elektros energijos poreikis skatina ieškoti naujų ir efektyvių būdų atsinaujinančios energijos saugojimui. Elektrocheminės baterijos šiuo metu yra laikomos viena iš patraukliausių technologijų, jos pasižymi aukštu energijos vartojimo efektyvumu, mažu poveikiu aplinkai, lengvu matmenų keitimu ir, svarbiausia, plačiu galios ir energijos intervalu. Šiuo metu plačiausiai naudojamos ličio jonų baterijos (LIBs), pasižyminčios išskirtiniais energijos ir galios tankiais, tačiau aukšta ir nuolat kintanti ličio bei kai kurių kitų būtinų pereinamųjų metalų kaina, o taip pat jose naudojami labai degūs organiniai elektrolitai skatina ieškoti naujų ir tvaresnių alternatyvų energijos saugojimui.¹ Natrio jonų baterijos (SIBs), ypač naudojančios vandeninius elektrolitus, kelia vis didesnę susidomėjimą kaip stacionarios energijos kaupimo sistemos, kadangi jos yra žymiai saugesnės, nedegios, draugiškesnės aplinkai, lengviau utilizuojamos bei perdirbamos ir, žinoma, pigesnės nei LIB dėl neribotų natrio išteklių.²⁻⁴

Daugybė įvairių medžiagų yra plačiai tyrinėjamos kaip vandeninių SIBs elektrodų aktyviosios medžiagos. Jos gali būti suskirstytos į šias pagrindines grupes: sluoksniuotieji oksidai, NASICON-struktūros polianijoniniai junginiai ir prūsų mėlio analogai. Nors dauguma šių junginių pasižymi vertingomis elektrocheminėmis savybėmis, tačiau pagrindinės problemos, kurias būtina ištirti, suprasti ir išspręsti, yra susiję su prastu stabilumu įkrovimo/iškrovimo ciklinimo metu, mažu energijos tankiu bei žema baterijų įtampa, kurias būtina ištirti, suprasti ir išspręsti.⁵

Šios disertacijos **pagrindinis tikslas** - surasti, susintetinti ir ištirti naujas karkasines elektrodų medžiagas, tinkamas vandeninėms natrio jonų baterijoms. Darbo **naujumas** susijęs su tuo, kad dauguma šiame darbe analizuojamų junginių iki šiol buvo mažai tyrinėti ir dažniausiai kaip organinių Na⁺ jonų baterijų elektrodų aktyviosios medžiagos. Tikslui įgyvendinti buvo suformuluoti šie **uždaviniai**:

▣ Paruošti **NaTi₂(PO₄)₃** ir ištirti sintezės parametrų įtaką medžiagos fazės grynumui bei morfologijai; ištirti šios medžiagos elektrochemines savybes ir degradacijos procesą įvairiuose vandeniniuose elektrolituose, panaudojant ciklinę voltamperometriją, galvanostatinę įkrovimo/iškrovimo ciklinimą ir elementinę analizę, bei palyginti jas su rezultatais, gautais organiniame elektrolite.

▣ Susintetinti bei charakterizuoti **Na₄Mn₃(PO₄)₂(P₂O₇)** ir **Na₃MnPO₄CO₃** medžiagas; ištirti šių medžiagų elektrochemines savybes

įvairiuose vandeniniuose panaudojant ciklinę voltamperometriją ir galvanostatinį įkrovimo/iškrovimo ciklinimą bei palyginti jas su rezultatais, gautais organiniame elektrolite.

▣ Susintetinti bei charakterizuoti $\text{Na}_3\text{Fe}_2(\text{PO}_4)_3$, $\text{Na}_4\text{Fe}_3(\text{PO}_4)_2(\text{P}_2\text{O}_7)$ ir $\text{Na}_{2-x}\text{Fe}[\text{Fe}(\text{CN})_6]\cdot y\text{H}_2\text{O}$ medžiagas, ištirti šių medžiagų elektrochemines savybes įvairiuose vandeniniuose elektrolituose panaudojant ciklinę voltamperometriją ir galvanostatinį įkrovimo/iškrovimo ciklinimą bei palyginti jas su rezultatais, gautais organiniame elektrolite.

▣ Susintetinti bei charakterizuoti $\text{Na}_7\text{V}_4(\text{PO}_4)(\text{P}_2\text{O}_7)_4$ medžiagą; ištirti šios medžiagos elektrochemines savybes įvairiuose vandeniniuose elektrolituose panaudojant ciklinę voltamperometriją ir galvanostatinį įkrovimo/iškrovimo ciklinimą bei palyginti jas su rezultatais, gautais organiniame elektrolite.

▣ Susintetinti bei charakterizuoti $\text{Na}_3\text{VFe}(\text{PO}_4)_3$ medžiagą, ištirti šios medžiagos elektrochemines savybes įvairiuose vandeniniuose elektrolituose panaudojant ciklinę voltamperometriją ir galvanostatinį įkrovimo/iškrovimo ciklinimą bei palyginti jas su rezultatais, gautais organiniame elektrolite.

Ginamieji šios disertacijos teiginiai yra:

▣ $\text{NaTi}_2(\text{PO}_4)_3$ gali būti susintetintas su skirtingais tirpikliais (įvairūs alkoholiai ir jų mišiniai su vandeniu) hidro(solvo)terminiu metodu. Vandens aktyvumas yra pagrindinis parametras įtakojantis NTP fazės grynumą, nanodalelių morfologiją ir dydį. Negrįžtama NTP elektrodų talpos degradacija vandeniuose elektrolituose yra susijusi su elektrochemiškai inicijuotu cheminiu aktyviosios medžiagos tirpimu.

▣ $\text{Na}_4\text{Mn}_3(\text{PO}_4)_2(\text{P}_2\text{O}_7)$ ir $\text{Na}_3\text{MnPO}_4\text{CO}_3$ gali būti susintetinami kietafazės ir hidroterminiu metodais, atitinkamai. Šios Mn turinčios medžiagos pasižymi labai ribotu elektrocheminiu aktyvumu vandeniniuose elektrolituose.

▣ $\text{Na}_3\text{Fe}_2(\text{PO}_4)_3$ gali būti susintetintas kietafazės metodu, tačiau ši medžiaga pasižymi ribotu elektrocheminiu aktyvumu vandeniniame elektrolite. $\text{Na}_4\text{Fe}_3(\text{PO}_4)_2(\text{P}_2\text{O}_7)$ gali būti susintetintas kietafazės ir zolių-gelių metodais. Nors ši medžiaga pasižymi pakankamai geromis pradinėmis talpomis, tačiau joms yra būdinga elektrocheminė degradacija. Skirtingos $\text{Na}_{2-x}\text{Fe}[\text{Fe}(\text{CN})_6]\cdot y\text{H}_2\text{O}$ fazės gali būti susintetintos hidroterminiu arba išsodinimo metodais priklausimai nuo sintezės temperatūros, pradinių medžiagų ir džiovavimo sąlygų. Monoklininė fazė pasižymi puikiu elektrocheminiu stabilumu rūgštiniame vandeniniame elektrolite.

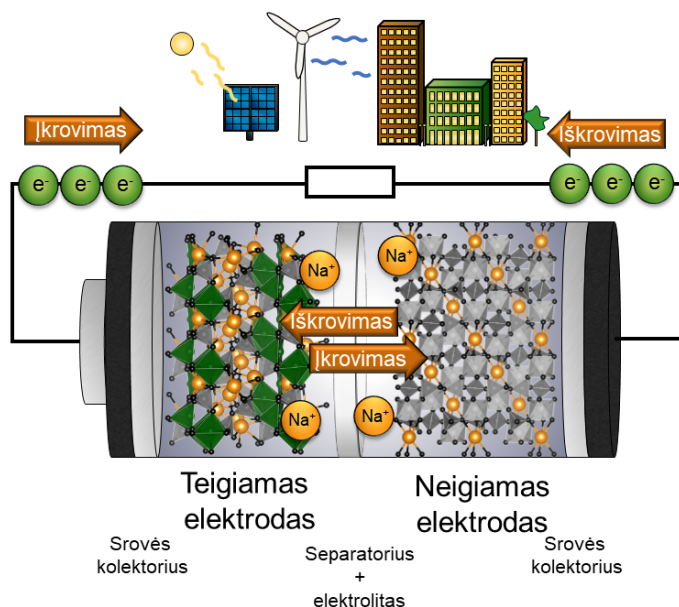
■ $\text{Na}_7\text{V}_4(\text{PO}_4)(\text{P}_2\text{O}_7)_4$ gali būti susintetintas kietafazės metodu, tačiau ši medžiaga pasižymi labai ribotu elektrocheminiu aktyvumu vandeniniuose elektrolituose.

■ $\text{Na}_3\text{VFe}(\text{PO}_4)_3$ gali būti susintetintas kietafazės metodu. Ši medžiaga pasižymi pakankamai geromis pradinėmis talpomis kai aktyvios yra tik $\text{Fe}^{2+}/\text{Fe}^{3+}$ ir $\text{V}^{3+}/\text{V}^{4+}$ redukcijos-oksidacijos poros, kadangi $\text{V}^{4+}/\text{V}^{5+}$ aktyvavimas destabilizuoja struktūrą.

2. Literatūros apžvalga

Elektrocheminė baterija, kurią 1800-aisiais išrado A. Volta,¹⁵ itin efektyviai per oksidacijos-redukcijos reakcijas konvertuoja cheminę energiją į elektros energiją.¹⁶ Baterija dažniausiai susideda iš keleto tarpusavyje sujungtų elektrocheminių vienetų – celių, taip gaunant didesnę bendrą talpą ir įtampą. Pagrindinės celės sudedamosios dalys yra neigiamas ir teigiamas elektrodai bei elektrolitas (jonų laidininkas).^{17, 18}

Natrio jonų baterijos veikimo schema yra pateikta 123 pav.: iškrovimo metu, neigiamas elektrodas yra oksiduojamas ir atiduoda elektronus išorinei grandinei, o teigiamas elektrodas juos priima ir yra redukuojamas. Tuo pačiu metu elektrolite esantys jonai keliauja link elektrodų, kad būtų išlaikomas sistemos elektrinis neutralumas: katijonai juda link neigiamai poliarizuoto teigiamo elektrodo, o anijonai priešingai. Įkrovimo metu oksidacijos-redukcijos reakcijos vyksta atvirkščiai. Bendra celės įtampa priklauso nuo cheminio potencialo skirtumo tarp neigiamo ir teigiamo elektrodų medžiagų.¹⁶ Priklausomai nuo elektrocheminių reakcijų grįžtamumo celės yra skirstomos į pirmines (neįkraunamos arba vienkartinės) ir antrines (įkraunamos arba daugkartinės).^{16, 17}



123 pav. Natrio jonų baterijos veikimo schema

Pakraunamos baterijos yra naudojamos įvairiausių srityse: elektrinėse transporto priemonėse, nešiojamuose elektros įrenginiuose, stacionariuose ar nešiojamuose elektros energijos saugyklose ir kt.. Dėl unikalių elektrocheminių savybių rinkoje šiuo metu dominuoja LIB, tačiau ribotas ličio prieinamumas, kylanti žaliavų, kaina, didėjantys saugumo bei aplinkosaugos reikalavimai skatina ieškoti alternatyvių technologijų.³⁶

Na^+ , K^+ , Mg^{2+} , Ca^{2+} , Al^{3+} ir Zn^{2+} jonų baterijos dėl daug didesnio medžiagų prieinamumo ir mažesnės kainos kelia didelį susidomėjimą kaip potencialios LIB alternatyvos.⁴¹ Ypatingas dėmesys skiriamas SIB. Natrius yra antrasis pagal lengvumą šarminis metalas po ličio, o elektrocheminis Na^+/Na potencialas yra tik 0,3 V mažesnis už Li^+/Li .⁴² Nors žemas energijos tankis, ribotas įkrovimo greičio pasirinkimas ir pakankamai trumpas tarnavimo laikas riboja SIB pritaikymą nešiojamuosiuose prietaisuose ar elektrinėse transporto priemonėse, tačiau jos puikiai tinka stacionariam elektros energijos saugojimui, kur baterijos dydis ir svoris nėra tokie svarbūs kaip kaina ir draugiškumas aplinkai.⁴⁶

Elektrodų aktyviosios medžiagos yra esminės celės sudedamosios dalys, nes būtent nuo jų priklauso baterijos našumas, bendroji talpa, įtampa, energijos tankis, kaina ir saugumas, todėl daug dėmesio skiriama šių medžiagų paieškai ir tyrimams. Neigiamiems elektrodams gali būti

naudojama anglis, titano junginiai ir lydiniai, o teigiamiems - sluoksniuotieji oksidai, polianijoniniai junginiai ir Prūsų mėlio analogai.⁵

Ne mažiau svarbus ir elektrolitas, kuris užtikrina efektyvią jonų (Na^+) pernašą tarp elektrodų. Elektrolitas turi pasižymėti aukštu joniniu ir žemu elektroniniu laidumu, plačiu elektrocheminio stabilumo langu, cheminiu stabilumu ir terminiu stabilumu, inertiškumu kitiems celės komponentams, kuo mažesniu toksiškumu bei, pageidautina, maža kaina.^{86, 87} SIB sistemose naudojami elektrolitai pagal savo prigimtį yra skirstomi į vandeninius, organinius,⁸⁸ joninius skysčius,⁸⁹ kietafazius,⁹⁰ ir hibridinius.⁹¹ Nors dėl plataus elektrocheminio stabilumo lango (iki 4 V) dažniausiai naudojami organiniai elektrolitai, tačiau jie yra labai toksiški, degūs ir brangūs.⁸⁶ Tuo tarpu vandeniniai elektrolitai yra daug saugesni, nedegūs, pigesni, lengvai utilizuojami ir pasižymi aukštesniu joniniu laidumu nei organiniai.⁹² Pagrindinis vandeninių tirpalų trūkumas - pakankamai siauras elektrocheminio stabilumo langas (gryno H_2O $\sim 1,23$ V), kurį sąlygoja vandens oksidacijos ir redukcijos reakcijos.⁹³ Tam tikrų druskų ar tiesiog didesnių jų koncentracijų naudojimas gali šiek tiek praplėsti stabilumo ribas.⁹⁵ Kita nemažiau svarbi problema yra ribotas cheminis ir elektrocheminis medžiagų stabilumas vandeniniuose elektrolituose. Kai kurios elektrodų medžiagos pasižymi puikiu elektrocheminiu aktyvumu organiniame elektrolite, tačiau vandenyje jos yra linkusios tirpti, o tai skatina talpos degradaciją.^{96, 97} Todėl renkantis aktyviasias medžiagas ir elektrolitą reikalingi išsamūs tyrimai.

3. Eksperimentiniai metodai

Šiame darbe buvo tiriamos $\text{NaTi}_2(\text{PO}_4)_3$, $\text{Na}_4\text{Mn}_3(\text{PO}_4)_2\text{P}_2\text{O}_7$, $\text{Na}_3\text{MnPO}_4\text{CO}_3$, $\text{Na}_3\text{Fe}_2(\text{PO}_4)_3$, $\text{Na}_4\text{Fe}_3(\text{PO}_4)_2\text{P}_2\text{O}_7$, $\text{Na}_{2-x}\text{Fe}[\text{Fe}(\text{CN})_6] \cdot y\text{H}_2\text{O}$, $\text{Na}_7\text{V}_4(\text{PO}_4)(\text{P}_2\text{O}_7)_4$ ir $\text{Na}_3\text{VFe}(\text{PO}_4)_3$ medžiagos, kurių sintezės yra apibendrintos 1 lentelėje. Dalelių dydžio pasiskirstymo suvienodinimui visi mėginiai po sintezių buvo sumalami, naudojant planetarinį malūną (350 rpm, 2 h). Taip pat, elektroniniam laidumui pagerinti, priklausomai nuo medžiagos terminių savybių, kai kurie mėginiai buvo papildomai dengiami anglies sluoksniu pirolizės metodu.

Visi susintetinti mėginiai buvo tiriami Rentgeno spindulių difrakcijos (Rigaku MiniFlex II, Bruker Phaser D2 ir Bruker Advance D8), skenuojančios elektroninės mikroskopijos (Hitachi SU-70, Helios Nanolab 650, FEI ir Hitachi TM4000Plus) ir terminės analizės metodais (STA600 PerkinElmer). Kai kurios medžiagos buvo papildomai analizuotos peršviečiamąja elektronine mikroskopija (Tecnai G2 F20 X-TWIN, FEI), dalelių paviršiaus

ploto analizatoriumi (BET, Anton Paar Brunauer-Emmett-Teller) ir induktyviai susietos plazmos optinės emisijos spektroskopija.

1 lentelė. Darbe tiriamų medžiagų sintezės metodų apibendrinimas

Medžiaga	Sintezės metodas	Dengimas anglimi
$\text{NaTi}_2(\text{PO}_4)_3$	hidro(solvo)terminė	30% citrinos rūgštis
$\text{Na}_4\text{Mn}_3(\text{PO}_4)_2\text{P}_2\text{O}_7$	kietafazė	30% gliukozė
$\text{Na}_3\text{MnPO}_4\text{CO}_3$	hidroterminė	-
$\text{Na}_3\text{Fe}_2(\text{PO}_4)_3$	kietafazė	30% citrinos rūgštis
$\text{Na}_4\text{Fe}_3(\text{PO}_4)_2\text{P}_2\text{O}_7$	kietafaze ir zolių-gelių	30% gliukozė, -
$\text{Na}_{2-x}\text{Fe}_2(\text{CN})_6 \cdot y\text{H}_2\text{O}$	hidroterminė ir išsodinimo	-
$\text{Na}_7\text{V}_4(\text{PO}_4)(\text{P}_2\text{O}_7)_4$	kietafazė	30% citrinos rūgštis
$\text{Na}_3\text{VFe}(\text{PO}_4)_3$	kietafazė	30% citrinos rūgštis

Iš susintetintų ir charakterizuotų miltelių malūno pagalba buvo paruošta suspensija, susidedanti iš 70 % aktyviosios medžiagos, 20 % anglies ir 10 % rišiklio (PVDF), kuri ruošiant darbinius elektrodus 100 – 300 μm storio sluoksniu buvo užtepama ant aliuminio folijos. Dėl nepakankamos adhezijos tarp aliuminio folijos ir darbinio elektrodo kompozito vandeniniuose elektrolituose, gauta plėvelė buvo perkeliama ant nerūdijančio plieno tinklelio, naudojant hidraulinį presą.

Paruoštų elektrodų elektrocheminės savybės įvairiuose vandeniniuose (1 M Na_2SO_4 , 17 m NaClO_4 , 8 m NaTFSI , 28 m KAc + 8 m NaAc) ir organiniuose (1 M NaPF_6 (DG, EC:PC, EC:DEC)) elektrolituose buvo charakterizuojamos naudojant ciklinės voltamperometrijos (SP-240, Biologic ir PGSTAT-302 Metrohm Autolab) ir galvanostatinio įkrovimo/iškrovimo metodus (MACCOR, Series 4000 ir Neware CT-4008).

4. Rezultatai ir jų aptarimas

4.1. $\text{NaTi}_2(\text{PO}_4)_3$

$\text{NaTi}_2(\text{PO}_4)_3$ (NTP) medžiaga susintetinta hidro(solvo)terminiu metodu. Buvo tiriama sintezės parametų įtaka medžiagos fazinei sudėčiai ir morfologijai. Pirmiausia buvo nustatyta, jog sintezės temperatūra (120 – 220 $^\circ\text{C}$) neturi įtakos medžiagos grynumui ir visais atvejais gaunama aukšto kristališkumo NTP fazė, tačiau didėjanti temperatūra įtakojo didesnių kubinės formos nanodalelių formavimąsi (120 $^\circ\text{C}$ - ~60 nm, 220 $^\circ\text{C}$ – ~142 nm). Taip pat buvo tiriama sintezėje naudojamo tirpiklio įtaka

medžiagos fazinei sudėčiai ir morfologijai. Tyrimams pasirinkti šie tirpikliai: metanolis (MeOH), etanolis (EtOH), 1-propanolis (1-PrOH), 2-propanolis (2-PrOH), etilenglikolis (EG) ir jų mišiniai su vandeniu, naudojant 5:0, 4:1, 2:3 ir 3:2 alkoholio su vandeniu tūrinius santykius. Nustatyta, jog sintetinant gryname alkoholyje gaunam gryna NTP fazė, o papildomas H₂O kiekis įtakoja α -Ti(HPO₄)₂·H₂O priemaišos formavimąsi. MeOH atveju ši papildoma fazė pradėjo formuotis esant 2:3 mišiniui, EtOH – 3:2, 1-PrOH – 4:1, 2-PrOH ir EG – 3:2, o toliau didėjantis vandens kiekis augino net tik šios priemaišos kiekį, bet ir NTP dalelių dydį. Naudoti alkoholiai ir jų mišiniai su vandeniu formavo skirtingos morfologijos nanodaleles, pvz., gryno EG atveju buvo gautos sferinės ir mažiausios (~58 nm) dalelės, o MeOH – kubinės. Prieita išvados, kad toks skirtingas dalelių formos ir fazės formavimasis priklauso nuo vandens aktyvumo naudotuose tirpikliuose. Taip pat buvo išmatuotas visų mėginių paviršiaus plotas ir anglies kiekis po papildomos pirolizės.

NTP elektrodų elektrocheminės savybės buvo ištirtos 1 M Na₂SO₄ (aq) elektrolite užrašant ciklines voltamperogramas. Jose matomos NTP būdingos katodinė ir anodinė smailės (ties -1,0 V/-0,6 V (Ag/AgCl), atitinkamai), priskiriamos grįžtamai Ti³⁺/Ti⁴⁺ oksidacijai – redukcijai. Pastebėta, jog mėginiai, kurių dalelės turi didesnę paviršiaus plotą ir mažiau paviršiaus defektų (sintetintos grynuose MeOH ir EG), pasižymi aukštesnėmis srovėmis. Tuo tarpu geriausiomis krūvio talpomis (96 mAh g⁻¹) ir jų stabilumu galvanostatinio ciklinimo 1 M Na₂SO₄ (aq) elektrolite metu pasižymėjo NTP, kuris buvo susintetintas naudojant 1-PrOH. Elektrodas išlaikė 95% pradinės talpos per 100 ciklų. Nors šios dalelės buvo didžiausios iš grynų alkoholių serijos, tolimesnis dalelių augimas pridėdam vandens nepagerino krūvio talpos rezultatų, todėl prieita išvados, kad, kai pasiekiamas optimalus NTP nanodalelių dydis (~120 nm), morfologija tampa svarbesniu veiksnium lemiančiu elektrocheminį aktyvumą ir stabilumą.

Taip pat ištirta galvanostatinio įkrovimo-iškrovimo greičio (*angl.* C-rate) įtaka NTP specifinei krūvio talpai 0,1 – 1000C intervale (1C = 0,133 A g⁻¹). Rezultatai parodė, kad didinant greitį, gerėjo krūvio talpų stabilumas ir įkrovimo/iškrovimo procesų kuloninis našumas, tačiau teorinė NTP talpa (133 mAh g⁻¹) nebuvo pasiekama. ICP metodu ištyrus titano ir fosforo kiekį elektrolituose po 100 ciklų, paaiškėjo, jog NTP tirpsta. Nustatyta, kad kuo mažesnis C-greitis (t.y. kuo ilgiau trunka eksperimentas), tuo daugiau ištirpusio P randama elektrolite. Tuo tarpu ištirpusio Ti kiekis buvo daug mažesnis už P ir jokios koreliacijos su įkrovimo/iškrovimo greičiu nepastebėta. Padaryta prielaida, kad ant elektrodo paviršiaus susidaro amorfinis mažai tirpių Ti(HPO₄)₂/Ti(H₂PO₄)₄ junginių sluoksniu, kuris taip pat limituoja Na jonų difuziją ir prisideda prie talpos mažėjimo. Taip pat

nustatyta, jog NTP talpos mažėjimą lemia ir savaiminis NTP išsikrovimas, kurį skatina elektrolite ištirpęs deguonis. NTP elektrodų elgsena tirta ir organiniuose elektrolituose. Nustatyta, kad po 100 ciklų 1 M NaPF₆ diglymo (DG) elektrolite NTP išlaiko net 98% pradinės krūvio talpos, o tai patvirtina, jog degradacija vandeniniame elektrolite yra susijusi ne su pačia medžiaga, o su šalutinėmis reakcijomis, vykstančiomis vandeniniame elektrolite. Apibendrinus gautus rezultatus, galima teigti, jog NTP yra puikus neigiamas elektrodas tiek vandeninėms, tiek organinėms SIB, tačiau yra būtina atsižvelgti ir išspręsti electrocheminio tirpumo problemą.

4.2. Na₄Mn₃(PO₄)₂P₂O₇

Na₄Mn₃(PO₄)₂P₂O₇ (NMPP) netaisyklingų formų mikrodalelės buvo susintetintos kietafazės sintezės metodu. Nors medžiaga pasižymėjo aukštu kristališkumu, tačiau aptikta ir ~22,0 sv.% NaMnPO₄ priemaišinės fazės. Nustatyta, jog papildomam dengimui anglimi tinkama tik gliukozė, kadangi naudojant citrinos rūgštis pirolizės metu NMPP suskyla iki Mn₂O₃.

NMPP elektrodo ciklinės voltamperogramose, užrašytos naudojant 1 M Na₂SO₄ (aq) elektrolitą, pirmame cikle matoma tik viena anodinė smailė ties 1,0 V (Ag/AgCl), kuri gali būti priskirta Mn²⁺/Mn³⁺ oksidacijai, tuo tarpu katodinių smailių nebuvo pastebėta. Tačiau ši smailė išnyko jau antrame cikle, o tai rodo itin greitą NMPP elektrocheminę degradaciją. Galvanostatinis ciklinimas taip pat patvirtino, jog ši medžiaga yra aktyvi tik pirmajame cikle. Buvo pasiekta 74 mAh g⁻¹ krūvio talpa, kuomet teorinė NMPP talpa yra 129 mAh g⁻¹. Labiausiai tikėta, kad degradacija atsiranda dėl riboto NMPP stabilumo vandeniniame tirpale¹⁸³ ir elektrochemiškai neaktyvaus, netirpus sluosnio formavimosi ant elektrodo paviršiaus pirmuosiuose cikluose, kas limituoja Na jonų difuziją. Elektrocheminės NMPP elgsenos tyrimai organiniame elektrolite (1 M NaPF₆ DG) taip pat neparodė gerų rezultatų. Oksidacijos-redukcijos smailės išnyko po dviejų ciklų, o pradinė specifinė iškrovimo krūvio talpa siekė tik 20 mAh g⁻¹. Rezultatų visuma byloja, jog NMPP nėra tinkama teigiamų elektrodų medžiaga nei vandeninėms, nei organinėms SIB.

4.3. Na₃MnPO₄CO₃

Na₃MnPO₄CO₃ (NMPC) mikrodalelės buvo sintetamos hidroterminiu metodu. Pirmiausia, buvo nustatyta, jog norint gauti gryną aukšto kristališkumo NMPC, optimali sintezės temperatūra yra 180 °C, o pradinių medžiagų kiekiai - 0,01 mol Mn(NO₃)₂ ir 0,02 mol (NH₄)₂HPO₄. Dėl CO₃

grupės NMPC medžiaga yra termiškai stabili tik iki ~ 550 °C, todėl papildomas dengimas anglimi nebuvo atliktas.

NMPC elektrodo ciklinės voltamperogramos, užrašytos naudojant 1 M $\text{Na}_2\text{SO}_4(\text{aq})$ elektrolitą, parodė dvi anodines smailes pirmajame cikle, kurios gali būti priskirtos $\text{Mn}^{2+}/\text{Mn}^{3+}$ ir $\text{Mn}^{3+}/\text{Mn}^{4+}$ oksidacijos reakcijoms. Šios smailės išnyko jau antrame cikle dėl NMPC elektrocheminio tirpimo, tačiau nuo ketvirtojo ciklo buvo galima pastebėti naujų anodinių ir katodinių smailių atsiradimą ties 0,85 V/ 1,0 V (Ag/AgCl), kurios gali būti priskirtos elektrochemiškai aktyviems NMPC tirpimo produktams. Galvanostatinis ciklinimas taip pat patvirtino greitą talpos degradaciją, kurios priežastys galimai yra tos pačios kaip ir NMPP atveju. Elektrocheminės NMPC elgsenos tyrimai organiniame elektrolite (1 M NaPF_6 DG) taip pat parodė sparčią degradaciją. Apibendrinus rezultatus, galima teigti, jog NMPC nėra tinkama teigiamų elektrodų medžiaga nei vandeninėms, nei organinėms SIB.

4.4. $\text{Na}_3\text{Fe}_2(\text{PO}_4)_3$

$\text{Na}_3\text{Fe}_2(\text{PO}_4)_3$ (NFP) netaisyklingų formų mikrodalelės buvo susintetintos kietafazės sintezės metodu. Gauta aukšto kristališkumo medžiaga be jokių papildomų priemaišų. NFP dalelės buvo apdengtos papildomu anglies sluoksniu citrinos rūgšties pirolizės metodu.

NFP elektrodo ciklinės voltamperogramos, užrašytos naudojant 1 M $\text{Na}_2\text{SO}_4(\text{aq})$ elektrolitą, parodė keletą grįžtamų ir stabilų anodinių ir katodinių smailių ties -0,5 V/-0,35 V, -0,1 V/0,0 V ir -0,05 V/0,2 V (Ag/AgCl), kurios gali būti priskirtos $\text{Fe}^{2+}/\text{Fe}^{3+}$ oksidacijai-redukcijai. Tuo tarpu galvanostatinio ciklinimo metu išmatuota pradinė specifinė įkrovimo talpa siekė tik 42 mAh g^{-1} (teorinė NFP talpa - 115 mAh g^{-1}) ir antrame cikle sumažėjo iki ~ 15 mAh g^{-1} . Greita krūvio talpos degradacija gali būti paaiškinta NFP tirpimu vandeninėje terpėje elektrocheminių procesų metu. Remiantis gautais rezultatais galima teigti, kad NFP nėra tinkama medžiaga vandeninių SIB elektrodams.

4.5. $\text{Na}_4\text{Fe}_3(\text{PO}_4)_2\text{P}_2\text{O}_7$

$\text{Na}_4\text{Fe}_3(\text{PO}_4)_2\text{P}_2\text{O}_7$ (NFPP) netaisyklingų formų mikrodalelės buvo susintetintos zolių-gelių ir kietafazės sintezės metodais. Zolių-gelių sintezės atveju buvo nustatyta, jog optimaliausi kristališkumo ir grynumo rezultatai gaunami naudojant Fe-fumaratą kaip geležies šaltinį ir citrinos rūgštis, gliukozę bei CTAB kaip koordinuojančius agentus. Tuo tarpu kietafazės

syntezės būdu gautas NFPP pasižymėjo didesniu grynumu ir kristališkumu nei su zolių-gelių metodu susintetinta medžiaga.

NFPP elektrodų ciklinės voltamperogramos, užrašytos naudojant 1 M Na₂SO_{4(aq)} elektrolitą, parodė dvi grįžtamų bei stabilių anodinių ir katodinių smailių poras ties -0,4 V/0,9 V ir -0,7 V/1,0 V (Ag/AgCl), kurios gali būti priskirtos Fe²⁺/Fe³⁺ oksidacijai-redukcijai. Galvanostatinio įkrovimo/iškrovimo ciklinimo metu nustatyta, jog iš visų zolių-gelių metodu susintetintų mėginių geriausia pradine specifine krūvio talpa (65,9 mAh g⁻¹) ir talpos stabilumu (38% po 100 ciklų) pasižymėjo bandiniai, gauti naudojant Fe-fumaratą, citrinos rūgštį, gliukozę ir CTAB. Teorinė NFPP krūvio talpa yra 129 mAh g⁻¹. Tuo tarpu kietafazės sintezės būdu gauto NFPP pradinė talpa buvo 60,1 mAh g⁻¹, o talpos stabilumas – 43,9% po 100 ciklų. Talpos degradacija galimai yra susijusi su daliniu medžiagos tirpimu vandeninėje terpėje elektrocheminių procesų metu. Elektrocheminės NFPP elgsenos tyrimai organiniame elektrolite (1 M NaPF₆ DG) parodė puikius rezultatus: pradinė krūvio talpa – 86 mAh g⁻¹, o talpos stabilumas – 95% po 100 ciklų. Apibendrinus gautus duomenis, galima teigti, jog išsprendus NFPP tirpimą, ši medžiaga galėtų būti naudojama teigiamiems vandeninių SIB elektrodams, ir yra puikiai tinkama organinėms SIB.

4.6. Na_{2-x}Fe[Fe(CN)₆]·yH₂O

Na_{2-x}Fe[Fe(CN)₆]·yH₂O (NFCN) kubinės mikrodalelės buvo susintetintos hidroterminiu metodu, tačiau nustatėms, kad optimali sintezės temperatūra yra tik 80 °C, buvo pereita prie pigesnio išsodinimo metodo. Pastarosios sintezės metu buvo nustatyta, jog priklausomai nuo sintezės pH ir džiovavimo sąlygų yra gaunamos skirtingos fazės: su HCl – kubinė, be HCl – monoklininė, o išdžiovinus monoklininę vakuume (170 °C, 10⁻² mbar) – romboedrinė. ICP ir termogravimetrijos analizės metodais nustatyta, jog monoklininė fazė, kurią ir siekta gauti, atitinka Na_{1,86}Fe[Fe(CN)₆]·2.28H₂O formulę.

NFCN elektrodų ciklinės voltamperogramos, užrašytos naudojant 1 M Na₂SO_{4(aq)} elektrolitą, parodė keletą grįžtamų bei stabilių anodinių ir katodinių smailių ties -0,05 V/0,25 V ir 1 V/1,2 V (Ag/AgCl), kurios gali būti priskirtos, atitinkamai, Fe³⁺/Fe²⁺-N (azotu koordinuota redokso pora) ir Fe³⁺/Fe²⁺-C (anglimi koordinuota redokso pora) oksidacijai-redukcijai. Galvanostatinio įkrovimo/iškrovimo ciklinimo metu nustatyta, jog praktiškai naudoti galima tik pirmąją geležies smailių porą (Fe³⁺/Fe²⁺-N), nes antroji yra pernelyg arti vandens oksidacijos reakcijos (deguonies išsiskyrimo) potencialo, o tai itin apsunkina Fe³⁺/Fe²⁺-C proceso pasiekiamumą ir mažina

kuloninį našumą. Naudojant skirtingo pH vandeninius buferius (pH = 4,0, 7,0 ir 10,0) nustatyta, jog geriausias NFCN krūvio talpos stabilumas pasiekiamas rūgštinėje terpėje (88% po 1000 ciklų), kuomet pradinė krūvio talpa yra apie 70 mAh g⁻¹. Teorinė NFCN talpa vienam elektronui yra 85 mAh g⁻¹, o dviem – 170 mAh g⁻¹. Elektrocheminės NFCN elgsenos tyrimai organiniame elektrolite (1 M NaPF₆ DG) parodė tris oksidacijos-redukcijos procesus, tačiau trečioji smailių pora buvo elektrochemiškai nestabili. Monoklininės NFCN fazės elektrodo pradinė specifinė krūvio talpa buvo 111 mAh g⁻¹, o talpos stabilumas – 64% po 100 ciklų. Apibendrinus gautus rezultatus, galima teigti, jog NFCN medžiaga būtų tinkama teigiamiems SIB elektrodams tiek vandeniniuose, tiek organiniuose elektrolituose.

4.7. Na₇V₄(PO₄)(P₂O₇)₄

Na₇V₄(PO₄)(P₂O₇)₄ (NVPP) netaisyklingų formų mikrodalelės buvo susintetintos kietafazės reakcijos metodu. Nors medžiaga pasižymėjo aukštu kristališkumu, tačiau aptikta ir priemaišinių Na₃V₂(PO₄)₃ (~10,2 sv.%) bei NaVP₂O₇ (~6,6 sv.%) fazių. NVPP buvo apdengtas papildomu anglies sluoksniu, naudojant citrinos rūgštį, pirolizės metodu.


NVPP elektrodo ciklinės voltamperogramos, užrašytos naudojant 1 M Na₂SO_{4(aq)} elektrolitą, parodė keletą grįžtamų anodinių ir katodinių smailių porų. Pirmoji smailių pora, matoma tik pirmuose cikluose ties 0 V/0,1 V (Ag/AgCl), yra prisiskiriama Na₃V₂(PO₄)₃ fazės V³⁺/V⁴⁺ oksidacijos-redukcijos procesui. Tuo tarpu NVPP junginiui galima priskirti dvi anodines smailes ties 0,63 V ir 0,72 V ir vieną katodinę ties 0,3 V, tačiau jų intensyvumas ciklinant mažėja, kas rodo prastą NVPP elektrocheminį aktyvumą vandeniniame elektrolite. Galvanostatinis įkrovimo/iškrovimo ciklinimas taip pat patvirtino greitą medžiagos degradaciją, kadangi krūvio talpa po 100 ciklų siekė vos 2,4% pradinės, kuri buvo 55 mAh g⁻¹, kai teorinė NVPP talpa yra 93 mAh g⁻¹. Tuo tarpu, elektrocheminės NVPP elgsenos tyrimai organiniame elektrolite (1 M NaPF₆ DG) parodė puikius rezultatus: po 100 ciklų NVPP elektrodas išlaikė net 83% pradinės talpos, o tai patvirtina, jog degradaciją vandeniniame elektrolite lemia medžiagos sąveika su vandeniu. Apibendrinus gautus duomenis galima teigti, jog NVPP puikiai tinka organinėms SIB kaip teigiamo elektrodo medžiaga, tačiau vandeninėms – ne.

4.8. Na₃VFe(PO₄)₃

Na₃VFe(PO₄)₃ (NVFP) netaisyklingų formų mikrodalelės buvo susintetintos kietafazės sintezės metodu. Nors medžiaga pasižymėjo aukštu kristališkumu, tačiau aptiktas ir mažas kiekis priemaišinės NaFePO₄ fazės. NVFP dalelės buvo apdengtos papildomu anglies sluoksniu citrinos rūgšties pirolizės būdu.

NVFP elektrodo ciklinės voltamperogramos, užrašytos naudojant 1 M Na₂SO₄(aq) elektrolitą, parodė keletą anodinių smailių ties -0,3 V, 0,6 V ir 1,16 V (Ag/AgCl), kurios, atitinkamai, yra priskiriamos Fe²⁺/Fe³⁺, V³⁺/V⁴⁺ ir V⁴⁺/V⁵⁺ oksidacijai ir tik vieną katodinę smailę ties 0,43 V (Ag/AgCl), kuri priskiriama V⁴⁺/V³⁺ redukcijai. Visų jų smailių srovės ciklinant mažėjo. Tačiau pastebėta, kad, jei potencialo ruožas yra apribojamas tik Fe²⁺/Fe³⁺ arba tik V³⁺/V⁴⁺ procesams, smailės išlieka stabilios. Tai leidžia manyti, kad ciklinant plačiame potencialų ruože V⁴⁺/V⁵⁺ procesas destabilizuoja visą NVFP karkasą. Galvanostatinis įkrovimo/iškrovimo ciklinimas skirtinguose potencialų intervaluose (Fe²⁺/Fe³⁺ + V³⁺/V⁴⁺, Fe²⁺/Fe³⁺, V³⁺/V⁴⁺) parodė, kad geležis yra daug stabilesnė nei vanadis, kuris limituoja bendrą NVFP stabilumą (18.4% pradinės talpos po 100 ciklų). Elektrocheminės NVFP elgsenos tyrimai organiniame elektrolite (1 M NaPF₆ DG), taip pat patvirtino, kad V⁴⁺/V⁵⁺ pora stipriai destabilizuoja NVFP medžiagą, o ciklinant tik Fe²⁺/Fe³⁺ + V³⁺/V⁴⁺, Fe²⁺/Fe³⁺, arba V³⁺/V⁴⁺ oksidacijos- redukcijos procesų ruožuose gaunamos talpos yra itin stabilios, tačiau organinio elektrolito atveju, priešingai nei vandeninio, V³⁺/V⁴⁺ pasižymi geresniu elektrocheminiu aktyvumu nei Fe²⁺/Fe³⁺. Apibendrinus gautus rezultatus galima teigti, jog NFCN gali būti naudojamas kaip aktyvi SIB elektrodų medžiaga, tačiau svarbu išspręsti dalinį medžiagos tirpimą.

5. Išvados

 NaTi₂(PO₄)₃ nanodalelės buvo sėkmingai susintetintos hidro(solvo)terminiu metodu. Nustatyta, kad sintezės temperatūra įtakoja dalelių dydį, bet ne NTP fazės grynumą. Parodyta, kad sintezėje naudojamas tirpiklis (įvairūs alkoholiai ir jų mišiniai su vandeniu) ženkliai įtakoja nanodalelių morfologiją ir fazės grynumą. Netaisyklingų formų NaTi₂(PO₄)₃ nanodalelės su paviršiaus defektais pasižymėjo mažesnėmis pradinėmis krūvio talpomis bei spartesne talpos degradacija palyginti su sferinėmis ar kubinėmis nanodalelėmis.

▣ Parodyta, kad negrįžtamas NTP talpos mažėjimas vandeniniuose elektrolituose yra susijęs su elektrochemine medžiagos degradacija, kuri ypač pastebima lėto įkrovimo/iškrovimo metu ($\leq 1C$) ir koreliuoja su elektrolite ištirpusio fosforu kiekiu ir yra susijęs su chemine medžiagos degradacija. Nustatyta, kad elektrolite ištirpusio deguonies redukcija yra pagrindinė šalutinė reakcija, lemianti pH padidėjimą ir su tuo susijusį $\text{NaTi}_2(\text{PO}_4)$ tirpimą, krūvio talpos degradaciją, savaiminį $\text{NaTi}_2(\text{PO}_4)$ išsikrovimą ir mažą kuloninį našumą. Apibendrinus gautus rezultatus, $\text{NaTi}_2(\text{PO}_4)$ yra tinkama neigiamo elektrodo medžiaga tiek vandeninėms, tiek organinėms Na^+ jonų baterijoms.

▣ Polianijoniniai Mn junginiai - $\text{Na}_4\text{Mn}_3(\text{PO}_4)_2\text{P}_2\text{O}_7$ ir $\text{Na}_3\text{MnPO}_4\text{CO}_3$ buvo susintetinti kietfazės ir hidroterminiu būdu, atitinkamai. Nustatytos optimalios sintezių sąlygos. Elektrocheminės elgsenos tyrimai parodė itin greitą degradaciją bei ribotą elektrocheminį aktyvumą tiek vandeniniuose, tiek organiniuose elektrolituose, dėl ko šie junginiai nėra tinkami naudoti kaip Na^+ jonų baterijų teigiamų elektrodų medžiagos.

▣ Darbe buvo susintetinti ir išsamiai ištirti keletas geležies turinčių junginių. $\text{Na}_3\text{Fe}_2(\text{PO}_4)_3$, pagamintas kietfazės sintezės metodu, pasižymėjo netaisyklinga dalelių morfologija, mažomis pradinėmis krūvio talpomis ir sparčia degradacija, todėl nėra tinkamas naudoti kaip neigiamo elektrodo medžiaga vandeninėms Na^+ jonų baterijose. $\text{Na}_4\text{Fe}_3(\text{PO}_4)_2\text{P}_2\text{O}_7$ susintetintas kietfazės ir zolių-gelių sintezės metodais. Jo elektrocheminį aktyvumą vandeniniuose elektrolituose galima limituoja su geležies tirpimu susijusi degradacija, tačiau organiniuose elektrolituose $\text{Na}_4\text{Fe}_3(\text{PO}_4)_2\text{P}_2\text{O}_7$ pasižymi išskirtiniu stabilumu. $\text{Na}_{2-x}\text{Fe}[\text{Fe}(\text{CN})_6] \cdot y\text{H}_2\text{O}$ buvo susintetintas hidroterminiu ir išsodinimo metodais. Parodyta, kad priklausomai nuo sintezės temperatūros, terpės pH ir džiovavimo sąlygų gali būti gaunama kubinė, monoklininė ar romboedrinė NFCN fazės. Šis junginys pasižymi puikiu krūvio talpos stabilumu vieno elektrono reakcijos metu vandeniniuose elektrolituose, ir dviejų elektronų reakcijos metu – organiniuose. $\text{Na}_{2-x}\text{Fe}[\text{Fe}(\text{CN})_6] \cdot y\text{H}_2\text{O}$ yra tinkama teigiamo elektrodo medžiaga tiek vandeninėms, tiek organinėms Na^+ jonų baterijose.

▣ $\text{Na}_7\text{V}_4(\text{PO}_4)(\text{P}_2\text{O}_7)_4$ sėkmingai pagamintas kietfazės sintezės metodu. Nustatyta, kad šios medžiagos elektrodai vandeniniuose elektrolituose pasižymi greita krūvio talpos degradacija, kurią galima sukelti V^{4+} nestabilumas vandeninėje terpėje, tuo tarpu organiniuose elektrolituose

gautos aukštos pradinės NVPP krūvio talpos bei geras jų stabilumas įkrovimo/iškrovimo ciklinimo metu.

☐ Grynios fazės ir netaisyklingos formos $\text{Na}_3\text{VFe}(\text{PO}_4)_3$ dalelės buvo sėkmingai susintetintos kietafazės sintezės metodu. Elektrocheminiai tyrimai parodė, kad apimant visas tris galimas oksidacijos-redukcijos poras ($\text{Fe}^{2+}/\text{Fe}^{3+}$, $\text{V}^{3+}/\text{V}^{4+}$, ir $\text{V}^{4+}/\text{V}^{5+}$), $\text{Na}_3\text{VFe}(\text{PO}_4)_3$ talpos tiek vandeniniuose, tiek organiniuose elektrolituose, degraduoja itin sparčiai. Parodyta, kad junginio struktūrą destabilizuoja $\text{V}^{4+}/\text{V}^{5+}$ procesas. Taip pat, pastebėta, kad $\text{Fe}^{2+}/\text{Fe}^{3+}$ pora yra žymiai stabilesnė nei $\text{V}^{3+}/\text{V}^{4+}$ vandeniniuose elektrolituose, kai tuo tarpu organiniuose yra atvirkščiai. Išsprendus dalinį $\text{Na}_3\text{VFe}(\text{PO}_4)_3$ elektrocheminį degradavimą, šis junginys būtų tinkama elektrodo medžiaga tiek vandeninėse, tiek organinėse Na^+ jonų baterijose.

ACKNOWLEDGEMENTS

Thank You* so much!

* Linas Vilčiauskas, my doctoral supervisor, for not only providing the opportunity to be a part of battery field but also for being invested and involved in all steps of my research. Your mentorship was immensely beneficial and contributed to my growth as a researcher. Your expertise, encouragement and dedication are inspiring!

* Jurgis Pilipavičius for being the best consultant and answering all the random questions. Your guidance, competence and experimental support improved my research thousands of times.

* Jurga Juodkazytė, Milda Petrulevičienė, Skirmantė Tutlienė, Laurynas Staišiūnas and Davit Tediashvili for valuable friendship, guidance, interesting discussions during theLunch, scientific collaborations, and, most important, being an awesome team.

* Nadežda for being more than just a lab-office-mate. Our daily conversations about work challenges, how to make graphs look better, and just simple (or not) life things such as reminders to drink more water, made this time much more enjoyable and easier.

* Ieva and Aldona Beganskienė for bringing me to the “science world”, your kindness and all the support throughout my bachelor and master studies.

* Maider Zarrabeitia and Stefano Passerini for accepting me in your group, being my supervisors, sharing your knowledge and warm welcome during fellowship in Ulm, Germany. Additionally, Deutsche Bundesstiftung Umwelt for funding these amazing six months.

* Aleksej Žarkov, Audrius Drabavičius, Algirdas Selskis, Saulius Daugėla and Tomas Šalkus for contributing to experimental part of this research.

* Family and friends for supporting the idea to study science for that long even if You did not quite understand what I am doing. And for all the questions “so is your battery working? when can we use them?” which were motivation to keep going.

* Pranas, who has been by my side all these hard, interesting and exciting 10 years of chemistry studies, for listening, trying to understand the things I was telling about and, most important, for providing comfort.

* Kolba for all the joy and emotional support.

* You, who read or just looked at the images of this dissertation.

LIST OF PUBLICATIONS AND CONFERENCES

Publications included in the thesis:

■ **G. Gečė.** M. Zarrabeitia, J. Pilipavičius, S. Passerini L. Vilčiauskas, A Comparative Study of Mixed Phosphate-Pyrophosphate Materials for Aqueous and Non-Aqueous Na-ion Batteries, ChemRxiv. October 4 (2023), doi: 10.26434/chemrxiv-2023-t5b07.

■ **G. Gečė.** J. Pilipavičius, N. Traškina, A. Drabavičius, L. Vilčiauskas, Solvothermal Engineering of $\text{NaTi}_2(\text{PO}_4)_3$ Nanomorphology for Applications in Aqueous Na-Ion Batteries, ACS Sustainable Chemistry & Engineering, 11, 8, 3429–3436 (2023), doi: 10.1021/acssuschemeng.2c06732.

■ D. Tediashvili, **G. Gečė,** J. Pilipavičius, S. Daugėla, T. Šalkus, J. Juodkazytė, L. Vilčiauskas, Synthesis, Characterization, and Degradation Study of Mn-based Phosphate Frameworks ($\text{Na}_3\text{MnTi}(\text{PO}_4)_3$, $\text{Na}_3\text{MnPO}_4\text{CO}_3$, $\text{Na}_4\text{Mn}_3(\text{PO}_4)_2\text{P}_2\text{O}_7$) as Aqueous Na-ion Battery Positive Electrodes, Electrochimica Acta 417, 140294 (2022), doi: 10.1016/j.electacta.2022.140294.

■ **G. Plečkaitytė,** M. Petrulevičienė, L. Staišiūnas, D. Tediashvili, J. Pilipavičius, J. Juodkazytė, L. Vilčiauskas, Understanding and mitigation of $\text{NaTi}_2(\text{PO}_4)_3$ degradation in aqueous Na-ion batteries, Journal of Material Chemistry A, 9, 12670-12683 (2021), doi: 10.1039/d1ta01215k.

Publications not included in the thesis:

■ N. Traškina, **G. Gečė,** J. Pilipavičius, L. Vilčiauskas, Polydopamine Derived $\text{NaTi}_2(\text{PO}_4)_3$ –Carbon Core–Shell Nanostructures for Aqueous Batteries and Deionization Cells, Applied Nano Materials, 6, 13, 11780-11787 (2023), doi: 10.1021/acsanm.3c01687.

■ M. Petrulevičienė, M. Parvin, I. Savickaja, **G. Gečė,** A. Naujokaitis, V. Pakštas, J. Pilipavičius, A. Gegeckas, G. Gaigalas, J. Juodkazytė, WO_3 coatings for photoelectrochemical synthesis of persulfate: efficiency, stability and applicability, Journal of Solid State Electrochemistry, 26, 1021–1035 (2022), doi: 10.1007/s10008-022-05144-8.

■ I. Mikalauskaitė, **G. Plečkaitytė,** L. Sinušaitė, V. Plaušinitienė, A. Katelnikovas, A. Beganskienė, Temperature Induced Emission Enhancement and Investigation of $\text{Nd}^{3+} \rightarrow \text{Yb}^{3+}$ Energy Transfer Efficiency in $\text{NaGdF}_4:\text{Nd}^{3+}$, Yb^{3+} , Er^{3+} Upconverting Nanoparticles, Journal of Luminescence (2020), doi: 10.1016/j.jlumin.2020.117237.

■ D. Moon, **G. Plečkaitytė,** T. Choi, M. Seol, B. Kim, D. Lee, J. Han, M. Meyyappan, On-Demand Printing of Wearable Thermotherapy Pad,

Attended conferences:

■ **G. Gečė**, J. Pilipavičius, L. Vilčiauskas, Prussian white as cathode material for aqueous sodium ion batteries, Open Readings – 66th International Conference for students of physics and natural sciences, April 18-21, 2022, Vilnius, Lithuania. (Oral) (Best oral presentation)

■ **G. Gečė**, J. Pilipavičius, Jurga Juodkazytė, M. Zarrabeitia, S. Passerini, L. Vilčiauskas, Synthesis and investigation of $\text{Na}_7\text{V}_4(\text{PO}_4)(\text{P}_2\text{O}_7)_4$, $\text{Na}_4\text{Fe}_3(\text{PO}_4)_2(\text{P}_2\text{O}_7)$ and $\text{Na}_4\text{Mn}_3(\text{PO}_4)_2(\text{P}_2\text{O}_7)$ materials for Na-ion batteries, 7th ICNaB 2022 International Conference on Sodium Batteries, 5-8 December 2022, Ulm, Vilnius. (Poster)

■ **G. Gečė**, J. Pilipavičius, Jurga Juodkazytė, M. Zarrabeitia, S. Passerini, L. Vilčiauskas, Synthesis and investigation of mixed-polyanion cathode materials for Na-ion batteries, 12-toji doktorantų ir jaunųjų mokslininkų konferencija „FizTech 2022”, October 19-20, 2022, Vilnius, Lithuania. (Oral) (Best oral presentation)

■ **G. Gečė**, J. Pilipavičius, J. Juodkazytė, L. Vilčiauskas, $\text{Na}_4\text{FeV}(\text{PO}_4)_3$ -Alternative cathode for aqueous sodium ion batteries, Open Readings – 65th International Conference for students of physics and natural sciences, March 15-18, 2022, Vilnius, Lithuania (Poster)

■ **G. Gečė**, J. Pilipavičius, J. Juodkazytė, L. Vilčiauskas, How to control morphology of $\text{NaTi}_2(\text{PO}_4)_3$ nanoparticles?, 11-toji doktorantų ir jaunųjų mokslininkų konferencija „FizTech 2021”, October 20-21, 2021, Vilnius, Lithuania. (Oral)

■ **G. Plečkaitytė**, J. Pilipavičius, S. Daugėla, T. Šalkus, J. Juodkazytė, L. Vilčiauskas, Synthesis of $\text{Na}_4\text{Mn}_3(\text{PO}_4)_2(\text{P}_2\text{O}_7)$ and $\text{Na}_3\text{MnPO}_4\text{CO}_3$ as cathode materials for aqueous Na-ion batteries, Chemistry & Chemical Technology, September 24, 2021 Vilnius, Lithuania. (Poster)

■ **G. Plečkaitytė**, D. Tediashvili, J. Pilipavičius, M. Petrulevičienė, J. Juodkazytė, L. Vilčiauskas, Mn-based (mixed)phosphate cathode materials for aqueous Na-ion batteries, European Congress and Exhibition on Advanced Materials and Processes EUROMAT2021, September 12-16, 2021, Graz, Austria, virtual. (Poster)

■ **G. Plečkaitytė**, J. Pilipavičius, M. Petrulevičienė, N. Traškina, J. Juodkazytė, L. Vilčiauskas, Synthesis and investigation of $\text{Na}_4\text{Fe}_3(\text{PO}_4)_2(\text{P}_2\text{O}_7)$ for aqueous Na-ion batteries, Advanced Materials and Nanotechnologies, August 23-27, 2021, Palanga, Lithuania. (Poster)

📄 **G. Plečkaitytė**, J. Pilipavičius, J. Juodkazytė, L. Vilčiauskas, Investigation of $\text{Na}_4\text{Fe}_3(\text{PO}_4)_2\text{P}_2\text{O}_7$ as cathode for aqueous Na-ion batteries, Open Readings – 64th International Conference for students of physics and natural sciences, March 16-19, 2021, Vilnius, Lithuania. (Poster)

📄 **G. Plečkaitytė**, J. Pilipavičius, M. Petrulevičienė, J. Juodkazytė, L. Vilčiauskas, Hydro(solvo)thermal synthesis of NASICON-type materials for Na-ion batteries, Functional materials and nanotechnologies, November 23-25, 2020, Vilnius, Lithuania. (Poster) (Best Poster Award).

📄 **G. Plečkaitytė**, J. Pilipavičius, M. Petrulevičienė, J. Juodkazytė, L. Vilčiauskas, Hidro(solvo)terminė $\text{NaTi}_2(\text{PO}_4)_3$ skirto Na-jonų baterijoms sintezė ir charakterizavimas, 10-toji doktorantų ir jaunųjų mokslininkų konferencija „FizTech 2020“, October 22-23, 2020, Vilnius, Lithuania. (Oral) (Best Oral Presentation Award).

📄 **G. Plečkaitytė**, J. Pilipavičius, M. Petrulevičienė, J. Juodkazytė, L. Vilčiauskas, Solvothermal Synthesis of NASICON-type $\text{NaTi}_2(\text{PO}_4)_3$ for Aqueous Na-ion Batteries, Advanced Materials and Nanotechnologies, August 24-28, 2020, Palanga, Lithuania (Poster) (Best Poster Award).

Not attended conferences:

📄 J. Juodkazytė, **G. Gečė**, M. Petrulevičienė, J. Pilipavičius, D. Tediashvili, L. Staišiūnas, L. Vilčiauskas, Understanding the capacity fade of $\text{NaTi}_2(\text{PO}_4)_3$ anode in aqueous Na-ion batteries, 18th International conference on electroanalysis (ESEAC 2022), 5 - 9 June 2022, Vilnius, Lithuania. (Poster)

📄 D. Tediashvili, **G. Plečkaitytė**, J. Pilipavičius, L. Vilčiauskas, Characterization of Mn-based cathode materials for aqueous Na-ion batteries using the rotating ring-disc technique, 11-toji doktorantų ir jaunųjų mokslininkų konferencija „FizTech 2021“, October 20-21, 2021, Vilnius, Lithuania. (Oral)

📄 N. Traškina, **G. Plečkaitytė**, J. Pilipavičius, J. Juodkazytė, L. Vilčiauskas, Precisely Controlled Carbon Coating of $\text{NaTi}_2(\text{PO}_4)_3$ for Enhanced Electrochemical Performance, Advanced Materials and Nanotechnologies, August 23-27, 2021, Palanga, Lithuania. (Poster)

📄 **G. Plečkaitytė**, L. Vilčiauskas, S. Daugėla, T. Šalkus, A.F. Orliukas, M. Mosiałek, Synthesis, structure and electrical properties of $\text{Na}_4\text{Mn}_3(\text{PO}_4)_2(\text{P}_2\text{O}_7)$ and $\text{Na}_3\text{MnPO}_4\text{CO}_3$ ceramics, 6th International Symposium on Surface Imaging/Spectroscopy at the Solid/Liquid Interface, June 6-9th, 2021, virtual.

CURRICULUM VITAE

Name and surname Gintarė Gečė (née Plečkaitytė)
Date of birth 1994-05-08
Email gintare.pleckaityte@ftmc.lt

Education

2019 – 2023 PhD studies in Chemistry, Center for Physical sciences and Technology, Vilnius University.
2017 – 2019 Master of Physical Sciences (Study field: Chemistry, study program: Chemistry of Nanomaterials), Vilnius University.
2013 – 2017 Bachelor of Chemistry (Study program: Nanotechnologies and material science), Vilnius University.
2016-02 – 2016-07 Erasmus+, Charles University, Czech Republic.
2009 – 2013 Secondary Education, Šakiai “Žiburys” Gymnasium.
2001 – 2009 Šakiai “Varpas“ Secondary School.

Experience

2019-11 – present Young Researcher, Center for Physical sciences and Technology.
2019-09 – 2021-10 Engineer, Center for Physical sciences and Technology.
2017-09 – 2018-08 Senior Specialist, Faculty of Chemistry and Geosciences, Vilnius University.

Fellowships

2022-02 – 2022-08 Research Fellow, Helmholtz Institute Ulm, Germany.
2018-08 – 2018-12 Intern, Ames Research Center, National Aeronautics and Space Administration (NASA), United States of America.
2016-07 – 2016-09 Intern, Superior Tecnico Institute, University of Lisbon, Portugal.

Awards

2023-03	Nominal scholarship of Theodor von Grotthuss for scientific achievements, The Lithuanian Academy of Science.
2022/2023	Additional doctoral scholarship for academic and scientific achievements, Research Council of Lithuania.
2020-02	Laureate of the competition for the best research works by the students in higher education 2019, The Lithuanian Academy of Sciences.
2017-11	Nominal scholarship of Gražinos Romualdos Klimavičius for academic and scientific achievements, Vilnius University.
2014 – 2019	Incentive scholarships for academic achievements, Vilnius University.

Other activity

2019-10 – 2022-01	Participation in the research project "Understanding and Applications of Aqueous Na-ion Technologies for Energy Storage (NaAquaCell)" (Project No. 01.2.2-LMTK-718-02-0005 under the grant agreement with the Lithuanian Research Council), Center for Physical sciences and Technology.
2015-09 – 2019-06	Member of 'Sol-Gel' Scientific Group, Vilnius University. Research topic: Synthesis, characterization and luminescence properties investigation of upconverting nanoparticles.
2017-10 – 2018-04	Participation in the student's research project 'Developing students' abilities to carry out research and development activities, Research Council of Lithuania and Vilnius University.
2017-09 – 2018-09	Member of Study Program (Chemistry of Nanomaterials) Committee, Vilnius University.

LIST OF REFERENCES

1. Pu, X.; Wang, H.; Zhao, D.; Yang, H.; Ai, X.; Cao, S.; Chen, Z.; Cao, Y., Recent Progress in Rechargeable Sodium-Ion Batteries: toward High-Power Applications. *Small* **2019**, *15*, 1805427.
2. Nayak, P. K.; Yang, L.; Brehm, W.; Adelhelm, P., From Lithium-Ion to Sodium-Ion Batteries: Advantages, Challenges, and Surprises. *Angewandte Chemie International Edition* **2018**, *57*, 102-120.
3. Kim, H.; Kim, H.; Ding, Z.; Lee, M. H.; Lim, K.; Yoon, G.; Kang, K., Recent Progress in Electrode Materials for Sodium-Ion Batteries. *Advanced Energy Materials* **2016**, *6*, 1600943.
4. Bin, D.; Wang, F.; Tamirat, A. G.; Suo, L.; Wang, Y.; Wang, C.; Xia, Y., Progress in Aqueous Rechargeable Sodium-Ion Batteries. *Advanced Energy Materials* **2018**, *8*, 1703008.
5. Tapia-Ruiz, N.; Armstrong, A. R.; Alptekin, H.; Amores, M. A.; Au, H.; Barker, J.; Boston, R.; Brant, W. R.; Brittain, J. M.; Chen, Y.; Chhowalla, M.; Choi, Y.-S.; Costa, S. I. R.; Crespo Ribadeneyra, M.; Cussen, S. A.; Cussen, E. J.; David, W. I. F.; Desai, A. V.; Dickson, S. A. M.; Eweka, E. I.; Forero-Saboya, J. D.; Grey, C. P.; Griffin, J. M.; Gross, P.; Hua, X.; Irvine, J. T. S.; Johansson, P.; Jones, M. O.; Karlsmo, M.; Kendrick, E.; Kim, E.; Kolosov, O. V.; Li, Z.; Mertens, S. F. L.; Mogensen, R.; Monconduit, L.; Morris, R. E.; Naylor, A. J.; Nikman, S.; O'Keefe, C. A.; Ould, D. M. C.; Palgrave, R. G.; Poizot, P.; Ponrouch, A.; Renault, S.; Reynolds, E. M.; Rudola, A.; Sayers, R.; Scanlon, D. O.; Sen, S.; Seymour, V. R.; Silván, B.; Sougrati, M. T.; Stievano, L.; Stone, G. S.; Thomas, C. I.; Titirici, M.-M.; Tong, J.; Wood, T. J.; Wright, D. S.; Younesi, R., 2021 roadmap for sodium-ion batteries. *Journal of Physics: Energy* **2021**, *3*, 031503.
6. Agency, I. E., World Energy Outlook 2022. **2022**.
7. United Nations, C. C. The Paris Agreement. <https://unfccc.int/process-and-meetings/the-paris-agreement>
8. Comission, E. Implementing the SET Plan 2020 report. https://setis.ec.europa.eu/implementing-set-plan-2020-report-2020-11-23_en (March 2023),
9. Yang, Y.; Bremner, S.; Menictas, C.; Kay, M., Battery energy storage system size determination in renewable energy systems: A review. *Renewable and Sustainable Energy Reviews* **2018**, *91*, 109-125.
10. Ould Amrouche, S.; Rekioua, D.; Rekioua, T.; Bacha, S., Overview of energy storage in renewable energy systems. *International Journal of Hydrogen Energy* **2016**, *41*, 20914-20927.

11. Olabi, A. G., Renewable energy and energy storage systems. *Energy* **2017**, *136*, 1-6.
12. Kundu, D.; Talaie, E.; Duffort, V.; Nazar, L. F., The emerging chemistry of sodium ion batteries for electrochemical energy storage. *Angew Chem Int Ed Engl* **2015**, *54*, 3431-48.
13. Goodenough, J. B., Evolution of strategies for modern rechargeable batteries. *Acc Chem Res* **2013**, *46*, 1053-61.
14. European Battery Alliance. <https://www.eba250.com/> (March 2023),
15. Sudduth, W. M., The Voltaic Pile and Electro-Chemical Theory in 1800. *Ambix* **1980**, *27*, 26-35.
16. Bresser, D.; Passerini, S., Handbook of Battery Materials. Second Edition; Edited by Claus Daniel and Jürgen O. Besenhard. *Energy Technology* **2013**, *1*, 617-618.
17. Linden, D., *Handbook of batteries*. 2nd ed.; McGraw-Hill: New York, **1995**.
18. Muñoz, M. J. P.; Martínez, E. C., *Prussian Blue Based Batteries*. Springer International Publishing 2018.
19. Dell, R. M., Batteries: fifty years of materials development. *Solid State Ionics* **2000**, *134*, 139-158.
20. Dirkse, T. P., The Silver Oxide Electrode. *Journal of The Electrochemical Society* **1959**, *106*, 453.
21. Viswanathan, B., Chapter 12 - Batteries. In *Energy Sources*, Viswanathan, B., Ed. Elsevier: Amsterdam, **2017**; pp 263-313.
22. Liu, Y.; Su, M.-Y.; Gu, Z.-Y.; Zhang, K.-Y.; Wang, X.-T.; Du, M.; Guo, J.-Z.; Wu, X.-L., Advanced Lithium Primary Batteries: Key Materials, Research Progresses and Challenges. *The Chemical Record* **2022**, *22*, e202200081.
23. Li, Y.; Dai, H., Recent advances in zinc-air batteries. *Chem Soc Rev* **2014**, *43*, 5257-75.
24. Pavlov, D., *Lead-Acid Batteries: Science and Technology*. Elsevier Science **2011**.
25. Petrovic, S., Nickel–Cadmium Batteries. In *Battery Technology Crash Course: A Concise Introduction*, Petrovic, S., Ed. Springer International Publishing: Cham, 2021; pp 73-88.
26. Ruetschi, P.; Meli, F.; Desilvestro, J., Nickel-metal hydride batteries. The preferred batteries of the future? *Journal of Power Sources* **1995**, *57*, 85-91.
27. Kumar, D.; Rajouria, S. K.; Kuhar, S. B.; Kanchan, D. K., Progress and prospects of sodium-sulfur batteries: A review. *Solid State Ionics* **2017**, *312*, 8-16.

28. Yoshio, M.; Brodd, R. J.; Kozawa, A., Lithium-ion batteries. *Springer* **2009**; Vol. 1.
29. Hwang, J.-Y.; Myung, S.-T.; Sun, Y.-K., Sodium-ion batteries: present and future. *Chemical Society Reviews* **2017**, *46*, 3529-3614.
30. Brodd, R. J., Recent Developments in Batteries for Portable Consumer Electronics Applications. *The Electrochemical Society Interface* **1999**, *8*, 20.
31. Kebede, A. A.; Kalogiannis, T.; Van Mierlo, J.; Berecibar, M., A comprehensive review of stationary energy storage devices for large scale renewable energy sources grid integration. *Renewable and Sustainable Energy Reviews* **2022**, *159*, 112213.
32. Liang, Y.; Zhao, C.-Z.; Yuan, H.; Chen, Y.; Zhang, W.; Huang, J.-Q.; Yu, D.; Liu, Y.; Titirici, M.-M.; Chueh, Y.-L.; Yu, H.; Zhang, Q., A review of rechargeable batteries for portable electronic devices. *InfoMat* **2019**, *1*, 6-32.
33. Müller, T.; Friedrich, B., Development of a recycling process for nickel-metal hydride batteries. *Journal of Power Sources* **2006**, *158*, 1498-1509.
34. Dhar, S. K.; Ovshinsky, S. R.; Gifford, P. R.; Corrigan, D. A.; Fetcenko, M. A.; Venkatesan, S., Nickel/metal hydride technology for consumer and electric vehicle batteries—a review and up-date. *Journal of Power Sources* **1997**, *65*, 1-7.
35. Wen, Z.; Cao, J.; Gu, Z.; Xu, X.; Zhang, F.; Lin, Z., Research on sodium sulfur battery for energy storage. *Solid State Ionics* **2008**, *179*, 1697-1701.
36. Korthauer, R., Lithium-Ion Batteries: Basics and Applications. *Springer Berlin Heidelberg* **2018**.
37. Whittingham, M. S.; Gamble, F. R., The lithium intercalates of the transition metal dichalcogenides. *Materials Research Bulletin* **1975**, *10*, 363-371.
38. Mizushima, K.; Jones, P.; Wiseman, P.; Goodenough, J. B., Li_xCoO_2 ($0 < x < 1$): A new cathode material for batteries of high energy density. *Materials Research Bulletin* **1980**, *15*, 783-789.
39. Wang, J.; Sun, Z.; Wei, X. In Performance and characteristic research in LiFePO_4 battery for electric vehicle applications, 2009 *IEEE Vehicle Power and Propulsion Conference*, 7-10 Sept, **2009**; pp 1657-1661.
40. Tian, Y.; Zeng, G.; Rutt, A.; Shi, T.; Kim, H.; Wang, J.; Koettgen, J.; Sun, Y.; Ouyang, B.; Chen, T.; Lun, Z.; Rong, Z.; Persson, K.; Ceder, G., Promises and Challenges of Next-Generation “Beyond Li-ion” Batteries for Electric Vehicles and Grid Decarbonization. *Chemical Reviews* **2021**, *121*, 1623-1669.
41. Yang, Y.; Zhou, J.; Wang, L.; Jiao, Z.; Xiao, M.; Huang, Q.-a.; Liu, M.; Shao, Q.; Sun, X.; Zhang, J., Prussian blue and its analogues as cathode materials for Na-, K-, Mg-, Ca-, Zn- and Al-ion batteries. *Nano Energy* **2022**, *99*, 107424.

42. Xiang, X.; Zhang, K.; Chen, J., Recent Advances and Prospects of Cathode Materials for Sodium-Ion Batteries. *Advanced materials (Deerfield Beach, Fla.)* **2015**, *27*, 5343-64.
43. Chen, S.; Yang, X.; Zhang, J.; Ma, J.; Meng, Y.; Tao, K.; Li, F.; Geng, J., Aluminum–lithium alloy as a stable and reversible anode for lithium batteries. *Electrochimica Acta* **2021**, *368*, 137626.
44. Zhou, W.; Zhang, M.; Kong, X.; Huang, W.; Zhang, Q., Recent Advance in Ionic-Liquid-Based Electrolytes for Rechargeable Metal-Ion Batteries. *Advanced Science* **2021**, *8*, 2004490.
45. Chen, J.; Chua, D. H. C.; Lee, P. S., The Advances of Metal Sulfides and In Situ Characterization Methods beyond Li Ion Batteries: Sodium, Potassium, and Aluminum Ion Batteries. *Small Methods* **2020**, *4*, 1900648.
46. Pan, H.; Hu, Y.-S.; Chen, L., Room-temperature stationary sodium-ion batteries for large-scale electric energy storage. *Energy & Environmental Science* **2013**, *6*, 2338-2360.
47. Nobuhara, K.; Nakayama, H.; Nose, M.; Nakanishi, S.; Iba, H., First-principles study of alkali metal-graphite intercalation compounds. *Journal of Power Sources* **2013**, *243*, 585-587.
48. Moriwake, H.; Kuwabara, A.; Fisher, C. A. J.; Ikuhara, Y., Why is sodium-intercalated graphite unstable? *RSC Advances* **2017**, *7*, 36550-36554.
49. Lee, B.; Paek, E.; Mitlin, D.; Lee, S. W., Sodium Metal Anodes: Emerging Solutions to Dendrite Growth. *Chemical Reviews* **2019**, *119*, 5416-5460.
50. Perveen, T.; Siddiq, M.; Shahzad, N.; Ihsan, R.; Ahmad, A.; Shahzad, M. I., Prospects in anode materials for sodium ion batteries - A review. *Renewable and Sustainable Energy Reviews* **2020**, *119*, 109549.
51. Usiskin, R.; Lu, Y.; Popovic, J.; Law, M.; Balaya, P.; Hu, Y.-S.; Maier, J., Fundamentals, status and promise of sodium-based batteries. *Nature Reviews Materials* **2021**, *6*, 1020-1035.
52. Dou, X.; Hasa, I.; Saurel, D.; Vaalma, C.; Wu, L.; Buchholz, D.; Bresser, D.; Komaba, S.; Passerini, S., Hard carbons for sodium-ion batteries: Structure, analysis, sustainability, and electrochemistry. *Materials Today* **2019**, *23*, 87-104.
53. Dahbi, M.; Yabuuchi, N.; Kubota, K.; Tokiwa, K.; Komaba, S., Negative electrodes for Na-ion batteries. *Physical Chemistry Chemical Physics* **2014**, *16*, 15007-15028.
54. Stevens, D. A.; Dahn, J. R., High Capacity Anode Materials for Rechargeable Sodium-Ion Batteries. *Journal of The Electrochemical Society* **2000**, *147*, 1271.
55. Kamiyama, A.; Kubota, K.; Igarashi, D.; Youn, Y.; Tateyama, Y.; Ando, H.; Gotoh, K.; Komaba, S., MgO-Template Synthesis of Extremely High

Capacity Hard Carbon for Na-Ion Battery. *Angewandte Chemie International Edition* **2021**, *60*, 5114-5120.

56. Yabuuchi, N.; Kubota, K.; Dahbi, M.; Komaba, S., Research Development on Sodium-Ion Batteries. *Chemical Reviews* **2014**, *114*, 11636-11682.

57. Ohzuku, T.; Takehara, Z.; Yoshizawa, S., Nonaqueous lithium/titanium dioxide cell. *Electrochimica Acta* **1979**, *24*, 219-222.

58. Xu, Y.; Memarzadeh Lotfabad, E.; Wang, H.; Farbod, B.; Xu, Z.; Kohandehghan, A.; Mitlin, D., Nanocrystalline anatase TiO₂: a new anode material for rechargeable sodium ion batteries. *Chemical Communications* **2013**, *49*, 8973-8975.

59. Wu, L.; Buchholz, D.; Bresser, D.; Gomes Chagas, L.; Passerini, S., Anatase TiO₂ nanoparticles for high power sodium-ion anodes. *Journal of Power Sources* **2014**, *251*, 379-385.

60. Rudola, A.; Saravanan, K.; Mason, C. W.; Balaya, P., Na₂Ti₃O₇: an intercalation based anode for sodium-ion battery applications. *Journal of Materials Chemistry A* **2013**, *1*, 2653-2662.

61. Delmas, C.; Cherkaoui, F.; Nadiri, A.; Hagenmuller, P., A nasicon-type phase as intercalation electrode: NaTi₂(PO₄)₃. *Materials Research Bulletin* **1987**, *22*, 631-639.

62. Senguttuvan, P.; Rouse, G.; Arroyo y de Dompablo, M. E.; Vezin, H.; Tarascon, J. M.; Palacín, M. R., Low-Potential Sodium Insertion in a NASICON-Type Structure through the Ti(III)/Ti(II) Redox Couple. *Journal of the American Chemical Society* **2013**, *135*, 3897-3903.

63. Hong, H. Y. P., Crystal structures and crystal chemistry in the system Na_{1+x}Zr₂Si_xP_{3-x}O₁₂. *Materials Research Bulletin* **1976**, *11*, 173-182.

64. Goodenough, J. B.; Hong, H. Y. P.; Kafalas, J. A., Fast Na⁺-ion transport in skeleton structures. *Materials Research Bulletin* **1976**, *11*, 203-220.

65. Anantharamulu, N.; Koteswara Rao, K.; Rambabu, G.; Vijaya Kumar, B.; Radha, V.; Vithal, M., A wide-ranging review on Nasicon type materials. *Journal of Materials Science* **2011**, *46*, 2821-2837.

66. Delmas, C.; Fouassier, C.; Hagenmuller, P., Structural classification and properties of the layered oxides. *Physica B+C* **1980**, *99*, 81-85.

67. Yabuuchi, N.; Kajiyama, M.; Iwatate, J.; Nishikawa, H.; Hitomi, S.; Okuyama, R.; Usui, R.; Yamada, Y.; Komaba, S., P2-type Na_x[Fe_{1/2}Mn_{1/2}]O₂ made from earth-abundant elements for rechargeable Na batteries. *Nature Materials* **2012**, *11*, 512-517.

68. Han, M. H.; Gonzalo, E.; Singh, G.; Rojo, T., A comprehensive review of sodium layered oxides: powerful cathodes for Na-ion batteries. *Energy & Environmental Science* **2015**, *8*, 81-102.

69. Masquelier, C.; Croguennec, L., Polyanionic (Phosphates, Silicates, Sulfates) Frameworks as Electrode Materials for Rechargeable Li (or Na) Batteries. *Chemical Reviews* **2013**, *113*, 6552-6591.
70. Fang, Y.; Zhang, J.; Xiao, L.; Ai, X.; Cao, Y.; Yang, H., Phosphate Framework Electrode Materials for Sodium Ion Batteries. *Advanced Science* **2017**, *4*, 1600392.
71. Kim, J.; Seo, D.-H.; Kim, H.; Park, I.; Yoo, J.-K.; Jung, S.-K.; Park, Y.-U.; Goddard III, W. A.; Kang, K., Unexpected discovery of low-cost maricite NaFePO_4 as a high-performance electrode for Na-ion batteries. *Energy & Environmental Science* **2015**, *8*, 540-545.
72. Jian, Z.; Zhao, L.; Pan, H.; Hu, Y.-S.; Li, H.; Chen, W.; Chen, L., Carbon coated $\text{Na}_3\text{V}_2(\text{PO}_4)_3$ as novel electrode material for sodium ion batteries. *Electrochemistry Communications* **2012**, *14*, 86-89.
73. Senthilkumar, B.; Murugesan, C.; Sharma, L.; Lochab, S.; Barpanda, P., An Overview of Mixed Polyanionic Cathode Materials for Sodium-Ion Batteries. *Small Methods* **2019**, *3*, 1800253.
74. Li, H.; Xu, M.; Zhang, Z.; Lai, Y.; Ma, J., Engineering of Polyanion Type Cathode Materials for Sodium-Ion Batteries: Toward Higher Energy/Power Density. *Advanced Functional Materials* **2020**, *30*, 2000473.
75. He, L.; Li, H.; Ge, X.; Li, S.; Wang, X.; Wang, S.; Zhang, L.; Zhang, Z., Iron-Phosphate-Based Cathode Materials for Cost-Effective Sodium-Ion Batteries: Development, Challenges, and Prospects. *Advanced Materials Interfaces* **2022**, *9*, 2200515.
76. Yang, W.; Liu, Q.; Zhao, Y.; Mu, D.; Tan, G.; Gao, H.; Li, L.; Chen, R.; Wu, F., Progress on Fe-Based Polyanionic Oxide Cathodes Materials toward Grid-Scale Energy Storage for Sodium-Ion Batteries. *Small Methods* **2022**, *6*, 2200555.
77. Fernández-Ropero, A. J.; Zarrabeitia, M.; Reynaud, M.; Rojo, T.; Casas-Cabanas, M., Toward Safe and Sustainable Batteries: $\text{Na}_4\text{Fe}_3(\text{PO}_4)_2\text{P}_2\text{O}_7$ as a Low-Cost Cathode for Rechargeable Aqueous Na-Ion Batteries. *The Journal of Physical Chemistry C* **2018**, *122*, 133-142.
78. Kim, H.; Yoon, G.; Park, I.; Park, K.-Y.; Lee, B.; Kim, J.; Park, Y.-U.; Jung, S.-K.; Lim, H.-D.; Ahn, D.; Lee, S.; Kang, K., Anomalous Jahn–Teller behavior in a manganese-based mixed-phosphate cathode for sodium ion batteries. *Energy & Environmental Science* **2015**, *8*, 3325-3335.
79. Nose, M.; Nakayama, H.; Nobuhara, K.; Yamaguchi, H.; Nakanishi, S.; Iba, H., $\text{Na}_4\text{Co}_3(\text{PO}_4)_2\text{P}_2\text{O}_7$: A novel storage material for sodium-ion batteries. *Journal of Power Sources* **2013**, *234*, 175-179.

80. Senthilkumar, B.; Ananya, G.; Aashok, P.; Ramaprabhu, S., Synthesis of Carbon coated Nano- $\text{Na}_4\text{Ni}_3(\text{PO}_4)_2\text{P}_2\text{O}_7$ as a Novel Cathode Material for Hybrid Supercapacitors. *Electrochimica Acta* **2015**, *169*, 447-455.
81. Wang, B.; Han, Y.; Wang, X.; Bahlawane, N.; Pan, H.; Yan, M.; Jiang, Y., Prussian Blue Analogs for Rechargeable Batteries. *iScience* **2018**, *3*, 110-133.
82. Li, W.-J.; Han, C.; Cheng, G.; Chou, S.-L.; Liu, H.-K.; Dou, S.-X., Chemical Properties, Structural Properties, and Energy Storage Applications of Prussian Blue Analogues. *Small* **2019**, *15*, 1900470.
83. You, Y.; Wu, X.-L.; Yin, Y.-X.; Guo, Y.-G., High-quality Prussian blue crystals as superior cathode materials for room-temperature sodium-ion batteries. *Energy & Environmental Science* **2014**, *7*, 1643-1647.
84. Yang, D.; Xu, J.; Liao, X.-Z.; He, Y.-S.; Liu, H.; Ma, Z.-F., Structure optimization of Prussian blue analogue cathode materials for advanced sodium ion batteries. *Chemical Communications* **2014**, *50*, 13377-13380.
85. Wang, B.; Wang, X.; Liang, C.; Yan, M.; Jiang, Y., An All-Prussian-Blue-Based Aqueous Sodium-Ion Battery. *ChemElectroChem* **2019**, *6*, 4848-4853.
86. Ponrouch, A.; Monti, D.; Boschini, A.; Steen, B.; Johansson, P.; Palacín, M. R., Non-aqueous electrolytes for sodium-ion batteries. *Journal of Materials Chemistry A* **2015**, *3*, 22-42.
87. Daniel, C.; Besenhard, J. O., *Handbook of Battery Materials*. Wiley 2012.
88. Beck, F.; Rüetschi, P., Rechargeable batteries with aqueous electrolytes. *Electrochimica Acta* **2000**, *45*, 2467-2482.
89. Hasa, I.; Passerini, S.; Hassoun, J., Characteristics of an ionic liquid electrolyte for sodium-ion batteries. *Journal of Power Sources* **2016**, *303*, 203-207.
90. Wang, Y.; Song, S.; Xu, C.; Hu, N.; Molenda, J.; Lu, L., Development of solid-state electrolytes for sodium-ion battery—A short review. *Nano Materials Science* **2019**, *1*, 91-100.
91. Zhou, H.; Wang, Y.; Li, H.; He, P., The Development of a New Type of Rechargeable Batteries Based on Hybrid Electrolytes. *ChemSusChem* **2010**, *3*, 1009-1019.
92. Liu, M.; Ao, H.; Jin, Y.; Hou, Z.; Zhang, X.; Zhu, Y.; Qian, Y., Aqueous rechargeable sodium ion batteries: developments and prospects. *Materials Today Energy* **2020**, *17*, 100432.
93. Liu, Z.; Huang, Y.; Huang, Y.; Yang, Q.; Li, X.; Huang, Z.; Zhi, C., Voltage issue of aqueous rechargeable metal-ion batteries. *Chemical Society Reviews* **2020**, *49*, 180-232.
94. Millet, P., Fundamentals of Water Electrolysis. In *Hydrogen Production*, 2015; pp 33-62.

95. Han, J.; Zarrabeitia, M.; Mariani, A.; Jusys, Z.; Hekmatfar, M.; Zhang, H.; Geiger, D.; Kaiser, U.; Behm, R. J.; Varzi, A.; Passerini, S., Halide-free water-in-salt electrolytes for stable aqueous sodium-ion batteries. *Nano Energy* **2020**, *77*, 105176.
96. Li, Y.; Xu, J.; Liu, H.; Hu, X.; Zhang, Q.; Peng, W.; Li, Y.; Zhang, F.; Han, Y.; Fan, X., Suppressing Vanadium Dissolution in “Water-in-Salt” Electrolytes for 3.2 V Aqueous Sodium-Ion Pseudocapacitors. *ACS Applied Materials & Interfaces* **2022**, *14*, 35485-35494.
97. Ren, Q.; Yuan, Y.; Wang, S., Interfacial Strategies for Suppression of Mn Dissolution in Rechargeable Battery Cathode Materials. *ACS Applied Materials & Interfaces* **2022**, *14*, 23022-23032.
98. Pilipavičius, J.; Traškina, N.; Juodkazytė, J.; Vilčiauskas, L., The mechanism of $\text{NaTi}_2(\text{PO}_4)_3$ aqueous electrochemical degradation revisited. *Electrochimica Acta* **2023**, 142993.
99. Pahari, D.; Puravankara, S., Greener, Safer, and Sustainable Batteries: An Insight into Aqueous Electrolytes for Sodium-Ion Batteries. *ACS Sustainable Chemistry & Engineering* **2020**, *8*, 10613-10625.
100. B. H. Toby, R. B. V. D., GSAS-II: the genesis of a modern open-source all purpose crystallography software package. *Journal of Applied Crystallography* **2013**, *46*, 544-549.
101. Momma, K.; Izumi, F., VESTA 3 for three-dimensional visualization of crystal, volumetric and morphology data. *Journal of Applied Crystallography* **2011**, *44*, 1272-1276.
102. Schneider, C. A.; Rasband, W. S.; Eliceiri, K. W., NIH Image to ImageJ: 25 years of image analysis. *Nature Methods* **2012**, *9*, 671-675.
103. Chen, S.; Wu, C.; Shen, L.; Zhu, C.; Huang, Y.; Xi, K.; Maier, J.; Yu, Y., Challenges and Perspectives for NASICON-Type Electrode Materials for Advanced Sodium-Ion Batteries. *Advanced Materials* **2017**, *29*, 1700431.
104. Wu, M.; Ni, W.; Hu, J.; Ma, J., NASICON-Structured $\text{NaTi}_2(\text{PO}_4)_3$ for Sustainable Energy Storage. *Nano-Micro Letters* **2019**, *11*, 44.
105. Zhang, X.; Cheng, X.; Zhang, Q., Nanostructured energy materials for electrochemical energy conversion and storage: A review. *Journal of Energy Chemistry* **2016**, *25*, 967-984.
106. Gryaznov, D.; Stauffer, S. K.; Kotomin, E. A.; Vilčiauskas, L., Hybrid density functional theoretical study of NASICON-type $\text{Na}_x\text{Ti}_2(\text{PO}_4)_3$ ($x = 1-4$). *Physical Chemistry Chemical Physics* **2020**, *22*, 11861-11870.
107. Zhan, X.; Shirpour, M., Evolution of solid/aqueous interface in aqueous sodium-ion batteries. *Chem Commun (Camb)* **2016**, *53*, 204-207.
108. Wu, W.; Yan, J.; Wise, A.; Rutt, A.; Whitacre, J. F., Using Intimate Carbon to Enhance the Performance of $\text{NaTi}_2(\text{PO}_4)_3$ Anode Materials: Carbon

- Nanotubes vs Graphite. *Journal of The Electrochemical Society* **2014**, *161*, A561.
109. Usiskin, R. E.; Maier, J., Guidelines for optimizing the architecture of battery insertion electrodes based on the concept of wiring lengths. *Physical Chemistry Chemical Physics* **2018**, *20*, 16449-16462.
110. Cao, X.; Yang, Y., Facile synthesis of $\text{NaTi}_2(\text{PO}_4)_3$ -carbon composite through solid state method and its application in aqueous sodium ion battery. *Materials Letters* **2018**, *231*, 183-186.
111. Zhou, Z. F.; Li, N.; Zhang, C.; Chen, X.; Xu, F.; Peng, C., Preparation of carbon layer and carbon nanotube co-decorated $\text{NaTi}_2(\text{PO}_4)_3$ anode and its application in sodium-ion batteries. *Solid State Ionics* **2018**, *324*, 87-91.
112. Zhang, Q.; Man, P.; He, B.; Li, C.; Li, Q.; Pan, Z.; Wang, Z.; Yang, J.; Wang, Z.; Zhou, Z.; Lu, X.; Niu, Z.; Yao, Y.; Wei, L., Binder-free $\text{NaTi}_2(\text{PO}_4)_3$ anodes for high-performance coaxial-fiber aqueous rechargeable sodium-ion batteries. *Nano Energy* **2020**, *67*, 104212.
113. Liu, H. X.; Zhang, H. R.; Su, C. N.; Li, X. M.; Guo, Y., Three-dimensional $\text{NaTi}_2(\text{PO}_4)_3@C$ microsphere as a high-performance anode material for advanced sodium-ion batteries. *Solid State Ionics* **2018**, *322*, 79-84.
114. Wei, P.; Liu, Y. X.; Wang, Z. H.; Huang, Y. Y.; Jin, Y.; Liu, Y.; Sun, S. X.; Qiu, Y. G.; Peng, J.; Xu, Y.; Sun, X. P.; Fang, C.; Han, J. T.; Huang, Y. H., Porous $\text{NaTi}_2(\text{PO}_4)_3/C$ Hierarchical Nanofibers for Ultrafast Electrochemical Energy Storage. *Acs Applied Materials & Interfaces* **2018**, *10*, 27039-27046.
115. Grover, V.; Mandal, B. P.; Tyagi, A. K., Solid State Synthesis of Materials. In Handbook on Synthesis Strategies for Advanced Materials : Volume-I: Techniques and Fundamentals, Tyagi, A. K.; Ningthoujam, R. S., Eds. *Springer Singapore*: Singapore, **2021**; pp 1-49.
116. Tutlienė, S.; Petrulėvičienė, M.; Pilipavičius, J.; Žarkov, A.; Selskis, A.; Stanionytė, S.; Juodkazytė, J.; Vilčiauskas, L., Electrochemical Performance of Sol-Gel Synthesized $\text{NaTi}_2(\text{PO}_4)_3$ - Carbon Composites as Aqueous Na-Ion Battery Anodes. *Journal of The Electrochemical Society* **2021**, *168*, 060545.
117. Sakka, S., Handbook of sol-gel science and technology. 1. Sol-gel processing. *Springer Science & Business Media* **2005**; Vol. 1.
118. Devaraju, M. K.; Honma, I., Hydrothermal and Solvothermal Process Towards Development of LiMPO_4 (M = Fe, Mn) Nanomaterials for Lithium-Ion Batteries. *Advanced Energy Materials* **2012**, *2*, 284-297.
119. Zhu, C.; Usiskin, R. E.; Yu, Y.; Maier, J., The nanoscale circuitry of battery electrodes. *Science* **2017**, *358*, eaao2808.

120. Wang, K.; Liu, Y.; Ding, Z.; Chen, Z.; Zhu, G.; Xu, X.; Lu, T.; Pan, L., Controlled synthesis of $\text{NaTi}_2(\text{PO}_4)_3$ /Carbon composite derived from Metal-organic-frameworks as highly-efficient electrodes for hybrid capacitive deionization. *Separation and Purification Technology* **2021**, *278*, 119565.
121. Wei, T.; Yang, G.; Wang, C., Iso-Oriented $\text{NaTi}_2(\text{PO}_4)_3$ Mesocrystals as Anode Material for High-Energy and Long-Durability Sodium-Ion Capacitor. *ACS Applied Materials & Interfaces* **2017**, *9*, 31861-31870.
122. Xu, C.; Xu, Y.; Tang, C.; Wei, Q.; Meng, J.; Huang, L.; Zhou, L.; Zhang, G.; He, L.; Mai, L., Carbon-coated hierarchical $\text{NaTi}_2(\text{PO}_4)_3$ mesoporous microflowers with superior sodium storage performance. *Nano Energy* **2016**, *28*, 224-231.
123. Huang, Z.; Liu, L.; Yi, L.; Xiao, W.; Li, M.; Zhou, Q.; Guo, G.; Chen, X.; Shu, H.; Yang, X.; Wang, X., Facile solvothermal synthesis of $\text{NaTi}_2(\text{PO}_4)_3/\text{C}$ porous plates as electrode materials for high-performance sodium ion batteries. *Journal of Power Sources* **2016**, *325*, 474-481.
124. Xu, Y.; Cao, W.; Yin, Y.; Sheng, J.; An, Q.; Wei, Q.; Yang, W.; Mai, L., Novel $\text{NaTi}_2(\text{PO}_4)_3$ nanowire clusters as high performance cathodes for Mg-Na hybrid-ion batteries. *Nano Energy* **2019**, *55*, 526-533.
125. Jiang, X.; Wang, Y.; Li, M., Selecting water-alcohol mixed solvent for synthesis of polydopamine nano-spheres using solubility parameter. *Scientific Reports* **2014**, *4*, 6070.
126. Clarke, C. J.; Tu, W.-C.; Levers, O.; Bröhl, A.; Hallett, J. P., Green and Sustainable Solvents in Chemical Processes. *Chemical Reviews* **2018**, *118*, 747-800.
127. Byrne, F. P.; Jin, S.; Paggiola, G.; Petchey, T. H. M.; Clark, J. H.; Farmer, T. J.; Hunt, A. J.; Robert McElroy, C.; Sherwood, J., Tools and techniques for solvent selection: green solvent selection guides. *Sustainable Chemical Processes* **2016**, *4*, 7.
128. Capello, C.; Fischer, U.; Hungerbühler, K., What is a green solvent? A comprehensive framework for the environmental assessment of solvents. *Green Chemistry* **2007**, *9*, 927-934.
129. Rodrigo, J. L.; Carrasco, P.; Alamo, J., Thermal expansion of $\text{NaTi}_2(\text{PO}_4)_3$ studied by rietveld method from X-ray diffraction data. *Materials Research Bulletin* **1989**, *24*, 611-618.
130. M. A. Salvadó, P. P., S. García-Granda, J. R. García, J. Rodríguez and M. T. Fernández-Díaz, Neutron powder diffraction study of $\alpha\text{-Ti}(\text{HPO}_4)_2\cdot\text{H}_2\text{O}$ and $\alpha\text{-Hf}(\text{HPO}_4)_2\cdot\text{H}_2\text{O}$; H-atom positions. *Acta Crystallographica Section B: Structural Science, Crystal Engineering and Materials* **1997**, *B53*.

131. Nan, C.; Lu, J.; Chen, C.; Peng, Q.; Li, Y., Solvothermal synthesis of lithium iron phosphate nanoplates. *Journal of Materials Chemistry* **2011**, *21*, 9994-9996.
132. Ortíz-Oliveros, H. B.; Flores-Espinosa, R. M.; Ordoñez-Regil, E.; Fernández-Valverde, S. M., Synthesis of α -Ti(HPO₄)₂·H₂O and sorption of Eu (III). *Chemical Engineering Journal* **2014**, *236*, 398-405.
133. Thanh, N. T. K.; Maclean, N.; Mahiddine, S., Mechanisms of Nucleation and Growth of Nanoparticles in Solution. *Chemical Reviews* **2014**, *114*, 7610-7630.
134. Azizian, S.; Hemmati, M., Surface Tension of Binary Mixtures of Ethanol + Ethylene Glycol from 20 to 50 °C. *Journal of Chemical & Engineering Data* **2003**, *48*, 662-663.
135. Vazquez, G.; Alvarez, E.; Navaza, J. M., Surface Tension of Alcohol Water + Water from 20 to 50 .degree.C. *Journal of Chemical & Engineering Data* **1995**, *40*, 611-614.
136. Zuend, A.; Marcolli, C.; Booth, A. M.; Lienhard, D. M.; Soonsin, V.; Krieger, U. K.; Topping, D. O.; McFiggans, G.; Peter, T.; Seinfeld, J. H., New and extended parameterization of the thermodynamic model AIOMFAC: calculation of activity coefficients for organic-inorganic mixtures containing carboxyl, hydroxyl, carbonyl, ether, ester, alkenyl, alkyl, and aromatic functional groups. *Atmos. Chem. Phys.* **2011**, *11*, 9155-9206.
137. AIOMFAC homepage. <https://aiomfac.lab.mcgill.ca> (August 2023),
138. Zuend, A.; Marcolli, C.; Luo, B. P.; Peter, T., A thermodynamic model of mixed organic-inorganic aerosols to predict activity coefficients. *Atmos. Chem. Phys.* **2008**, *8*, 4559-4593.
139. Dalard, F.; Deroo, D.; Foscallo, D.; Merienne, J. L., Theoretical study of a composite electrode using an intercalation compound: Influence of the particle size distribution on the depth of discharge. *Journal of Power Sources* **1985**, *14*, 209-213.
140. Hawley, W. B.; Li, J., Electrode manufacturing for lithium-ion batteries—Analysis of current and next generation processing. *Journal of Energy Storage* **2019**, *25*, 100862.
141. Niu, Y.; Xu, M.; Zhang, Y.; Han, J.; Wang, Y.; Li, C. M., Detailed investigation of a NaTi₂(PO₄)₃ anode prepared by pyro-synthesis for Na-ion batteries. *RSC Advances* **2016**, *6*, 45605-45611.
142. Ali, G.; Islam, M.; Jung, H.-G.; Nam, K.-W.; Chung, K. Y., Probing the Sodium Insertion/Extraction Mechanism in a Layered NaVO₃ Anode Material. *ACS Applied Materials & Interfaces* **2018**, *10*, 18717-18725.

143. Wang, Y.; Meng, X.; Sun, J.; Liu, Y.; Hou, L., Recent Progress in “Water-in-Salt” Electrolytes Toward Non-lithium Based Rechargeable Batteries. *Frontiers in Chemistry* **2020**, *8*.
144. Hu, Q.; Liao, J.-Y.; Li, C.-T.; He, X.-D.; Ding, X.; Chen, C.-H., Synthesis of porous carbon-coated $\text{NaTi}_2(\text{PO}_4)_3$ nanocubes with a high-yield and superior rate properties. *Journal of Materials Chemistry A* **2018**, *6*, 24503-24508.
145. Ye, S.; Li, Z.; Song, T.; Cheng, D.; Xu, Q.; Liu, H.; Wang, Y., Self-generated hollow $\text{NaTi}_2(\text{PO}_4)_3$ nanocubes decorated with graphene as a large capacity and long lifetime anode for sodium-ion batteries. *RSC Advances* **2017**, *7*, 56743-56751.
146. Mohamed, A. I.; Whitacre, J. F., Capacity Fade of $\text{NaTi}_2(\text{PO}_4)_3$ in Aqueous Electrolyte Solutions: Relating pH Increases to Long Term Stability. *Electrochimica Acta* **2017**, *235*, 730-739.
147. Hu, X.; Tian, X.; Lin, Y.-W.; Wang, Z., Nickel foam and stainless steel mesh as electrocatalysts for hydrogen evolution reaction, oxygen evolution reaction and overall water splitting in alkaline media. *RSC Advances* **2019**, *9*, 31563-31571.
148. Jiang, L.; Liu, L.; Yue, J.; Zhang, Q.; Zhou, A.; Borodin, O.; Suo, L.; Li, H.; Chen, L.; Xu, K.; Hu, Y.-S., High-Voltage Aqueous Na-Ion Battery Enabled by Inert-Cation-Assisted Water-in-Salt Electrolyte. *Advanced Materials* **2020**, *32*, 1904427.
149. Chao, D.; Qiao, S.-Z., Toward High-Voltage Aqueous Batteries: Super- or Low-Concentrated Electrolyte? *Joule* **2020**, *4*, 1846-1851.
150. Yu, F.; Du, L.; Zhang, G.; Su, F.; Wang, W.; Sun, S., Electrode Engineering by Atomic Layer Deposition for Sodium-Ion Batteries: From Traditional to Advanced Batteries. *Advanced Functional Materials* **2020**, *30*, 1906890.
151. Meng, X., Atomic-scale surface modifications and novel electrode designs for high-performance sodium-ion batteries via atomic layer deposition. *Journal of Materials Chemistry A* **2017**, *5*, 10127-10149.
152. Zhao, Y.; Zheng, K.; Sun, X., Addressing Interfacial Issues in Liquid-Based and Solid-State Batteries by Atomic and Molecular Layer Deposition. *Joule* **2018**, *2*, 2583-2604.
153. Plečkaitytė, G.; Petrulevičienė, M.; Staišiūnas, L.; Tediashvili, D.; Pilipavičius, J.; Juodkazytė, J.; Vilčiauskas, L., Understanding and mitigation of $\text{NaTi}_2(\text{PO}_4)_3$ degradation in aqueous Na-ion batteries. *Journal of Materials Chemistry A* **2021**, *9*, 12670-12683.
154. Staišiūnas, L.; Pilipavičius, J.; Tediashvili, D.; Juodkazytė, J.; Vilčiauskas, L., Engineering of Conformal Electrode Coatings by Atomic

Layer Deposition for Aqueous Na-ion Battery Electrodes. *Journal of The Electrochemical Society* **2023**, *170*, 050533.

155. Wu, C.; Kopold, P.; Ding, Y.-L.; van Aken, P. A.; Maier, J.; Yu, Y., Synthesizing Porous NaTi₂(PO₄)₃ Nanoparticles Embedded in 3D Graphene Networks for High-Rate and Long Cycle-Life Sodium Electrodes. *ACS Nano* **2015**, *9*, 6610-6618.

156. Song, J.; Xiao, B.; Lin, Y.; Xu, K.; Li, X., Interphases in Sodium-Ion Batteries. *Advanced Energy Materials* **2018**, *8*, 1703082.

157. Heubner, C.; Nikolowski, K.; Reuber, S.; Schneider, M.; Wolter, M.; Michaelis, A., Recent Insights into Rate Performance Limitations of Li-ion Batteries. *Batteries & Supercaps* **2021**, *4*, 268-285.

158. Ding, C.; Chen, Z.; Cao, C.; Liu, Y.; Gao, Y., Advances in Mn-Based Electrode Materials for Aqueous Sodium-Ion Batteries. *Nano-Micro Letters* **2023**, *15*, 192.

159. Li, H.; Zhang, W.; Sun, K.; Guo, J.; Yuan, K.; Fu, J.; Zhang, T.; Zhang, X.; Long, H.; Zhang, Z.; Lai, Y.; Sun, H., Manganese-Based Materials for Rechargeable Batteries beyond Lithium-Ion. *Advanced Energy Materials* **2021**, *11*, 2100867.

160. Gao, Y.; Yang, H.; Bai, Y.; Wu, C., Mn-based oxides for aqueous rechargeable metal ion batteries. *Journal of Materials Chemistry A* **2021**, *9*, 11472-11500.

161. Kim, S.-W.; Seo, D.-H.; Kim, H.; Park, K.-Y.; Kang, K., A comparative study on Na₂MnPO₄F and Li₂MnPO₄F for rechargeable battery cathodes. *Physical Chemistry Chemical Physics* **2012**, *14*, 3299-3303.

162. Park, C. S.; Kim, H.; Shakoor, R. A.; Yang, E.; Lim, S. Y.; Kahraman, R.; Jung, Y.; Choi, J. W., Anomalous Manganese Activation of a Pyrophosphate Cathode in Sodium Ion Batteries: A Combined Experimental and Theoretical Study. *Journal of the American Chemical Society* **2013**, *135*, 2787-2792.

163. Ortiz-Vitoriano, N.; Drewett, N. E.; Gonzalo, E.; Rojo, T., High performance manganese-based layered oxide cathodes: overcoming the challenges of sodium ion batteries. *Energy & Environmental Science* **2017**, *10*, 1051-1074.

164. Zuo, D.; Wang, C.; Wu, J.; Qiu, H.; Zhang, Q.; Han, J.; Liu, X., Comprehensive study of Na_{2-x}MnFe(CN)₆·yH₂O cathodes with cube morphology: Structure, valence state and electrochemical properties. *Solid State Ionics* **2019**, *340*, 115025.

165. Whitacre, J. F.; Wiley, T.; Shanbhag, S.; Wenzhuo, Y.; Mohamed, A.; Chun, S. E.; Weber, E.; Blackwood, D.; Lynch-Bell, E.; Gulakowski, J.; Smith, C.; Humphreys, D., An aqueous electrolyte, sodium ion functional,

large format energy storage device for stationary applications. *Journal of Power Sources* **2012**, *213*, 255-264.

166. Jung, R.; Linsenmann, F.; Thomas, R.; Wandt, J.; Solchenbach, S.; Maglia, F.; Stinner, C.; Tromp, M.; Gasteiger, H. A., Nickel, Manganese, and Cobalt Dissolution from Ni-Rich NMC and Their Effects on NMC622-Graphite Cells. *Journal of The Electrochemical Society* **2019**, *166*, A378.

167. Nikman, S.; Zhao, D.; Gonzalez-Perez, V.; Hoster, H. E.; Mertens, S. F. L., Surface or bulk? Real-time manganese dissolution detection in a lithium-ion cathode. *Electrochimica Acta* **2021**, *386*, 138373.

168. Zhan, C.; Wu, T.; Lu, J.; Amine, K., Dissolution, migration, and deposition of transition metal ions in Li-ion batteries exemplified by Mn-based cathodes – a critical review. *Energy & Environmental Science* **2018**, *11*, 243-257.

169. Yaghoobnejad Asl, H.; Manthiram, A., Proton-Induced Disproportionation of Jahn–Teller-Active Transition-Metal Ions in Oxides Due to Electronically Driven Lattice Instability. *Journal of the American Chemical Society* **2020**, *142*, 21122-21130.

170. Choi, J. U.; Park, Y. J.; Jo, J. H.; Kuo, L.-Y.; Kaghadzchi, P.; Myung, S.-T., Unraveling the Role of Earth-Abundant Fe in the Suppression of Jahn–Teller Distortion of P'2-Type $\text{Na}_{2/3}\text{MnO}_2$: Experimental and Theoretical Studies. *ACS Applied Materials & Interfaces* **2018**, *10*, 40978-40984.

171. Liu, L.; Wu, Y.-C.; Huang, L.; Liu, K.; Duployer, B.; Rozier, P.; Taberna, P.-L.; Simon, P., Alkali Ions Pre-Intercalated Layered MnO_2 Nanosheet for Zinc-Ions Storage. *Advanced Energy Materials* **2021**, *11*, 2101287.

172. Poyraz, A. S.; Laughlin, J.; Zec, Z., Improving the cycle life of cryptomelane type manganese dioxides in aqueous rechargeable zinc ion batteries: The effect of electrolyte concentration. *Electrochimica Acta* **2019**, *305*, 423-432.

173. Kim, H.; Park, I.; Seo, D.-H.; Lee, S.; Kim, S.-W.; Kwon, W. J.; Park, Y.-U.; Kim, C. S.; Jeon, S.; Kang, K., New Iron-Based Mixed-Polyanion Cathodes for Lithium and Sodium Rechargeable Batteries: Combined First Principles Calculations and Experimental Study. *Journal of the American Chemical Society* **2012**, *134*, 10369-10372.

174. Chen, H.; Hautier, G.; Jain, A.; Moore, C.; Kang, B.; Doe, R.; Wu, L.; Zhu, Y.; Tang, Y.; Ceder, G., Carbonophosphates: A New Family of Cathode Materials for Li-Ion Batteries Identified Computationally. *Chemistry of Materials* **2012**, *24*, 2009-2016.

175. Xie, B.; Sakamoto, R.; Kitajou, A.; Nakamoto, K.; Zhao, L.; Okada, S.; Kobayashi, W.; Okada, M.; Takahara, T., Cathode Properties of

$\text{Na}_3\text{MnPO}_4\text{CO}_3$ Prepared by the Mechanical Ball Milling Method for Na-Ion Batteries. *Energies* **2019**, *12*, 4534.

176. Moring, J.; Kostiner, E., The crystal structure of NaMnPO_4 . *Journal of Solid State Chemistry* **1986**, *61*, 379-383.

177. Rui, X. H.; Li, C.; Chen, C. H., Synthesis and characterization of carbon-coated $\text{Li}_3\text{V}_2(\text{PO}_4)_3$ cathode materials with different carbon sources. *Electrochimica Acta* **2009**, *54*, 3374-3380.

178. Tang, H.; Tang, Z., Effect of different carbon sources on electrochemical properties of $\text{Li}_2\text{ZnTi}_3\text{O}_8/\text{C}$ anode material in lithium-ion batteries. *Journal of Alloys and Compounds* **2014**, *613*, 267-274.

179. Wang, J.; Bi, J.; Wang, W.; Xing, Z.; Bai, Y.; Leng, M.; Gao, X., $\text{Na}_2\text{Ti}_6\text{O}_{13}$ Coated with Carbon Produced by Citric Acid as an Anode Material in Sodium Ion Batteries. *Journal of The Electrochemical Society* **2020**, *167*, 090539.

180. Zachariasen, W. H., Untersuchungen über die Kristallstrukturen von Sesquioxiden und Verbindungen ABO_3 . *Geologiska Föreningen i Stockholm Förhandlingar* **1929**, *51*, 123-123.

181. Wang, C.; Sawicki, M.; Emani, S.; Liu, C.; Shaw, L. L., $\text{Na}_3\text{MnCO}_3\text{PO}_4$ – A High Capacity, Multi-Electron Transfer Redox Cathode Material for Sodium Ion Batteries. *Electrochimica Acta* **2015**, *161*, 322-328.

182. E. N. Maslen, V. A. S., N. R. Streltsova and N. Ishizawa, Electron density and optical anisotropy in rhombohedral carbonates. III. Synchrotron X-ray studies of CaCO_3 , MgCO_3 and MnCO_3 . *Acta Crystallographica Section B: Structural Science, Crystal Engineering and Materials* **1995**, *B51*, 929-939.

183. Tediashvili, D.; Gečė, G.; Pilipavičius, J.; Daugėla, S.; Šalkus, T.; Juodkazytė, J.; Vilčiauskas, L., Synthesis, characterization, and degradation study of Mn-based phosphate frameworks ($\text{Na}_3\text{MnTi}(\text{PO}_4)_3$, $\text{Na}_3\text{MnPO}_4\text{CO}_3$, $\text{Na}_4\text{Mn}_3(\text{PO}_4)_2\text{P}_2\text{O}_7$) as aqueous Na-ion battery positive electrodes. *Electrochimica Acta* **2022**, *417*, 140294.

184. Ryu, S.; Wang, J. E.; Kim, J.-H.; Ruffo, R.; Jung, Y. H.; Kim, D. K., A study on cobalt substitution in sodium manganese mixed-anion phosphates as positive electrode materials for Na-ion batteries. *Journal of Power Sources* **2019**, *444*, 227274.

185. Chen, H.; Hao, Q.; Zivkovic, O.; Hautier, G.; Du, L.-S.; Tang, Y.; Hu, Y.-Y.; Ma, X.; Grey, C. P.; Ceder, G., Sidorenkite ($\text{Na}_3\text{MnPO}_4\text{CO}_3$): A New Intercalation Cathode Material for Na-Ion Batteries. *Chemistry of Materials* **2013**, *25*, 2777-2786.

186. Zhang, Y.; Huo, Q.-y.; Du, P.-p.; Wang, L.-z.; Zhang, A.-q.; Song, Y.-h.; Lv, Y.; Li, G.-y., Advances in new cathode material LiFePO_4 for lithium-ion batteries. *Synthetic Metals* **2012**, *162*, 1315-1326.

187. Fang, Y.; Chen, Z.; Xiao, L.; Ai, X.; Cao, Y.; Yang, H., Recent Progress in Iron-Based Electrode Materials for Grid-Scale Sodium-Ion Batteries. *Small* **2018**, *14*, 1703116.
188. Fang, Y.; Liu, Q.; Xiao, L.; Ai, X.; Yang, H.; Cao, Y., High-Performance Olivine NaFePO_4 Microsphere Cathode Synthesized by Aqueous Electrochemical Displacement Method for Sodium Ion Batteries. *ACS Applied Materials & Interfaces* **2015**, *7*, 17977-17984.
189. Jeong, S.; Kim, B. H.; Park, Y. D.; Lee, C. Y.; Mun, J.; Tron, A., Artificially coated NaFePO_4 for aqueous rechargeable sodium-ion batteries. *Journal of Alloys and Compounds* **2019**, *784*, 720-726.
190. Sun, A.; Beck, F. R.; Haynes, D.; Poston, J. A.; Narayanan, S. R.; Kumta, P. N.; Manivannan, A., Synthesis, characterization, and electrochemical studies of chemically synthesized NaFePO_4 . *Materials Science and Engineering: B* **2012**, *177*, 1729-1733.
191. Qiu, S.; Wu, X.; Wang, M.; Lucero, M.; Wang, Y.; Wang, J.; Yang, Z.; Xu, W.; Wang, Q.; Gu, M.; Wen, J.; Huang, Y.; Xu, Z. J.; Feng, Z., NASICON-type $\text{Na}_3\text{Fe}_2(\text{PO}_4)_3$ as a low-cost and high-rate anode material for aqueous sodium-ion batteries. *Nano Energy* **2019**, *64*, 103941.
192. Liu, Y.; Zhou, Y.; Zhang, J.; Xia, Y.; Chen, T.; Zhang, S., Monoclinic Phase $\text{Na}_3\text{Fe}_2(\text{PO}_4)_3$: Synthesis, Structure, and Electrochemical Performance as Cathode Material in Sodium-Ion Batteries. *ACS Sustainable Chemistry & Engineering* **2017**, *5*, 1306-1314.
193. Wang, S.; Gao, N.; Wang, G.; He, C.; Lv, S.; Qiu, J., Three-dimensional hierarchical $\text{Na}_3\text{Fe}_2(\text{PO}_4)_3/\text{C}$ with superior and fast sodium uptake for efficient hybrid capacitive deionization. *Desalination* **2021**, *520*, 115341.
194. Cao, Y.; Liu, Y.; Chen, T.; Xia, X.; Zhang, L.-C.; Zhang, J.; Xia, Y., Sol-gel synthesis of porous $\text{Na}_3\text{Fe}_2(\text{PO}_4)_3$ with enhanced sodium-ion storage capability. *Ionics* **2019**, *25*, 1083-1090.
195. Cao, Y.; Liu, Y.; Zhao, D.; Zhang, J.; Xia, X.; Chen, T.; Zhang, L.-c.; Qin, P.; Xia, Y., K-doped $\text{Na}_3\text{Fe}_2(\text{PO}_4)_3$ cathode materials with high-stable structure for sodium-ion stored energy battery. *Journal of Alloys and Compounds* **2019**, *784*, 939-946.
196. Yuan, T.; Wang, Y.; Zhang, J.; Pu, X.; Ai, X.; Chen, Z.; Yang, H.; Cao, Y., 3D graphene decorated $\text{Na}_4\text{Fe}_3(\text{PO}_4)_2(\text{P}_2\text{O}_7)$ microspheres as low-cost and high-performance cathode materials for sodium-ion batteries. *Nano Energy* **2019**, *56*, 160-168.
197. Wang, L.; Song, J.; Qiao, R.; Wray, L. A.; Hossain, M. A.; Chuang, Y.-D.; Yang, W.; Lu, Y.; Evans, D.; Lee, J.-J.; Vail, S.; Zhao, X.; Nishijima, M.; Kakimoto, S.; Goodenough, J. B., Rhombohedral Prussian White as Cathode

- for Rechargeable Sodium-Ion Batteries. *Journal of the American Chemical Society* **2015**, *137*, 2548-2554.
198. Song, J.; Wang, L.; Lu, Y.; Liu, J.; Guo, B.; Xiao, P.; Lee, J.; Yang, X.; Henkelman, G.; Goodenough, J., Removal of interstitial H₂O in hexacyanometallates for superior cathode of sodium-ion battery. *Journal of The American Chemical Society* **2015**, *137*, 2658-2664
199. Brant, W. R.; Mogensen, R.; Colbin, S.; Ojwang, D. O.; Schmid, S.; Häggström, L.; Ericsson, T.; Jaworski, A.; Pell, A. J.; Younesi, R., Selective Control of Composition in Prussian White for Enhanced Material Properties. *Chemistry of Materials* **2019**, *31*, 7203-7211.
200. Maddar, F. M.; Walker, D.; Chamberlain, T. W.; Compton, J.; Menon, A. S.; Copley, M.; Hasa, I., Understanding dehydration of Prussian white: from material to aqueous processed composite electrodes for sodium-ion battery application. *Journal of Materials Chemistry A* **2023**, *11*, 15778-15791.
201. Fernández-Roperro, A. J.; Piernas-Muñoz, M. J.; Castillo-Martínez, E.; Rojo, T.; Casas-Cabanas, M., Electrochemical characterization of NaFe₂(CN)₆ Prussian Blue as positive electrode for aqueous sodium-ion batteries. *Electrochimica Acta* **2016**, *210*, 352-357.
202. Lucero, M.; Armitage, D. B.; Yang, X.; Sandstrom, S. K.; Lyons, M.; Davis, R. C.; Sterbinsky, G. E.; Kim, N.; Reed, D. M.; Ji, X.; Li, X.; Feng, Z., Ball Milling-Enabled Fe^{2.4+} to Fe³⁺ Redox Reaction in Prussian Blue Materials for Long-Life Aqueous Sodium-Ion Batteries. *ACS Applied Materials & Interfaces* **2023**, *15*, 36366-36372.
203. Masquelier, C.; d'Yvoire, F.; Rodier, N., Crystal structure of the sodium ion conductor α -Na₇Fe₃(P₂O₇)₄: Evidence for a long-range ordering of the Na⁺ ions. *Journal of Solid State Chemistry* **1991**, *95*, 156-167.
204. Chen, M.; Hua, W.; Xiao, J.; Cortie, D.; Chen, W.; Wang, E.; Hu, Z.; Gu, Q.; Wang, X.; Indris, S.; Chou, S.-L.; Dou, S.-X., NASICON-type air-stable and all-climate cathode for sodium-ion batteries with low cost and high-power density. *Nature Communications* **2019**, *10*, 1480.
205. Angenault, J.; Counturier, J. -C.; Querton, M.; Robert, F., Structure of Na_{3.12}Fe_{2.44}(P₂O₇)₂. *ChemInform* **1995**, *26*.
206. Wang, W.; Gang, Y.; Hu, Z.; Yan, Z.; Li, W.; Li, Y.; Gu, Q.-F.; Wang, Z.; Chou, S.-L.; Liu, H.-K.; Dou, S.-X., Reversible structural evolution of sodium-rich rhombohedral Prussian blue for sodium-ion batteries. *Nature Communications* **2020**, *11*, 980.
207. Cao, Y.; Liu, Y.; Zhao, D.; Xia, X.; Zhang, L.; Zhang, J.; Yang, H.; Xia, Y., Highly Stable Na₃Fe₂(PO₄)₃@Hard Carbon Sodium-Ion Full Cell for Low-Cost Energy Storage. *ACS Sustainable Chemistry & Engineering* **2020**, *8*, 1380-1387.

208. Ma, X.; Pan, Z.; Wu, X.; Shen, P. K., $\text{Na}_4\text{Fe}_3(\text{PO}_4)_2(\text{P}_2\text{O}_7)@\text{NaFePO}_4@\text{C}$ core-double-shell architectures on carbon cloth: A high-rate, ultrastable, and flexible cathode for sodium ion batteries. *Chemical Engineering Journal* **2019**, *365*, 132-141.
209. Ma, X.; Wu, X.; Shen, P., Rational Design of $\text{Na}_4\text{Fe}_3(\text{PO}_4)_2(\text{P}_2\text{O}_7)$ Nanoparticles Embedded in Graphene: Toward Fast Sodium Storage Through the Pseudocapacitive Effect. *ACS Applied Energy Materials* **2018**, *1*, 6268-6278.
210. Radtke, V.; Stoica, D.; Leito, I.; Camões, F.; Krossing, I.; Anes, B.; Roziková, M.; Deleebeeck, L.; Veltzé, S.; Näykki, T.; Bastkowski, F.; Heering, A.; Dániel, N.; Quendera, R.; Liv, L.; Uysal, E.; Lawrence, N., A unified pH scale for all solvents: part I – intention and reasoning (IUPAC Technical Report). *Pure and Applied Chemistry* **2021**, *93*, 1049-1060.
211. Li, C.; Wang, X.; Deng, W.; Liu, C.; Chen, J.; Li, R.; Xue, M., Size Engineering and Crystallinity Control Enable High-Capacity Aqueous Potassium-Ion Storage of Prussian White Analogues. *ChemElectroChem* **2018**, *5*, 3887-3892.
212. Sui, Y.; Ji, X., Anticatalytic Strategies to Suppress Water Electrolysis in Aqueous Batteries. *Chemical Reviews* **2021**, *121*, 6654-6695.
213. Salazar, P.; Martín, M.; O'Neill, R. D.; Roche, R.; González-Mora, J. L., Improvement and characterization of surfactant-modified Prussian blue screen-printed carbon electrodes for selective H_2O_2 detection at low applied potentials. *Journal of Electroanalytical Chemistry* **2012**, *674*, 48-56.
214. Wang, Q.; Xu, J.; Zhang, W.; Mao, M.; Wei, Z.; Wang, L.; Cui, C.; Zhu, Y.; Ma, J., Research progress on vanadium-based cathode materials for sodium ion batteries. *Journal of Materials Chemistry A* **2018**, *6*, 8815-8838.
215. Raju, V.; Rains, J.; Gates, C.; Luo, W.; Wang, X.; Stickle, W. F.; Stucky, G. D.; Ji, X., Superior Cathode of Sodium-Ion Batteries: Orthorhombic V_2O_5 Nanoparticles Generated in Nanoporous Carbon by Ambient Hydrolysis Deposition. *Nano Letters* **2014**, *14*, 4119-4124.
216. Hamani, D.; Ati, M.; Tarascon, J.-M.; Rozier, P., NaVO_2 as possible electrode for Na-ion batteries. *Electrochemistry Communications* **2011**, *13*, 938-941.
217. Song, W.; Ji, X.; Zhu, Y.; Zhu, H.; Li, F.; Chen, J.; Lu, F.; Yao, Y.; Banks, C. E., Aqueous Sodium-Ion Battery using a $\text{Na}_3\text{V}_2(\text{PO}_4)_3$ Electrode. *ChemElectroChem* **2014**, *1*, 871-876.
218. Law, M.; Balaya, P., NaVPO_4F with high cycling stability as a promising cathode for sodium-ion battery. *Energy Storage Materials* **2018**, *10*, 102-113.

219. Wei, Q.; DeBlock, R. H.; Butts, D. M.; Choi, C.; Dunn, B., Pseudocapacitive Vanadium-based Materials toward High-Rate Sodium-Ion Storage. *Energy & Environmental Materials* **2020**, *3*, 221-234.
220. Tang, L.; Zhang, J.; Li, Z.; Liu, X.; Xu, Q.; Liu, H.; Wang, Y.; Xia, Y.; Ma, Z., Using $\text{Na}_7\text{V}_4(\text{P}_2\text{O}_7)_4(\text{PO}_4)$ with superior Na storage performance as bipolar electrodes to build a novel high-energy-density symmetric sodium-ion full battery. *Journal of Power Sources* **2020**, *451*, 227734.
221. Lim, S. Y.; Kim, H.; Chung, J.; Lee, J. H.; Kim, B. G.; Choi, J. J.; Chung, K. Y.; Cho, W.; Kim, S. J.; Goddard, W. A., 3rd; Jung, Y.; Choi, J. W., Role of intermediate phase for stable cycling of $\text{Na}_7\text{V}_4(\text{P}_2\text{O}_7)_4\text{PO}_4$ in sodium ion battery. *Proc Natl Acad Sci U S A* **2014**, *111*, 599-604.
222. Deng, C.; Zhang, S., 1D Nanostructured $\text{Na}_7\text{V}_4(\text{P}_2\text{O}_7)_4(\text{PO}_4)$ as High-Potential and Superior-Performance Cathode Material for Sodium-Ion Batteries. *ACS Applied Materials & Interfaces* **2014**, *6*, 9111-9117.
223. Deng, C.; Zhang, S.; Wu, Y., Hydrothermal-assisted synthesis of the $\text{Na}_7\text{V}_4(\text{P}_2\text{O}_7)_4(\text{PO}_4)/\text{C}$ nanorod and its fast sodium intercalation chemistry in aqueous rechargeable sodium batteries. *Nanoscale* **2015**, *7*, 487-491.
224. Zhang, L.-m.; Ren, N.-Q.; Wang, S.; Deng, W.-J.; Chen, F.; Wen, Z.-Y.; Chen, C.-H., Submicrometer Rod-Structured $\text{Na}_7\text{V}_4(\text{P}_2\text{O}_7)_4(\text{PO}_4)/\text{C}$ as a Cathode Material for Sodium-Ion Batteries. *ACS Applied Energy Materials* **2021**, *4*, 10298-10305.
225. Fang, W.; An, Z.; Xu, J.; Zhao, H.; Zhang, J., Superior performance of $\text{Na}_7\text{V}_4(\text{P}_2\text{O}_7)_4\text{PO}_4$ in sodium ion batteries. *RSC Advances* **2018**, *8*, 21224-21228.
226. Zlatovskiy, I. V., NASICON-type $\text{Na}_3\text{V}_2(\text{PO}_4)_3$. *Acta Crystallographica Section E: Crystallographic Communications* **2010**, *E66*.
227. Wang Y.P., L. K.-H., Wang S.-L., Structure of $\text{Na V P}_2 \text{O}_7$. *Acta Crystallographica C* **1989**, *45*, 1417-1418.
228. Zhang, H.; Qin, B.; Buchholz, D.; Passerini, S., High-Efficiency Sodium-Ion Battery Based on NASICON Electrodes with High Power and Long Lifespan. *ACS Applied Energy Materials* **2018**, *1*, 6425-6432.
229. Davit Tediashvili, J. P., Jurga Juodkazytė, Linas Vilčiauskas, On the degradation of vanadium-based phosphate framework electrode materials in aqueous environments. *ECSarXiv* **2023**.
230. Snarskis, G.; Pilipavičius, J.; Gryaznov, D.; Mikoliūnaitė, L.; Vilčiauskas, L., Peculiarities of Phase Formation in Mn-Based Na SuperIonic Conductor (NaSICON) Systems: The Case of $\text{Na}_{1+2x}\text{Mn}_x\text{Ti}_{2-x}(\text{PO}_4)_3$ ($0.0 \leq x \leq 1.5$). *Chemistry of Materials* **2021**, *33*, 8394-8403.

231. Gao, H.; Goodenough, J. B., An aqueous symmetric sodium-ion battery with NASICON-structured $\text{Na}_3\text{MnTi}(\text{PO}_4)_3$. *Angewandte Chemie* **2016**, *128*, 12960-12964.
232. Gao, H.; Seymour, I. D.; Xin, S.; Xue, L.; Henkelman, G.; Goodenough, J. B., $\text{Na}_3\text{MnZr}(\text{PO}_4)_3$: A High-Voltage Cathode for Sodium Batteries. *Journal of the American Chemical Society* **2018**, *140*, 18192-18199.
233. Chen, F.; Kovrugin, V. M.; David, R.; Mentré, O.; Fauth, F.; Chotard, J.-N.; Masquelier, C., A NASICON-Type Positive Electrode for Na Batteries with High Energy Density: $\text{Na}_4\text{MnV}(\text{PO}_4)_3$. *Small Methods* **2019**, *3*, 1800218.
234. Petrulėvičienė, M.; Pilipavičius, J.; Juodkazytė, J.; Gryaznov, D.; Vilčiauskas, L., Electrochemical Performance of NASICON-structured $\text{Na}_{3-x}\text{V}_{2-x}\text{Ti}_x(\text{PO}_4)_3$ ($0.0 < x < 1.0$) as aqueous Na-ion battery positive electrodes. *Electrochimica Acta* **2022**, *424*, 140580.
235. Hadouchi, M.; Yaqoob, N.; Kaghazchi, P.; Tang, M.; Liu, J.; Sang, P.; Fu, Y.; Huang, Y.; Ma, J., Fast sodium intercalation in $\text{Na}_{3.41}\text{Fe}_{0.59}\text{V}(\text{PO}_4)_3$: A novel sodium-deficient NASICON cathode for sodium-ion batteries. *Energy Storage Materials* **2021**, *35*, 192-202.
236. Park, S.; Chotard, J.-N.; Carlier, D.; Moog, I.; Courty, M.; Duttine, M.; Fauth, F.; Iadecola, A.; Croguennec, L.; Masquelier, C., Crystal Structures and Local Environments of NASICON-Type $\text{Na}_3\text{FeV}(\text{PO}_4)_3$ and $\text{Na}_4\text{FeV}(\text{PO}_4)_3$ Positive Electrode Materials for Na-Ion Batteries. *Chemistry of Materials* **2021**, *33*, 5355-5367.
237. Park, S.; Chotard, J.-N.; Carlier, D.; Moog, I.; Duttine, M.; Fauth, F.; Iadecola, A.; Croguennec, L.; Masquelier, C., An Asymmetric Sodium Extraction/Insertion Mechanism for the Fe/V-Mixed NASICON $\text{Na}_4\text{FeV}(\text{PO}_4)_3$. *Chemistry of Materials* **2022**, *34*, 4142-4152.
238. Zhou, W.; Xue, L.; Lü, X.; Gao, H.; Li, Y.; Xin, S.; Fu, G.; Cui, Z.; Zhu, Y.; Goodenough, J. B., $\text{Na}_x\text{MV}(\text{PO}_4)_3$ (M = Mn, Fe, Ni) Structure and Properties for Sodium Extraction. *Nano Letters* **2016**, *16*, 7836-7841.
239. Barpanda, P.; Liu, G.; Ling, C. D.; Tamaru, M.; Avdeev, M.; Chung, S.-C.; Yamada, Y.; Yamada, A., $\text{Na}_2\text{FeP}_2\text{O}_7$: A Safe Cathode for Rechargeable Sodium-ion Batteries. *Chemistry of Materials* **2013**, *25*, 3480-3487.

Vilnius University Press
Saulėtekio Ave., 9, Building III, LT-10222 Vilnius
mail: info@leidykla.vu.lt, www.leidykla.vu.lt
bookshop.vu.lt, journals.vu.lt
Print run copies 35